

NBSIR 87-3630

Composite Materials Interface Characterization

H. N. G. Wadley, J. A. Simmons, R. B. Clough, F. Biancaniello,
E. Drescher-Krasicka, M. Rosen, T. Hsieh, and K. Hirschman

U.S. DEPARTMENT OF COMMERCE
National Bureau of Standards
Institute for Materials Science and Engineering
Gaithersburg, MD 20899

March 1988



Stimulating America's Progress
1913-1988

U.S. DEPARTMENT OF COMMERCE
NATIONAL BUREAU OF STANDARDS

NBSIR 87-3630

COMPOSITE MATERIALS INTERFACE CHARACTERIZATION

H. N. G. Wadley, J. A. Simmons, R. B. Clough, F. Biancaniello,
E. Drescher-Krasicka, M. Rosen, T. Hsieh, and K. Hirschman

U.S. DEPARTMENT OF COMMERCE
National Bureau of Standards
Institute for Materials Science and Engineering
Gaithersburg, MD 20899

March 1988

U.S. DEPARTMENT OF COMMERCE, C. William Verity, *Secretary*
NATIONAL BUREAU OF STANDARDS, Ernest Ambler, *Director*

**This program supported by the Strategic Defense Initiative
Office/Innovative Science and Technology under
ONR Contract N00014-85-F-0087
Program Monitor Dr. S.G. Fishman**

TABLE OF CONTENTS

Table of Contents	i
1. Executive Summary	1
2. Introduction	3
2.1 Interface Elastic Properties.	5
2.2 Interface Adhesion.	6
3. Calculation of Ultrasonic Scattering and Guided Interface Waves from Near-interface Properties.	8
3.1 General Theory for an Isolated Interphase	9
3.1.1 Constitutive Relations.	11
3.1.2 Conservation Relations.	13
3.1.3 The Boundary Conditions and the Propagation Vector.	14
3.1.4 Equations of Motion as Propagation Equations.	16
3.1.5 Energy Flow and Group Velocity.	17
3.1.6 Representation of Eigenwaves Outside the Interphase	19
3.1.7 The Scattering Matrix.	22
3.1.8 Normal Modes and Leaky Waves	26
3.2 Cylindrical Interfaces	29
3.2.1 Basic Equations.	29
3.2.2 Propagation Equations in Cylindrical Coordinates	31
3.2.3 Potential Functions and the Bessel Representation for Eigenwaves in Regions I and III.	33
3.2.4 Radial Mode Interface Waves.	36
3.3 Future Directions.	40
3.4 References	41
4. Experimental Study of Guided Interface Waves	42
4.1 Planar Interfaces.	42
4.1.1 Background Research.	43
4.1.2 Measurement Methodology.	46
4.1.3 Experimental Results	48
4.1.4 Discussion	50
4.1.5 Summary of Results for Planar Interface.	54

4.2	Cylindrical Interfaces	54
4.2.1	Wave Propagation of Embedded Cylinders	55
4.2.2	Aluminum-Steel Interfaces.	61
4.2.3	Aluminum-SiC Interfaces.	65
4.3	Future Directions.	67
4.4	References	68
5.	Acoustic Emission Assisted Measurement of Fiber and Interface Strength	69
5.1	Microscopic Origins of Acoustic Emission	69
5.2	Fibrous Composite Fracture Micromechanisms	71
5.2.1	Load Transfer from the Matrix to the Fiber	71
5.2.2	Micromechanics of Fiber and Interface Fracture	73
5.2.3	Interphase Effects on Fiber Fracture	78
5.3	Model Experimental Approach.	80
5.4	Discussion	84
5.5	Future Directions.	89
5.6	References	91
	Appendix I.	93

1. Executive Summary

The designs for many of tomorrow's defense systems cannot be implemented with the materials available today. Lighter, stiffer, stronger materials with higher temperature stability are required. A new generation of advanced composites with metal and even ceramic matrices show the greatest promise for satisfying many of these needs. Early attempts at processing these materials met with mixed success. The properties needed have in some cases come close to fulfillment, but other batches of material have been found to exhibit very poor behavior. Micromechanical modeling studies have directed attention to the microscopic interfaces between matrix and reinforcement. Bulk behavior has been predicted to be strongly influenced by the local elastic properties, residual stresses and adhesion of the interface. Techniques to measure these newly perceived quantities of importance do not exist. Thus it is not possible experimentally to (i) confirm the micromechanical model predictions, (ii) explore the relationships between interface properties and processing variables and (iii) ensure acceptable interface properties in materials destined for defense systems.

This research program is directed at developing experimental techniques for characterizing interfaces in composite materials and coupling this expertise to other ONR composite programs to enable optimum interfaces to be designed for the next generation of advanced composites. We have explored two approaches, guided interface waves and acoustic emission. The former refers to a family of ultrasonic techniques with potential for characterizing interface elastic and anelastic properties. The latter utilizes acoustic emission to provide measurements of the adhesion of an interface.

This year, we have achieved the following substantial achievements:

- o Formulation of the ultrasonic scattering/interface wave propagation problem for a general interface.
- o Theoretical prediction of the suspected existence of guided interface waves at model Al-Fe, Al-SiC, Al-B, and Al-Graphite cylindrical interfaces. The velocity was found to contain both real and imaginary components. The values of both were calculated as functions of frequency and cylinder radius.
- o Experimental verification of the theoretically predicted real part of the velocity for model Al-Fe and Al-SiC cylindrical interfaces and detection of leaky radiation due to the non-zero imaginary velocity component.
- o Determination of the effect of microstructure and stress upon the velocity of pure Stoneley waves at planar Fe-Ti interfaces.
- o Development of an experimental approach using composite single crystals to determine interface and fiber mechanical properties in both metal and ceramic matrix composites.
- o Determination of SiC fiber strength and Al-SiC interface shear strengths in model single crystal composites as a function of liquid metal-SiC contact time during processing.

These achievements have, we believe, significantly advanced us toward our goal of determining the elastic properties and adhesion of interfaces in advanced composites. We have begun to devise schemes for implementing these approaches on actual composites. In our future work, we propose to evaluate these methods and develop data from the advanced composites developed in the SDIO/IST Consortium.

2. Introduction

The materials needs of tomorrow's defense systems cannot be met with the materials available to us today. Greater specific stiffness, higher strength, creep resistance at high temperature and better corrosion resistance are needed for future materials. These properties are beyond the reach of traditional metals and alloys, and ceramics suffer from high mass density and low temperature brittleness. Advanced composites, composed from either metal or ceramic matrices with graphite, Al_2O_3 , B_4C and SiC reinforcement, show great promise of satisfying many of our future materials needs.

Because of the dissimilar chemical and physical properties (particularly thermal expansion coefficient differences) of advanced composite constituents, extensive chemical reactions and residual stresses can be found at the internal interfaces between matrix and reinforcements. The strong local stresses, due to elastic inhomogeneity, that result during subsequent loading interact with the weakened interface to retard the load bearing and fracture resisting mechanisms of advanced composites. Micromechanical modeling of these processes is revealing the need for optimized interface properties to realize the full potential of these composites.

Among the properties of greatest importance are the local elastic properties at and near the interface, the adhesion between matrix and reinforcement and the residual stress distribution in and around the reinforcement. The measurement of these quantities with a spatial resolution on the order of 1-10 μm is required if the interaction between interface and bulk behavior is to be fully understood, and processing schemes for interface optimization developed.

These measurement needs are a great challenge. No methods exist for measuring these quantities at the microscopic level needed for composites. Bulk methods of modulus measurement using either static or dynamic loads, yield a poorly defined "average" modulus in multiple fiber composites, and the techniques of Broutman et al. that were developed for adhesion measurements in transparent polymer-based composites fail in opaque metal/ceramic matrices.

The purpose of the NBS/JHU program is to (i) develop methods for the in-situ characterization of interfaces in metal (and, perhaps later, ceramic) matrix composites, (ii) use these in-situ techniques to better understand the micromechanics of composites and (iii) explore the relationships between process variables and interface properties. It is our view that this approach will allow optimization of interface properties and maximize exploitation of advanced composites.

The measurement of the quantities of import: local elastic properties, adhesion and residual stress, were initially being addressed through three techniques:

- o Guided Interface Waves (GIWs) to determine the local elastic properties.
- o Acoustic emission to determine the local adhesion.
- o Energy dispersive x-ray diffractometry to determine local residual stresses.

Funding cut-backs have regrettably forced temporary curtailment of the third technique, residual stress profiling, even though proof of concept experiments were successful (see first Progress Report).

2.1 Interface Elastic Properties

The aim of the GIW study is to use the measured propagation velocity to determine the elastic constants (moduli) of the interface. It is an extension of the procedure utilized in solid state physics to determine the single crystal elastic constants by measuring the velocities of longitudinal and transverse bulk ultrasonic waves. The extension to interfaces is a challenging topic not devoid of considerable risk.

Important milestones for this approach include:

- o Confirmation of the existence of interface waves at the metal-ceramic interfaces of importance in MMCs.
- o Calculation and experimental confirmation of GIW characteristics from the near-interface elastic (and anelastic) properties.
- o Exploration of the effects of reinforcement geometry upon GIW velocity expressions.
- o Development of robust inverse methods for determination of near-interface elastic properties from GIW measurements.
- o Establishment of GIW measurement methods at the μm size range.

Each milestone carries with it the responsibility to apply the information gained to MMCs being studied in other parts of the SDI/SDIO Advanced Composites Consortium.

In sections 3 and 4 we report on our progress toward fulfilling the first three of our milestones. While much still remains to be done, we have found that interface waves do exist at metal-ceramic interfaces in all composite systems studied. The effect of cylindrical fiber geometry has

been thoroughly explored and found to provide new opportunities for ultrasonic characterization. We also have reason to suspect that a modified form of acoustic microscopy may facilitate velocity measurement at the μm scale, and are beginning to explore the nature of the inverse problem.

Our approach has deliberately been a general one. The additional complexity introduced to the mathematical modeling is acceptable since the resultant measurement methodologies promise to reveal anelastic behavior and interface defects as well as elastic properties. This approach has been carefully risk managed, however, by first solving restrictive subsets of the general problem and experimentally confirming their solutions. This coupling of theory and experiment is turning out to be a productive approach to this complex research topic.

2.2 Interface Adhesion

Adhesion at interfaces in MMCs is being explored through the use of acoustic emission techniques applied to specially designed test samples. We are using acoustic emission as a means for detecting, locating and characterizing individual interface or fiber failures in MMCs. The load at which each emission is generated is related to the local stress at the fracture site, thus allowing determination of the local strength, provided the fiber/matrix geometry is simple and well defined.

Our research to date has utilized single SiC fibers embedded in aluminum single crystal matrices to make tractable the stress analysis. The aluminum single crystal matrix is extremely soft and provides a starting point from which we may also investigate the effect of matrix properties (by alloying) upon the micromechanisms of interface failure independent of the interface state. The high purity of the matrix also provides a starting point from which we may investigate interface segregation and interphase formation; and the system provides us with the opportunity to

explore the role of interphases upon adhesion by varying the temperature and time of contact of either liquid aluminum with SiC or other combinations of interest to ONR. All of these effects can be studied independently of fiber-fiber stress interactions. Conversely, having once established the behavior for single fibers, we can begin to study the role of fiber-fiber interactions, again independently of other effects.

3. Calculation of Ultrasonic Scattering and Guided Interface Waves from Near-interface Properties

In this part of our program, we want to determine the elastic properties of the interphase by utilizing data gathered through propagating ultrasonic waves across or along interfaces in MMCs which have an interphase region between the reinforcement and matrix phases. Our strategy has been to construct a general model of the interphase from which ultrasonic wave behavior can be calculated while pursuing a practically important subproblem in parallel.

The solution for the general model will then be used for solving specific inverse problems to quantify interphase properties.

A model composite may be thought of as having either a layered, fibrous or particulate configuration. In our program we are especially interested in the physics near an interface. However, in models with many layers, fibers or particles, multiple scattering between reinforcements can obscure wave behavior associated to individual interphases. Consequently our model will concentrate on a single reinforcing element embedded in a matrix. In the idealized layered case, this would involve two planar half-spaces separated by an interphase layer; the fibrous model would be that of a cylinder surrounded by an interphase layer and embedded in a matrix, while the particulate case would be of a similar nature but with a spheroidal particle.

For layered or fibrous models, the wavelength is not limited to the μm range, because the reinforcing material can be of macroscopic size in at least one direction. The particulate case does not have this feature and so requires very high frequency waves to interrogate individual particle/interphase configurations. While such experimental

measurements are possible, they are not yet at hand. So the formulation as given, while encompassing the particulate geometry, will center on the layered and fibrous cases.

In section 3.1 we develop the general theory and exemplify it using the planar geometry of the layered model. (Section 4.1 deals with an experimental application of Stoneley waves in the planar geometry.) Section 3.2 examines the cylindrical geometry of the fibrous composite and gives detailed expressions, including leaky wave predictions, for the special case of perfect bonding (no interphase) involving isotropic media. (Section 4.2 gives experimental confirmation to the leaky wave calculations of section 3.2 and points toward exciting novel applications of these waves.) Section 3.3 discusses possible directions for future theoretical work.

3.1 General Theory for an Isolated Interphase

In this section we set forth the basic elements needed to determine both ultrasonic scattering from guided wave motion along composite interphases of thickness down to atomic dimensions and illustrate it for the case of planar interfaces.

We first give the geometric model for the composite material with interphase. A general set of constitutive relations from which ultrasonic wave behavior can be computed is then set out. Conservation relations, yielding three invariants of motion (frequency and two slownesses) follow from the geometry of the model and the equations of motion. They allow us to express the result of any scattering or interface wave experiment in terms of the superposition of monochromatic eigenwaves characteristic of the composite structure.

An eigenwave is the simplest type of monochromatic wave which can travel through the infinite composite medium without internal stimulus, the energy being supplied at infinity. The name derives from the time separated wave equation giving rise to a generalized type of Helmholtz equation from which these waves arise as eigenfunctions. The remainder of the section concentrates on calculating these eigenwaves, which are themselves physically measurable. Each of these eigenwaves is shown to be determined everywhere in the composite by specifying its three displacements and three displacement derivatives (in a direction normal to the interface) at any single point in the composite. The method for calculating the energy flow, needed for many ultrasonic experiments, is given for any eigenwave.

Each eigenwave has a fixed representation in either the matrix or the reinforcement. This is shown in the plane interface example using the natural plane waves for each region. The relationship between these two representations defines a transformation matrix. Distinguishing the incoming from the outgoing components in an eigenwave allows us to write down the scattering matrix which, from a different perspective, shows how each eigenwave may be thought of as a complete scattering experiment with both inputs and outputs. Interface waves are shown to arise under conditions where the scattering matrix fails to exist, because, physically, such waves need no external energy source from the bulk material, only from along the interface at infinity. Stoneley waves are specifically discussed, but this general approach indicates that there is a rich variety of other interface waves which might be experimentally detectable, and therein provide a means for characterizing the interphase. A number of such waves are discussed in the context of experimental results in sections 4.1 and 4.2.

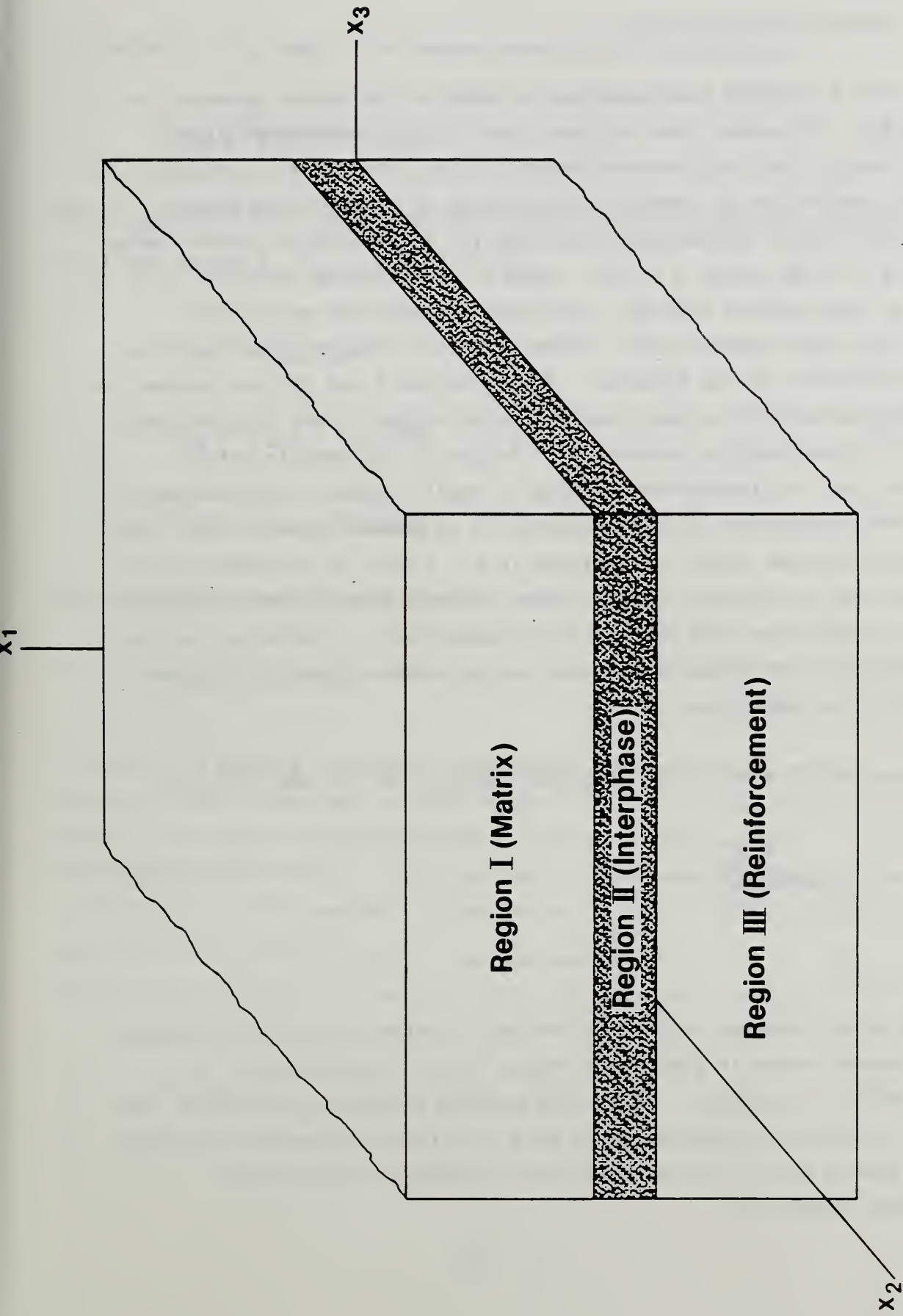


Fig. 3.1 Schematic representation of a planar interfacial region (interphase) sandwiched between two materials.

3.1.1 Constitutive Relations

The I-II-III sandwich configuration is shown in the planar geometry in Figure 3.1. We assume that regions I and III are homogeneous linear elastic matrix and reinforcement media with an interphase of material II. We then seek to use as general a description of region II as possible consistent with a one-parameter solution for scattering of elastic waves entering II from either I or III. Such a "constitutive relation" will have the same general form for the planar, fibrous and particulate models, but each geometry will impose different symmetry constraints on the coefficients of the relation. Here, regions I and III are assumed to be linear anisotropic elastic solids, while region II may be anisotropic elastic, viscoelastic or anelastic.¹ Region II may contain defects provided that the interdefect spacing is small compared with wavelength. The elastic properties in all regions will be assumed constant over each of a one-parameter family of surfaces (e.g., planes or cylinders) which fill out the interfacial region. These surfaces must possess certain symmetry properties with respect to the equations of elasticity, so that we have restricted ourselves to considering such surfaces to be planar, cylindrical or spheroidal.

The equations of elasticity for either region I or III take the form:

$$C_{ijkl} \frac{\partial^2 u_k}{\partial x_l \partial x_j} = \rho \frac{\partial^2 u_i}{\partial t^2} \quad (1a)$$

¹It may be of interest to include anelastic dislocation motion produced by ultrasonic waves in a matrix stressed beyond its yield point by differential CTE effects. This would involve a slight extension of the matrix constitutive relation which does not affect the general features of the theory at all and has only been excluded for the sake of notational simplicity.

or, using "j", "l" and "t" to denote partial differentiation,

$$C_{ijkl} u_{k,jl} = \rho u_{i,tt} \quad (1b)$$

Here C_{ijkl} represent the linear, generally anisotropic elastic constants in either region I, C_{ijkl}^I , or III, C_{ijkl}^{III} .

$$\sigma_{ij} = C_{ijkl} \epsilon_{kl} \quad (1c)$$

$$\epsilon_{kl} = (u_{k,l} + u_{l,k})/2 \quad (1d)$$

$$C_{ijkl} = C_{klij} = C_{ijlk} \quad (1e)$$

with potential elastic energy density given by

$$\frac{1}{2} \epsilon_{ij} C_{ijkl} \epsilon_{kl} \quad (1f)$$

To permit the maximum latitude in describing the interfacial region II within a linear formalism, we shall allow it to be a linear viscoelastic material, so that it includes ordinary elasticity and possible dislocation anelasticity. The properties of the medium can vary in the x_1 direction, but are assumed independent of x_2 and x_3 (the inclusion of local scattering centers will not be discussed in this report). The constitutive relation for the interfacial region takes the form:

$$\sigma_{ij}(\underline{x}, t) = \int_{-\infty}^{\infty} C_{ijkl}^{II}(x_1, t) u_{k,l}(\underline{x}, t-\tau) d\tau \quad (2a)$$

or

$$\sigma_{ij} = C_{ijkl}^{II} * u_{k,\ell} \quad (2b)$$

where * denotes convolution in time [1]. Here C_{ijkl}^{II} depends only on t and the space variable x_1 with $C_{ijkl}^{II}(x_1, t) \equiv 0$ for $t < 0$. Note that C_{ijkl}^{II} has a delta function component at $t = 0$ which gives the ordinary elastic response.

For $t < 0$ in the constitutive equation, no disturbance has occurred and \underline{u} is zero, so that the integral in equation (2a) actually only extends between the limits 0 and t . However, equation (2b) can be Fourier transformed and written in terms of frequency, ω :

$$\sigma_{ij}(\underline{x}, \omega) = C_{ijkl}^{II}(x_1, \omega) u_{k,\ell_j}(\underline{x}, \omega) \quad (2c)$$

thus removing the convolution in time and producing a simpler, frequency by frequency, constitutive relation. Note that this constitutive relation reduces to ordinary linear homogeneous anisotropic elasticity if C_{ijkl}^{II} is independent of x_1 and ω , i.e., $C_{ijkl}^{II}(x_1, \omega) = C_{ijkl}^{II}$.

3.1.2 Conservation Relations

The conservation relations follow from well-known techniques used in wave scattering theory. If we write down the elasticity operator

$$L(u) \equiv \frac{\partial}{\partial x_j} \left[C_{ijkl} * \frac{\partial u}{\partial x_\ell} \right] - \frac{\partial^2 u_i}{\partial t^2} \quad (3a)$$

and the three homogeneous shift operators:

$$S_{x_2^0} \left[u(x_1, x_2, x_3, t) \right] = u(x_1, x_2 + x_2^0, x_3, t) \quad (3b)$$

$$S_{x_3^0} \left[u(x_1, x_2, x_3, t) \right] = u(x_1, x_2, x_2 + x_3^0, t) \quad (3c)$$

$$S_{t_0} \left[u(x_1, x_2, x_3, t) \right] = u(x_1, x_2, x_3, t + t_0) \quad (3d)$$

then all four operators commute and, consequently, under quite general conditions, can be simultaneously diagonalized. We can then use the exponential eigenfunctions of the shift operators to represent the harmonic eigenwaves of the entire I-II-III ensemble:

$$\varphi(\underline{x}, t) = \text{Real} \left[\exp \left[i\omega(t - s_2 x_2 - s_3 x_3) \right] \underline{f}(x_1) \right] \quad (4)$$

where the frequency ω and the "slowness" values s_2 and s_3 are fixed constants for any eigenwave -- that is, they are conserved during the passage of the eigenwave φ through the sandwich.

3.1.3 The Boundary Conditions and the Propagation Vector

The geometries with which we are dealing are characterized by a one-parameter family of surfaces (planar, cylindrical or spheroidal) on each of which the material properties are assumed constant, only varying in the direction of the interface normal. The boundary conditions for a slab of such material are usually given by specifying a linear combination of the normal tractions and displacements on each of two bounding surfaces, thus giving three boundary conditions on each of two

surfaces, or six conditions in all. In the scattering formalism we allow the material to be of infinite extent, ignore the boundary conditions at infinity (which will be taken into account later), and instead determine the wave function by specifying six conditions on one surface, i.e., the three displacements and the three components of stress across the surface (normal tractions) -- the three in-plane stresses are not restricted, and can even be discontinuous on occasion. The conservation relations are then invoked to simplify the eigenwave, φ , and the equations of motion are used to propagate it through the material.

Let us consider the plane $x_1 = x_1^0$ in the planar geometry and write, using equations (2) and (4), the displacements and normal tractions on that surface. The displacements are given by

$$2u_i = 2 \operatorname{Real} \left[\exp \left[i\omega(t - s_2 x_2 - s_3 x_3) \right] f_i(x_1) \right] + \exp \left[-i\omega(t - s_2 x_2 - s_3 x_3) \right] \bar{f}_i(x_1) \quad (5)$$

when " — " denotes complex conjugate and the tractions are given by

$$\begin{aligned} 2\tau_i &= C_{i1k\ell}^* \left[-i\omega s_\ell \exp \left[i\omega(t - s_2 x_2 - s_3 x_3) \right] f_{k,1} + i\omega s_\ell \exp \left[-i\omega(t - s_2 x_2 - s_3 x_3) \right] \bar{f}_{k,1} \right] \\ &+ C_{i1k1}^* \left[\exp \left[i\omega(t - s_2 x_2 - s_3 x_3) \right] f_{k,1} + \exp \left[-i\omega(t - s_2 x_2 - s_3 x_3) \right] \bar{f}_{k,1} \right] \\ &= 2 \operatorname{Real} \left[(-i\omega s_\ell \bar{C}_{i1k\ell}(x_1, \omega) f_k(x_1) \right. \\ &\left. + \bar{C}_{i1k1}(x_1, \omega) f_{k,1}(x_1) \right) \exp \left[i\omega(t - s_2 x_2 - s_3 x_3) \right] \right] \quad (6) \end{aligned}$$

Here the index $\ell = 2$ or 3 and $f_{k,1} \equiv df_k(x_1)/dx_1$.

Although these expressions appear complicated, they yield the remarkable result that the displacements and surface tractions are determined over the entire surface $x_1 = x_1^0$ if the values of the displacements and tractions are known at any point on that surface. Thus, if only six complex numbers $f_i(x_1^0)$ and $\tau_i(x_1^0)$ or, equivalently, $f_i(x_1^0)$ and $f_{i,1}(x_1^0)$ are known, the entire wave function φ is determined, although not yet explicitly calculated. We call the six-dimensional vector constructed from either of these sets of six numbers the propagation vector.

The propagation vector, given in terms of displacements and tractions, has been used in geophysics for calculating wave motion through stratified media, and is called the Thompson-Haskell vector. Its continuity across strata is used to calculate the propagating wave [2]. However, we shall find it more convenient to express the propagation vector in terms of the complex vector \underline{f} and its first derivative $f_{i,j}$. Although these determine the Thompson-Haskell vector, they are not strictly determined by it. The vector \underline{f} and its first derivative will also be continuous throughout the medium.

3.1.4 Equations of Motion as Propagation Equations

The equations of motion $\sigma_{ij,j} = \rho u_{i,tt}$ may be written down from equations (5) and (6) by noticing that the expression for τ_i also contains the expression for the full stress σ_{ij} by replacing the index "1", occurring in the elastic constants, with a "j". These expressions only imply the equality of the real parts of two complex expressions, but if we write the more restrictive expressions requiring full complex equality, the

exponential dependence on ω , s_2 and s_3 drops out, producing the equation of motion in the form of a one-dimensional propagation equation:

$$\begin{aligned} \bar{C}_{ilk1} f_{k,11} + \left[\bar{C}_{ilk1,1}^{-i\omega s_\ell} \bar{C}_{ilk\ell} \right] f_{k,1} \\ + \left[\omega^2 \left[\rho \delta_{ik}^{-s_j s_\ell} \bar{C}_{ijk\ell} \right] - i\omega s_\ell \bar{C}_{ilk\ell,1} \right] f_k = 0 \quad (7) \end{aligned}$$

These are homogeneous ordinary differential equations which can be directly integrated to determine ϱ everywhere. Although they at first appear formidable, they can be routinely integrated on today's modern computers provided that the constitutive functions determining $C_{ijk\ell}$ in region II are reasonably well-behaved.

3.1.5 Energy Flow and Group Velocity

Sections 3.1.3 and 3.1.4 describe stress propagation for harmonic eigenwaves. Stress is a linear function of the displacements. In this section we describe the power flow, which is a quadratic function of displacement, for such eigenwaves. We can write down the power flow for a monochromatic elastic wave in terms of the energy change in an arbitrary region V :

$$\begin{aligned} \dot{E} &= \frac{1}{2} \frac{d}{dt} \left[\int_V (C_{ijk\ell}(x_1, \omega) u_{i,j} u_{k,\ell} + \rho \delta_{ij} \dot{u}_i \dot{u}_j) d\underline{x} \right] \\ &= \int_V \left[\rho \delta_{ij} \ddot{u}_j - (C_{ijk\ell}(x_1, \omega) u_{k,\ell})_{,j} \right] \dot{u}_i d\underline{x} + \int_{\partial V} \sigma_{ij} \dot{u}_i d\underline{s}_j \\ &= \int_{\partial V} \sigma_{ij} \dot{u}_i d\underline{s}_j = \int_V (\sigma_{ij} \dot{u}_i)_{,j} d\underline{x} \quad (8) \end{aligned}$$

where the first expression in the second equation of (8) contains the equilibrium equations and, consequently, vanishes. This expression allows us to define the power flow, or Poynting vector, for harmonic elastic waves. Such a vector with components P_j describes the energy per unit area and unit time flowing through a surface with normal in the x_j direction. To these three components of dimension $1/x^2 t$ we can add a fourth component P_0 , which is the total energy density. This component has dimension $1/x^3$ and can be thought of as the time component of the space-time generalization of the Poynting vector:

$$P_0 = E$$

$$P_j = -\sigma_{ij} \dot{u}_i \quad , \quad j = 1,2,3 \quad . \quad (9)$$

In a conservative system this four-dimensional energy flow vector, \underline{P} , is divergence free, $P_{j,j} = 0$. While the spatial component of \underline{P} defines the power flow or elastic Poynting vector, the vector with components P_j/P_0 describes the energy flow velocity field, and is, in fact, the generalized group velocity [3,4].

By integrating \underline{P} through time and over a volume, one can trace the distribution of energy associated to any eigenwave. Usually, however, we shall not be interested in the instantaneous ebb and flow of energy during any cycle, but rather in the time averaged power flow, that is, the power flow integrated over a period. This approach combines with the complex field representation to produce results which have simple physical interpretations. If one draws an arrow with components P_j/P_0 at each point, these arrows not only point in the direction of maximum energy flow, but no energy flows perpendicular to the arrows. Thus, in a

conservative system, starting from a surface at time t_0 , one can use the arrows (vector field) to develop a four-dimensional tube inside of which energy is conserved and from which one can follow the energy transfer.

3.1.6 Representation of Eigenwaves Outside the Interphase

In order to describe scattering across an interphase, we must first find a simple representation for the harmonic eigenwaves in the outer regions. An eigenwave φ takes a particularly simple form in such regions. In the planar geometry, for example, φ can be decomposed into the sum of six plane waves.

To see this decomposition, consider a trial plane wave solution from the infinite body, $\varphi_0 = \underline{p} \exp(i\omega(t - \underline{s} \cdot \underline{x}))$, $\omega \neq 0$, with polarization vector \underline{p} , $|\underline{p}| = 1$, and phase "slowness" vector \underline{s} , each of whose components has dimensions of 1/velocity [2]. Equation (1) then takes the form $C_{ijkl} s_j s_l p_k = \rho p_i$, or $\underline{K} \underline{p} = \rho \underline{p}$, where \underline{K} is the matrix given by

$$K_{ik} = C_{ijkl} s_j s_l \quad . \quad (10)$$

For φ_0 to be a plane wave solution, then, the vector \underline{p} must be an eigenvector of the matrix \underline{K} with eigenvalue ρ . Thus, it must satisfy the determinant equation

$$S(\underline{s}) = |C_{ijkl} s_j s_l - \rho \delta_{ij}| = 0 \quad . \quad (11)$$

The set of real vectors in \underline{s} space satisfying this equation is called the slowness surface.² To determine the eigenfunction φ in region III bounded by the plane at $x_1 = 0$, for example, we seek those plane waves which conserve the quantities ω , s_2 and s_3 . Such waves are those whose s_1 value is obtained by the intersection of the line in \underline{s} space parallel to the s_1 axis and passing through the point $(0, s_2, s_3)$ (Fig. 3.2). This line hits the 6th order slowness surface at six different values for s_1 (some of which may be complex) and thus determines six possible "plane" waves in III which satisfy the conservation relations. It can be shown that all real roots for s_1 occur in pairs such that the Poynting vector for one root points towards the interface while that for the other root points away from the interface. Complex roots appear in conjugate pairs and are associated to "inhomogeneous plane waves" which decay or grow

²Since (11) is a bicubic equation for \underline{s} ($\pm \underline{s}$ are each solutions), the slowness surface is a three-sheeted surface symmetric with respect to reflection through the origin. Positive definitiveness of the energy expression guarantees three independent solutions in every direction in slowness space. This surface determines both phase and group velocity directions for all plane waves in any homogeneous elastic material. In particular: 1) If \underline{x} is some point in real space with magnitude x , and if the vectors in \underline{s} space are scaled in units of x , then the intersection of the slowness surface with the plane perpendicular to \underline{x} and lying at a distance t units from the origin, parameterizes all plane waves passing through the point \underline{x} at time t . 2) The direction of the normal to the slowness surface at any point is parallel to the time-averaged Poynting vector for the associated plane wave, and, therefore, indicates the directions of energy flow for that plane wave [4].

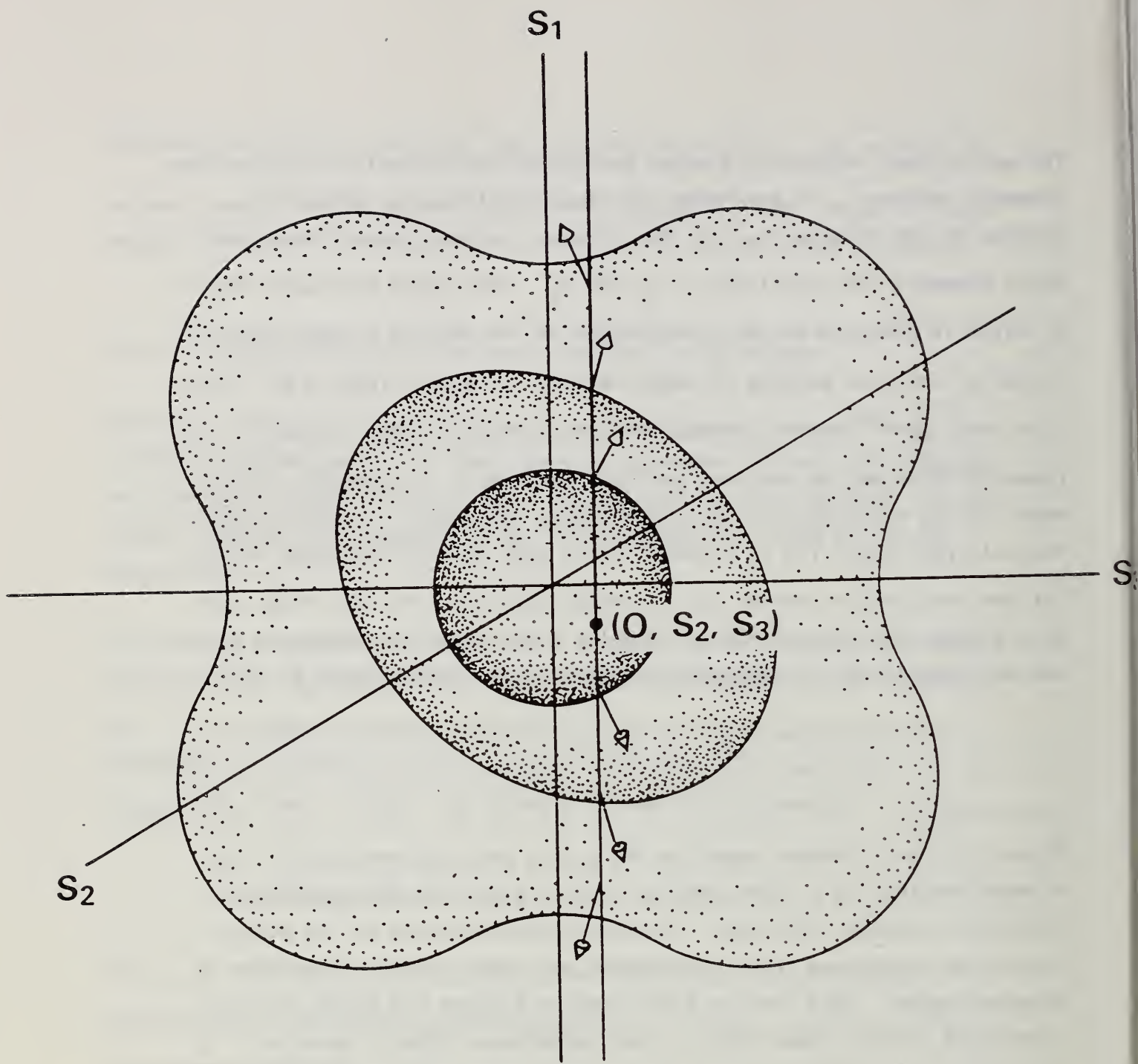


Fig. 3.2 Diagram showing six real plane waves possible in one material during a scattering reaction at an interface. Each of the six points of intersection determines a different possible plane wave. The vectors normal to the slowness surface at each point of intersection give the Poynting vector for that plane wave. Three of the plane waves carry energy towards the interface, and three carry energy away from the interface. Each material needs a separate slowness diagram.

exponentially away from the interface. The time-averaged Poynting vector for such waves is parallel to the interface [4].

The sum of six plane waves in region III can be represented

as $\sum_{M=1}^6 a_M p_M \exp\left[i\omega\left(t-s_1^M x_1 - s_2^M x_2 - s_3^M x_3\right)\right]$, where the a_1, \dots, a_6 are arbitrary

constants. On the plane $x_1 = 0$, we have already seen that φ is

completely determined by the six values of f_k and $f_{k,1}$ at, say, $t = 0$,

$x_2 = 0$ and $x_3 = 0$. We can solve the six linear equations giving the

quantities f_k and $f_{k,1}$ in terms of the unknown constants a_M for the six

constants $a_1^{\text{III}}, \dots, a_6^{\text{III}}$. The function φ represented as the sum of the

six plane waves, $\sum_{M=1}^6 a_M^{\text{III}} p_M \exp\left[i\omega\left(t-s_1^M x_1 - s_2^M x_2 - s_3^M x_3\right)\right]$, is an elastic

eigenwave in all of region III and matches the six boundary conditions

not only at $t = 0$, $x_1 = 0$, $x_2 = 0$, $x_3 = 0$, but for all t , x_2 and x_3 on

the plane $x_1 = 0$, and is, therefore, uniquely determined.

The boundary conditions can also be expressed in terms of the

Thompson-Haskell vector which gives the displacements and normal

tractions on $x_1 = 0$. In that case, if the displacements and tractions

are known at $x_2 = x_3 = t = 0$, then the equations to determine the $a_M^{\text{III},s}$

are

$$\text{Real} \left[\sum_{M=1}^6 a_M^{\text{III}} p_{Mi} \right] = u_i \text{ and}$$

$$\text{Real} \left[-i\omega \sum_{M=1}^6 a_M^{\text{III}} \left[C_{ilk} s_\ell + C_{ilk1} s_1^M \right] p_{Mk} \right] = \tau_i \quad (12)$$

Since the a_M^{III} can be freely chosen as any complex numbers, and since u_i and τ_i are real numbers, we can remove the Real operators, leaving six ordinary complex linear equations for the a_M^{III} 's, completing the description of the eigenfunction φ in region III.

In a similar manner the values of the functions f_k and $f_{k,1}$ (or those of the Thompson-Haskell vector) at one point on the plane $x_1 = x_1^0$ contained in or bounding region I are equivalent to a set of six complex numbers a_1^I, \dots, a_6^I describing φ in region I. Thus any eigenwave in the planar geometry has a plane wave representation in each of the outer half spaces I and III in terms of their own natural set of plane waves. (The representation for eigenwaves in cylindrical geometry is carried out in terms of potential functions. That representation is discussed for the isotropic case in section 3.3.)

3.1.7 The Scattering Matrix

In section 3.2.6 we saw that any primitive monochromatic wave (eigenwave) which can exist in a model composite with an interphase region has a fixed representation in either the matrix or reinforcement phases. For the planar geometry this representation was in terms of the sum of six plane waves. From another perspective, each of these eigenwaves is a self-contained solution to a scattering problem and all interphase scattering solutions are included as combinations of these eigenwaves. We need only extract that scattering information from the eigenwave representation. This will be accomplished using the scattering matrix; and this matrix is best introduced through what is called the transformation matrix. The equation determining guided interface waves can be found as a consequence of the relationship between these two matrices.

Continuing with our example of the planar geometry, any eigenwave in the I-II-III sandwich has a plane wave representation in each of the outer half spaces I and III in terms of the natural plane waves of that region. The eigenwave can be integrated across region II using a one-dimensional form of the equations of motion as described in section 3.2.4. Thus, for any set of coefficients, a_1^I, \dots, a_6^I in region I, the eigenwave so obtained gives rise to a corresponding set of coefficients a_M^{III} in region III.

Clearly this is a linear correspondence, since linear combinations of the a_M^I 's produce the same linear combinations of the a_M^{III} 's. Consequently, we can catalog all harmonic eigenwaves for the I-II-III sandwich in terms of a 6x6 invertible complex transformation matrix \underline{T} , where

$$T a_M^I = a_M^{III} \quad (13)$$

However, the matrix \underline{T} , while embodying the entire wave mechanics of the medium and interface, does not allow us to directly solve scattering problems. To do so, we need to derive a related quantity, the scattering matrix.

If all the plane wave components of an eigenwave in an outer region have real slowness, s_1 , then we have seen in section 3.2.6 that they break up into two groups of three plane waves in each region: those whose Poynting vector is oriented towards the interface (so that the energy flow is towards the interface) and those whose Poynting vector faces away from the interface. In this case three incoming waves are easily identified in each of the regions I and III as those transmitting energy toward the interphase, while the outgoing waves transport energy away from the interphase. The scattering matrix \underline{S} is that matrix which

connects the incoming and outgoing waves in both regions. However, before giving the form of the scattering matrix, we also recall that if the slowness s_1^M is not real, then there are two complex conjugate slownesses associated to inhomogeneous plane waves [4]. Each of these waves transmits energy parallel to the interphase, but one has exponential growth away from the interphase, while the other has exponential decay. In this case it's reasonable to identify the exponentially increasing waves with the incoming waves and the exponentially decreasing waves with the outgoing waves. Nonetheless, other identifications are possible, and as we shall see, are physically meaningful in describing leaky waves.

To obtain the scattering matrix $\underline{\underline{S}}$ from the transformation matrix $\underline{\underline{T}}$, let us order the plane wave bases according to their type, incoming (I) or outgoing (O), and decompose the matrix $\underline{\underline{T}}$ into a left half, $\underline{\underline{T}}_L$, and a right half, $\underline{\underline{T}}_R$:

$$\begin{array}{c} \text{III} \\ \left[\begin{array}{c} O_1 \\ O_2 \\ O_3 \\ I_1 \\ I_2 \\ I_3 \end{array} \right] \end{array} = \begin{array}{c} \underline{\underline{T}} \\ \left[\begin{array}{c} \underline{\underline{T}}_L \\ \underline{\underline{T}}_R \end{array} \right] \end{array} \begin{array}{c} \text{I} \\ \left[\begin{array}{c} I_1 \\ I_2 \\ I_3 \\ O_1 \\ O_2 \\ O_3 \end{array} \right] \end{array} \quad (14)$$

If region I is above region III, for example, the upward travelling waves would be incoming on region III and outgoing in region I. We can think of equation (14) in simple block form, where blocks of incoming or outgoing bases are grouped together:

$$\begin{bmatrix} 0^{III} \\ I^{III} \end{bmatrix} = \begin{bmatrix} L_{11} & R_{12} \\ L_{21} & R_{22} \end{bmatrix} \begin{bmatrix} I^I \\ 0^I \end{bmatrix}, \quad (15a)$$

or

$$\begin{aligned} 0^{III} &= L_{11} I^I + R_{12} 0^I \\ I^{III} &= L_{21} I^I + R_{22} 0^I \end{aligned} \quad (15b)$$

Here \underline{T}_L is comprised of the blocks L_{11} and L_{12} while \underline{T}_R is made up of the blocks R_{12} and R_{22} .

Regrouping, we have

$$\begin{aligned} 0^{III} - R_{12} 0^I &= L_{11} I^I \\ -R_{22} 0^I &= -I^{III} + L_{21} I^I \end{aligned} \quad (16a)$$

or

$$\begin{bmatrix} L_{11} & 0 \\ L_{21} & -1 \end{bmatrix} \begin{bmatrix} I^I \\ I^{III} \end{bmatrix} = \begin{bmatrix} 1 & -R_{12} \\ 0 & -R_{22} \end{bmatrix} \begin{bmatrix} 0^{III} \\ 0^I \end{bmatrix}, \quad (16b)$$

where we have arranged the bases so as to diagonalize as much as possible the block matrices on either side of equation (16b). This is done by putting the downward travelling waves first. Equation (14) then can be regrouped as:

$$\begin{bmatrix} \underline{\underline{S}}_L \\ \underline{\underline{T}}_L \end{bmatrix} \begin{bmatrix} 0 \\ -1 & 0 & 0 \\ 0 & -1 & 0 \\ 0 & 0 & -1 \end{bmatrix} \begin{bmatrix} I_1^I \\ I_2^I \\ I_3^I \\ I_1^{III} \\ I_2^{III} \\ I_3^{III} \end{bmatrix} = \begin{bmatrix} \underline{\underline{S}}_R \\ \underline{\underline{T}}_R \end{bmatrix} \begin{bmatrix} 1 & 0 & 0 \\ 0 & 1 & 0 \\ 0 & 0 & 1 \\ 0 \\ 0 \\ 0 \end{bmatrix} \begin{bmatrix} O_1^{III} \\ O_2^{III} \\ O_3^{III} \\ O_1^I \\ O_2^I \\ O_3^I \end{bmatrix} \quad (17)$$

from which we derive the scattering matrix

$$\underline{\underline{S}} = \underline{\underline{S}}_R^{-1} \underline{\underline{S}}_L \quad (18)$$

It can be shown that, if the scattering process is reversible (no energy loss, etc.), then the matrix $\underline{\underline{S}}$ is unitary, i.e., $\underline{\underline{S}}^{-1} = \bar{\underline{\underline{S}}}$ [2].

Equation (18) completes the scattering representation for the composite sandwich with interfacial region. Knowledge of this matrix allows us to predict how any monochromatic ultrasonic wave sent in towards the interphase region will both reflect backwards and refract through the interphase region. We have shown how this matrix can be computed if the constitutive relation of the interphase region and the elastic constants of the outer regions are known. It forms the basis for inverting ultrasonic scattering data to determine local elastic properties.

3.1.8 Normal Modes and Leaky Waves

As seen from equation (17), the scattering matrix $\underline{\underline{S}}$, given by equation (18), exists provided that the matrix $\underline{\underline{S}}_R$ is invertible. If

$|S_R| = 0$, then \underline{S} does not exist, but then all the input waves can be set equal to zero and a viable output wave can still be found. This is exactly the condition for the existence of normal modes, so that the equation

$$|S_R| = 0 \tag{19}$$

becomes the normal mode equation in terms of the variables ω , s_2 and s_3 .

Guided interface waves is a relative term describing detectable normal modes whose attenuation in the direction of motion along the interface is sufficiently small that the waves can be detected at interface positions remote from their point of injection.

For the planar case there are actually $2^6 = 64$ possible combinations of incoming and outgoing waves in the regions I and III, and these give rise to 64 variants or branches for equation (19). Of these branches only one, which must have all s_1 slowness roots complex, can have the signs of all six slowness roots chosen so that exponential decay (rather than growth) of the amplitude will occur away from the interface on both sides for the outgoing waves and thus describe a normal mode of finite energy.³ This "regular" branch contains the nondissipative Stoneley and Rayleigh

³The representation of the function f_1 in section 3.1.3 was shown in section 3.1.6 to be a combination of exponentials outside the interphase region. The real component of the exponent, which we call the growth exponent, arises from the imaginary part of each s_1 slowness root and describes the asymptotic behavior away from the interface. In the cylindrical geometry, the behavior outside the interphase also becomes asymptotically exponential.

waves generalized to anisotropic media [5].⁴ The other 63 "irregular" branches, however, can still give rise to "leaky" interface waves.

As we shall discuss in detail for the cylindrical geometry in the case of isotropic elasticity, where there are only four possible branches, the "irregular" branches of equation (19) can have complex s_2 and s_3 roots over a range of real frequency values. Such values, corresponding to a normal mode with complex phase velocity, describe coherent but attenuating "leaky" waves. These waves also include physically detectable guided interface waves (see section 4).

The properties of the scattering matrix as well as the velocities and other characteristics of both nondissipative and leaky modes, depend -- often strongly -- on the constitutive relation of region II and the elastic constants of regions I and III. If we can describe the entire configuration in terms of a limited number of parameters, then the formulation we have presented allows us to solve the forward problem and predict both the scattering and normal mode properties as a function of frequency. Usually the properties of regions I and III are well known so that one needs only parameterize the constants of the interfacial region through its possibly unknown thickness. Then the experimentally measurable scattering and/or dispersion relations serve as input data for the inverse problem of interface characterization whose goal is to extract the unknown parameters of the interfacial region.

⁴The above is true if one passes to the limit of zero density for one material while maintaining a shear velocity above the Rayleigh velocity of the remaining material. Otherwise the Rayleigh wave will appear as the limit of a leaky wave, as has been noted in the geophysics literature [5].

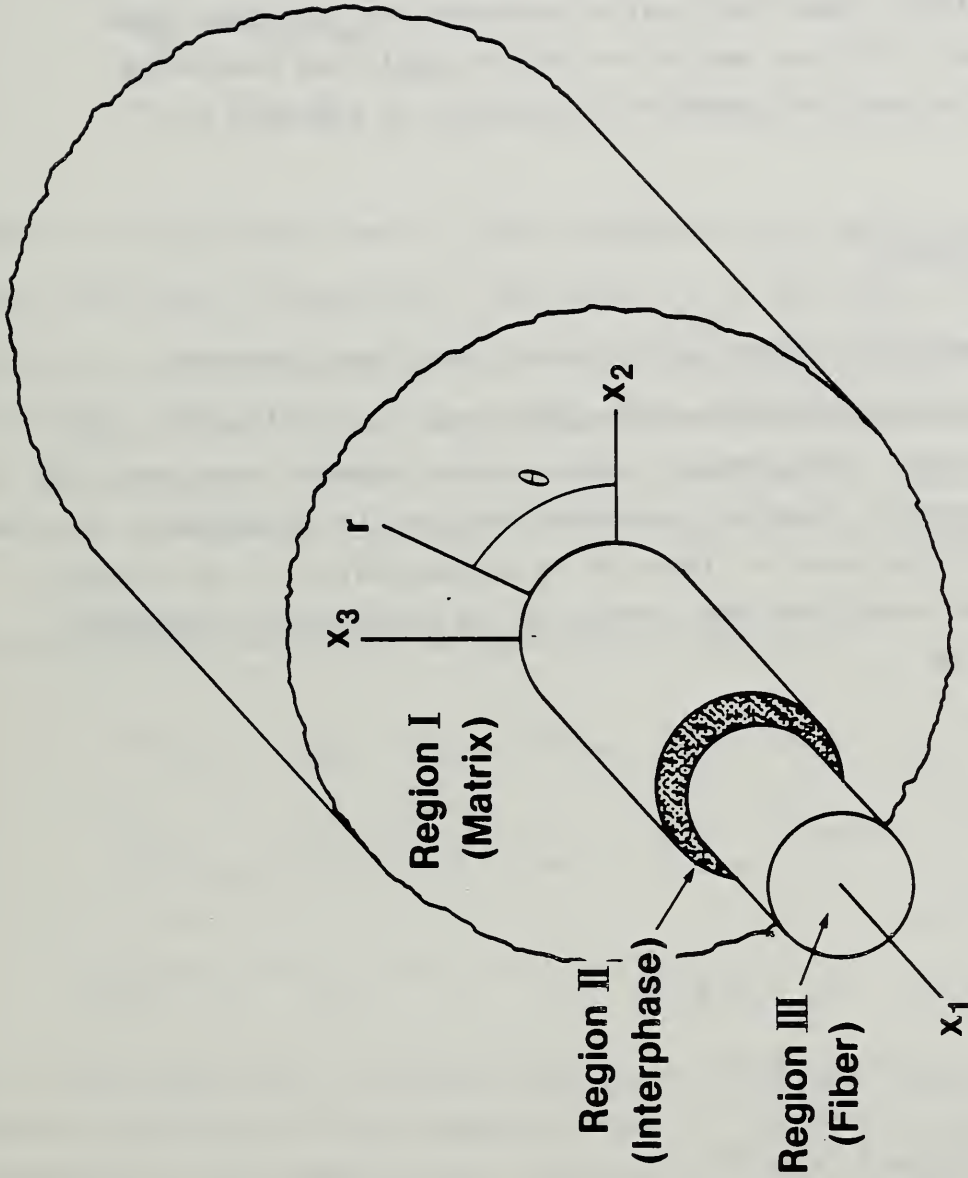


Fig. 3.3 Schematic representation of a cylindrical interfacial region (interphase), matrix and fiber.

3.2 Cylindrical Interfaces

In section 3.1 we showed how the scattering matrix and normal modes can be obtained, with particular emphasis on the planar geometry. In that geometry a material of any elastic anisotropy may be described in the scattering formalism, since the elastic constants are invariant under linear translation. In this section we wish to apply the scattering formalism to the cylindrical geometry illustrated in Figure 3.3.

3.2.1 Basic Equations

Translational symmetry in the x_2 direction in the planar geometry corresponds to polar rotational symmetry about the cylinder axis in the cylindrical geometry. This symmetry restricts the elastic constants for the cylindrical case to those of transverse isotropy (or hexagonal symmetry) in which the plane of isotropy is perpendicular to the cylinder axis. Under these conditions the strains in the cylindrical coordinate system are given by:

$$\begin{aligned}e_{rr} &= u_{r,r} \\e_{\theta\theta} &= (u_r + u_{\theta,\theta})/r \\e_{zz} &= u_{z,z} \\e_{r\theta} &= (ru_{\theta,r} - u_\theta + u_{r,\theta})/2r \\e_{rz} &= (u_{r,z} + u_{z,r})/2 \\e_{\theta z} &= (ru_{\theta,z} + u_{z,\theta})/2r\end{aligned}\tag{20}$$

and the stresses by:

$$\begin{aligned}
\sigma_{rr} &= C_{11} e_{rr} + C_{12} e_{\theta\theta} + C_{13} e_{zz} \\
\sigma_{\theta\theta} &= C_{12} e_{rr} + C_{11} e_{\theta\theta} + C_{13} e_{zz} \\
\sigma_{zz} &= C_{13} e_{rr} + C_{13} e_{\theta\theta} + C_{33} e_{zz} \\
\sigma_{rz} &= 2C_{44} e_{rz} \\
\sigma_{\theta z} &= 2C_{44} e_{\theta z} \\
\sigma_{r\theta} &= 2C_{66} e_{\theta r}
\end{aligned} \tag{21}$$

where the displacement vector \underline{u} has components u_r, u_θ and u_z in the r, θ and z directions, respectively, and where $\sigma_{\alpha\beta}$ is the force in the α direction across a planar section of unit area whose normal is in the β direction. Here also $C_{11} - C_{12} = 2C_{66}$ [6]. The five elastic constants for the transverse isotropic material are connected to λ and μ for the isotropic material by $C_{12} = C_{13} = \lambda$, $C_{44} = C_{66} = \mu$, $C_{11} = C_{33} = \lambda + 2\mu$.

In cylindrical coordinates the equations of motion are

$$\begin{aligned}
r\sigma_{rr,r} + \sigma_{r\theta,\theta} + \sigma_{rz,z} + (\sigma_{rr} - \sigma_{\theta\theta}) &= \rho r u_{r,tt} \\
r\sigma_{\theta z,z} + \sigma_{\theta\theta,\theta} + \sigma_{r\theta} + \sigma_{r\theta,r} &= \rho r u_{\theta,tt} \\
r\sigma_{zz,z} + \sigma_{\theta z,\theta} + \sigma_{rz} + \sigma_{rz,r} &= \rho r u_{z,tt}
\end{aligned} \tag{22}$$

As in the planar case, we assume that in the interfacial region II the elastic constants can only depend on r and ω . The elasticity operator, obtained here from equation (22), commutes with both the axial shift

operator and polar rotation operator, giving rise to a representation for eigenwaves in the cylindrical geometry as

$$\varphi(r, \theta, z, t) = \text{Real} \left[\underline{f}(r) \exp \left[i\omega \left(t - \frac{n}{\omega} \theta - sz \right) \right] \right] , \quad (23)$$

where n is an integer.

3.2.2 Propagation Equations in Cylindrical Coordinates

Equation (23) shows that the quantities ω and n are conserved during motion of a harmonic eigenwave in the cylindrical geometry. The variable parametrizing the change of structure is the radius, r . The six quantities making up the propagation vector in this case are $\underline{f}(r)$ and $\underline{f}_{,r}(r)$. The equations of motion are, as in the planar case, translatable to ordinary second order differential equations for $\underline{f}(r)$ which can be thought of also as linear algebraic equations for $\underline{f}_{,rr}(r)$ on any cylinder, given $\underline{f}(r)$ and $\underline{f}_{,r}(r)$ at some point on the cylinder. Knowledge of $\underline{f}_{,rr}$ (and $\underline{f}_{,r}$) allows one to increment the propagation vector through a distance dr : $\underline{f}(r + dr) = \underline{f}(r) + \underline{f}_{,r}(r)dr$ and $\underline{f}_{,r}(r + dr) = \underline{f}_{,r}(r) + \underline{f}_{,rr}(r)dr$. As in the planar case, simple models of interfacial regions (such as one, two, or three thin layers) can be directly calculated without integrating the differential equations by using a propagator matrix for each layer. Each transition between layers will produce artificial scattering, but these effects should be negligible unless the wavelengths become of the order of the interlayer thickness.

Taking the interface layer to be transversely isotropic viscoelastic, its wave propagation equations take the form:

$$\begin{aligned}
& C_{11}(r^2_{f,r,rr} + rf_{r,r} - f_r) + \rho\omega^2 r^2 f_r - C_{66} n^2 f_r - i(C_{12} + C_{66}) n r f_{\theta,r} \\
& + i(C_{11} + C_{66}) n f_{\theta} - i(C_{13} + C_{44}) k r^2 f_{z,r} + C_{11,r} r^2 f_{r,r} \\
& + C_{12,r} (r f_r - i n f_{\theta}) - i C_{13,r} k f_z = 0 \tag{24a}
\end{aligned}$$

$$\begin{aligned}
& - i(C_{12} + C_{66}) n r f_{r,r} - i(C_{11} + C_{66}) n f_r + C_{66} (r^2 f_{\theta,rr} + r f_{\theta,r} - f_{\theta}) \\
& + (\rho\omega^2 r^2 - C_{44} k^2 r^2 - C_{11} n^2) f_{\theta} - (C_{13} + C_{44}) n k f_z \\
& + C_{66,r} (-i n f_r + r f_{\theta,r} - f_{\theta}) = 0 \tag{24b}
\end{aligned}$$

$$\begin{aligned}
& - i(C_{13} + C_{44}) k r (r f_{r,r} + f_r) - (C_{13} + C_{44}) n k r f_{\theta} + C_{44} (r^2 f_{z,rr} + r f_{z,r} - n^2 f_z) \\
& + (\rho\omega^2 r^2 - C_{33} k^2 r^2) f_z + C_{44,r} (r f_{z,r} - i k r f_r) = 0 \tag{24c}
\end{aligned}$$

Equations (24a-c) also include the propagation equations in the matrix and fiber when the appropriate relations between isotropy and transverse isotropy are taken into account.

3.2.3 Potential Functions and the Bessel Representation for Eigenwaves in Regions I and III

Although the potential function approach outlined here can be extended to a transversely isotropic fiber and matrix, we shall restrict ourselves in this report to isotropic media surrounding the anisotropic interfacial region. The potential approach we present is the complex version of that given by Gazis [7].

Rather than using a plane wave representation of the solution in the outer regions, we attempt, for this cylindrical geometry, a representation of the solution in the general Helmholtz form:

$$\phi = \nabla\chi + \nabla \times \underline{\Psi} \quad (25a)$$

together with

$$\nabla \cdot \underline{\Psi} = F(\chi, t) \quad , \quad (25b)$$

where χ is a scalar potential, $\underline{\Psi}$ is a vector potential, and F an arbitrary selected gauge function.

Under these conditions, the equations of motion (22) separate in the homogeneous outside regions into two equations:

$$a^2 \nabla^2 \chi = \chi_{,tt} \quad (26a)$$

$$b^2 \nabla^2 \underline{\Psi}_i = \underline{\Psi}_{i,tt} \quad , \quad (26b)$$

where a is the longitudinal wave velocity of the appropriate region, $a^2 = (\lambda + 2\mu)/\rho$, and b is the shear wave velocity, $b^2 = \mu/\rho$. We assume for χ and each component of $\underline{\Psi}$ the eigenform (23):

$$\begin{aligned}
\chi &= f(r) e^{-in\theta} e^{i\omega(t-sz)} \\
\Psi_r &= ig_\theta(r) e^{-in\theta} e^{i\omega(t-sz)} \\
\Psi_\theta &= g_\theta(r) e^{-in\theta} e^{i\omega(t-sz)} \\
\Psi_z &= g_z(r) e^{-in\theta} e^{i\omega(t-sz)} \quad , \quad (27)
\end{aligned}$$

where we have used condition (24b) to set $g_\theta(r) = -ig_r(r)$. Then equations (22a-c) reduce to the 3 equations:

$$f_{,rr} + \frac{1}{r} f_{,r} - \left[\omega^2 \left[s^2 - \frac{1}{a^2} \right] + \frac{n^2}{r^2} \right] f = 0 \quad (28a)$$

$$g_{z,rr} + \frac{1}{r} g_{z,r} - \left[\omega^2 \left[s^2 - \frac{1}{b^2} \right] + \frac{n^2}{r^2} \right] g_z = 0 \quad (28b)$$

$$g_{\theta,rr} + \frac{1}{r} g_{\theta,r} - \left[\omega^2 \left[s^2 - \frac{1}{b^2} \right] + \frac{(n+1)^2}{r^2} \right] g_\theta = 0 \quad (28c)$$

In this case, the six components of the propagation vector can be thought of as given by f_r , df_r/dr , g_θ , dg_θ/dr , g_z and dg_z/dr . The displacement fields are then given by the real part of:

$$\varphi_r = \left[f_{,r} - \frac{in}{r} g_z + i\omega s g_\theta \right] e^{-in\theta} e^{i\omega(t-sz)} \quad (29a)$$

$$\varphi_e = \left[-\frac{in}{r} f - g_{z,r} + \omega s g_\theta \right] e^{-in\theta} e^{i\omega(t-sz)} \quad (29b)$$

$$\varphi_z = \left[-i\omega s f + g_{\theta,r} \frac{-g_\theta}{r} - \frac{ing_\theta}{r} \right] e^{-in\theta} e^{i\omega(t-sz)} \quad (29c)$$

The important feature to notice about equations (28a-c) is that they are all forms of Bessel's equation (where we have chosen to use the modified Bessel functions with notation more adaptable to the Lee and Corbly [8] type example to be given shortly). The solutions to these equations can be given as follows:

$$f = c_1 K_n(Ar) + c_2 I_n(Ar) \quad (30a)$$

$$g_z = c_3 K_n(Br) + c_4 I_n(Br) \quad (30b)$$

$$g_r = c_5 K_{n+1}(Br) + c_6 I_{n+1}(Br) \quad (30c)$$

where

$$A = \pm \sqrt{\omega^2 s^2 - \frac{\epsilon^2}{a^2}} \quad (31a)$$

and

$$B = \pm \sqrt{\omega^2 s^2 - \frac{\epsilon^2}{c^2}} \quad (31b)$$

The square root functions here give rise to four branches (see section 3.1.8), characteristic of the isotropic cylindrical problem, which does not permit exponential growth inside the cylinder, and, therefore, has only one representation inside the cylinder.

The boundary conditions on I_n and K_n imply that inside the fiber, $c_1 = c_3 = c_5 = 0$, while outside the fiber $c_2 = c_4 = c_6 = 0$, so that the solution inside the fiber is represented in terms of I_n and I_{n+1} , while the solution outside the interface can be represented in terms of K_n and K_{n+1} . The six degrees of freedom are described by the three non-zero c coefficients and the two branches of the square root defining A and B .

3.2.4 Radial Mode Interface Waves

The wave structure in the cylindrical geometry is particularly rich due to the curvature of the interface. In this report we want to investigate the most common class of interface waves -- those of axial-radial type -- that can occur in a fiber reinforced cylinder without an interfacial region. This class of waves contains the Stoneley waves generalized to the cylindrical geometry as well as leaky modes. The representation of these special waves in an NDE context was first given by Lee and Corbly [8], but not followed through by them in any detail, possibly because of imprecise codes for calculating Bessel functions of a complex argument or because of an error in the asymptotic representation of the I type modified Bessel functions.

If one sets $n = 0$ in equation (23) one obtains the ground state eigenwaves for the cylindrical geometry. Without an interfacial region present, the transformation matrix is obtained by matching boundary conditions at the interface between the fiber and the matrix. The free travelling normal modes requiring no inputs (c.f. equation (19) in section 3.2) then produce a sixth order determinant which is the product

of two factors, one second order factor corresponding to waves with displacements in the circumferential direction (torsional modes) and one fourth order factor corresponding to waves whose circumferential displacements are zero. In this section, we shall investigate these latter, axial-radial, waves. Because of the radial symmetry of these waves, the ordinary plane waves found in planar geometry will not be included -- they arise for $n > 0$.

To write down the fourth order equation giving the coefficient for the axial-radial waves, we specialize equations (30) to $n = 0$. With no tangential displacements, $\varphi_\theta = 0$ and g_z can be eliminated. Thus, we can write

$$\chi_I = \alpha K_0(A_I \omega r) \exp[i\omega(t-sz)]$$

$$\psi_I = \beta K_1(B_I \omega r) \exp[i\omega(t-sz)]$$

$$\chi_{III} = \gamma I_0(A_{III} \omega r) \exp[i\omega(t-sz)]$$

$$\psi_{III} = \delta I_1(B_{III} \omega r) \exp[i\omega(t-sz)] \quad , \quad (32)$$

and setting $v = \frac{1}{s}$ and $\kappa = \omega r$, we have:

$$2\rho_I b_I^2 v_A K_I(A_I \kappa)$$

$$\rho_I \{(v^2 - 2b_I^2) K_0(A_I \kappa) - 2b_I^2 v^2 A_I K_1(A_I \kappa) / \kappa\}$$

$$K_0(A_I \kappa)$$

$$v A_I K_1(A_I \kappa)$$

$$\rho_I (2b_I^2 - v^2) K_1(B_I \kappa)$$

$$-2\rho_I b_I^2 v (B_I K_0(B_I \kappa) + K_1(B_I \kappa) / \kappa)$$

$$v B_I K_0(B_I \kappa)$$

$$K_1(B_I \kappa)$$

$$2\rho_{III} b_{III}^2 v_A I_1(A_{III} \kappa)$$

$$\rho_{III} \{(2b_{III}^2 - v^2) I_0(A_{III} \kappa) - 2b_{III}^2 v^2 A_{III} I_1(A_{III} \kappa) / \kappa\}$$

$$-I_0(A_{III} \kappa)$$

$$v A_{III} I_1(A_{III} \kappa)$$

$$\rho_{III} (2b_{III}^2 - v^2) I_1(B_{III} \kappa)$$

$$2\rho_{III} b_{III}^2 v (B_{III} I_0(B_{III} \kappa) - I_1(B_{III} \kappa) / \kappa)$$

$$-v B_{III} I_0(B_{III} \kappa)$$

$$I_1(B_{III} \kappa)$$

$$\begin{bmatrix} \alpha \\ \gamma \\ -i\beta \\ +i\delta \end{bmatrix} = 0 \quad (33)$$

5

⁵This notation and representation differs somewhat from that of Lee and Corbly, who use the wave number k , a slightly different definition of the A's and B's, and who use the engineering representation $\exp[i(kz - \omega t)]$ rather than $\exp[i(\omega t - kz)]$.

The solution to these equations requires, of course, that the determinant of the coefficients on the left hand side be zero, after which the coefficients α , β , γ and δ can be found from the 3 x 3 minors of any row.

A difficulty with this determinant is that its value becomes exponentially large for most of the useful range of the arguments. This can be compensated by dividing out the asymptotic forms for $K_m(\zeta)$ and $I_m(\zeta)$, $e^{-\zeta}$ and $\cosh\zeta$, respectively. These asymptotic forms were chosen to be analytic functions so that the determinant would remain an analytic function of ζ and, hence, of v at every point of the v plane except branch points of the square root functions $A(v)$ or $B(v)$.

The fact that $I_0(\zeta)$ is an even function of ζ and $I_1(\zeta)$ is an odd function of ζ shows, by inspection of equation (33) that the \pm branches in region III produce the same solutions. Hence, instead of the 64 possible parameters in the anisotropic planar case, there are only 4 branches here. Physically, this corresponds to the fact that the fiber is a bounded region not admitting exponentially increasing solutions. Thus, exponential leakage can only occur outside the fiber. Of course, interchanging the two materials and thus reversing the curvature produces another four modes, but the possibility of leaky modes with exponential growth on both sides of the interface, as can happen in the planar geometry, is foreclosed in the cylindrical geometry.

To solve equation (33), improved high accuracy computer codes for calculating Bessel functions of a complex argument were developed. An adaptive Newton's technique was used to solve the equations and an adaptive integral implementation of Rouché's theorem (the integral of the logarithmic derivative of an analytic function around any closed contour equals $2\pi i$ times the number of zeroes minus the number of poles enclosed

by the contour) was used to guarantee that the approximate roots found were actual roots, and that no roots were overlooked.

Because each mode is a harmonic wave and because there is no tangential velocity, each particle traces out an elliptical trajectory in the (r,z) plane. Graphical representations of particle motion have been developed allowing one to visualize the interaction of each mode with the interface. In addition, using the results of 3.2.5, the time-averaged Poynting vector, generalized group velocity, energy flow curve, and attenuation along the interface were calculated, permitting comparison with experiments. For leaky modes, the displacement amplitude falls off exponentially along the z direction while the Poynting vector components and energy density drop off as the square of the amplitude. In contrast, the group velocity, which is their ratio, is independent of z and depends only on radius. Because of this independence of z , energy leaking away from the interface follows parallel curves.

3.3 Future Directions

The theory of interface and scattered waves in fiber-reinforced MMCs (cylindrical geometry) needs to be extended to include an interfacial region of variable characteristics surrounding a transversely isotropic fiber. The effect of fiber coatings needs also to be investigated and guided waves of non-radial symmetry should also be included.

We will begin an investigation of the inverse problem for backing out the thickness and elastic character of the interfacial region. To facilitate acoustic microscopic studies, we will also begin investigation of the injection coefficients for determining the efficiency with which a given external ultrasonic input is converted into distinct guided interface waves.

3.4 References

- [1] D. Graffi, "Mathematical models and waves in linear viscoelasticity", in Wave propagation in viscoelastic media, F. Mainardi, ed., Pitman Advanced Publishing Program, (1982), pp. 1-27.
- [2] C.M. Keith and S. Crampin, *Geophys. J.R. Astr. Soc.*, 49 (1977), pp. 181-208.
- [3] J. Lighthill, Waves in Fluids, Cambridge University Press, (1978), p. 317ff.
- [4] J.L. Synge, *Proc. Roy. Irish Acad.*, 58A (1956), pp. 13-21.
- [5] W.L. Pilant, *Bull. Seism. Soc. Amer.*, 62 (1972), pp. 285-299.
- [6] J.F. Nye, Physical Properties of Crystals, Oxford at the Clarendon Press (1957), pp. 140-143.
- [7] D.C. Gazis, *J. Acoust. Soc. Amer.*, 31 (1959), pp. 568-573.
- [8] D.A. Lee and D.M. Corbly, *IEEE Trans. on Sonics and Ultrasonics*, SU-24 (1977), pp. 206-212.

4. Experimental Study of Guided Interface Waves

The theoretical studies of guided interface waves presented in section 3 have been complemented with experiments on both planar and cylindrical model interfaces. The purpose of these experiments has been to test and verify the theoretical predictions and to evaluate experimental approaches that might subsequently be applied to actual MMC materials. The experimental study of planar interfaces has been conducted by Professor Moshe Rosen and his graduate students at Johns Hopkins University under subcontract.

4.1 Planar Interfaces

In this section we study the propagation of interface waves along planar interfaces without an interphase; the incorporation of scattering and finite interphases will be reserved for later work.

In an earlier series of experiments (see first progress report) interface waves were generated and detected using a Rayleigh mode conversion technique. Interface bonding was created by applied pressure in several pairs of materials, including titanium and 4340 steel, titanium and 1040 steel, aluminum and 1040 steel, aluminum and 4340 steel, and nickel and pyrex glass. In all pairs velocity increased with increasing bond quality, eventually approaching the theoretical interface wave velocity. That work has been extended herein to incorporate the effects of microstructure on interface waves. Several microstructures have been produced by heat treatment of a 4340 steel. Ultrasonic velocity was then measured for interface waves along the steel-titanium interface at various frequencies from 1 to 10 MHz, and the effect of the steel microstructure on interface wave velocity was observed.

4.1.1 Background Research

In 1927 Richard Stoneley [1] predicted the existence of an elastic wave which would propagate along the boundary interface between two adjacent layers of subterranean rock. By modeling these interfaces as plane boundaries between two isotropic half spaces and assuming continuity both of particle displacement and normal tractions across the boundary, Stoneley extended Lord Rayleigh's earlier work on surface waves to give a determinant equation [1,2] which is a special case of equation (19) in section 3.

The characteristic Stoneley equation for the planar case yields an algebraic equation with 8 roots for v^2 , when v is the complex velocity. This means that there are 16 possible values for v , but only 8 are independent, since all signs can be reversed. The equation is

complicated by the presence of four square root functions, $\sqrt{1 - \frac{v^2}{V^2}}$

(analogous to those discussed in section 3.2.2, but this time occurring on both sides of the interface), where V can be the shear or longitudinal velocity in either material. These square root functions are double valued (\pm) and introduce branch cuts into the space of solutions.

Pilant has found that, except at isolated branch points, the 16 solutions always exist, but most of them are usually complex. These complex roots are often associated to leaky waves. In fact, if one writes down the displacements for an interface wave (see section 3 or [3,4]) these square roots appear, together with the velocity, as an exponent in an exponential. The choice of which branch (\pm) to choose for the various square root functions then determines whether that function will contribute an exponentially increasing or exponentially decreasing part to the displacement field of the interface wave. Only one contribution need be exponentially increasing to dominate the entire displacement

field, so that only one branch will give rise to a displacement which is exponentially decaying on both sides of the interface. It is this branch, when it exists, that produces true Stoneley interface waves. As noted by Pilant and by Ginsburg and Strick [5], the Stoneley velocity is always less than the shear velocity in either material and greater than the Rayleigh velocity of the linear material.

In cases of complex roots for non-Stoneley branches, as will be illustrated later, physically meaningful roots are associated to "leaky" waves, which travel along the interface but radiate characteristic plane waves into one or both materials, thus leaking energy as they travel. The amplitude of such waves at the interface decays exponentially with distance very seriously along the interface [6]. The majority of Pilant's computations [2] were restricted, and applied only to the case where the Poisson ratio for each material is 0.25. Sezawa and Kenai [7] have graphically determined the range of material constants for Stoneley wave existence by rederiving the Stoneley equation and investigating the one real root. Scholte [8-10] also analyzed the real Stoneley root and described the range of existence for numerous theoretical pairs. A similar project was undertaken by Owen [11] who introduced real material constants to determine which material couples would support real Stoneley waves.

The expressions for Stoneley wave particle displacement derived by Yamaguchi and Sato [3] suggest that it is somewhat similar to shallow shear waves in the less dense material. However, the complex dependence of the displacements on material constants restricts the usefulness of these theoretical studies to that of valuable guidelines. The computer codes developed at NBS within this project already go beyond these studies and permit us the interface wave motion much more clearly in realistic models of the actual materials being tested.

Experimentally, interface waves have been observed in several material pairs and geometries. Stoneley waves and their leaky counterparts were generated in plane and cylindrical geometries by Lee and Corbly [4] in aluminum-steel, aluminum-titanium, and steel-titanium pairs. Utilizing a surface wave mode conversion technique, they measured interface wave velocities and suggested possible applications for NDE. Direct observation of Stoneley waves was made by Claus and Palmer [12] at a nickel-pyrex interface. The transparent material (7070 Pyrex)¹ allowed wave amplitude at the interface to be measured using a differential interferometer.

The existence of interface waves guided by a thin film between two bonded adherents was demonstrated by Rokhlin, Hefets and Rosen [13]. By measuring the velocity and attenuation of the wave, it was shown that a direct correlation could be made between the strength of the interfacial bond and the measured shear modulus and general transmission loss factor. From the dynamics of such interface waves an "effective" shear modulus was determined which strongly depends on the elastic properties and integrity of the bond and of the intermediate layer. An analogous situation may exist at interfaces in composite materials due to the reaction products between the matrix and the strengthening fibers.

¹Certain commercial equipment, instruments, or materials are identified in this paper in order to adequately specify the experimental procedure. Such identification does not imply recommendation or endorsement by the National Bureau of Standards, nor does it imply that the materials or equipment identified are necessarily the best available for the purpose.

Stoneley waves at planar interfaces have also been studied in anisotropic materials by Lim and Musgrave [14], and Chadwick and Curry [15]. The connection between planar Stoneley waves and interface waves in cylinders of isotropic materials has been discussed by Lee and Corbly [4] and by Thurston [16], who also presented an extensive review of higher mode (non-radial, polar angle dependent) waves in cylinders. The effect on Stoneley wave velocities and displacements caused by sliding at the interface, a realistic possibility with pressure bonded materials, has been discussed by Meleshko [17] and by Kumar and Murty [18]. Meleshko contrasts ordinary Stoneley waves with those interface waves in which the discontinuities in displacement can occur, but the tangential components of traction are zero across the interface. When this slippage is allowed, a great effect in displacements can occur at the interface, but in the examples shown, there is only a small effect on the interface wave velocity. The work of Kumar and Murty interposes a viscous layer between the two materials and may be compared with the work of Rokhlin et al. [13].

4.1.2 Measurement Methodology

Experiments have been conducted to generate interface waves in titanium-steel pairs, and to study the influences of microstructure variation in the steel and anisotropy in the titanium.

Different types of heat treated samples of 4340 steel approximately 18 cm x 9 cm x 3 cm were polished to a 30 μm finish. They were subsequently used as a base plate for Rayleigh wave generation. Samples of Ti-6Al-4V rolled sheet of size approximately 4 cm x 4 cm x 2 cm were

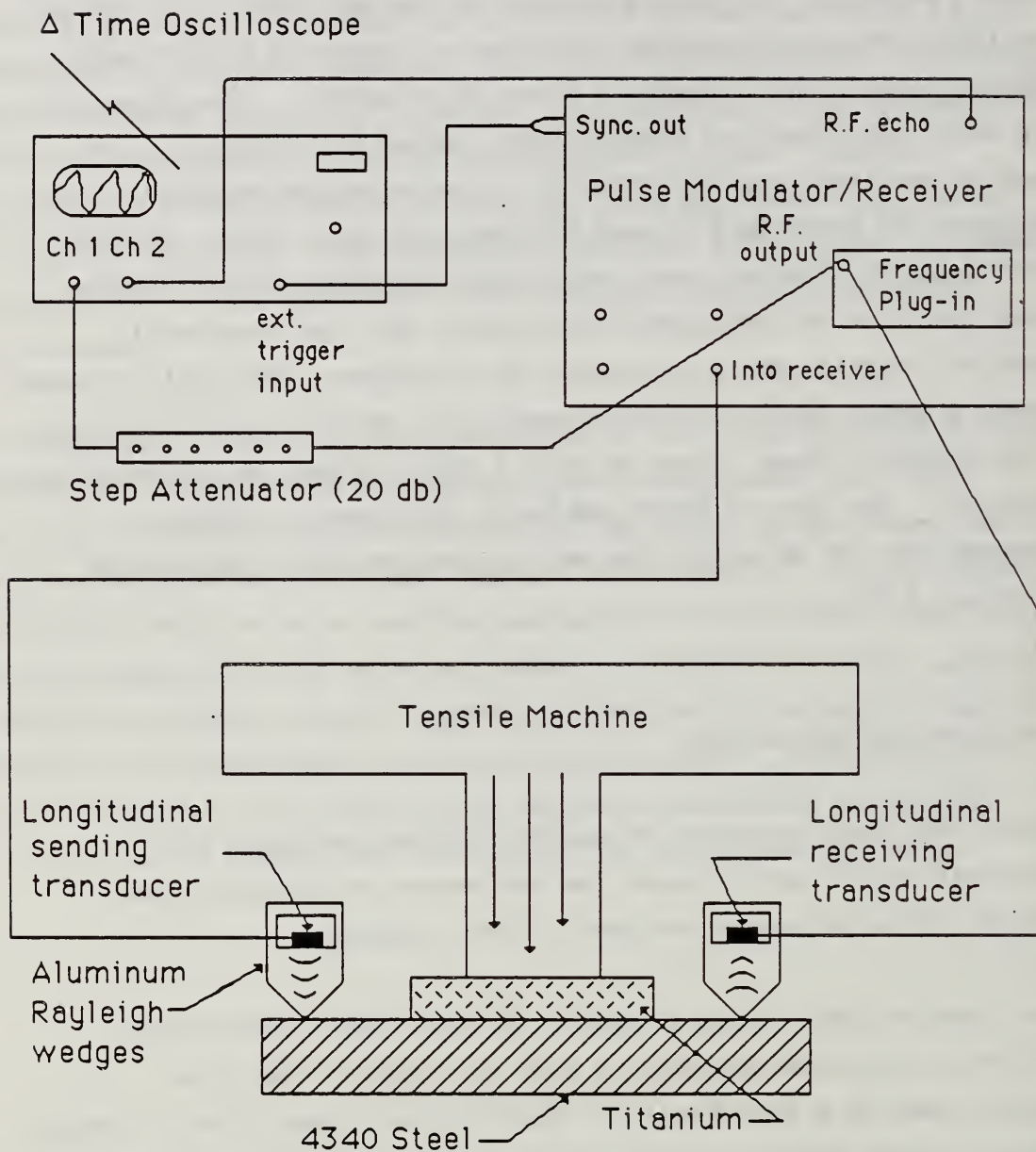


Fig. 4.1 Schematic diagram for generation and detection of interface waves in a compressed duplex block of titanium mounted on steel by using conversion from and to Rayleigh waves on the steel block.

also polished to a 30 μm finish and used to create the desired interface by placing it upon the appropriate base plate. The titanium plate contained a rolling texture. By rotating the titanium plate 90° on the steel base plate, it could be oriented so that the rolling direction was either parallel or perpendicular to the direction of interface wave propagation with a consequent change in shear modulus in the direction of interface wave propagation.

At the interface the particle motion of interface waves in the linear material is similar to that of Rayleigh waves. In addition most of the energy of the wave tends to be carried by the denser material over a large range of material constant combinations. This suggests a possible Stoneley wave generation technique by mode conversion from Rayleigh waves. Indeed, Rayleigh waves were generated and detected on the base plates using two techniques. The first was a direct surface wave generation method utilizing a broadbanded conical transducer to obtain Rayleigh waves over a wide frequency range (DC to 2 MHz). The second technique involved the use of a mode conversion wedge which produced a directed Rayleigh wave. A schematic of this device is included in Figure 4.1.

Two machined aluminum wedges are placed into a sliding mount such that contact is made with the specimen through the knife-edge surfaces of the wedges. Longitudinal waves are piezoelectrically generated and propagated down through one wedge. Mode conversion of the longitudinal wave to a Rayleigh wave occurs at the point of contact between the knife-edge and specimen surface. Rayleigh wave detection at the second wedge is accomplished through a similar mode conversion of the Rayleigh wave to a longitudinal wave. The longitudinal wave is subsequently detected by the second piezoelectric transducer. Although the Rayleigh

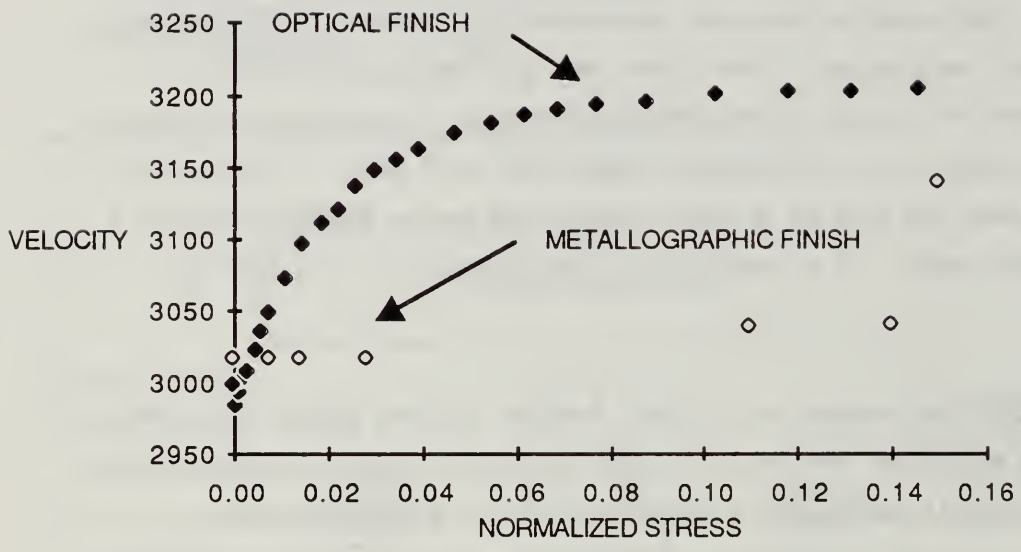


Fig. 4.2 Interface wave velocity versus applied load at a 4340 steel/Ti-6Al-4V interface. Optical finish $0.5 \mu\text{m}$, metallographic finish $\sim 4.5 \mu\text{m}$.

path length is typically much shorter than the multiply-reflected bulk waves, actual identification of the surface wave is accomplished by physically damping the travel surface and detecting the amplitude decrease on an oscilloscope display. Only the Rayleigh wave will be affected by the surface damping. Typical Rayleigh velocity measurements were on the order of 2955 m/s for titanium in the rolling direction, 3055 m/s perpendicular to the rolling direction and 2980 m/s for 4340 steel. Measurement precision was $\pm 5 \text{ ms}^{-1}$ for Rayleigh waves and $\pm 15 \text{ ms}^{-1}$ for the (weaker) interface waves.

In order to force a mode conversion from Rayleigh to interface waves, the mode conversion wedges were modified to allow a controlled interface to be placed in the Rayleigh path. Interface quality was controlled as a function of applied force using a tensile machine in the compressive mode as shown in Figure 4.1. The Rayleigh wave travels on the base plate from one wedge to the interface where it is mode converted to an interface wave. This propagates along the interface to the end of the top plate whereupon it re-converts to a Rayleigh wave that travels along the base plate to the second wedge.

4.1.3 Experimental Results

The mode conversion technique, described above, was employed to demonstrate the effect of surface finish and microstructure at the interface on interface wave velocity for planar interfaces between titanium and 4340 steel.

Figure 4.2 shows the effects of varying two parameters, surface finish and applied pressure, upon interface wave velocity. Specimen preparation

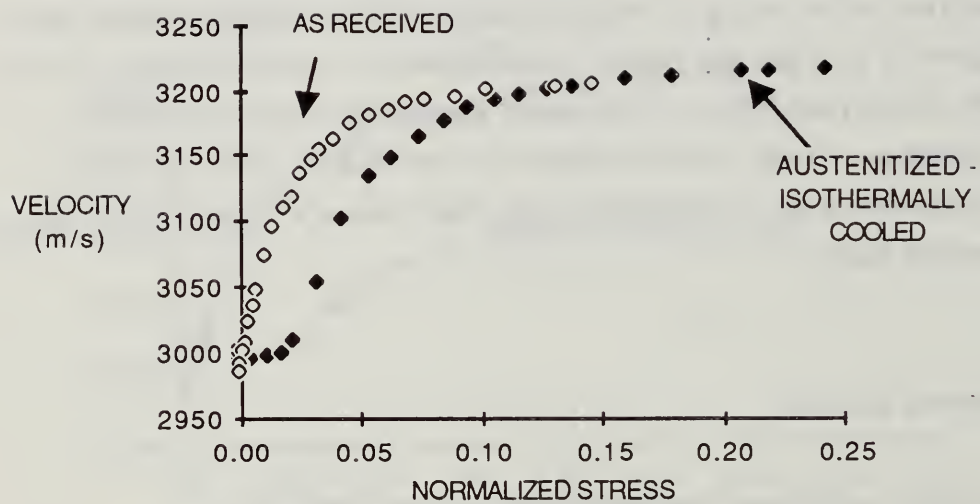


Fig. 4.3 Interface wave velocity versus normalized stress for pearlitic specimens. The stress was normalized to the yield stress for the as-received material (480 MPa) and for the austenitized and isothermally cooled material (380 MPa).

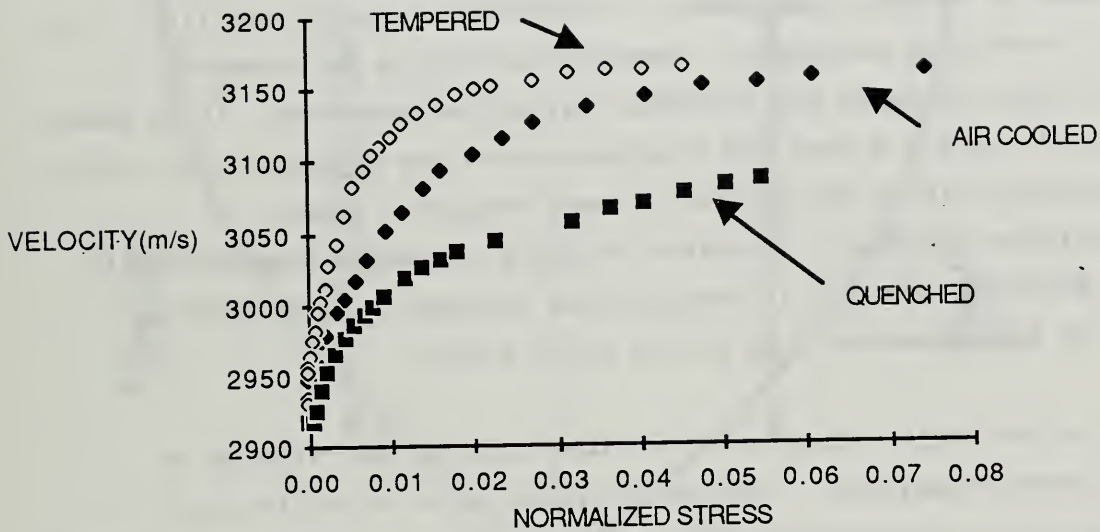


Fig. 4.4 Interface wave velocity versus normalized stress for martensitic specimens. The stress was normalized to the yield stress for the air-cooled material (1035 MPa) and for the quenched and tempered materials (both 1550 MPa).

involved polishing samples of titanium and steel to two different finishes. The first was a metallurgical polish which achieved a surface finish of approximately 3-4 μm . The second polish achieved an optical finish of less than half a μm . In all cases, wave velocities increased from the Rayleigh velocity at zero pressure to the theoretical interface velocity at the required pressure to achieve a coherent interface. The interfaces with the optically finished surfaces required less force to reach the interface velocity than the metallurgically polished interfaces. These results suggest that interface waves may be used to measure interface coherence and integrity in a nondestructive manner utilizing only measurements of wave velocity.

The sensitivity of interface waves to microstructural variations was demonstrated by several experiments. Specimens of coarse pearlite, fine pearlite, air-cooled martensite, tempered martensite and quenched martensite were produced and interface velocities measured. It is shown in Figures 4.3 and 4.4 that the interface waves are sensitive not only to microstructure, but to the particular heat treatment these microstructures received. Interface velocity increased asymptotically from the Rayleigh velocity at zero applied pressure to the limiting velocity at approximately 0.25 of the yield stress.

In order to ascertain the effects of anisotropy in the titanium on interface wave velocities, limiting interface wave velocities were prepared on four specimens of 4340 steel of varying microstructure using the titanium block oriented first in the rolling direction and then in the transverse direction. The results of these measurements are summarized in Table 4.1. The measurements taken using the titanium block oriented in the rolling direction agree very well with the theoretical predictions discussed below. A fifth specimen with a hard martensitic structure was also examined, but the amount of pressure available on our test machine was inadequate to reach a plateau in velocity.

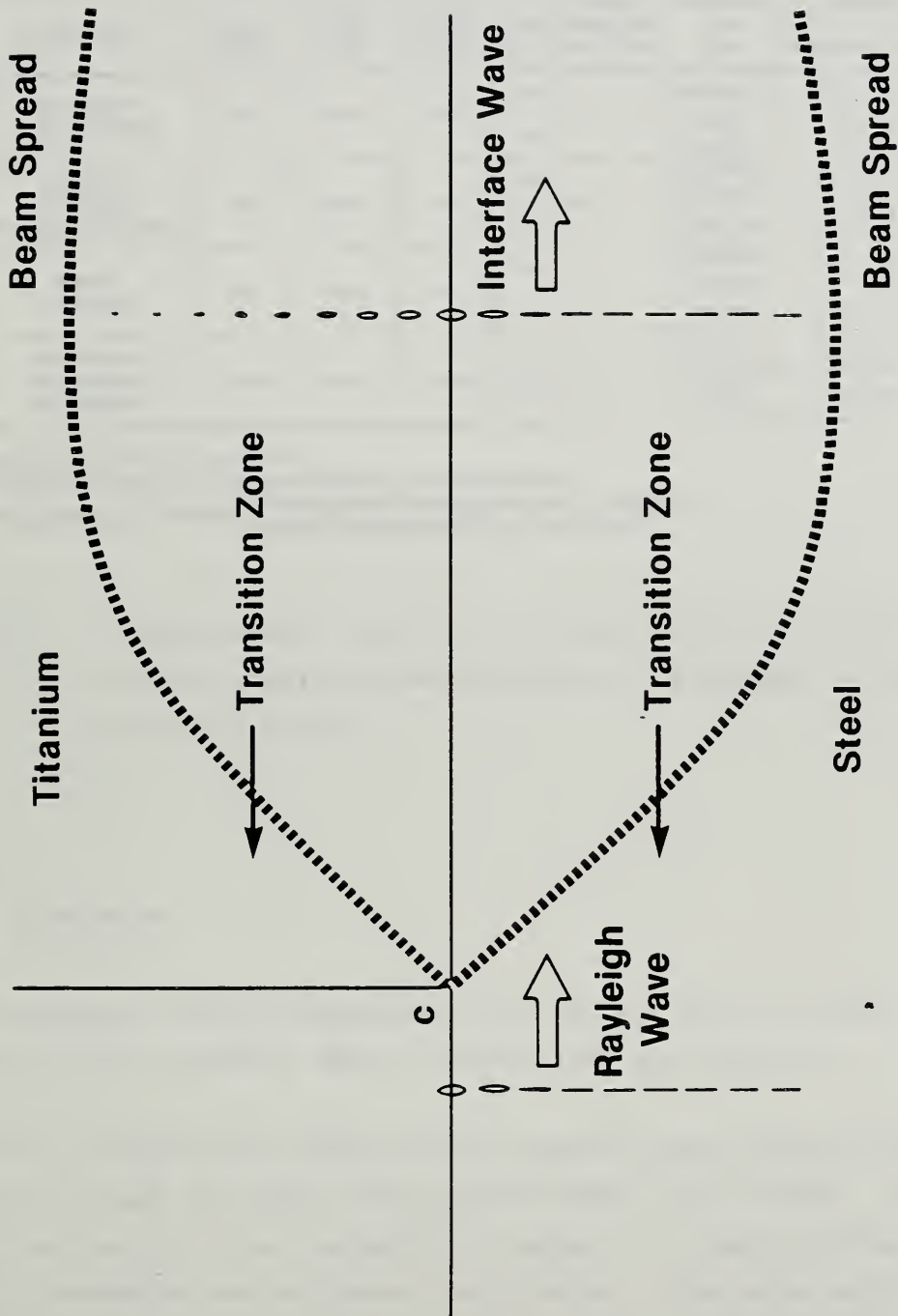


Fig. 4.5 Schematic diagram showing conversion of Rayleigh wave to interface wave.

4340 STEEL PROPERTIES				STEEL/TITANIUM* DUPLEX PLATE				
Microstructure	Density (kg/m ³)	Long Velocity (m/s)	Shear Velocity (m/s)	Case No.	Rolling Direction of Ti Plate	Predicted Wave Type	Interface Wave Velocity	
							Measured (m/s)	Predicted (m/s)
Fine Pearlite (Held at 1200F)	7340	5952	3250	1A	⊥	Stoneley	3217 ± 15	3247
				1B	∥	Leaky In Ti	3217 ± 15	3232
Tempered Martensite (Quenched and Temp.)	7805	5868	3170	2A	⊥	Divergent In Steel	3216 ± 55	3170
				2B	∥	Stoneley	3166 ± 15	3162
Bainite (Air cooled)	7817	5869	3175	3A	⊥	Divergent In Steel	3221 ± 55	3175
				3B	∥	Stoneley	3162 ± 15	3166
Fine Pearlite (As Received-Hot Rolled)	7839	5934	3235	4A	⊥	Stoneley	3223 ± 15	3233
				4B	∥	Leaky in Ti	3206 ± 15	3218

*Density of Ti-6Al-4V = 4430 kg/m³,
Longitudinal velocity of Ti-6Al-4V = 6287 m/s in both directions
Shear velocity of Ti-6Al-4V: { Perpendicular to rolling direction (⊥) = 3287 m/s,
Parallel to rolling direction (∥) = 3171 m/s.

Table 4.1 Interface wave velocities for four different microstructures in 4340 steel and two different orientations of a block of rolled Ti-6Al-4V.

4.1.4 Discussion

The experimental results presented in the previous section have been compared, where possible, against theoretical calculations.

Figure 4.5 schematically depicts the situation when a Rayleigh wave traveling through the steel block passes under the titanium. The first change that occurs is at the point of contact, C, where a change in acoustic impedance occurs across the interface. The detailed reactions are very complex and not treatable using infinite medium models, but one




Fig. 4.6 Interface wave velocity versus shear velocity in duplex block of 4340 steel and Ti-6Al-4V using all measured, bulk elastic constants except the shear velocity in the steel, which is allowed to range over values encompassing all measured cases. In this case the shear velocity is taken as 3171 m/s as is the case for the titanium block oriented with the interface wave travel parallel to the rolling direction (B series in Table 4.1).

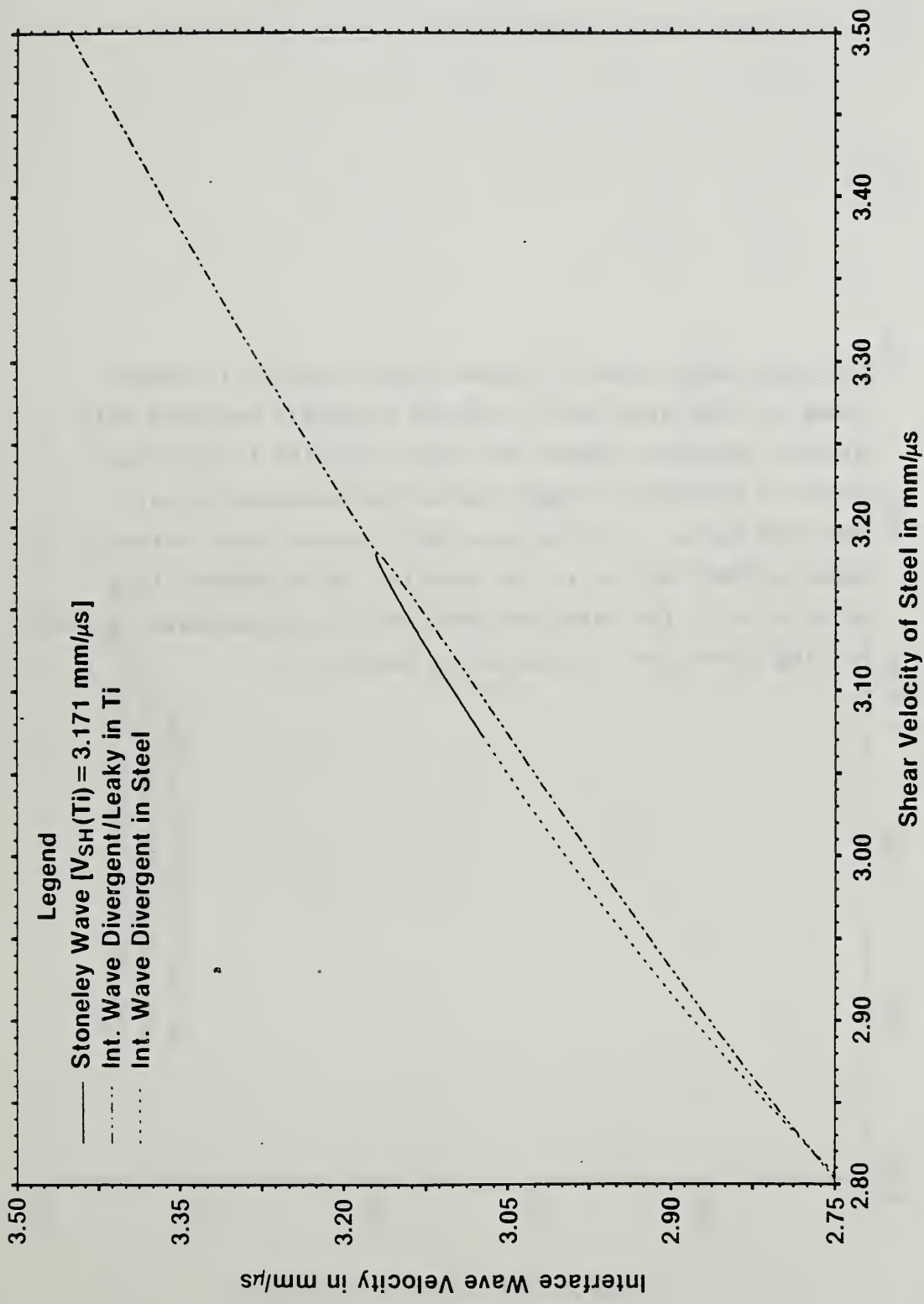
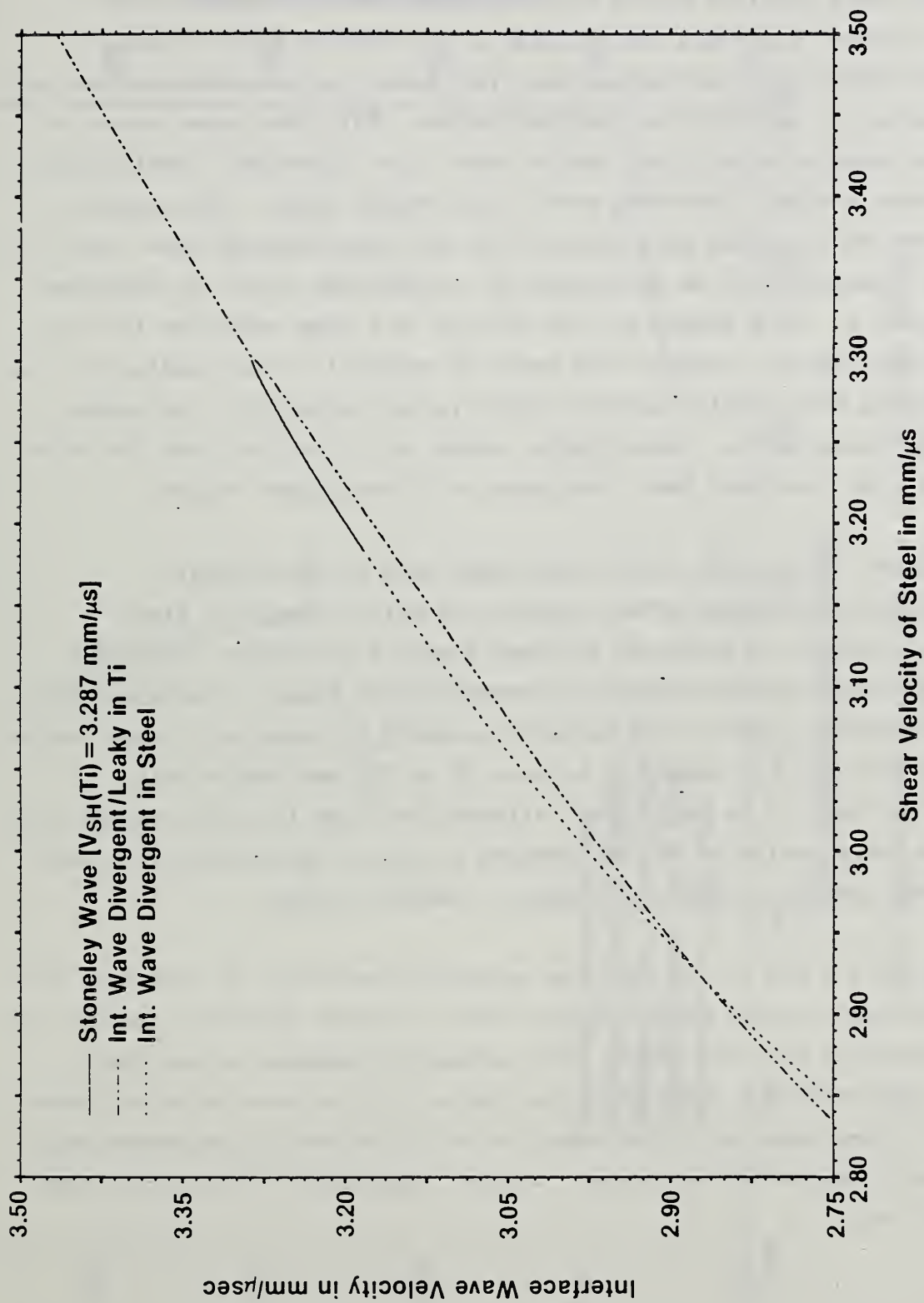


Fig. 4.7 Interface wave velocity versus shear velocity in duplex block of 4340 steel and Ti-6Al-4V using all measured bulk elastic constants except the shear velocity in the steel, which is allowed to range over values encompassing all measured cases. In this case the titanium shear velocity is taken as 3287 m/s as is the case for the titanium block oriented with the interface wave travel perpendicular to the rolling direction. (A series in Table 4.1)



can see that there will be a transition region lying near the point of contact where particle motion will be influenced by the geometries of both the steel block and the combined steel/titanium duplex block. Outside this transition region, the disturbance can be considered to be a combination of waves in the combined medium. With the proper choice of material constants and input surface wave, the "injection" coefficients will favor a single interface wave in the duplex block. The energy to make such an interface wave arises from the input Rayleigh wave, and its energy transport will be determined by its Poynting vector as discussed in section 3. This energy will be carried in a zone emanating from the transition region. Outside this zone the material in each medium will be interacting with similar material which is not moving with the proper interface mode motion. Accordingly, energy will leak out from the outer edges of the interface beam, resulting in a beam spread region.

Preliminary theoretical studies have been made of the velocity, displacement and energy effects associated with a change of steel vis-a-vis that of titanium at a planar steel/Ti interface. The NBS computer codes for the cylindrical geometry were found to describe the planar geometry results with suitable accuracy by choosing a large radius for the cylinder. A radius of between 30 to 300 wavelengths was generally found to be sufficient, although the code is stable enough that one can use a radius of 10^8 wavelengths at which time the error is much less than the algorithmic and computer roundoff errors.

In Figures 4.6 and 4.7 we show the calculated variation of interface wave velocity with varying shear velocity when all other material constants of both materials are held fixed. This assumption appears to accurately model the conditions under which the Table 4.1 data were collected where only the shear modulus of the steel varied significantly and where two distinct titanium velocities were present (according to the orientation of the block).

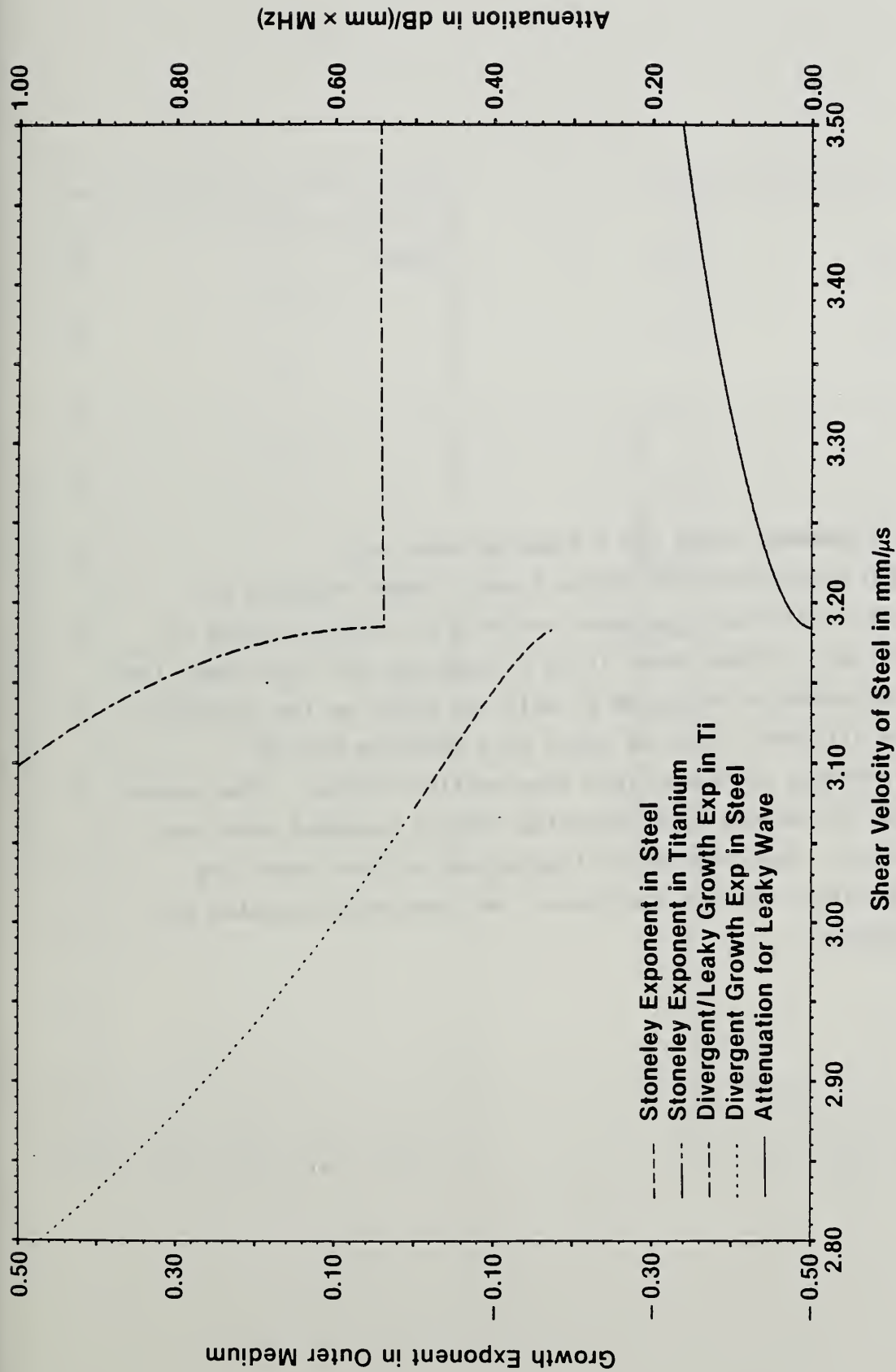


Fig. 4.8 Growth exponent and attenuation for the interface waves shown in Fig. 4.6 (shear wave velocity in titanium block = 3171 m/s). For leaky and divergent waves, the exponent is only shown on the side of the interface where exponential growth occurs.

Fig. 4.9 Displacement field for a Stoneley wave in a 4340 steel/Ti-6Al-4V duplex block. Shear velocity of steel = 3170 m/s and shear velocity of titanium block is 3171 m/s. Since there is no attenuation for this wave, the displacements are shown at only one point on the interface. The ellipses trace the orbit of a particle and the arrowheads on the ellipse show particle motion. The arrows show the energy flow (Poynting vector) averaged over one period. Poynting vector lengths and ellipse sizes are consistent between each other, but arbitrarily scaled for graphing.

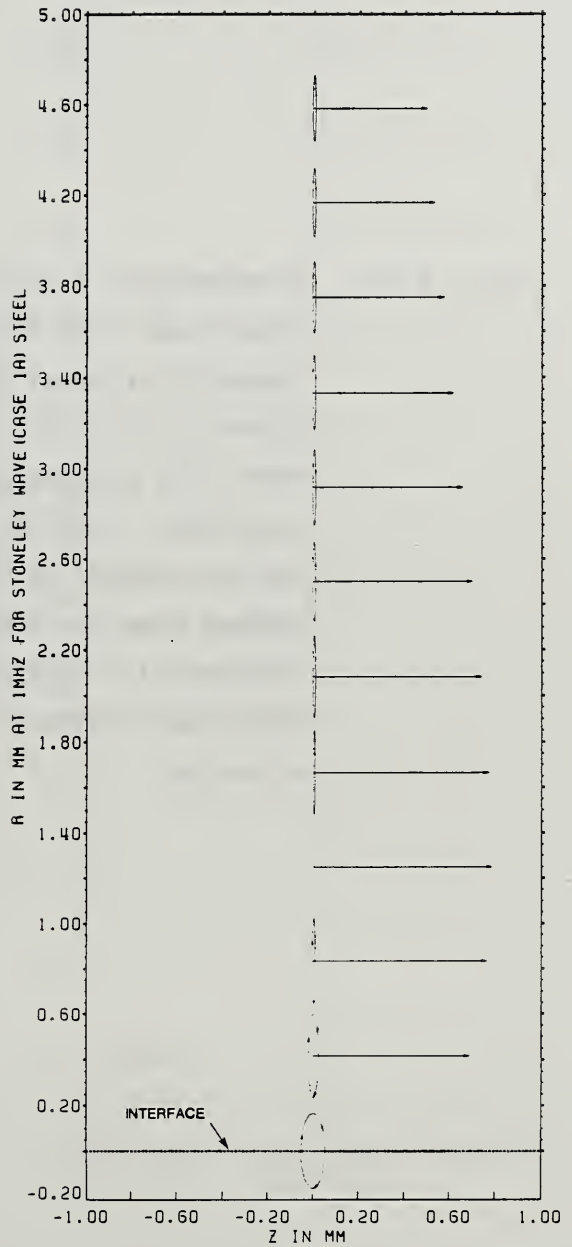
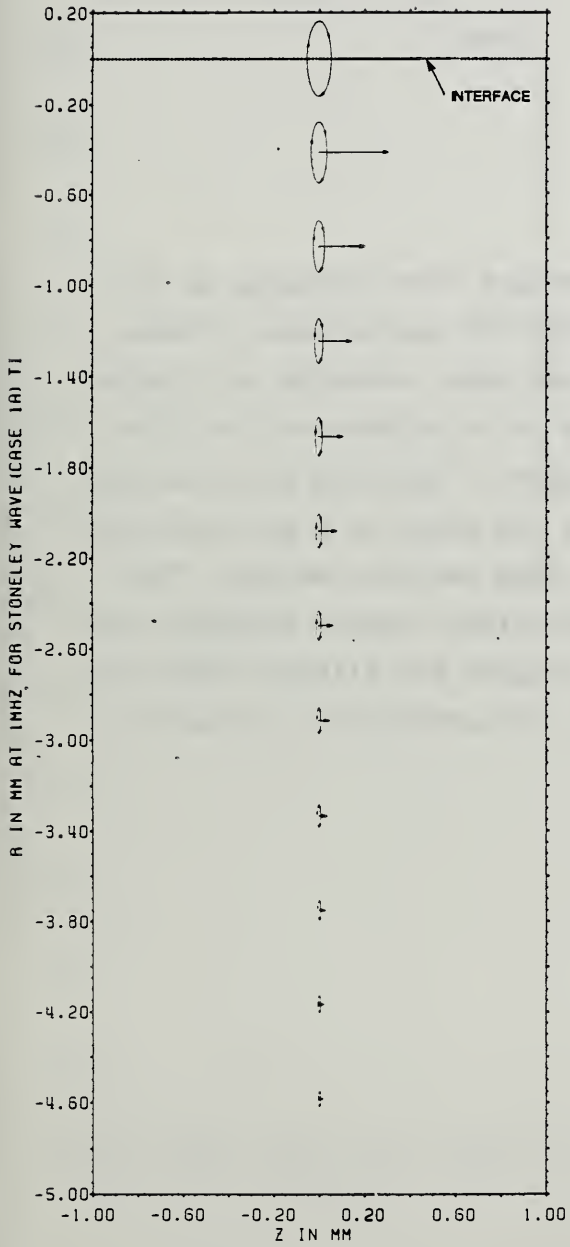


Fig. 4.10 Displacement field for an interface wave diverging on the steel side of a 4340 steel/Ti-6Al-4V duplex block. Shear velocity of steel = 3050 m/s and shear velocity of titanium block = 3171 m/s. Since there is no attenuation for this wave, the displacements are shown at only one point on the interface. The ellipses trace the orbit of a particle and the arrowheads on the ellipse show particle motion. The arrows show the energy flow (Poynting vector) averaged over one period. Poynting vector lengths and ellipse sizes are consistent between each other, but arbitrarily scaled for graphing.

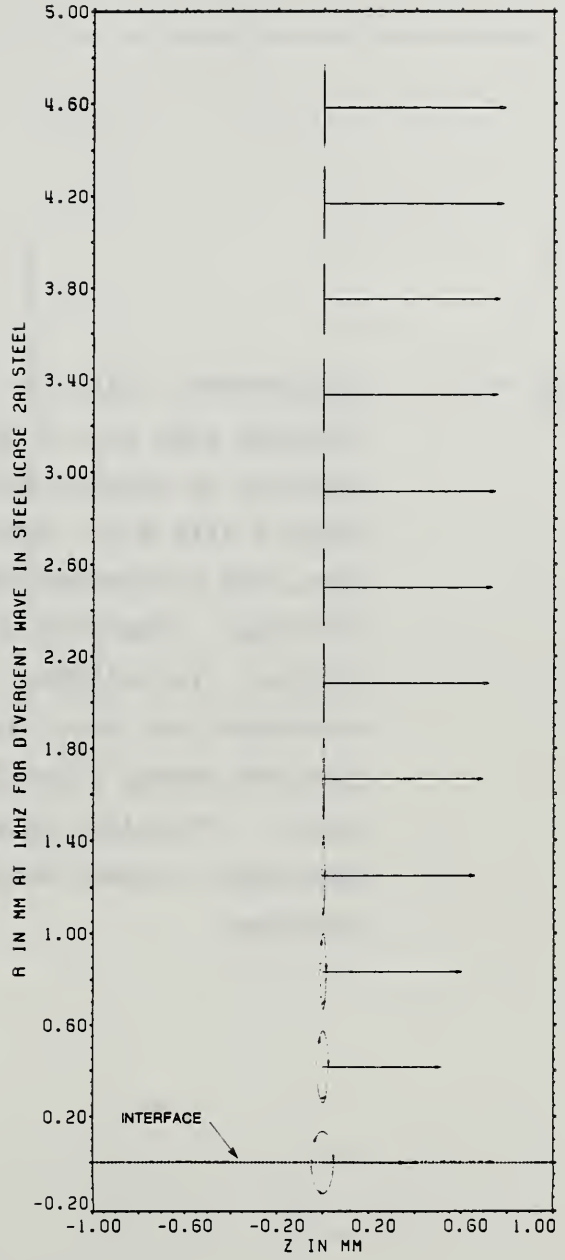
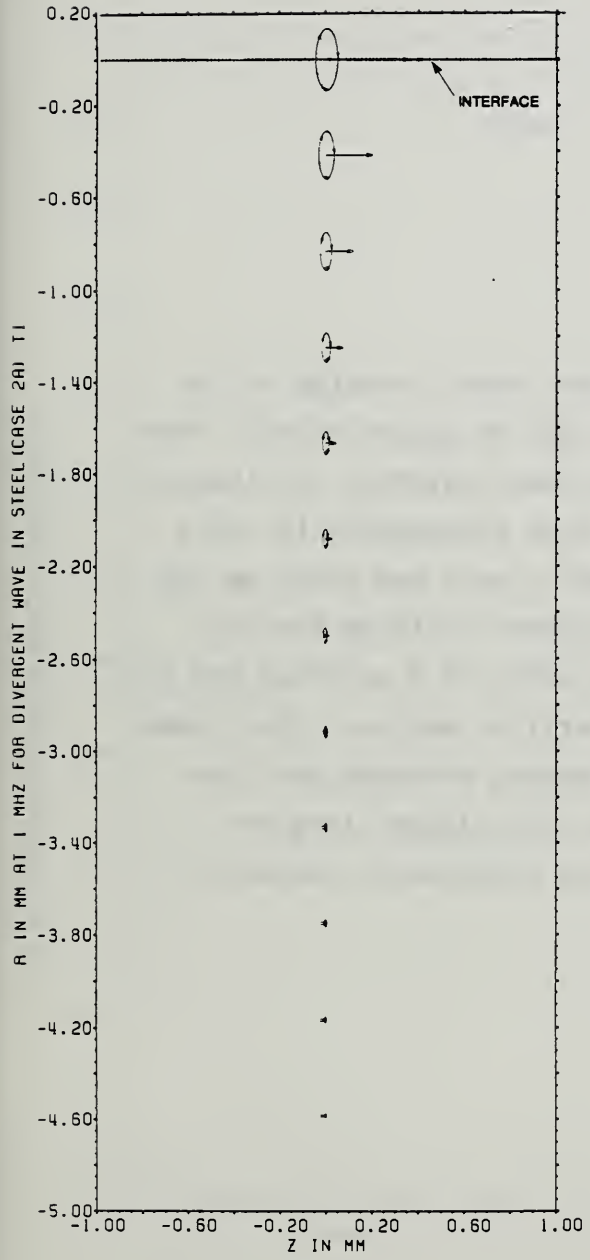


Fig. 4.11 Displacement field for an interface wave diverging on the titanium side of a 4340 steel/Ti-6Al-4V duplex block. Shear velocity of steel = 3170 m/s and shear velocity of titanium block = 3171 m/s. Since there is no attenuation for this wave, the displacements are shown at only one point on the interface. Poynting vectors that are too large are not plotted. The ellipses trace the orbit of a particle and the arrowheads on the ellipse show particle motion. The arrows show the energy flow (Poynting vector) averaged over one period. Poynting vector lengths and ellipse sizes are consistent between each other, but arbitrarily scaled for graphing.

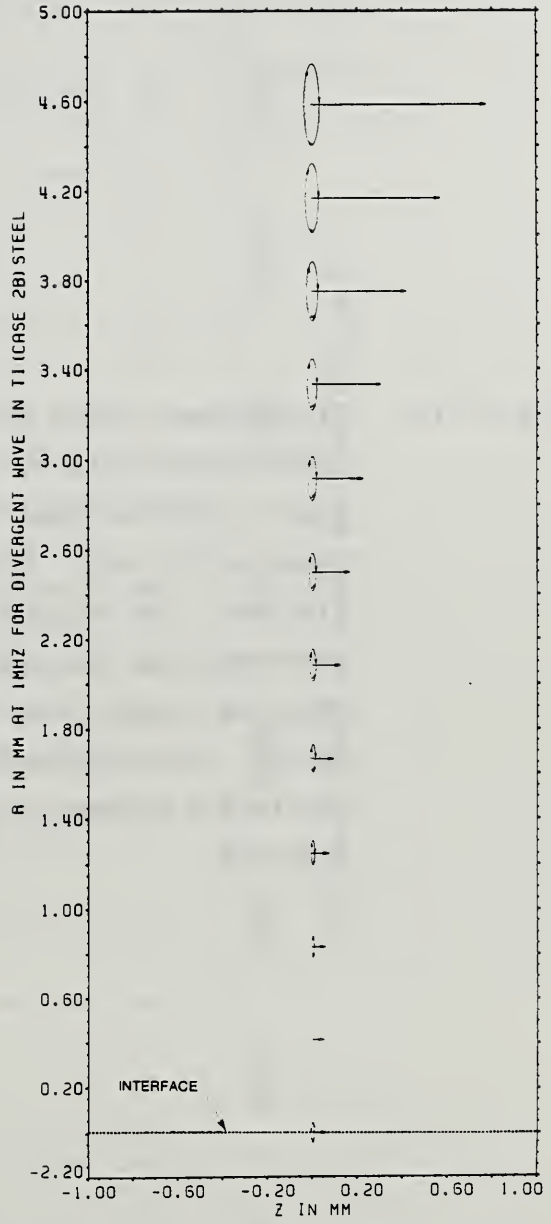
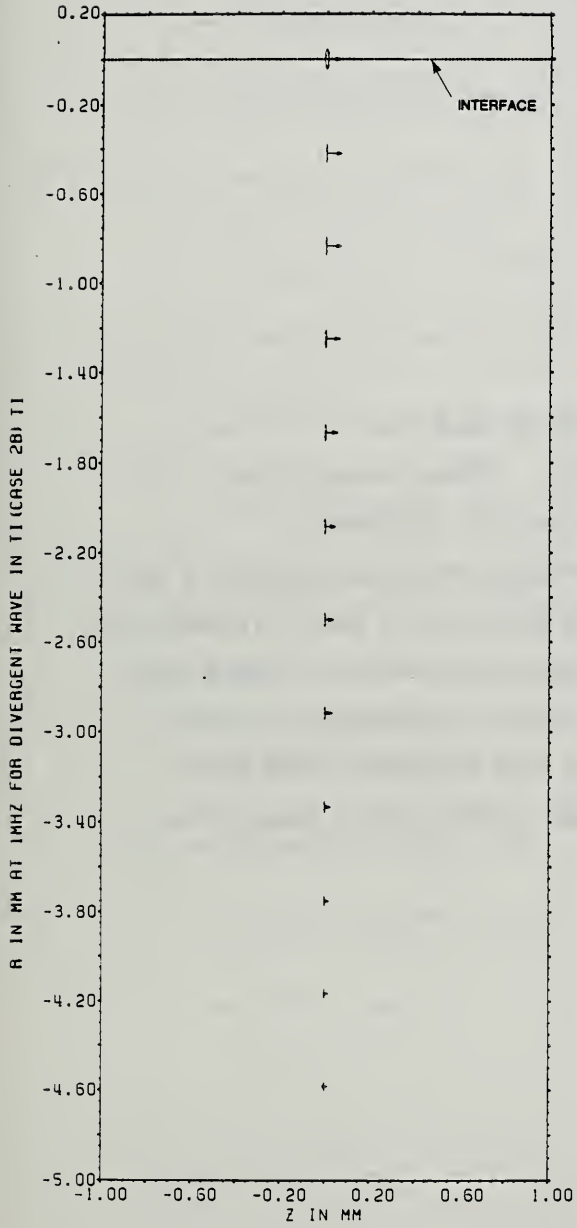
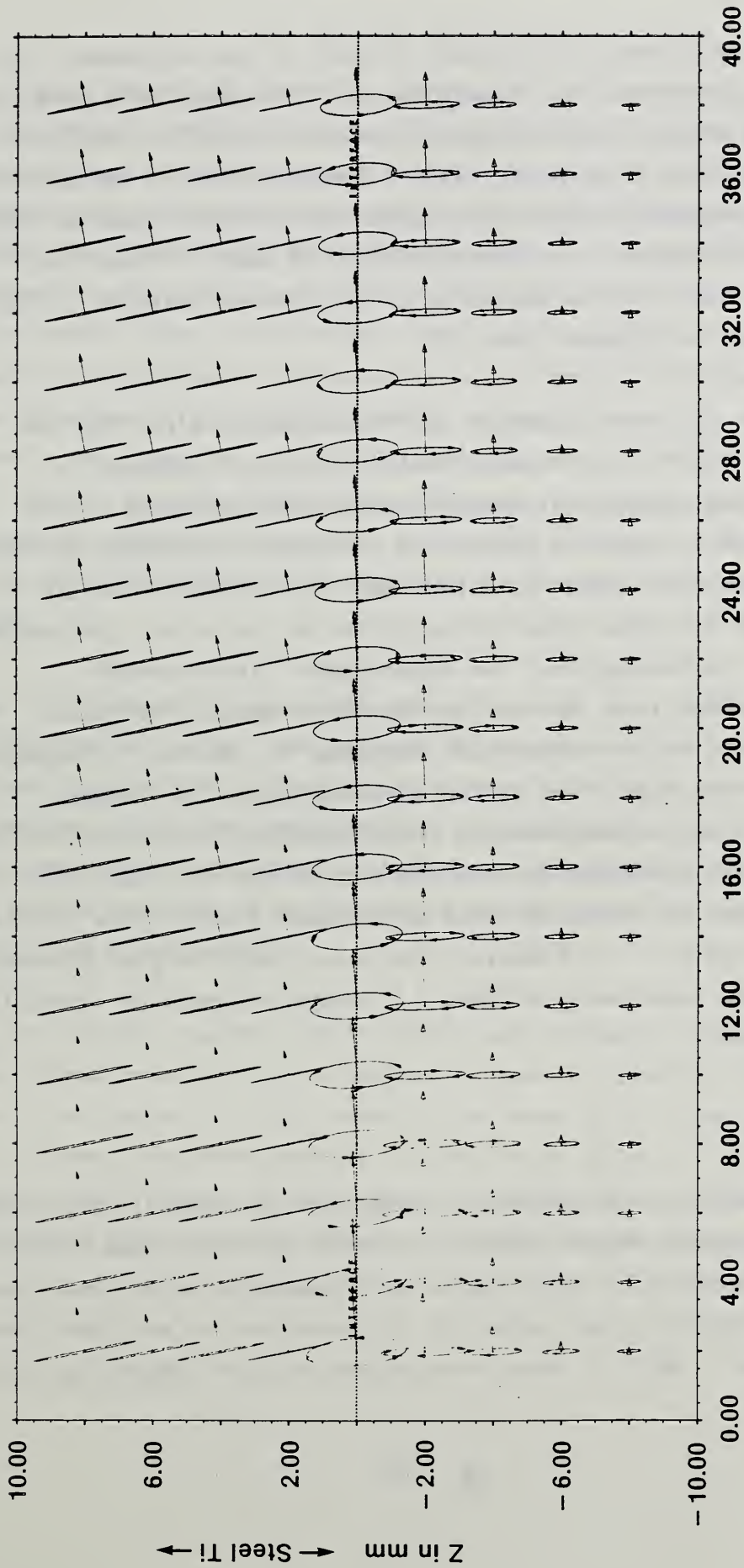


Fig. 4.12 Displacement field for a leaky wave in a 4340 steel/Ti-6Al-4V duplex block. Shear velocity of steel = 3250 m/s and shear velocity of titanium block = 3171 m/s. Displacements that are too large are not plotted. The ellipses trace the orbit of a particle and the arrowheads on the ellipse show particle motion. The arrows show the energy flow (Poynting vector) averaged over one period. Poynting vector lengths and ellipse sizes are consistent between each other, but arbitrarily scaled for graphing.



R in mm at 1MHz for Leaky Wave in Ti (Case 1B)

Four wave types are found to be present in each of the two cases. By varying the orientation of the titanium block, a Stoneley wave mode can be obtained over a shear modulus range in steel from 3070 to 3300 m/s. A greater range could be obtained by using titanium with more varied shear wave velocity. Outside the Stoneley region two different types of leaky waves can occur.² Some of the characteristics of each of these four waves are summarized, for the case of a titanium block oriented in the rolling direction, in Figures 4.8-4.12.

Figure 4.8 gives the growth exponent and the attenuation for the four modes. One sees that in the Stoneley modes the growth exponent is negative indicating exponential decay away from the interface. This displacement field is shown in Figure 4.9. However, the degree of this decay is not uniform over the "Stoneley" part of the shear velocity diagram; near the low steel shear-velocity end of the curve, the exponent approaches zero, indicating that the displacement field extends progressively farther into the steel as the shear modulus decreases. The energy of the wave, and the proportion contained in the steel, increase accordingly. At the "high" end of the Stoneley region the reverse situation holds with the displacement field extending infinitely far into the titanium. Also, although Rayleigh wave plots are not shown here, it is easy to see that the Stoneley waves extend much further into the steel than do Rayleigh waves. For Stoneley type waves there is good agreement between theory and experiment in Table 4.1 except for case 1A, which is being reevaluated.

²The computer codes for the cylindrical model are for radial-axial motion only and, by necessity, do not permit divergence of displacement inside the cylinder. Accordingly, waves modes with transverse motion and those leaking simultaneously on both sides of the interface are excluded from these calculations. Both of these restrictions will be removed in future work.

Near the upper end of the Stoneley region, Fig. 4.8, one sees three wave modes coalescing, corresponding to a branch point on the complex interface surface. Two other possible interface waves are obtained from our calculations. Each of these waves, designated divergent waves, corresponds to a leaky wave whose leakage angle is zero. Their displacement fields are illustrated in Figures 4.10 and 4.11. Thus they do not attenuate along the interface, but correspond to an interface mode whose amplitude increases exponentially away from the interface. Unless the growth exponent is relatively small, we expect these divergent waves will have a low injection coefficient and pick up only a small amount of energy from the input Rayleigh wave. Since the energy content of such a wave increases exponentially as one moves away from the interface, these waves can also be expected to be confined to a narrow zone near the interface.

However, in the case of samples 2A and 3A of Table 4.1, which lie just below the Stoneley region, the exponent is found to be quite small, so that it may be possible to detect such a wave. The large error spread associated with those two sample points requires reinvestigation. The divergent wave coexistent with the Stoneley wave generally has far too large a growth exponent to be detectable, except where the two wave velocities are almost equal.

Beyond the Stoneley region, the interface wave becomes a leaky wave, leaking a shear wave into the titanium as shown in Figures 4.8 and 4.12. One sees from Figure 4.12 that case 1B (and case 2B) are weakly-leaking waves. The two leaky wave samples, 1B and 2B in Table 4.1, show good agreement between theory and experiment. Radiation from one of the samples tested (1B) is predicted at 11° and may be measurable.

4.1.5 Summary of Results for Planar Interface

The results presented in this report demonstrate the following:

- o Feasibility of generating interface waves at planar interfaces of dissimilar materials by mode conversion of Rayleigh waves propagated in the more dense medium.
- o Effect of interface integrity upon the measured interface wave velocity. This type of measurement yields information on the degree of perfection of interface contact.
- o Effect of microstructure near the interface on interface wave velocity. Correlation of this data is not yet complete, but appears to indicate that over a range of frequencies where wavelength is substantially greater than bulk microstructure characteristics, the interface wave type and velocity can be predicted from bulk elastic moduli near the interface. When the bulk moduli vary with depth, the velocity will become dispersive, but should still be predictable from theory. This points to the possibility of carrying out inverse modelling to obtain information on the behavior of bulk moduli near the interface from interface wave measurements.

4.2 Cylindrical Interfaces

In this section we will discuss our work pointing to the application of leaky interface waves to the measurement of elastic properties in the interface region of fiber reinforced metal matrix composites. This work promises to lead to a technique for direct ultrasonic imaging of cylindrical interfaces.

As a leaky wave travels along an interface it radiates acoustic energy out of the interface. The leaked ultrasonic energy forms a displacement field at the surface of the matrix that can be ultrasonically detected. This wave field contains direct information on interface properties such as the quality of bonding the distribution of natural defects and the elastic constants. It is our ultimate aim to use the leaky interface wave in a novel form of acoustic microscopy so that local elastic constants can be measured and the three-dimensional structure of the interface reconstructed.

The viability of the approach depends first on the existence of suitable interface waves for the material combinations and geometries of interest in MMCs. This report addresses that first question in depth. Subsequent work will address methods for the microscopic measurement of interface waves in actual MMCs and the analysis of this data to obtain the quantities of importance.

4.2.1 Wave Propagation of Embedded Cylinders

The results reported in section 4.1 demonstrate that Stoneley and leaky waves can be propagated along planar interfaces in certain combinations of materials. However, as pointed by Owen [11], and now extended in our recent work to the case of cylindrical fiber geometries, true Stoneley type waves exist in only a limited range of materials (shear moduli of matrix and reinforcement approximately equal) which are generally not of importance for MMCs.

On the other hand it appears that leaky waves can be usefully propagated along the interface types -- high modulus reinforcements in a relatively low modulus matrix -- needed for metal matrix composite applications. We

have investigated this in detail, particularly in the fiber-reinforced cylindrical geometry. Detailed calculations and numerical experiments were conducted for this geometry on several model systems. We considered the behavior of model aluminum matrix composites embedded with various fibers, including stainless steel, SiC, boron and graphite.

The cylindrical interfaces in MMCs may be thought of as occurring between a rod-shaped fiber of fixed radius and a tunnel-like matrix of the same radius. Not only do these cylindrical interfaces exhibit dispersive wave behavior, but both empty tunnels and bare cylinders do also. This dispersive behavior can be conveniently summarized by a dispersion curve relating the phase velocity of a particular ultrasonic wave mode to normalized frequency. The velocity at a particular frequency ω is found by solution of a secular equation, (3.33). The root of this equation corresponds to a complex velocity

$$v(\omega) = v_R(\omega) + i v_I(\omega)$$

where $v_R(\omega)$ corresponds to the real part of the velocity and $v_I(\omega)$ is the imaginary part that leads to leakage from the interface and thus amplitude attenuation along the interface. The waves thus characterized are radially symmetric and have no displacements in the tangential direction. Since they propagate in the direction of the cylinder axis and have only radial and axial displacement components, we refer to them as radial-axial modes.

To determine the amount of attenuation along the interface of a radial-axial mode, we express the equation for the mode as:

$$\phi(z, t) = \phi_0(r) \exp [i(\omega t - kz)]$$

where $\phi(z,t)$ is the wave amplitude, $\phi_0(r)$ is the initial amplitude dependence on r , and $k = \omega/v$ is the wavenumber. It is useful, as in section 3.2.4, to introduce the factor $\kappa_0 = \omega r_0 = 2\pi r_0 f$, where r_0 is the interface radius and f is the frequency. The velocity, v , may then be thought of as a function of κ_0 . We can write:

$$\phi(z,t) = \phi_0(r) \exp[i\omega t] \exp[-i(\kappa_0/v) (z/r_0)]$$

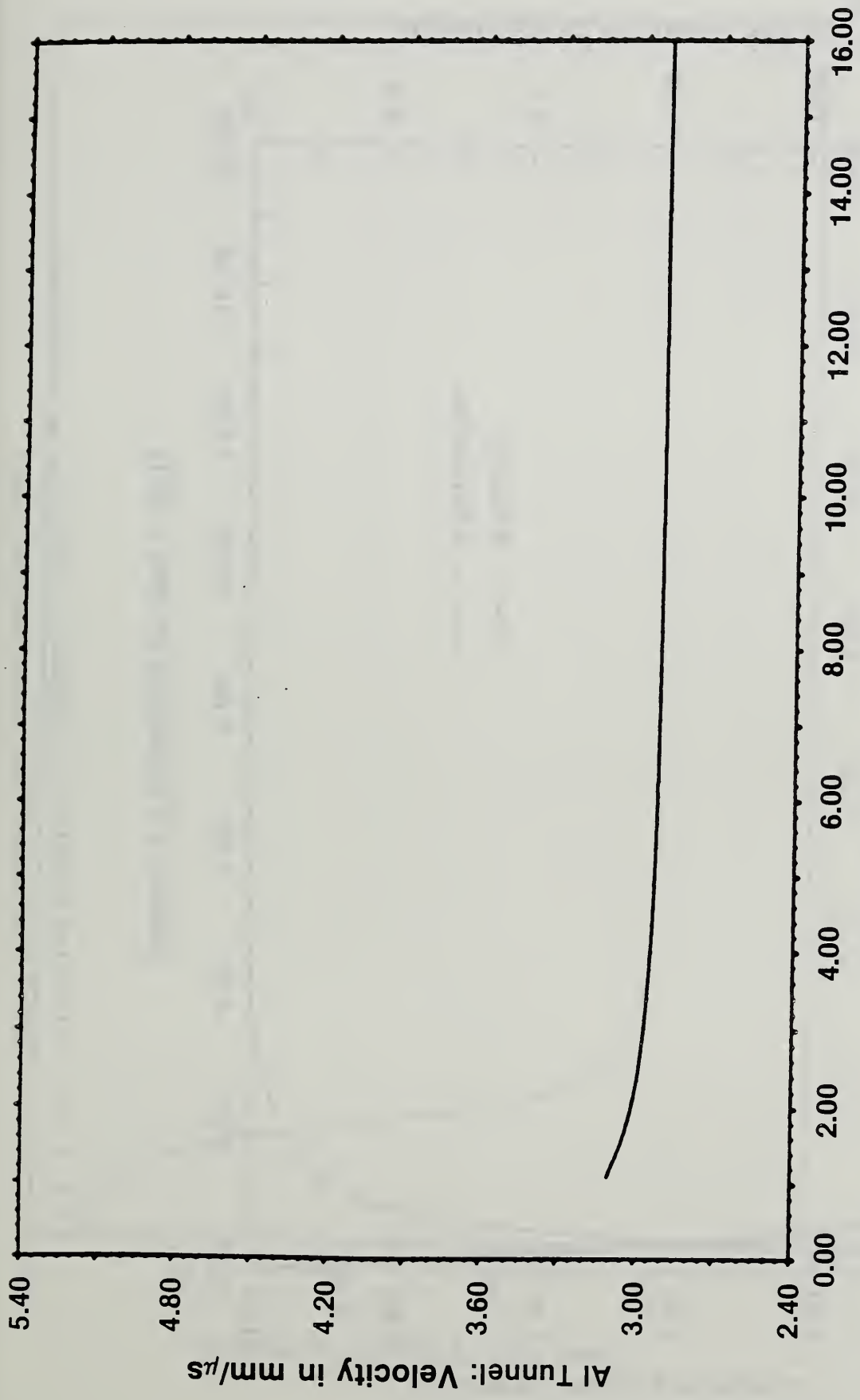
Multiplying both top and bottom of the exponent of the first term by the complex conjugate of v gives

$$\begin{aligned} \phi(z,t) &= \phi_0(r) \exp \left[i \left[\omega t - (z/r_0) (v_R \kappa_0 / (v_R^2 + v_I^2)) \right] \right] \\ &\quad \cdot \exp \left[-(z/r_0) (v_I \kappa_0 / (v_R^2 + v_I^2)) \right] \\ &= \phi_0(r) \times \text{phase factor} \times \text{attenuation.} \end{aligned}$$

We, then, define the quantity

$$\begin{aligned} &-20 \log_{10} \left[\exp \left[-v_I \kappa_0 / (v_R^2 + v_I^2) \right] \right] / (r_0 \cdot f) \\ &= 40\pi v_I \log_{10}(e) / (v_R^2 + v_I^2) \end{aligned} \quad (1)$$

as the attenuation coefficient. It represents the exponent governing the decrease in wave amplitude per unit frequency and per unit distance along the interface. Since the attenuation coefficient depends only on $r_0 \cdot f$, and since fibers in MMCs are of very small radius, this suggests that



Radius x Frequency in mm x MHz

Fig. 4.13 Calculated dependence of the velocity of a nonattenuated radial displacement mode for an aluminum tunnel vs. frequency x radius.

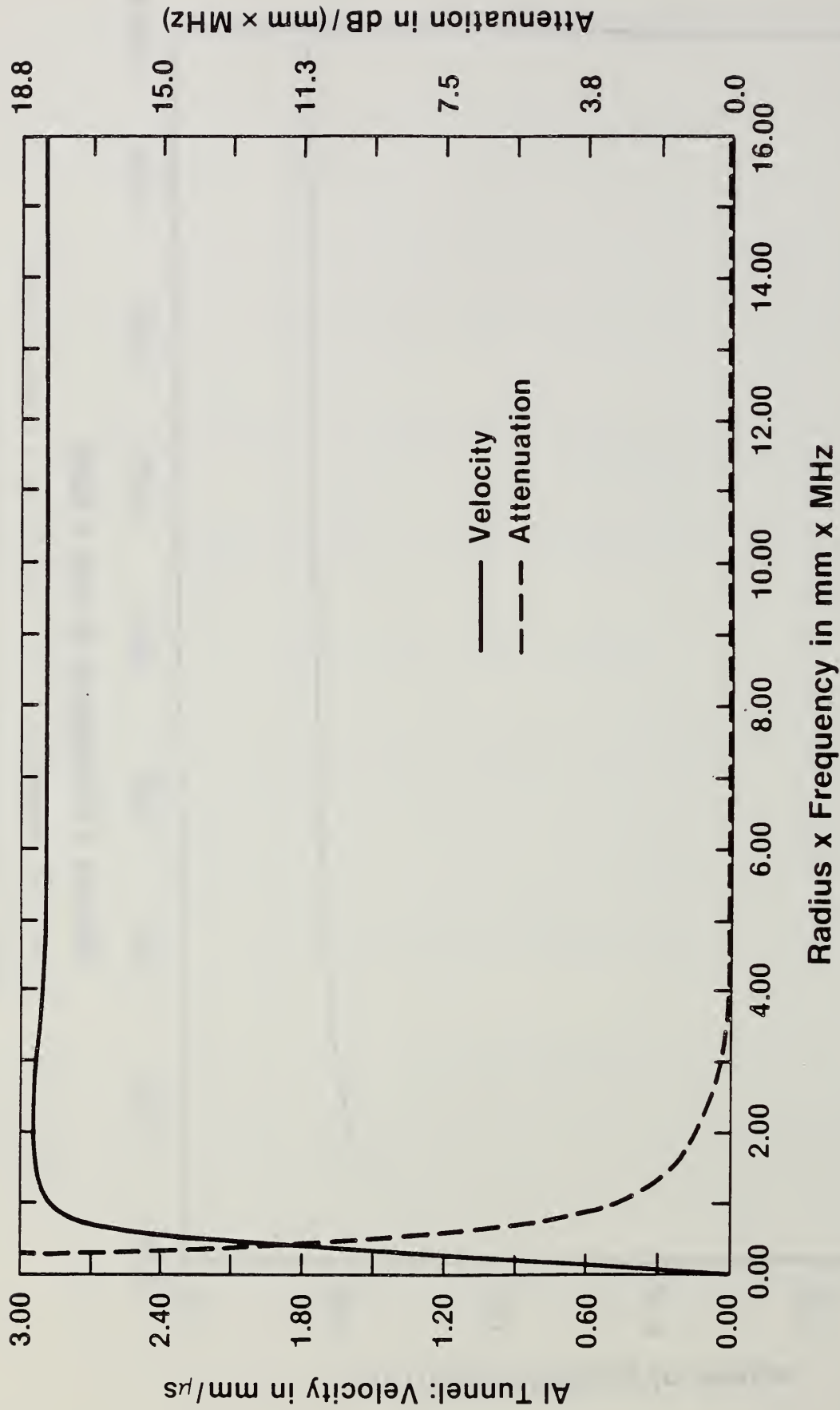


Fig. 4.14 Calculated velocity vs. frequency x radius for an attenuated radial displacement mode on an aluminum tunnel.

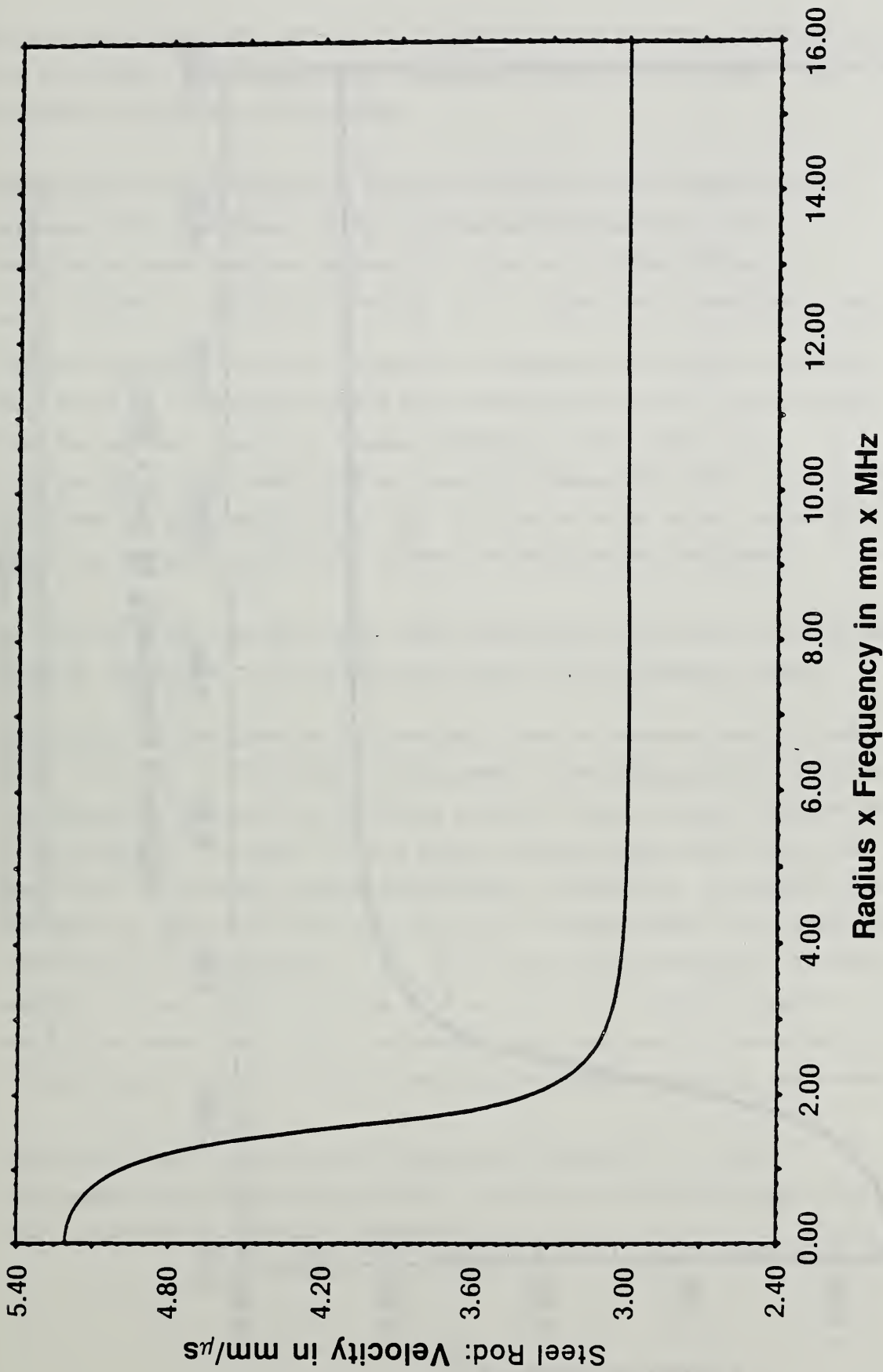


Fig. 4.15 Calculated velocity vs radius x frequency for a nonattenuated radial displacement mode in a steel rod.

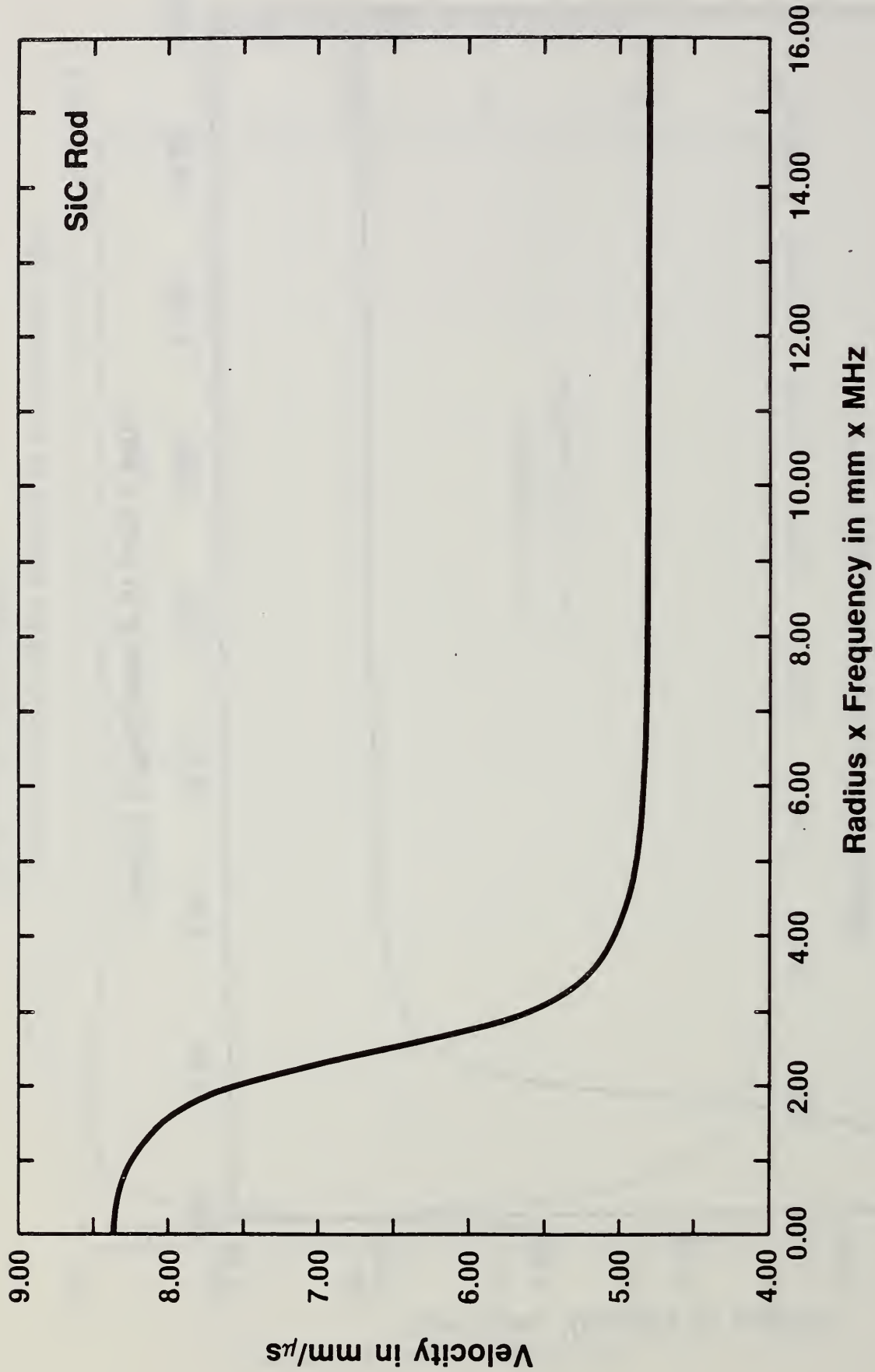


Fig. 4.16 Calculated velocity vs radius x frequency for a nonattenuated surface radial displacement mode in a silicon carbide rod.

guided interface waves may exist in fiber-matrix material combinations not previously considered, over frequency ranges and distance scales suitable for acoustic microscopy.

Knowledge of the attenuation factor is important for experimental purposes. For instance, if the calculated attenuation of an interfacial mode does not exceed the value of 2 dB/mm·MHz up to $r_0 \cdot f = \kappa_0 / 2\pi = 1$ mm·MHz for radius $r_0 = 1$, then the attenuation along a typical interface of 30 mm length at a frequency 1 MHz will be 60 dB. This level of attenuation would not preclude detection of the arrival. When the attenuation for a chosen frequency is too high, e.g. 5 dB/(mm·MHz), this mode will be totally attenuated at the far end of an interface of 30 mm length [150 dB] This permits us to determine which modes are detectable with our present techniques and equipment.

In the following, we plot both the attenuation coefficient and the phase velocity versus ωr_0 . The dispersion curve for an aluminum tunnel containing no fiber was calculated and found to contain several wave modes. In Fig. 4.13 a radial displacement mode propagating axially along the tunnel is shown. This mode has a purely real root and thus suffers no attenuation. In Fig. 4.14 we show a second radial-axial mode that has been found to exhibit frequency-dependent attenuation. As noted, this attenuation, when high, can for practical purposes make this second mode unobservable in experiments. If, for a particular frequency, we were to measure a velocity on the curve of Fig. 4.14 in a fibrous composite, we would know immediately that the bonding was very weak or nonexistent at the interface, because the wave would have propagated along the tunnel.

Figures 4.15 and 4.16 show the dispersion curves for a radial displacement mode propagating axially along bare fibers of stainless steel and silicon carbide, respectively.

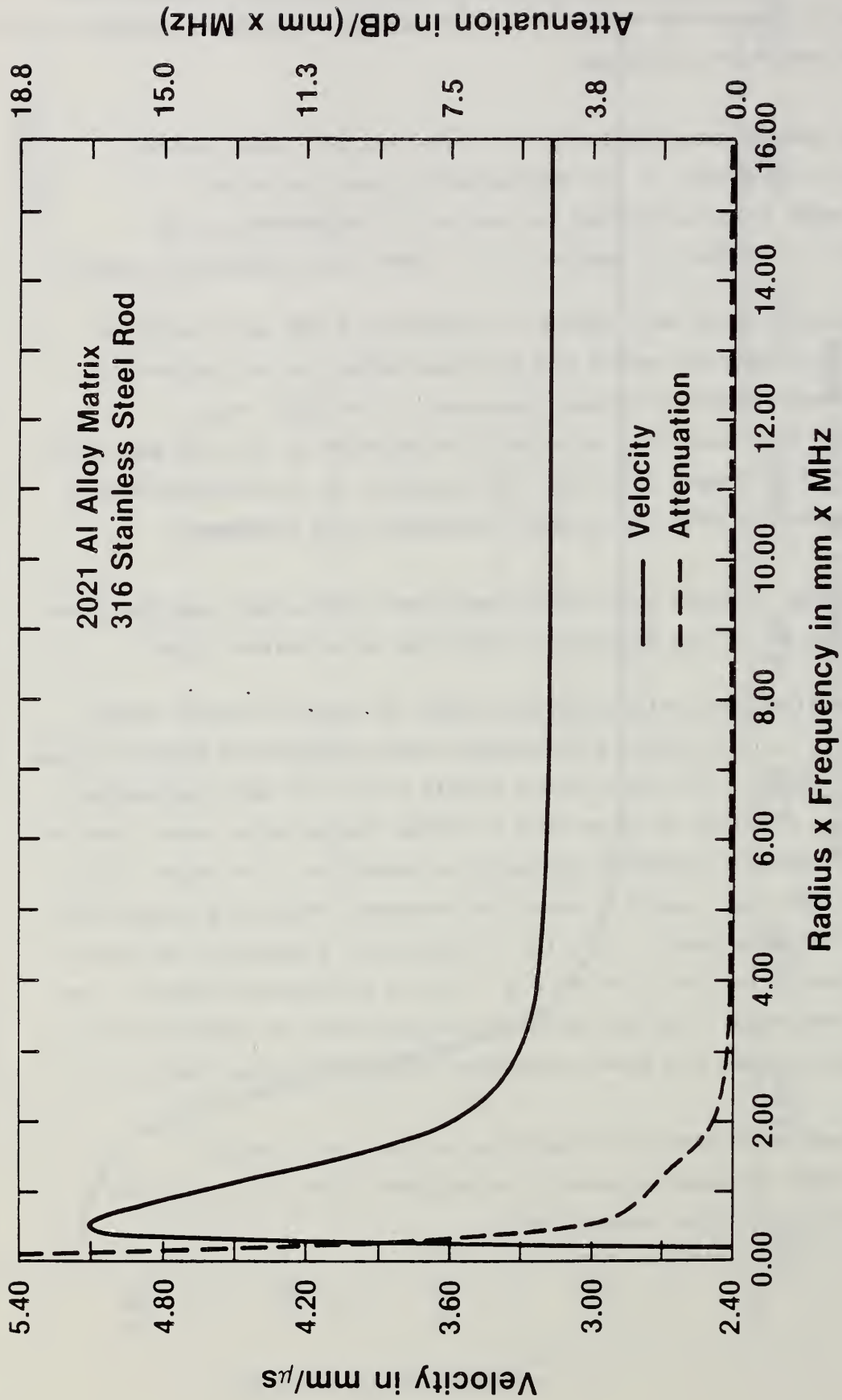


Fig. 4.17 Weakly attenuated radial displacement mode of leaky interface wave calculated for a aluminum-steel interface.

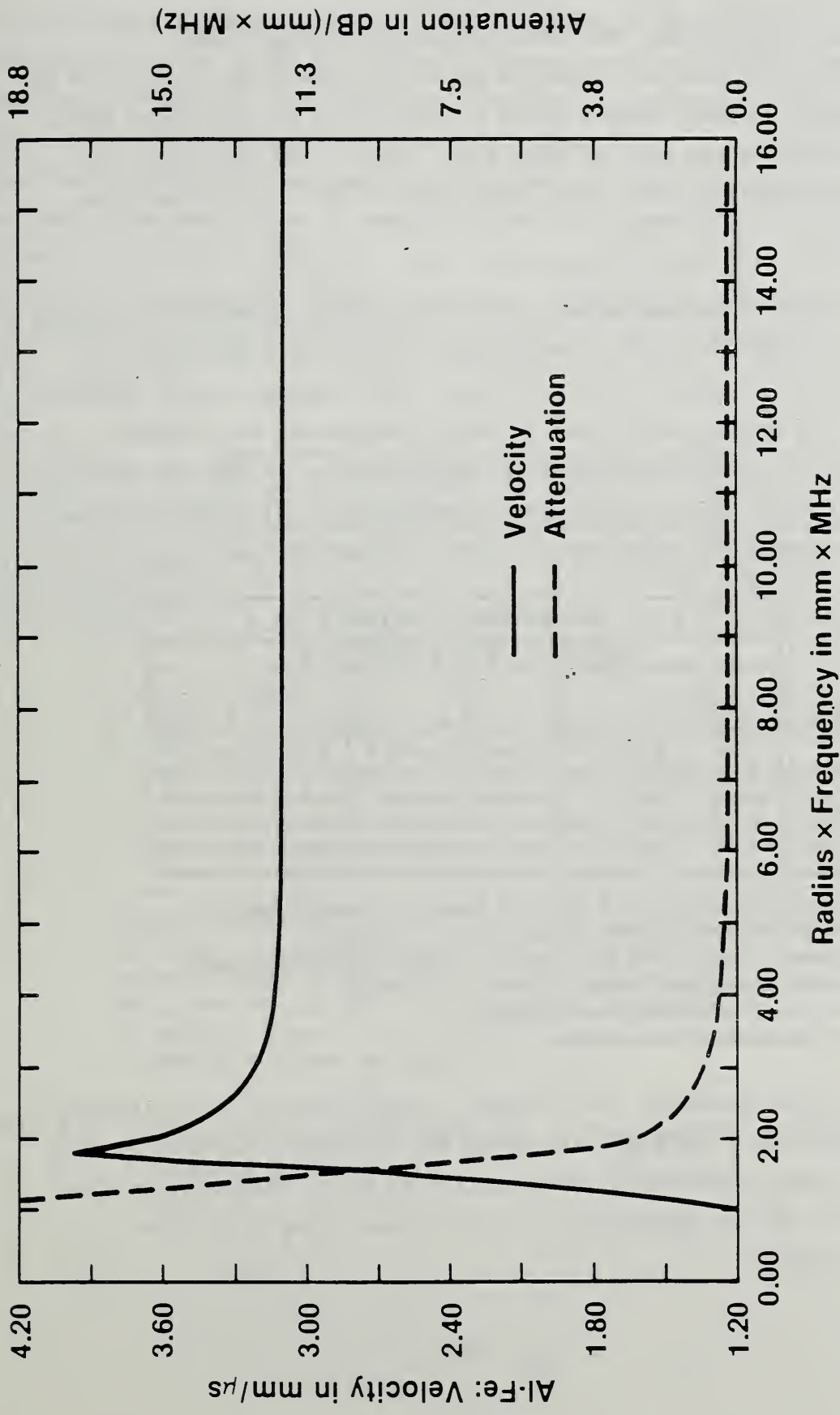


Fig. 4.18 Attenuated radial displacement mode calculated for an aluminum-steel interface.

The dispersion behavior for two interface waves at cylindrical aluminum-steel interfaces are shown in Figs. 4.17 and 4.18. The curve in Fig. 4.17 can be crudely thought of as a combination of the tunnel mode of Fig. 4.13 and the rod mode of Fig. 4.15. Similarly, the curve in Fig. 4.18 corresponds to the tunnel mode (Fig. 4.14) and the rod mode (Fig. 4.15).

We find that leaky interface waves in the cylindrical geometry are always connected to leakage of acoustic energy out of the interface into the metal of the matrix rather than vice versa. This leakage can be remotely detected and its measurement is an important feature of our planned approach to ultrasonic characterization of interfaces in MMCs by means of acoustic microscopy. Table 4.2 lists the calculated velocities for the three weakly attenuated radial-axial modes in aluminum-steel.

ALUMINUM - STEEL						
FREQUENCY X RADIUS [MHz x mm]						
MODE	8.0		16		32	
	V	A	V	A	V	A
I	3.18	1.04×10^{-2}	3.180	9.6×10^{-3}	3.18	9.55×10^{-3}
II	4.855	0.21	4.438	5.3×10^{-2}	4.31	2.3×10^{-2}
III	5.05	0.21	← cut off at 8.64 [MHz x mm] →			

Density of Aluminum $\rho = 2.77 \times 10^{-3}$ [g/mm³], Longitudinal Velocity of Al = 6.323 [mm/ μ s], Shear Velocity of Al = 3.10 [mm/ μ s]

Density of Steel $\rho = 7.9 \times 10^{-3}$ [g/mm³], Longitudinal Velocity of Steel = 5.92 [mm/ μ s], Shear Velocity of Steel = 3.25 [mm/ μ s]

V = velocity of interface wave [mm/ μ s]

A = attenuation dB per unit radius

Table 4.2 Three prominent leaky modes for steel fibers in an aluminum matrix. The modes are given for 3 values of frequency times radius, and the attenuation in the axial direction is given by dB per radius unit (i.e. distance along axis/fiber radius).

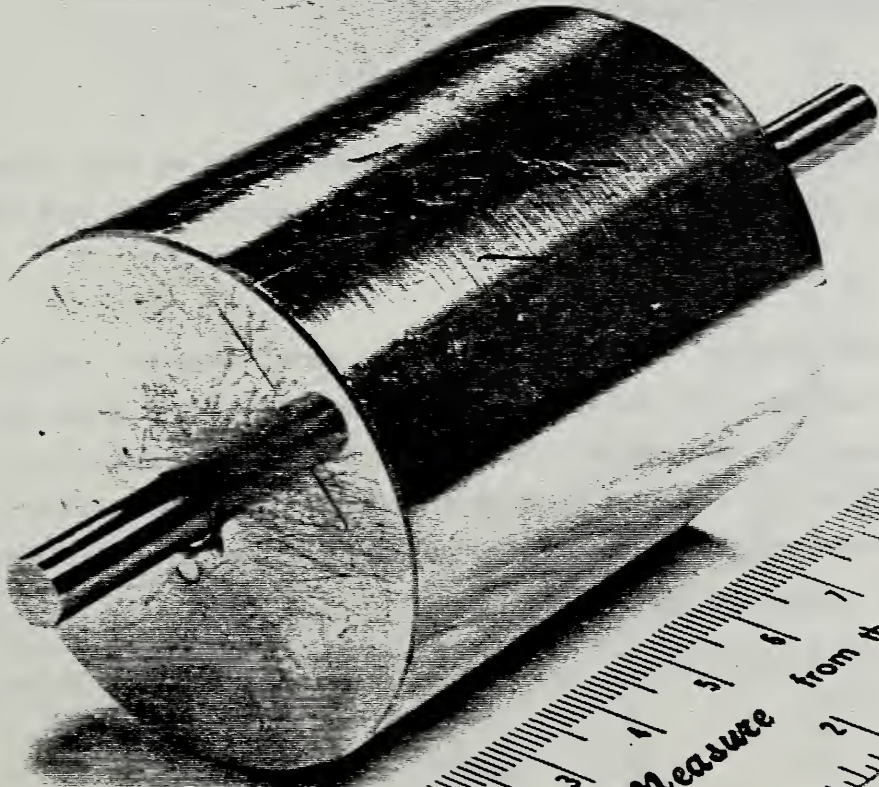
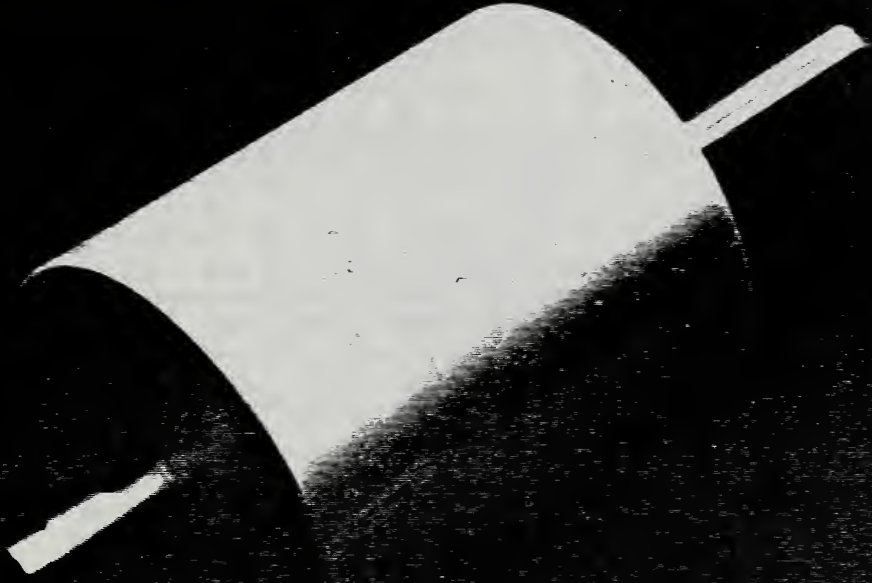
We have extended these theoretical calculations to several material combinations found in MMCs. Table 4.3 shows the velocity dependence as a function of frequency for five similar modes in aluminum-silicon carbide, while Table 4.4 displays such modes in aluminum-boron. Our preliminary experiments could only be designed after such calculations were available. We would like to emphasize that the presence of cylindrical curvature introduces new modes, and, therefore, new opportunities for the ultrasonic measurements of MMC interfaces. The use of leakage from the interface for interface characterization is one of the unexpected outputs of this program.

ALUMINUM-SILICON CARBIDE								
FREQUENCY x RADIUS [MHz x mm]								
MODE	1		2		5		10	
	V	A	V	A	V	A	V	A
I	6.1	4.00	5.6	3.8	4.8	3.2	4.7	5.5
II	5.8	2.00	7.8	2.9	8.6	8.0	8.25	18.0
III	7.6	2.50	8.1	3.2	9.0	5.0	5.5	2.2
IV	0.8	52.00	2.8	50.00	4.4	30.0	10.2	2.5
V	0.1	53.00	0.22	50.00	2.2	30.0	6.6	4.2
VI	0	23.2	1.30	20.0	7.5	5.5	5.6	1.25

Density of Aluminum $\rho = 2.77 \times 10^{-3}$ [g/mm³], Longitudinal Velocity of Al = 6.323 [mm/ μ s], Shear Velocity of Al = 3.1 [mm/ μ s]
 Density of Silicon Carbide = 3.2×10^{-3} [g/mm³], Longitudinal Velocity of SiC = 9.649 [mm/ μ s], Shear Velocity of SiC = 5.193 [mm/ μ s]
 V= velocity of interface wave [mm/ μ s]
 A= attenuation dB per unit radius

Table 4.3 Six prominent leaky modes for silicon carbide fibers in an aluminum matrix.

Fig. 4.19 Model metal matrix composite sample used to test theoretically predicted dispersion. Aluminum-steel interface composed of 3.2 mm radius 316 steel rod shrink fitted into a 2024 aluminum alloy cylinder.



Good Measure from the
National Bureau of Standards
Washington, D.C.

ALUMINUM - BORON								
FREQUENCY x RADIUS [MHz x mm]								
MODE	2		4		6		10	
	V	A	V	A	V	A	V	A
I	7.05	0.01	6.12	0.43	6.00	0.605	5.96	1.07
II	2.00	20.0	8.5	3.2	10.3	1.5	10.7	0.4
III	12.30	0.36	12.80	0.37	13.2	0.4	13.4	0.38
IV	cut off at 4.45 [MHz x mm]				23.4	0.5	12.7	0.4
V	2.50	9.5	5.50	3.7	7.7	2.6	8.21	3.05

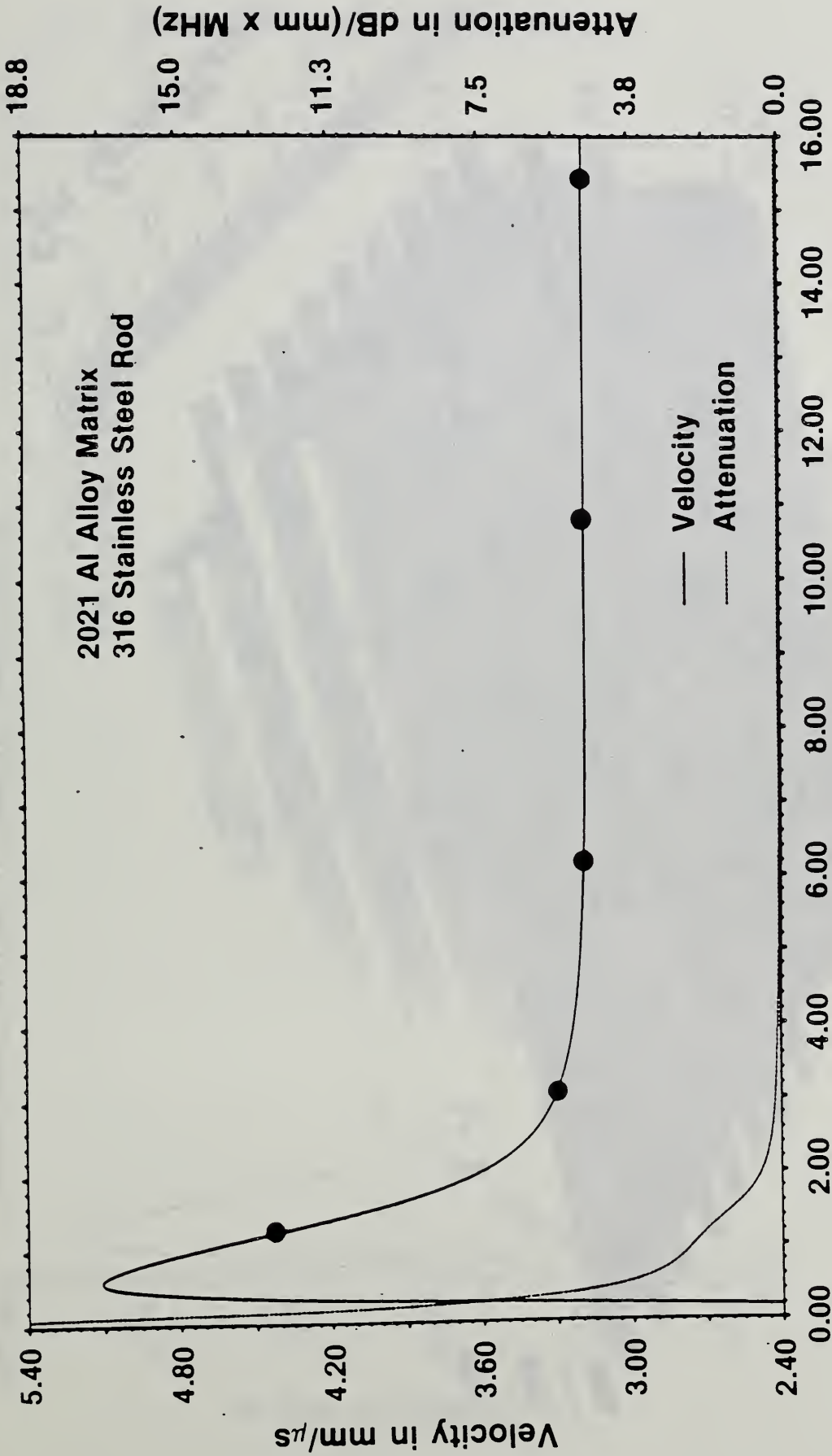
Density of Aluminum = 2.77×10^{-3} [g/mm³], Longitudinal Velocity of Al = 6.323 [mm/ μ s], Shear Velocity of Al = 3.1 [mm/ μ s]
 Density of Boron = 2.352×10^{-3} [g/mm³], Longitudinal velocity of Boron = 13.228 [mm/ μ s], Shear Velocity of Boron = 8.657 [mm/ μ s]
 V= velocity of interface wave [mm/ μ s]
 A= attenuation dB per unit radius

Table 4.4 Five prominent leaky modes for boron fibers in an aluminum matrix.

4.2.2 Aluminum-Steel Interfaces

To systematically confirm the theoretical predictions we have intensively studied model specimens containing an aluminum matrix-steel rod interface.

Two fabrication methods were used to prepare model samples, shrink fitting and casting. The first model was composed of a 3.2 mm radius 316 stainless steel rod, shrink fitted into a 2024 aluminum alloy cylinder (Fig. 4.19). Shrink fitting created a very good cylindrical interface between these two materials because of the large difference in their thermal expansion coefficients.



Radius x Frequency in mm x MHz

Fig. 4.20 The interface wave velocity measured as a function of frequency for the model shrink fit sample (points) and the theory (continuous line).

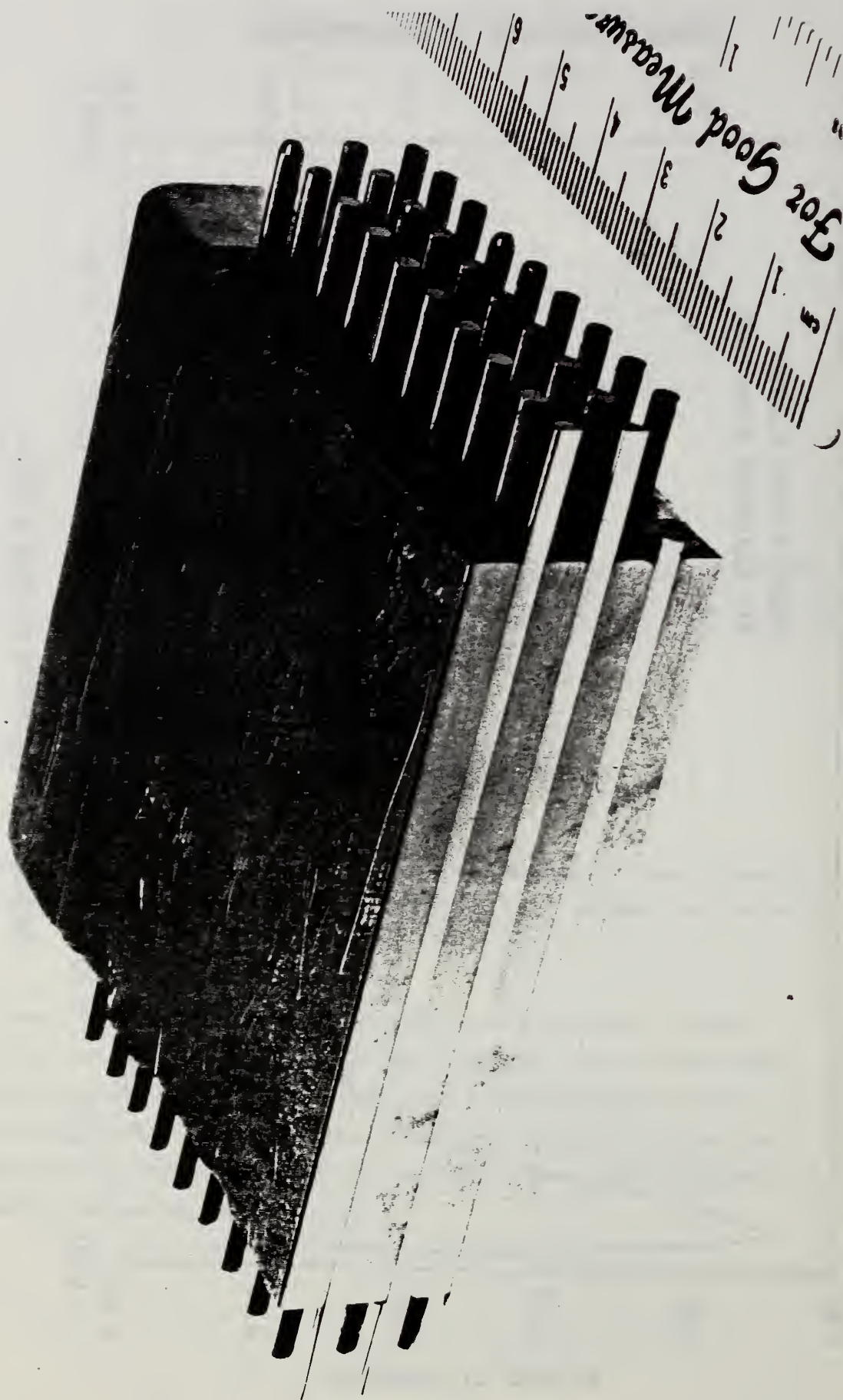


Fig. 4.21 A second model metal-matrix composite sample made by casting. Aligned steel rods of radius = 1.195 mm in an aluminum matrix. The spacing between the rods = 4 mm.

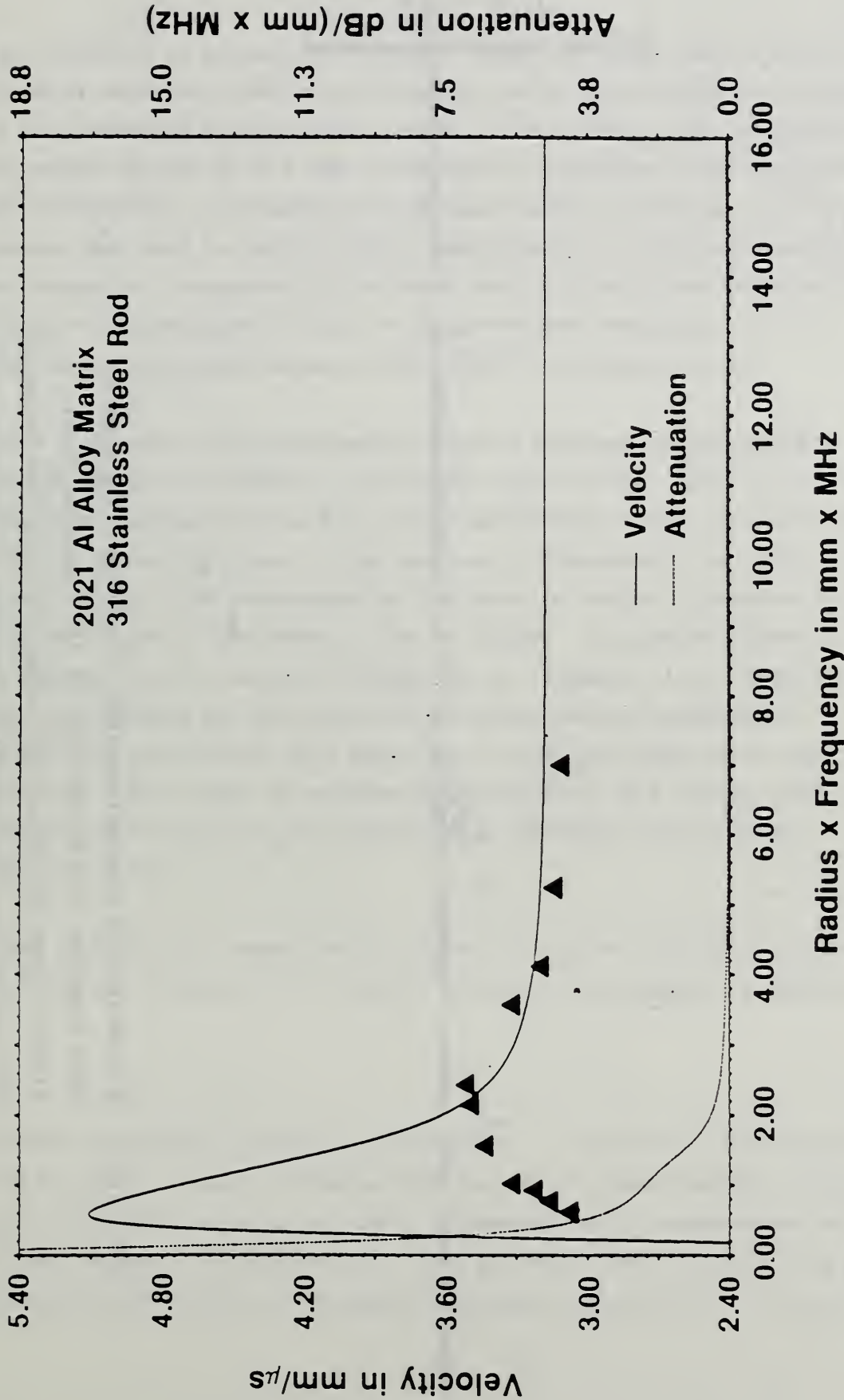


Fig. 4.22 Velocity of leaky interface mode measured as a function of frequency (triangles). Comparison with the theory for the aluminum-steel interface (continuous line).

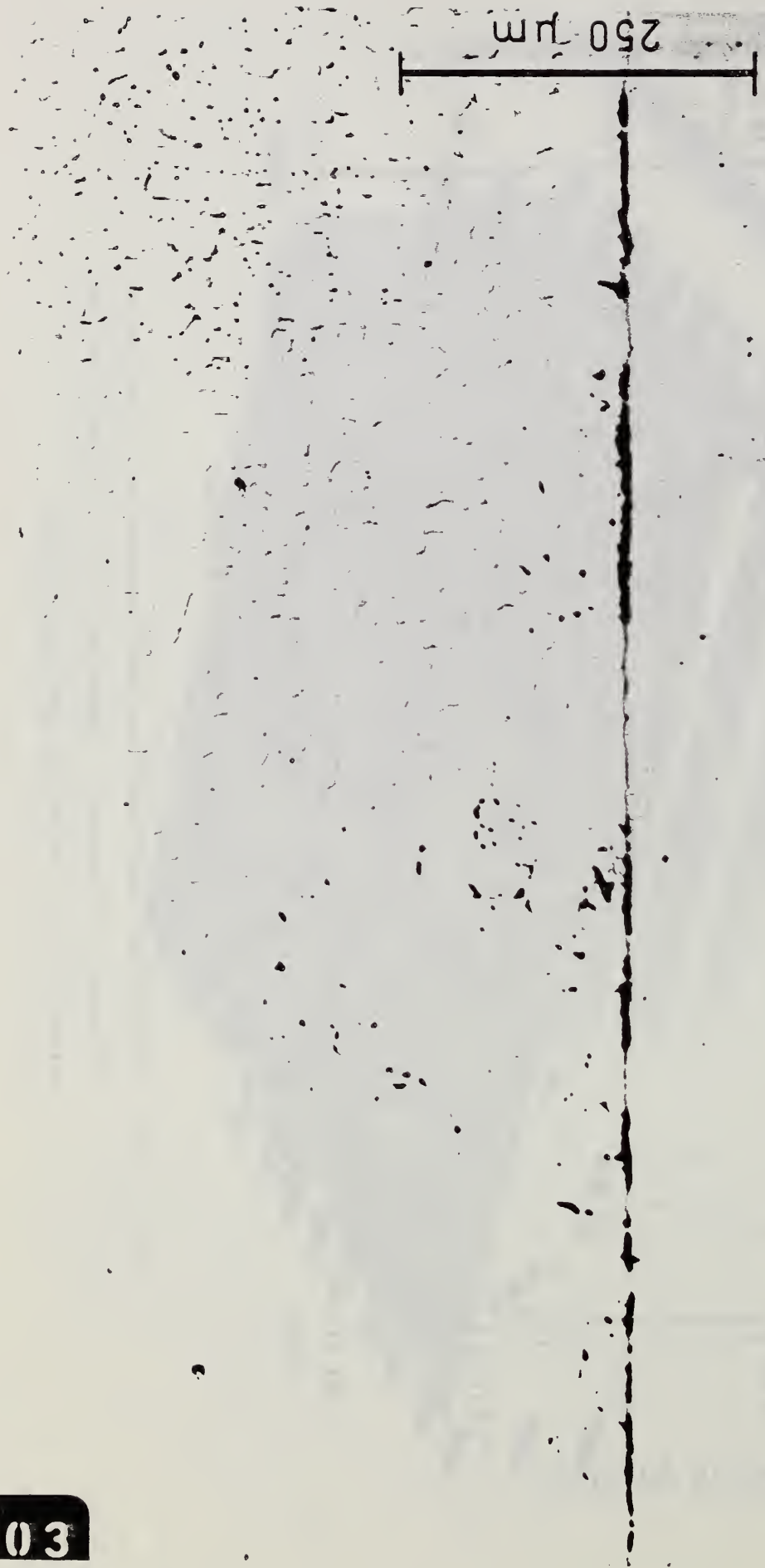


Fig. 4.23 Microstructure of aluminum-steel interface. Top side is 2024 aluminum, the bottom side is 316 stainless steel. Visible flaws and separations along the interface cause the decrease of interface velocity comparing to the calculated values. The vertical marker corresponds to 250 μm .

It is possible to measure the leakage energy for such modes as shown in Fig. 4.24 using an ultrasonic transducer or an interferometer to register the displacements at the outer surface of the matrix. We used surface wave wedges driven by 2.5 MHz transducers to generate interface waves by mode conversion. A broadband point longitudinal transducer of 1.5 mm diameter was used to detect normal displacements at the outer surface. The tangential components of the same leaky arrivals were detected using a shear wave transducer placed on a cone-shaped waveguide. All measurements were done using a MATEC 5100² ultrasonic system.

Figure 4.25 shows the experimental results obtained on the surface parallel to the interface of the sample shown in Fig. 4.19. There is a pronounced maximum visible for both polarizations along the direction parallel to the interface. This maximum is connected to an angle of maximal energy flow associated to the Poynting vector integrated from the point of origin of the mode at the interface. This maximum identifies the maximum flow of acoustic energy due to leakage. After this point the energy attenuates as the square of the displacement attenuation.

Figure 4.25 illustrates this angle for two of the modes listed in Table 4.2. This angle of maximum energy leakage is a valuable way to separate modes and thus contributes to a more detailed interface characterization.

Figure 4.25 shows a comparison of theory and experiment for the three modes listed in Table 4.2. Mode II of that table exhibits a maximum

²Certain commercial equipment, instruments, or materials are identified in this paper in order to adequately specify the experimental procedure. Such identification does not imply recommendation or endorsement by the National Bureau of Standards, nor does it imply that the materials or equipment identified are necessarily the best available for the purpose.

Δ (13.63°) Mode I (Aluminum-Steel)

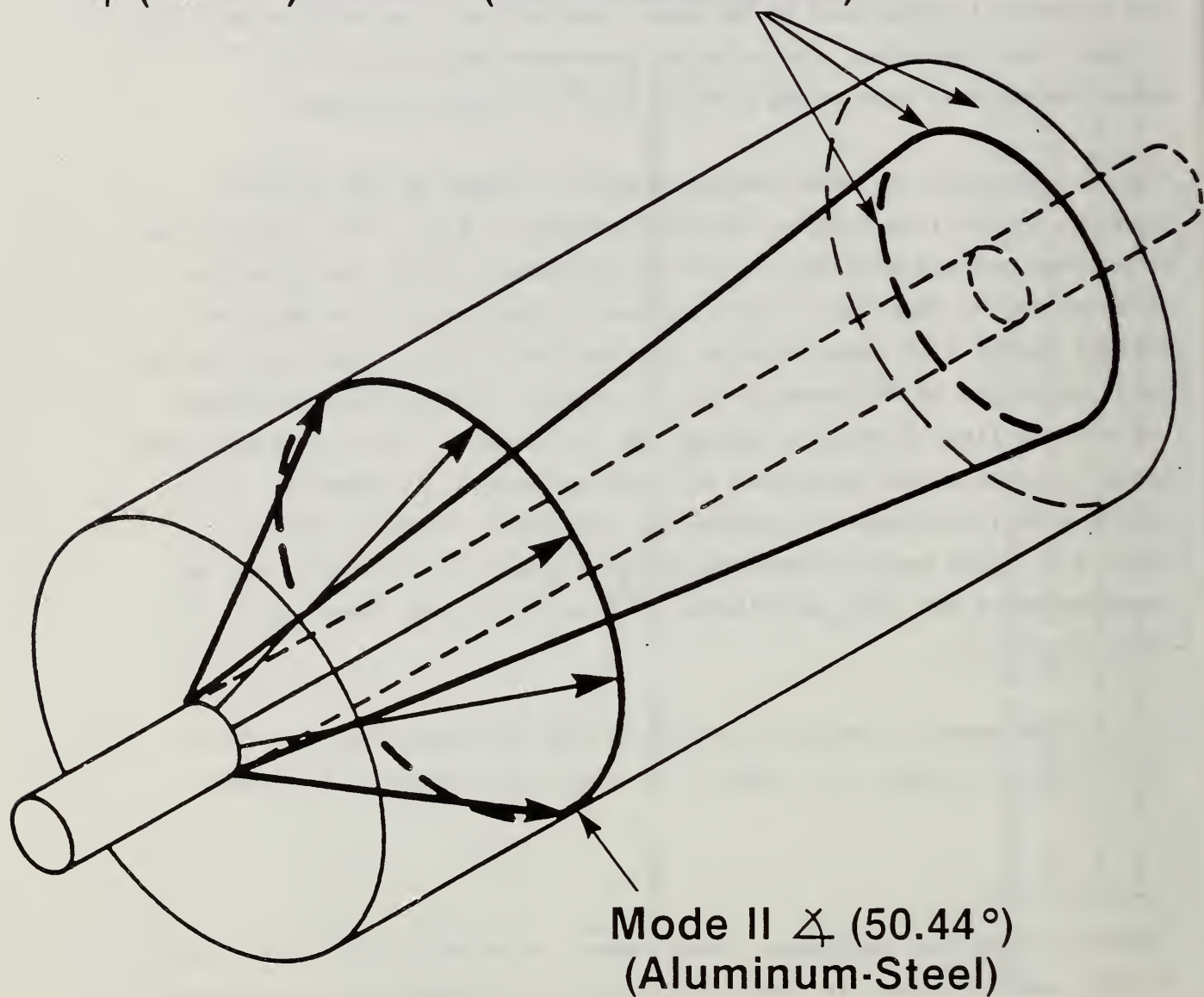


Fig. 4.26 Schematic diagram showing two possible arrivals (Modes I and II from Table 4.2) on the cylindrical sample.

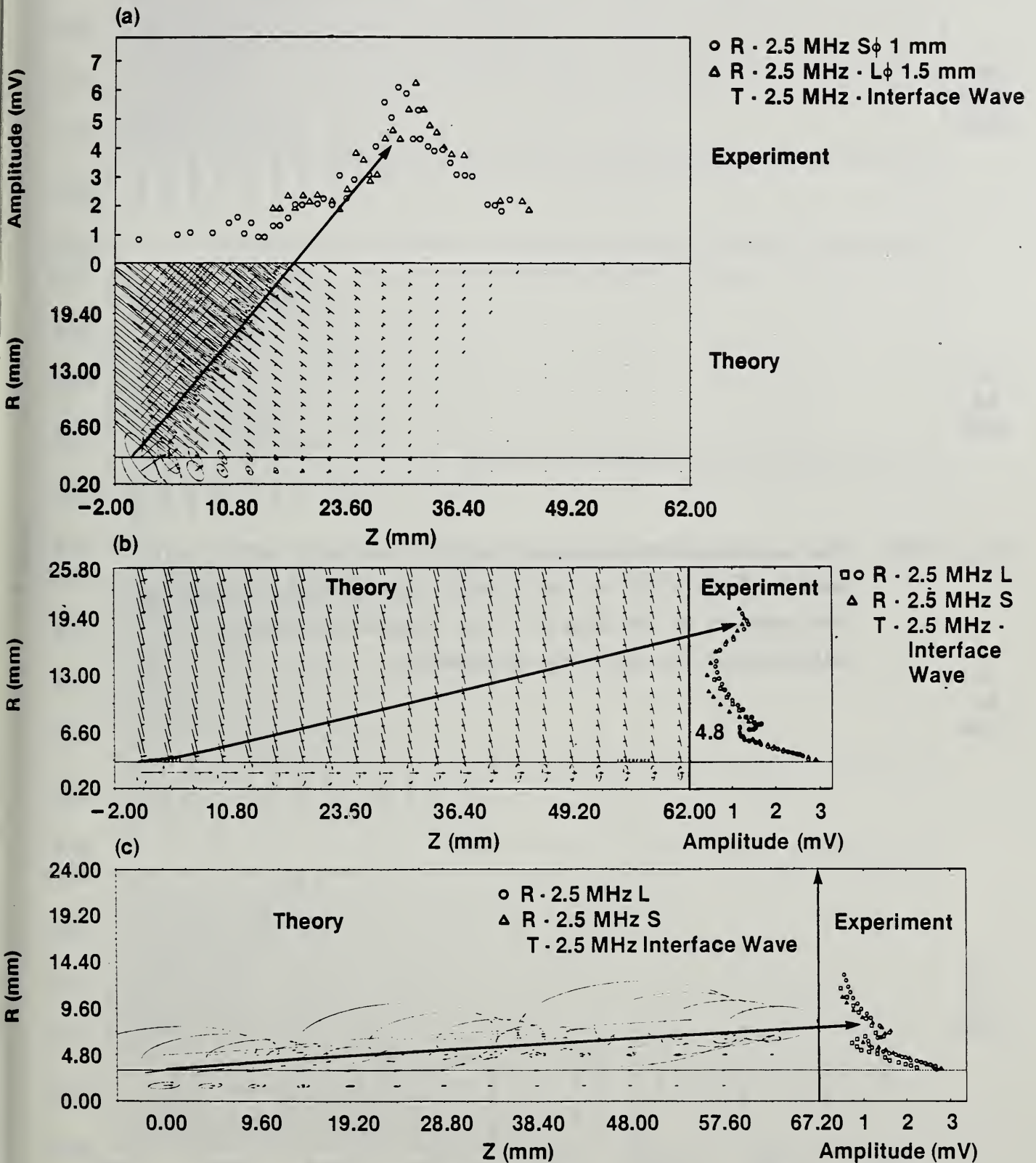
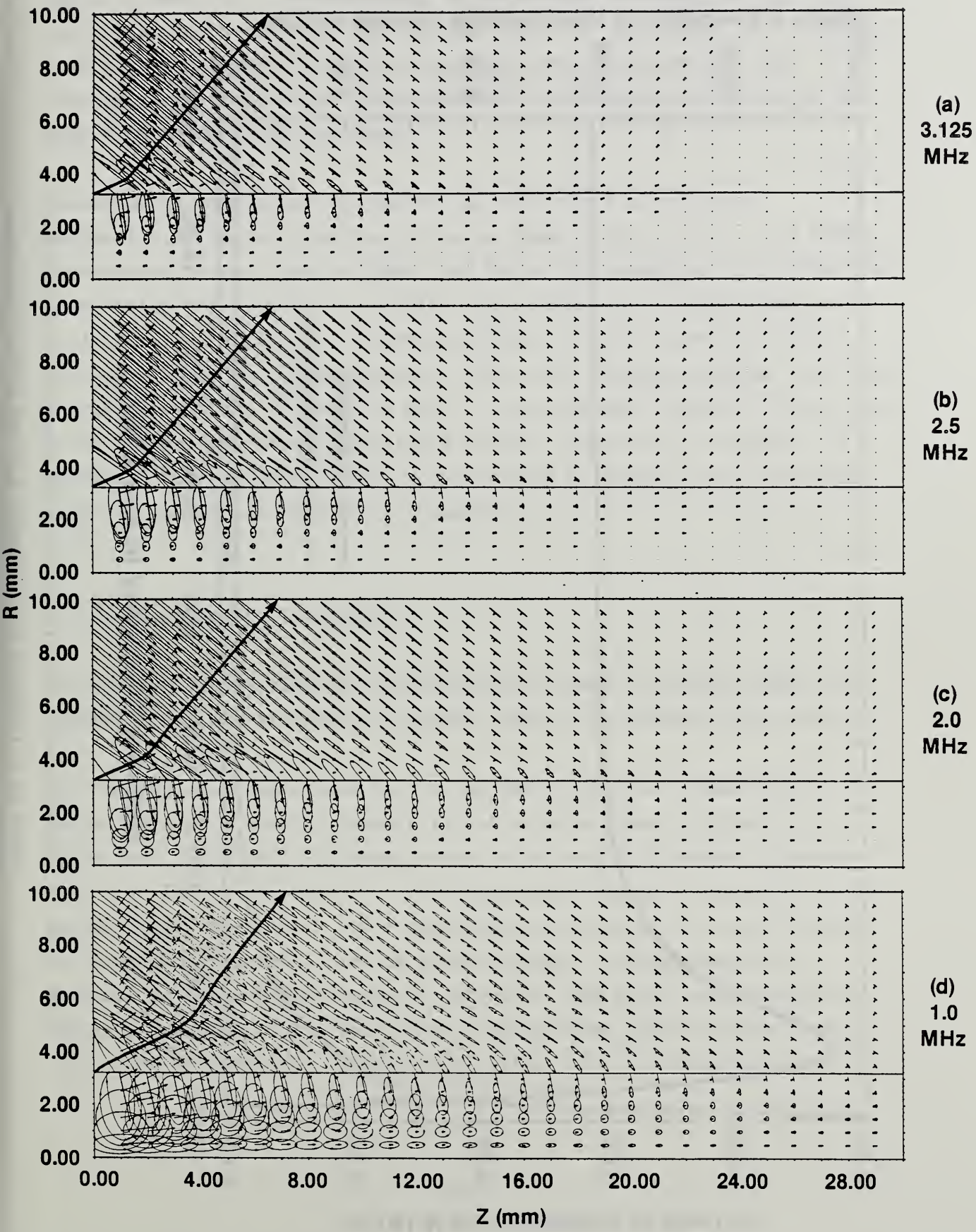


Fig. 4.27 Experimental identification of radial displacement modes created in the cylindrical sample by mode conversion.

Fig. 4.28 The calculated displacement field of the leaky radial axial mode I (Table 4.3) for the Al-SiC interface superimposed on the geometry of the sample. Each diagram represents calculations for different frequencies.



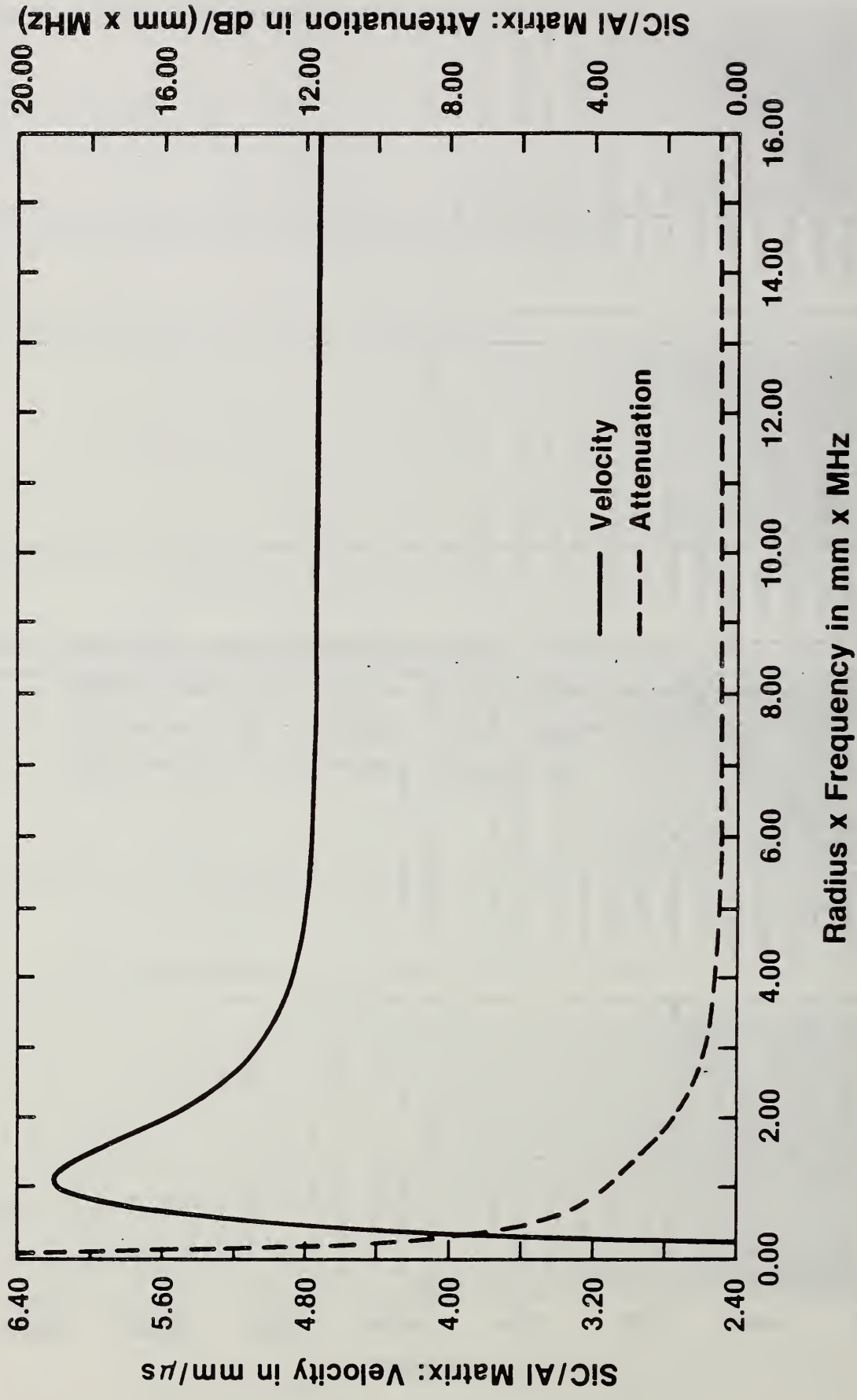


Fig. 4.29 The calculated velocity and attenuation of leaky interface waves as a function of frequency for the Al-SiC interface.

angle of about 50° , corresponding to the maximum measured in Fig. 4.25 and reproduced here. The high leakage angle is associated, in this case, to a high attenuation along the interface; this explains why the interface velocity of this mode could not be measured at the end of the sample 60 mm down the interface.

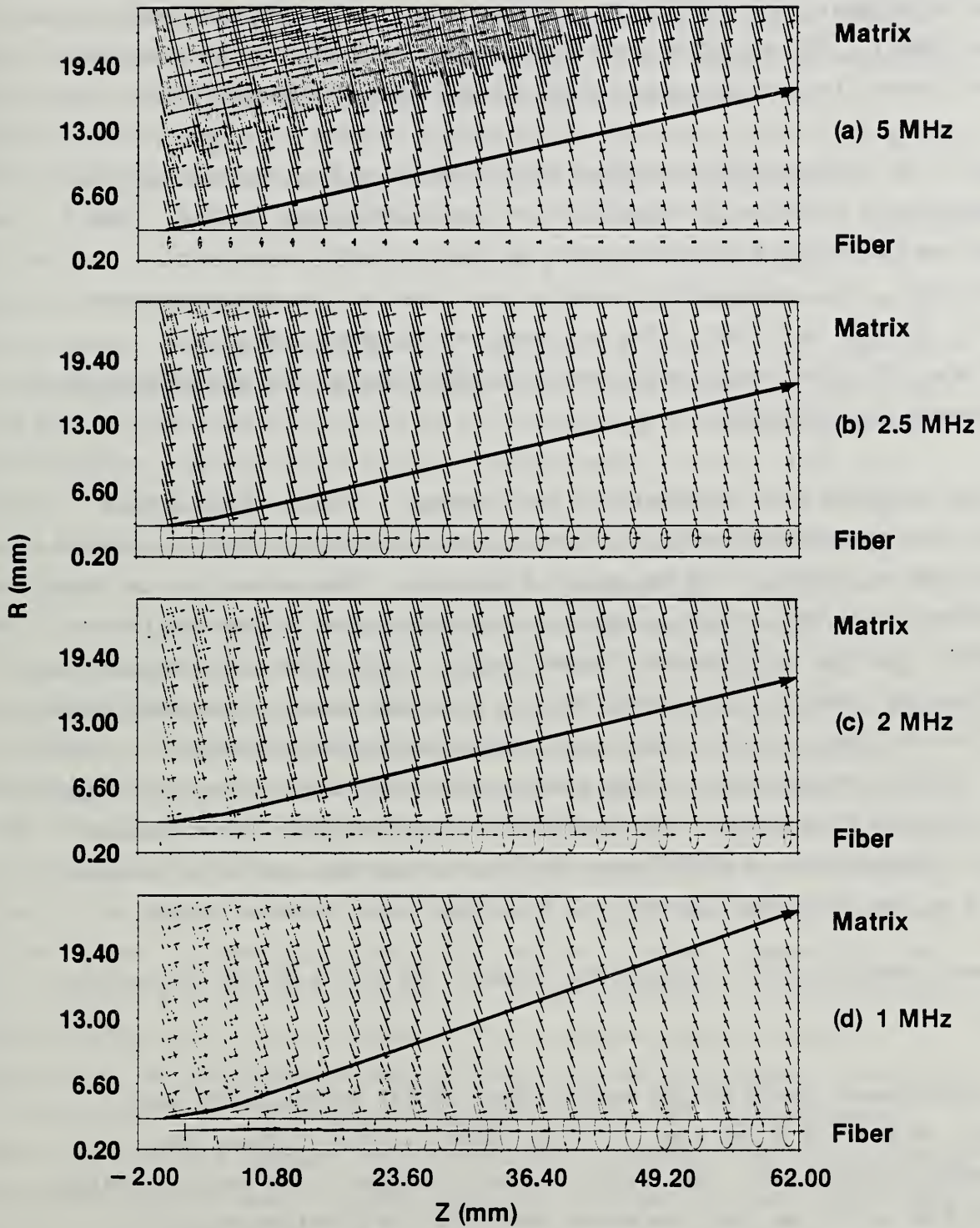
Measurements carried out at the end of the sample on the face perpendicular to the interface are also shown in Fig. 4.27. At 2.5 MHz, the maximum energy flow for Mode I of Table 4.2, which was also detected by velocity measurements, is 13.14° . The accuracy of measurement is still not very high, but an energy maximum in approximately the right place was found in all experiments. The small maximum occurring near the interface at about 3° could be due to the third mode listed in Table 4.1 or to another predicted mode with a similar low angle of leakage. We expect to increase measurement accuracy both of leakage angle and mode velocity to further explore this possibility.

4.2.3 Aluminum-SiC Interfaces

In this section we confirm the existence of leaky interface modes in a typical metal matrix composite system, that of aluminum-silicon carbide.

The theoretical predictions for the Al-SiC systems are summarized in Table 4.3 (and a similar summary for Al-boron systems is given in Table 4.4). Figure 4.28 presents the calculated displacement field for Mode I in Table 4.3 (that mode which was experimentally measured) for a variety of frequencies. The displacement field shows the main features of leaky interface waves in the Al-SiC system: strong dispersion; substantial attenuation along the interface, and a high characteristic angle of leakage. This figure also clearly shows the horizontal energy shift mentioned earlier. Figure 4.29 illustrates the dispersion and

Fig. 4.24 The displacement field of mode I (Table 4.2) for aluminum-steel interface calculated for each measured frequency a) 5 MHz, b) 2.5 MHz, c) 2 MHz, d) 1 MHz. The characteristic angle of leakage and the attenuation are frequency dependent. The ellipses trace the orbit of a particle and the arrowheads on the ellipse show particle motion. The arrows show the energy flow (Poynting vector) averaged over one period. Poynting vector lengths and ellipse sizes are consistent between each other, but arbitrarily scaled for graphing. The thick continuous integrated Poynting vector showing the energy flow of a wave packet starting at the edge of the interface. Flow lines starting from other interface points are parallel, and obtained by shifting this curve.



Following exploration of other possible methods, interface waves were found to be best generated by the conversion of rod surface acoustic waves (SAWs). Polymethyl-methacrylate wedges were used to generate and detect these ultrasonic surface waves over a range of frequencies.

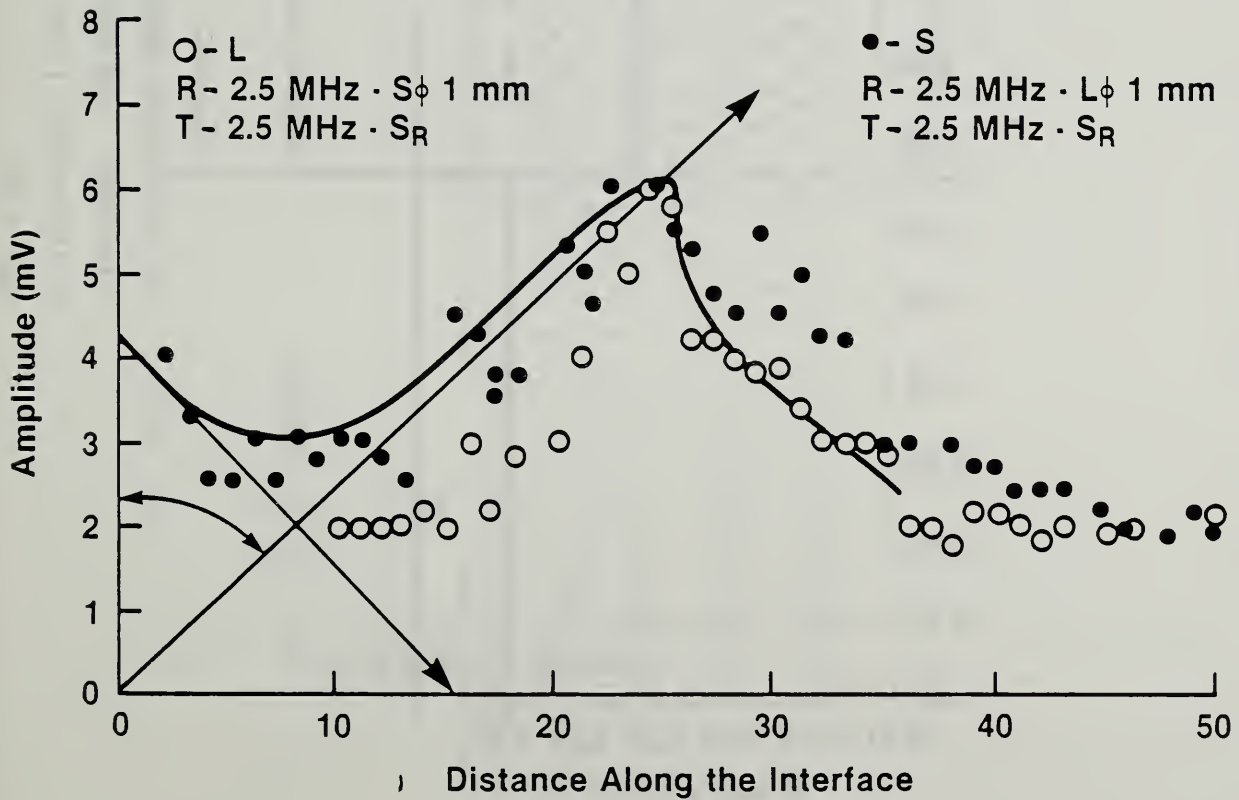
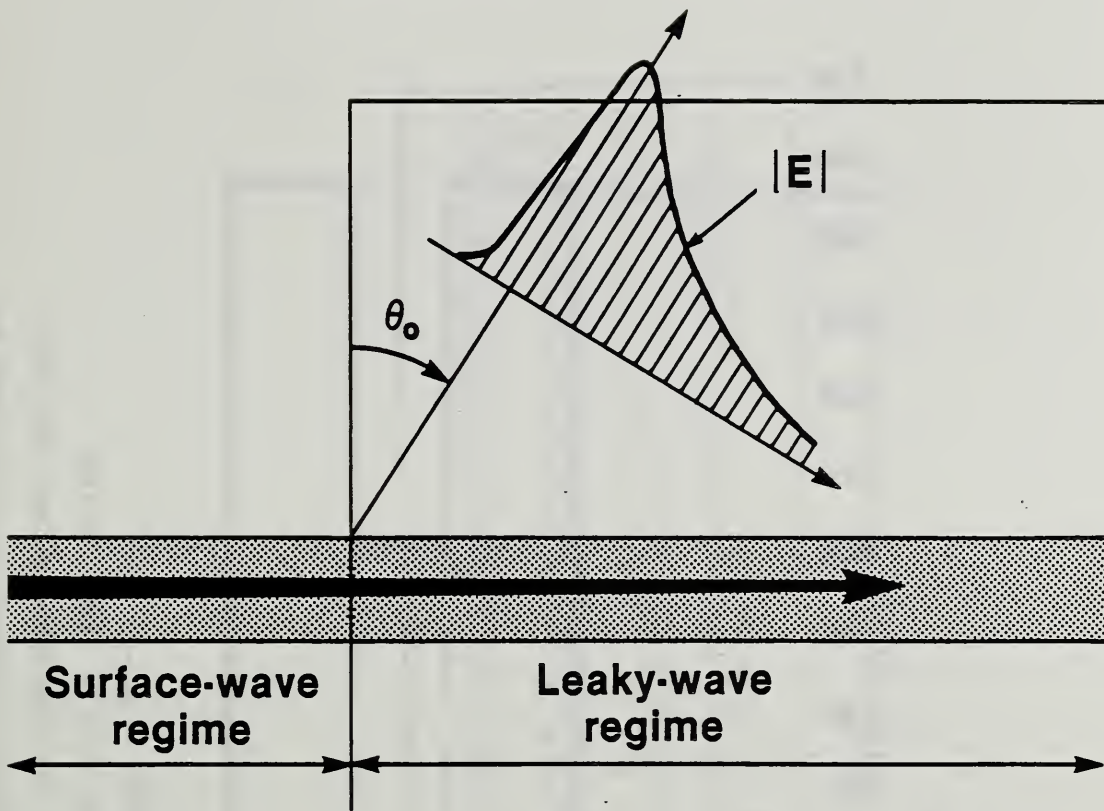
Figure 4.20 presents the interface wave velocities (as separate points) measured as a function of frequency for the sample shown in Fig. 4.19. These can be compared with the curve of theoretically predicted velocities. The experimental results were obtained for frequencies of 0.5, 1, 2, 3.5, and 5 MHz. The accuracy of the measurements was ± 15 m/s. In this case a very good agreement between the theory and the experiment was obtained.

Casting was also used to fabricate test samples. Figure 4.21 shows a metal matrix composite model of aluminum cast around a number of aligned steel rods of radius 1.195 mm spaced 4 mm apart. The velocities of leaky interface waves were measured along the interfaces as a function of frequency and the results are plotted in Fig. 4.22. For this sample, the experimental results (triangles) deviate from the theoretical predictions (continuous line). Small flaws, and separation at the interface (Fig. 4.23) were present in this sample, and are thought to be the origin of the slight deviation of the experimental results from the theory at higher frequencies. A much larger deviation from the predicted behavior occurs at low frequency for $f r_0 < 2.0$ mm·MHz, when the wave length becomes comparable with the spacing between the rods and rod interactions occur.

The displacement field of the weakly-leaky radial displacement mode (Mode I in Table 4.2 and Fig. 4.17) is shown in Figs. 4.24a-d for different frequencies. The length of the interface is 60 mm, the radius of the rod is 3.2 mm, and the outer radius of the aluminum matrix is 25 mm. The elliptical particle trajectories in these figures show the

relative amplitudes of the z (horizontal) and r (vertical) displacement components at points uniformly distributed in the sample. The direction of energy flow, the Poynting vector, is depicted by the arrow stemming from the center of each ellipse. The length of the arrows corresponds to the magnitude of the Poynting vector. These figures show the characteristic angle of leakage (given by the Poynting vector) as well as the decay of wave amplitude. Note that for higher frequencies, (e.g. 5 MHz), a clear boundary, defined by the Poynting vector, separates a field of evident exponential amplitude growth. Interestingly, this region's displacements are not associated with the transport of energy, which cannot occur perpendicular to the Poynting vector. The continuous thick lines show the energy path followed by a "wave-packet" starting at the edge of the interface as found by integrating the Poynting vector. For Stoneley type and other non-attenuating waves (such as Love type waves), the Poynting vector is parallel to the interface. For leaky waves, this non-zero characteristic angle of leakage depends on the imaginary part of the velocity and on the attenuation. The angle is, in fact, determined as that which balances the exponential growth in the r direction with the exponential decay in the z -direction. For the cylindrical geometry, the attenuation as well as the characteristic angle of leakage are frequency dependent. Both increase with increasing wavelength at constant r in Figs. 4.24a-d. Figure 4.24c shows that this mode propagates at an angle of about 14° at 2.5 MHz. Exact measurements of the angle of the Poynting vector are affected by the shift in energy flow in the matrix close to the interface. Rays close to the interface do not travel in straight lines. This effect is newly discovered, and has not been previously reported. It is of a different nature from the Goos-Hanchen shift [19,20] observed for a bounded beam at optical interfaces, or the Schoch effect [21,22] observed for planar interfaces in the vicinity of the critical angle of a reflected acoustic beam. Here, the observed changes due to curvature in energy flow are frequency dependent and are seen, for this mode, to be larger at lower frequencies.

Fig. 4.25 The upper diagram presents the idea of the characteristic angle of leaking. The lower diagram shows the experimental results obtained through an aluminum matrix parallel to the interface. Results were obtained for both in-plane (S) and normal (L) displacements along the sample length. The measured leakage maximum allows evaluation of the characteristic leakage angle.



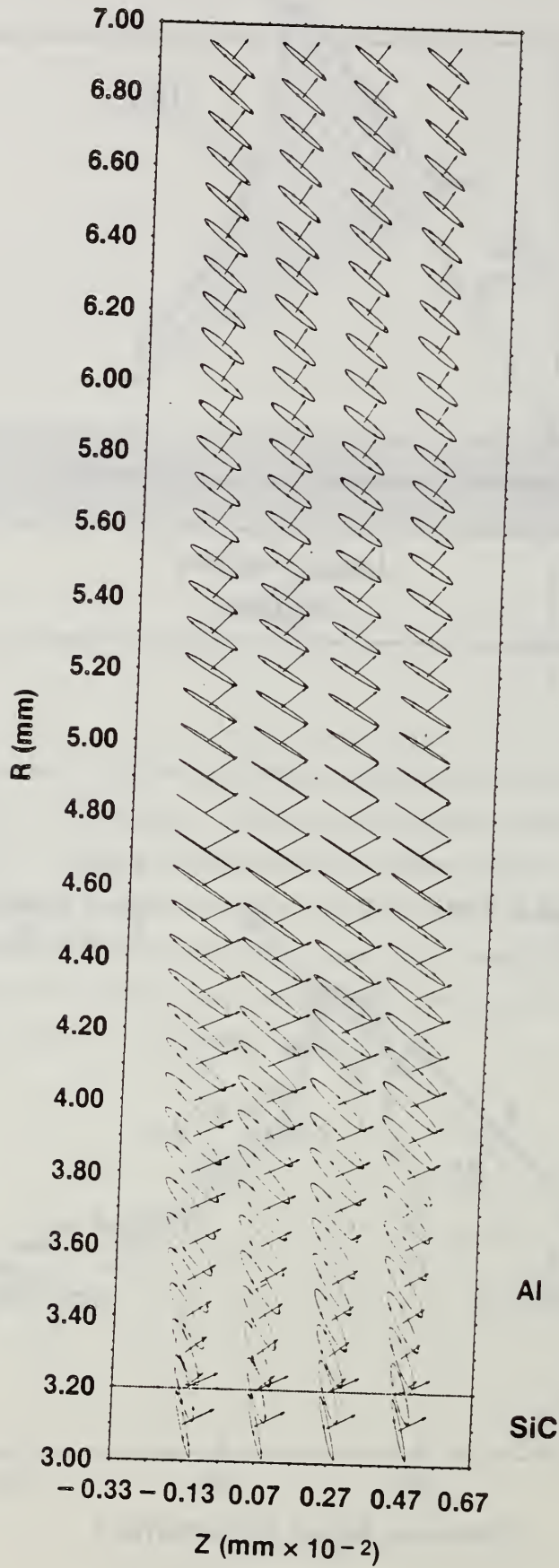


Fig. 4.30 The calculated energy flow for Al-SiC close to the interface. The amplitude of the displacement and the shift of the energy flow are frequency dependent, as was shown in Fig. 4.29.

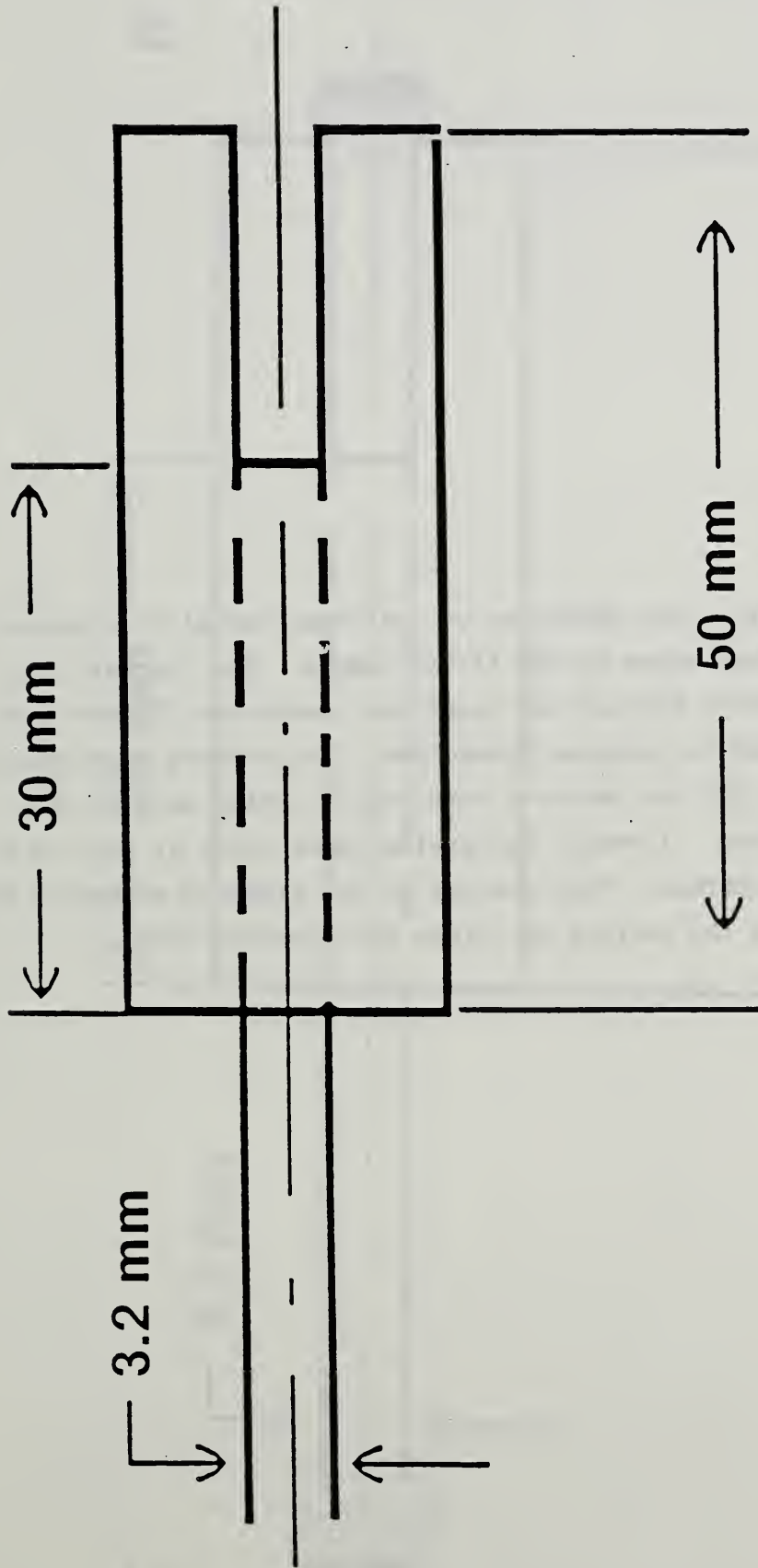


Fig. 4.31 The geometry of the Al-SiC sample. The 3.2 mm radius SiC rod was shrink fitted into a 2024 aluminum alloy cylinder.

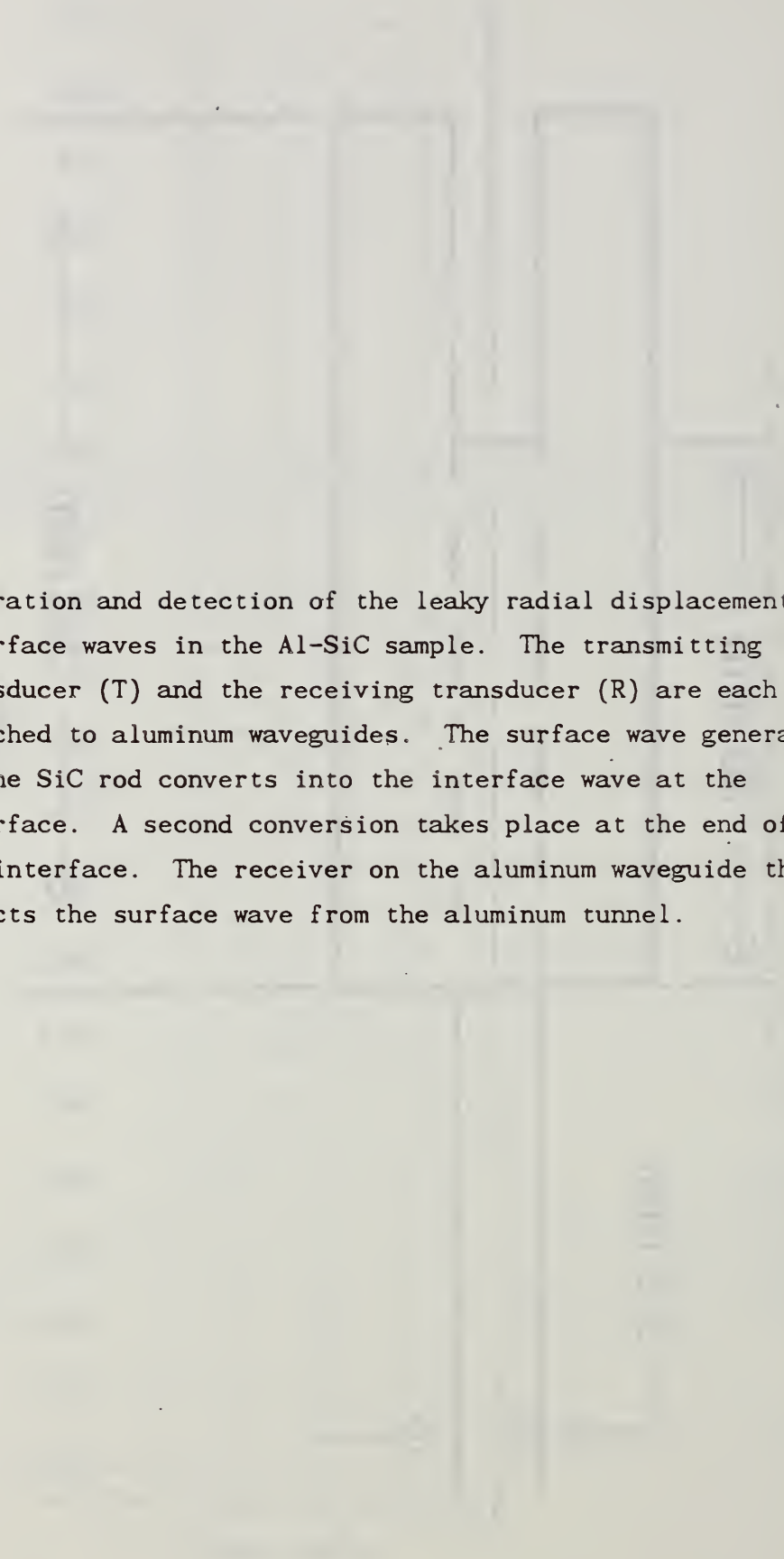
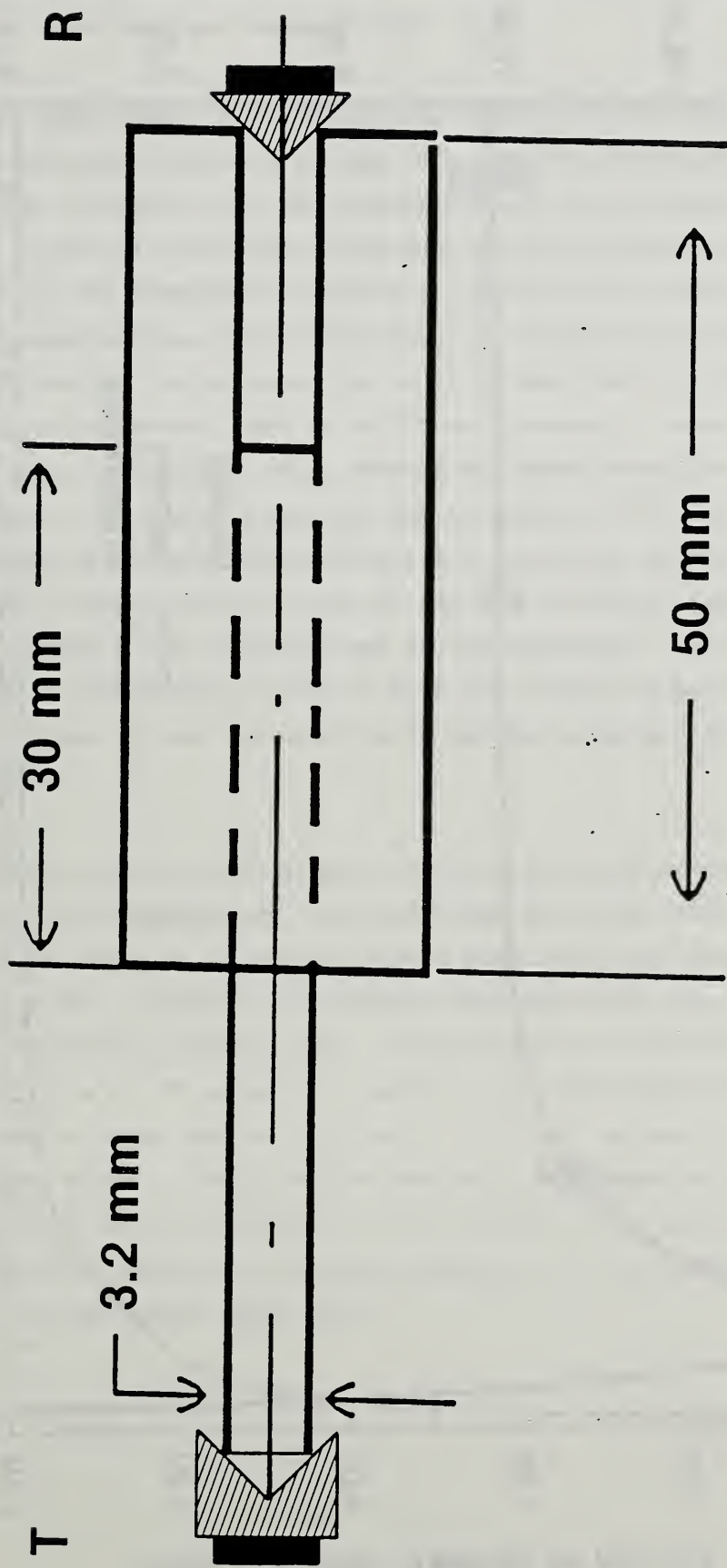
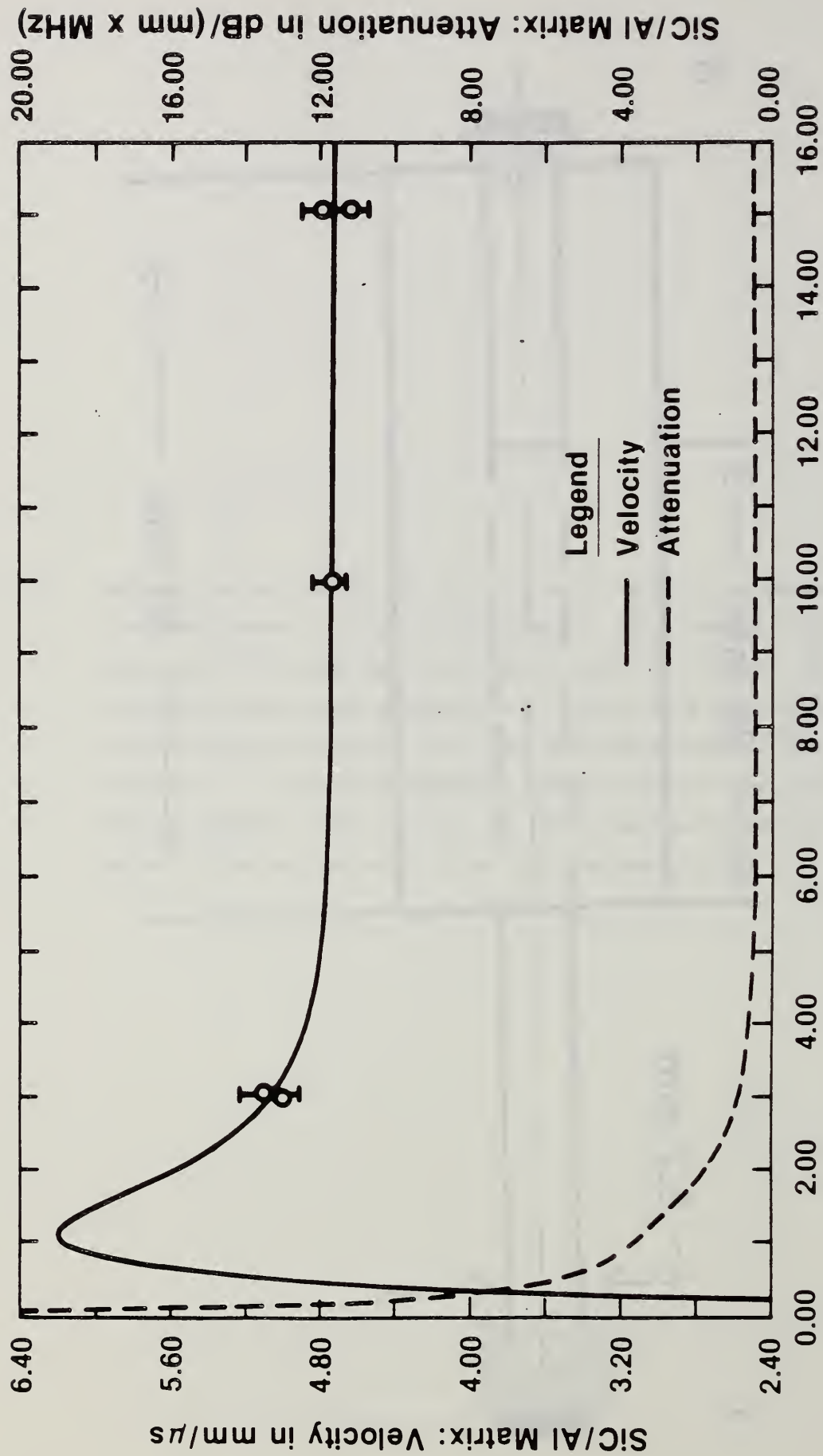


Fig. 4.32 Generation and detection of the leaky radial displacement interface waves in the Al-SiC sample. The transmitting transducer (T) and the receiving transducer (R) are each attached to aluminum waveguides. The surface wave generated on the SiC rod converts into the interface wave at the interface. A second conversion takes place at the end of the interface. The receiver on the aluminum waveguide then detects the surface wave from the aluminum tunnel.





Radius x Frequency in mm x MHz

Fig. 4.33 Measured velocities at the Al-SiC interface as a function of frequency (points) compared with the theory (continuous line).

attenuation respectively, for this mode. The displacements and energy flow close to the interface are shown in Fig. 4.30.

An Al-SiC sample, composed of a 3.2 mm radius SiC rod shrink fitted into a 2024 aluminum cylinder, was used to test the theoretical velocity predictions listed in Table 4.3. The sample's geometry is shown in Fig. 4.31. The ultrasonic shear and longitudinal velocities were measured on each of the components separately, and the data was used in the theoretical computations. The measurement technique for generation and detection of leaking radial-axial waves is schematically presented in Fig. 4.32. Three transducers, each of different frequency, were used as transmitters. These were placed on a concave aluminum waveguide. Only the circular edge of the silicon carbide was in contact with the transmitting waveguide. The interface wave was generated by mode conversion from a surface acoustic wave on the rod, which projected out from the matrix tunnel. At the other end of the interface, the interface wave reconverted into a surface acoustic wave and travelled along the aluminum tunnel, where it was detected using another aluminum waveguide of convex curvature.

Knowing (from theory) the surface wave velocities on the silicon carbide rod and aluminum tunnel separately, and measuring the delay time in the two waveguides, the velocity of the interface wave along the Al-SiC interface was obtained. Figure 4.33 presents the measured velocities along with the theoretical predictions. The accuracy of the velocity measurements was 60 m/s. We expect to improve upon this accuracy by modifying the sample shape and by using more efficient methods for generating surface waves. These results indicate, as suggested earlier, that leaky interface waves do exist in a form suitable for interface characterization using acoustic microscopy methods in fiber-matrix combinations of technological importance.

4.3 Future Directions

Weakly leaky modes in the cylindrical geometry provide a potential new tool for interface characterization in fiber reinforced MMCs. The leakage from these modes offers the opportunity for application of acoustic microscopy to image interfaces from the surface of a sample. Preliminary experiments at low frequencies appear very promising. These experiments will be continued and extended to high frequencies using fiber sizes typical in MMCs. The potential of microfocused laser generated ultrasound for such applications will also be studied.

The general theory discussed in section 3 offers the opportunity to characterize interphase regions of finite extent. Techniques for preparing controlled interphases are being developed in both cylindrical and planar geometries, and work will begin on correlating the theory with experiments. Work is also underway to study the effect of frequency on the generation depth of interface waves on determining the elastic properties near interface material.

These measurement methods will be applied to the study of the elastic properties near the interface in specially designed samples of MMCs produced by the SDIO/ONR Advanced Composites Consortium. Success in this project will greatly advance the ability to model and, therefore, design composites. Ultimately a combination of these techniques with acoustic microscopy methods may permit in situ diagnosis of metal matrix, and perhaps, ceramic composites.

4.4 References

- [1] R.N. Stoneley, Proc. Roy. Soc. (London), 106A (1924), pp. 416-429.
- [2] W.L. Pilant, Bull. Seism. Soc. Amer., 62 (1972), pp. 285-299.
- [3] R. Yamaguchi and K. Sato, Bull. Earthquake Res. Inst. of Tokyo Univ., 33 (1955), pp. 549-559.
- [4] D.A. Lee and D.M. Corbly, IEEE Trans. on Sonics and Ultrasonics, SU-24 (1977), pp. 206-212.
- [5] A.S. Ginzburg and E. Strick, Bull. Seism. Soc. Amer., 48 (1958), pp. 51-63.
- [6] R.A. Phinney, Bull. Seism. Soc. Amer., 51 (1961), pp. 527-555.
- [7] K. Sezawa and K. Kenai, Bull. Earthquake Res. Inst. of Tokyo Univ., 17 (1939), pp. 1-8.
- [8] J.G. Scholte, Proc. Ned. Akad. V. Wetensch. Amst., 45 (1942), pp. 20-25.
- [9] J.G. Scholte, Proc. Ned. Akad. V. Wetensch. Amst., 45 (1942), pp. 159-164.
- [10] J.G. Scholte, R. Astron. Soc. London Monthly Notices (Geophys. Suppl.), 5 (1947), pp. 120-126.
- [11] T.A. Owen, Prog. Appl. Mater. Res., 6 (1964), pp. 69-87.

- [12] R.O. Claus and C.H. Palmer, *Appl. Phys. Lett.*, 31 (1977), pp. 547-548.
- [13] S.I. Rokhlin, M. Hefets and M. Rosen, *J. Appl. Phys.*, 52 (1981), pp. 2847-2851.
- [14] T.C. Lim and J.P. Musgrave, *Nature*, 225 (1970), p. 372.
- [15] P. Chadwick and P.K. Currie, *Quart. J. Appl. Math.*, 27 (1974), pp. 497-503.
- [16] R.N. Thurston, *J. Acoust. Soc. Amer.*, 64 (1978), pp. 1-37.
- [17] V.V. Meleshko, *Soviet App. Mech.*, 16 (1980), pp. 382-385.
- [18] V. Kumar and G.S. Murty, *IEEE Trans. on Sonics and Ultrasonics*, SU-29 (1982), pp. 138-142.
- [19] F. Goos and H. Hanchen, *Ann. Physik*, 1 (1947), pp. 333-346.
- [20] F. Goos and H. Hanchen, *Ann. Physik*, 5 (1949), pp. 251-252.
- [21] A. Schoch, *Acustica*, 2 (1952), pp. 1-17.
- [22] A. Schoch, *Acustica*, 2 (1952), pp. 18-19.

5. Acoustic Emission Assisted Measurement of Fiber and Interface Strength

Our objective in this subtask is the in situ measurement of fiber and interface strength in MMCs. The need for strength measurements arises from the increasing awareness of the crucial role that interfaces play in the mechanical performance of composites. At the same time, sophisticated models of interfacial microfracture are now available (Argon et al, [1]) which can be used to predict the failure of bulk composites on the basis of interfacial strength. Such models require experimental corroboration and of course can not be used quantitatively without accurate data on interfacial strength.

In one type of method for determining interface strength, that of Broutman [2], a single fiber is embedded in a transparent polymer matrix, which is then loaded in compression. The load at which the interface fails is detected optically and a stress analysis used to determine the local stress at the interface at the point of failure. Since optical techniques are not applicable in opaque MMCs, we have proposed using acoustic emission (AE) as a means of acoustically detecting the failure. Moreover, since acoustic emissions are also emitted by other deformation processes, they may provide information on other aspects of MMC deformation micromechanisms. It is thus useful to begin with a very brief overview of the microscopic origins of acoustic emission.

5.1 Microscopic Origins of Acoustic Emission

Acoustic emission can be thought of as the naturally generated ultrasound created by local, rapid load changes within a body. If an ultrasonic transducer with sensitivity in the 0.1-1.0 MHz frequency range is attached to almost any type of composite, acoustic pulses are detected

during the application of load. To intuitively appreciate how such a natural phenomenon arises, consider the following "thought" experiment.

Imagine that a body has been placed under load and attained mechanical equilibrium throughout: the internal force field then exactly balances the tractions applied to the surface. Now suppose that a crack grows within the body: the crack surfaces move in order to make them stress free. Elastic waves radiate from the crack to restore equilibrium with the surface tractions. Behind the elastic wavefronts, the internal forces are relaxed. When the elastic wavefronts eventually reach the surface, they cause surface displacements. These displacements begin the process of restoring equilibrium between the cracked interior surface and the surface tractions. The subsequent arrival of elastic waves multiply scattered within the body is detected ultrasonically and called acoustic emission.

Obviously, any dynamic mechanical instability is capable of generating these displacements. Dislocation motion, shear fracture, fiber fracture and interface decohesions are all potential sources of acoustic emission. It would therefore be gratuitous to assume that only interface decohesion is detected acoustically in the metal matrix composite analogue of a Broutman-type test. Previous research however leads us to believe that we may be able to unambiguously attribute an acoustic emission signal to a particular micromechanism from the attributes of the emitted signals. The background to this is presented in the more extensive review of microscopic origins of acoustic emission included in Appendix I.

Our approach has been accordingly to begin with a review of the elementary micromechanisms of composite deformation and fracture, to then design model experiments where acoustic emission may be used to clarify the mechanisms, and finally to analyze these tests to deduce the strength of fiber-matrix interfaces produced by various processing routes. Here, solidification processing pathways are examined. Future work will extend

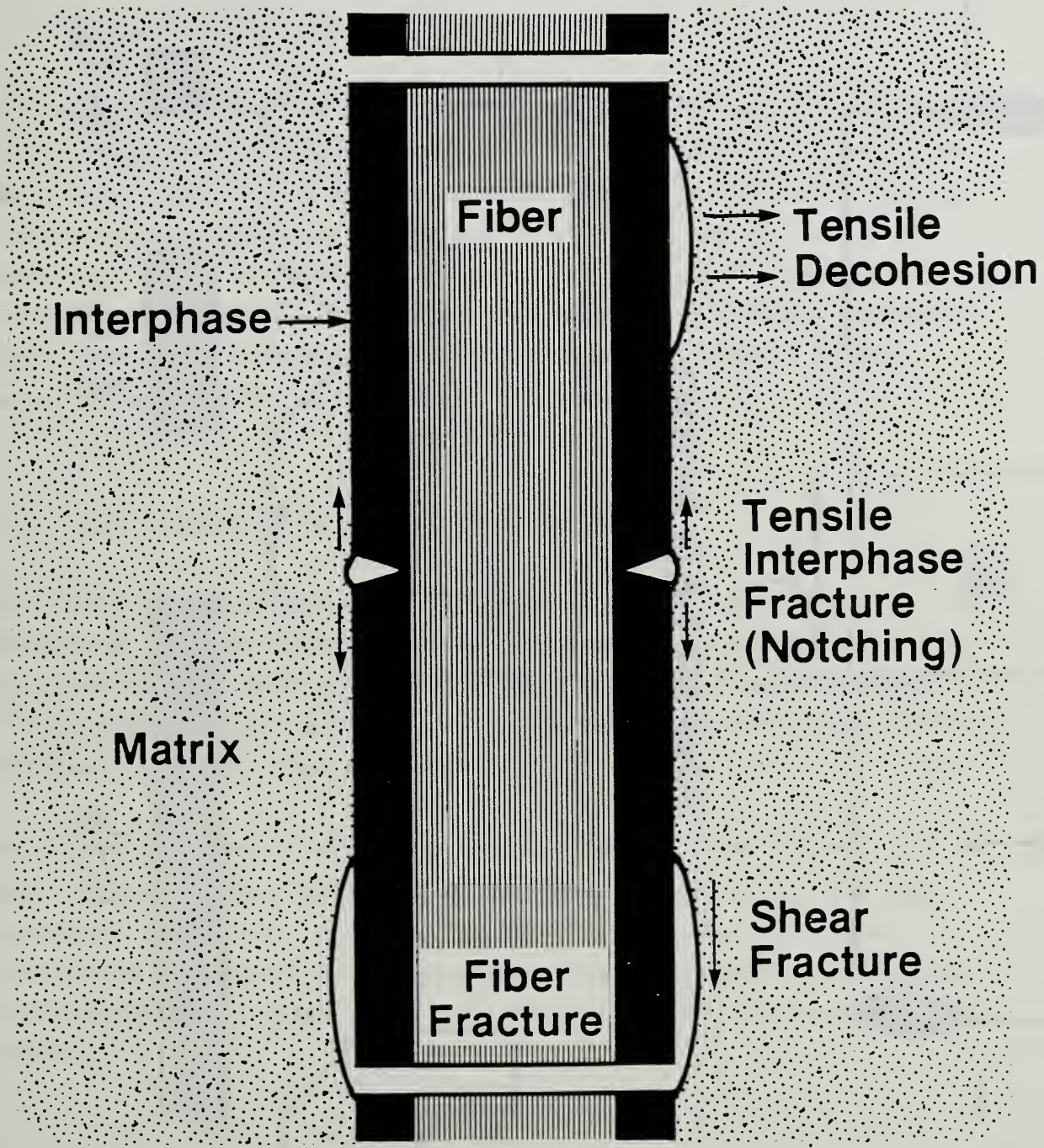
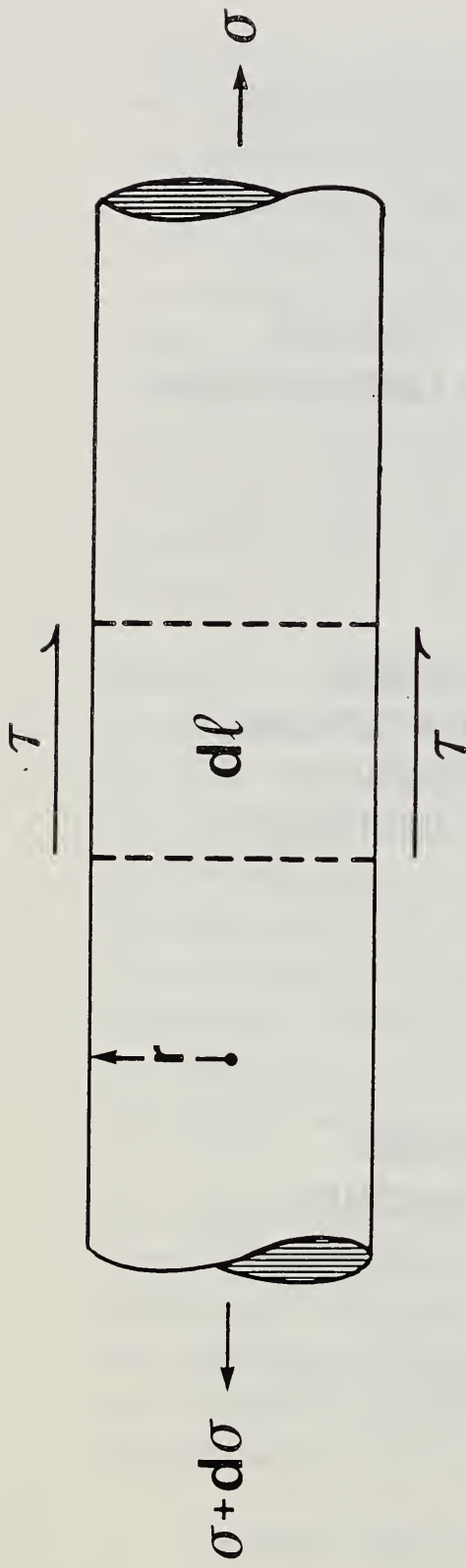


Fig. 5.1 Mechanisms of interface failure during longitudinal loading of a fiber reinforced composite.



SHEAR LAG MODEL

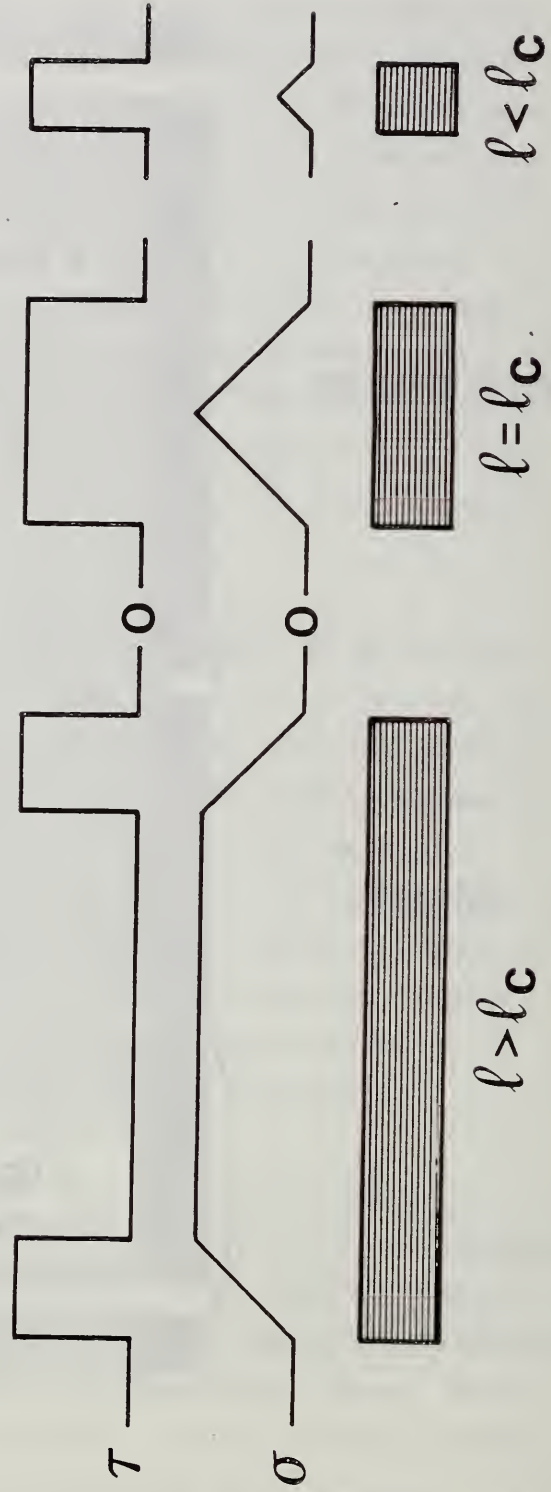


Fig. 5.2 Shear lag model of load transfer from matrix to fiber (longitudinal loading).

the approach to materials processed by other groups in the SDIO-IST/ONR Advanced Composites Consortium.

5.2 Fibrous Composite Fracture Micromechanisms

The mechanical properties of a fiber-reinforced metal matrix composite are in large part influenced by the transfer of load from the matrix to the fiber. This in turn depends upon the fiber's intrinsic strength and ductility, its orientation to the matrix stresses, and the mechanical properties of the interface and matrix. Let us begin by considering only longitudinally-oriented fiber composites under tensile load. Depending upon the relative strengths of fiber and interface, several failure sequences are possible and these are discussed below.

5.2.1 Load Transfer from the Matrix to the Fiber

If a fiber-reinforced composite is loaded along the fiber axis, deformation will at first be elastic throughout. If the interface does not fracture, with continued loading the matrix will eventually begin to flow plastically, work hardening until the tensile stress in the fiber is sufficient to cause fiber fracture.

The stress distribution along the length of such a fiber segment with an ideal interface can be estimated by the shear lag (or fiber loading) model [3], Figure 5.2. Consider the fiber element shown in Figure 5.2. If σ is the tensile stress in the fiber, τ is the interface shear stress and r is the fiber radius, then the force balance across an element of length $d\ell$ is

$$(\sigma + d\sigma)\pi r^2 = \sigma\pi r^2 + 2\pi r\tau d\ell$$

Thus, the shear stress is proportional to the gradient in the tensile stress in the fiber:

$$d\sigma/d\ell = 2\tau/r$$

so that everywhere at which there is a change in fiber tensile stress, such as at a pre-cut notch, or a crack, at the fiber ends, interfacial shear stresses are set up proportional to the stress gradient. Since the shear stresses are independent of the stress itself, they can exceed the interface strength even at relatively low fiber stresses, say, on reloading a previously strained specimen or during fatigue testing.¹

The stress distributions for various fiber lengths are shown in Figure 5.2. After integration, we find that the tensile stress increases from 0 at its free end (where it has fractured) up to some limiting value σ_f (the tensile strength of the fiber) at the "ineffective length" ℓ_e (over which reinforcement is minimal) from the free end. For simplicity we have treated the fiber strength as if it were a constant (cf. in Fig. 5.2), whereas it is well known that, owing to intrinsic defects, there is a statistical size-strength effect [3]. However, the experimental technique utilized here measures each fracture individually, so that σ_f is a floating constant and this variation is in practice taken into account.

¹For example, the shear stresses can be estimated from the above as $\tau = (r/2)(d\sigma/d\ell)$. At constant load, since $d\sigma/\sigma = -dA/A = -2dr/r$, only a 5% variation in radius will produce a 10% change in tensile stress. This has obvious implications for quality control. If there is a 10% change in stress over a distance of $r/10$, then $d\sigma = 0.1\sigma$ and $r/d\ell = 10$, so that $\tau = \sigma/2$, the flow stress in the matrix. Thus, even small changes in fiber diameter can act as a mechanism for generating large interfacial shear stresses capable of nucleating interfacial cracks.

If the fiber is shorter than $\ell_c \equiv 2\ell_e$, referred to as the "critical length," the fracture stress is not reached (nor is reinforcement very efficient), and the fiber can be pulled out of the matrix endwise without breaking it. If fibers of lengths greater than ℓ_c are present, they will repeatedly fracture under continued loading until this critical length is reached at a "critical aspect ratio"

$$\ell_c/d \equiv \sigma_f/2\tau_i$$

where $d \equiv 2r$ is the fiber diameter and τ_i is the shear strength of the interface, or matrix, whichever is lower. This ratio, attained after a stress large enough to fracture the strongest fiber segment is reached, will be useful in measurements of interface strength.

5.2.2 Micromechanics of Fiber and Interface Fracture

When a fiber fractures, the fiber stress is only relaxed along the end gradient length ℓ_e , so that the elastic energy released as AE ought to depend only on the load, not the total fiber segment length. For shear fracture of the interface, on the other hand, the crack may extend multiple values of this length ℓ_e and so in principle relax a larger volume, creating much larger emissions than fiber fracture, but this may be limited as discussed below. To understand these effects, as well as estimate interfacial energy from interfacial strength, it is necessary to briefly analyze the mechanics of fiber and interface fracture.

The total energy change due to fiber fracture is given by the sum of the changes in elastic and surface energy,

$$\Delta E_f = -2(A_f/2E_f) \left[\int_0^{\ell_e} \sigma^2(x)dx - \int_0^{\ell_e} \sigma'^2(x)dx \right] + 2\gamma_f A_f \leq 0$$

where $\sigma(x) = \sigma_f$ is the stress distribution before fracture and $\sigma'(x) = \sigma_f x/\ell_e$ is the distribution after. Note that fiber unloading only occurs over the end lengths $2\ell_e$ and not in the central portion, where the stress is still σ_f (Fig. 5.2). Hence, acoustic emission from fiber fracture ought to be independent of fiber length. Here γ_f and A_f are the surface energy and cross sectional area of the fiber. The factor of 2 arises in both terms since there are two ends and two fracture surfaces. After integration,

$$\Delta E_f = -2(A_f/3E_f) \ell_e \sigma_f^2 + 2\gamma_f A_f \leq 0$$

Using values for SiC fibers of $A_f = 1.53 \times 10^{-8} \text{ m}^2$, $2\ell_e = 10^{-3} \text{ m}$, $E_f = 480 \text{ GPa}$ and $\sigma_f = 3 \text{ GPa}$, we obtain the elastic energy release of $1.9 \times 10^{-4} \text{ J}$. The surface energy $2\gamma_f A_f$, using $\gamma_f = 20 \text{ J/m}^2$ [4], is $6.1 \times 10^{-7} \text{ J}$. Thus the surface energy term is negligible and the remainder of elastic energy is radiated as kinetic energy, i.e., acoustic emission. This is orders of magnitude larger than the kinetic energies produced by thermoelastic sources [5] which although inefficient are detectable, so that the acoustic emission from fiber fracture ought to be easily detectable.

An interfacial shear failure at the end of a fiber may be in the form of a circumferential crack that moves in from the end, advancing the tensile stress gradient ahead of it (Fig. 5.2). Once the stress gradient impinges on that at the other end, the available stored elastic energy will drop sharply (Fig. 5.2), and the crack should arrest. Thus

interfacial shear cracks should be less likely to form once the fiber has broken down into its critical lengths. The change in total energy by the advance of such a crack over distance $l-l_c$ is given by

$$\Delta E_s = -(A_f/2E_f) \left[\int_0^{l-l_e} \sigma^2(x) dx - \int_0^{l_e} \sigma'^2(x) dx \right] + 2\pi r \int_0^{l-l_c} 2\gamma_i dx \quad (5.1)$$

where

$$\begin{aligned} \sigma(x) &= \sigma_f, & \text{for } l_e \leq x \leq l-l_e \\ \sigma(x) &= \sigma_f x/l_e, & 0 \leq x \leq l_e \end{aligned}$$

and

$$\sigma'(x) = \sigma_f x/l_e, \quad \text{for } 0 \leq x \leq l_e$$

and where γ_i is the interfacial adhesive energy (the factor of 2 coming from the two surfaces of the crack).

The adhesive energy γ_i is defined by $2\gamma_i = \gamma_r + \gamma_m - \gamma_{rm} + \gamma_{irr}$, where γ_r is the reinforcement and γ_m the matrix surface energy, γ_{rm} is the interface bond energy, and γ_{irr} is a dissipative term which includes frictional and plasticity phenomena. In ceramic-reinforced metals, the reinforcement surface energy γ_r generally is \gg than γ_m or γ_{rm} so that the preferential path for "interfacial" fracture is often through the matrix if the interface bonding is good and matrix ductility limited (so that γ_{irr} is small); this has been observed by Evans, et al. [6], Crowe, et al. [7], Arsenault and Pande [8], and others.

This gives

$$\Delta E_s = - \left[A_f(\ell - \ell_c) / 2E_f \right] \sigma_f^2 + 2\gamma_i \left[2\pi r(\ell - \ell_c) \right]$$

Notice that the total energy change vanishes as $\ell \rightarrow \ell_c$, hence shear crack extension becomes thermodynamically less favorable as the fiber segments approach critical length.² On the other hand, in large segments, where $(\ell - \ell_c)$ is large, large interface cracks could produce large energy changes (acoustic emission) compared to fiber fractures, simply because of the potentially much larger volume $(\ell - \ell_c)$ of stressed fiber released. This can only occur, however, if the total energy change is large and negative, i.e., if the adhesive energy term $2\gamma_i$ is small relative to the elastic energy (i.e., brittle fracture). But this may not happen in MMCs because: (a) plastic deformation greatly increases the apparent surface energy $2\gamma_i$ of cracks, and (b) when the fiber is loaded in tension, the crack tends to close because of the greater Poisson contraction of the matrix, and frictional effects could become substantial, similarly increasing $2\gamma_i$. The reverse is true if the load is reversed and we hope to examine this latter effect through compressive loading tests.

There is a critical stress for such debonding, given by the Griffith condition that the incremental increase in surface energy of the crack be less than the incremental decrease in stored strain energy for a change in length dx :

²This phenomenon is similar to that of inclusion breakup in the working of steels, wherein fracture takes place at the largest inclusions first [9].

$$(2\pi r)(2\gamma_i)dx \leq (\partial E/\partial x)dx \quad (5.2)$$

where, from Eqn. 5.1 we obtain the stored energy density

$$(\partial E/\partial x) = (\pi r^2/2E_f) \left[\sigma_f^2 \left(1 - \frac{x^2}{\ell_e^2} \right) \right]$$

provided that $0 \leq x \leq (\ell - \ell_c)$. This stored energy density decreases continuously during straining until it is zero at the ineffective length halting further fiber breakup. Initiation is most likely at the fiber end ($x = 0$) where

$$(\partial E/\partial x) = (\partial E/\partial x)_{\max} = \pi r^2 \sigma_f^2 / 2E_f \quad (5.3)$$

so that interfacial fracture will occur at a debonding tensile stress in the fiber, combining (5.2) and (5.3),

$$\sigma^D = \sqrt{8\gamma_i E_f / r} \quad (5.4)$$

This is precisely equal to the expression derived independently by Outwater and Murphy [10], if we take $G_{II} = 2\gamma_i$, where G_{II} is the mode II energy release rate. It is also proportional to that derived by Gurland and Plateau [9] for failure at inclusions in metals. It was later rederived and verified experimentally by Wells and Beaumont [11] using compressively loaded filaments of steel of varying radii embedded in epoxy. The curve fit agreement was much better than that of critical stress theories, they noted. If we take $2\gamma_i = G_c$, the energy release rate, and $G_c = K_c^2/E_f$, where K_c is the critical stress intensity, we obtain

$$K_c = 2\sqrt{\gamma_i E_f} \quad (5.5)$$

It predicts that the interface fracture toughness should be independent of the fiber radius and crack size.

5.2.3 Interphase Effects on Fiber Fracture

A reaction zone (interphase) between the matrix and fiber may fail by a tensile microfracture (Fig. 5.1), subsequently serving as a notch on the fiber and possibly reducing its effective strength. The microfracture mechanics of such brittle layer failures has been studied by Ochiai and Murakami [4,12]. They employ a two-component model of a brittle layer and fiber (no matrix). The layer exhibits a size effect because thinner layers have statistically fewer defects and statistically higher strengths. If thin enough, the brittle layer may not fracture before the fiber. Above this critical thickness, the strength is reduced as $1/\sqrt{c}$, where c is the layer thickness.

Prolonged exposure of SiC to an aluminum melt degrades fiber strength, a possible contributing factor being such notch-induced fiber fractures. Since these can be prevented by shear fracture at the interphase/fiber boundary, one is interested in establishing the relative component strength levels for optimum strength. To do this, as suggested by the work of Ochiai and Murakami [12], it is necessary to define at least three critical stress levels:

$$\begin{aligned} \sigma^I &= \text{stress for initiating a notch} \\ \sigma^E &= \text{stress for extending the notch into the fiber, and} \\ \sigma^D &= \text{stress for debonding of interphase.} \end{aligned}$$

These give the possible failure sequences shown in Table 5.1:

TABLE 5.1
FAILURE SEQUENCES FOR WEAK AND STRONG INTERFACES

<u>Relative Strength</u>	<u>Failure Mechanism</u>	<u>Interface Type</u>
$\sigma^E > \sigma^I > \sigma^D$ $\sigma^I > \sigma^E > \sigma^D$	Debonding occurs; no notching	Weak
$\sigma^E > \sigma^D > \sigma^I$	Notches form interface debonds; no extension into fiber	Weak
$\sigma^D > \sigma^E > \sigma^I$	Notches form and later extend to cause fracture fiber; no debond.	Strong
$\sigma^D > \sigma^I > \sigma^E$	Notches immediately fracture fiber; no debond.	Strong

An important conclusion to be drawn is that the fiber fracture can be prevented by shear fracture of the interface at an interphase notch. Ochiai and Murakami define the maximum strength that an interface can have to permit extension of the notch into the fiber [4,12], but do not give an experimental method for measuring the actual (not this maximum) interface strength. In practice [4] they used a pull-out test which established the critical aspect ratio from which the interface strength was calculated using the shear lag model. They experimentally demonstrated the interphase thickness-strength reduction effect with data on B/Ti alloys [4]. Here the interphase thickness was systematically increased by high temperature anneals, and the strength accordingly dropped. The effect did not occur in the W/Al system, and they attributed this to interfacial cracking. The present tests indicate that

acoustic emission could be used to check for interfacial cracking and thus clarify such a situation.

5.3 Model Experimental Approach

Studies of MMC fracture micromechanisms usually must contend with both very complex stress distributions and slip mechanisms within a heterogeneous deforming body, and an absence of non-invasive methodologies for in-situ observation of the fracture processes at the microscale. The complex internal stress distributions arise, during loading, from elastic incompatibility between matrix and reinforcement and from spatially varying residual stresses due to differential thermal contraction of the constituents during cooling from process temperatures. Often the reinforcement is sufficiently randomly distributed so that the local stress is not directly predictable.

For these basic studies of MMC fracture micromechanisms, we have attempted to eliminate some of the problems associated with complex stress states in multiply-reinforced composites through the design of a model composite. This composite still retains the essential features of interest, but is in a configuration more amenable to analytic work with interfaces more accessible to direct NDE characterization. The model composite consists of a single ceramic fiber around which is grown a single crystal aluminum tensile sample. Using acoustic emission, interrupted test metallography and digitally recorded stress-strain behavior, we are exploring methodologies for quantitative determination of key microstructure parameters such as the fiber fracture strength, the fiber-matrix interface cohesion and the matrix slip behavior.

Dumbbell geometry single crystal tensile samples were used for this first study (later we will look at comparison tests). They were prepared from 99.99% aluminum and 140 μm diameter silicon carbide fibers with

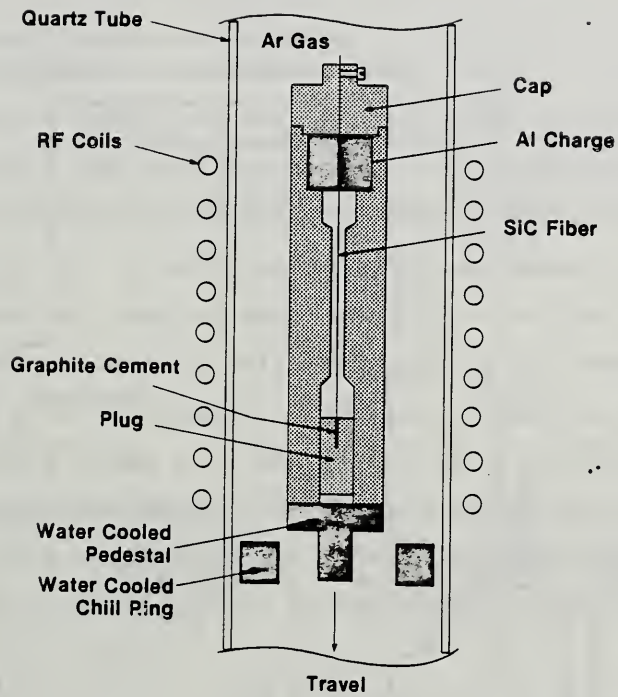


Fig. 5.3 Bridgman apparatus for growing directionally solidified monocrystal Al/SiC monofilament composites.

ACOUSTIC EMISSION INSTRUMENTATION FOR ADHESION MEASUREMENT

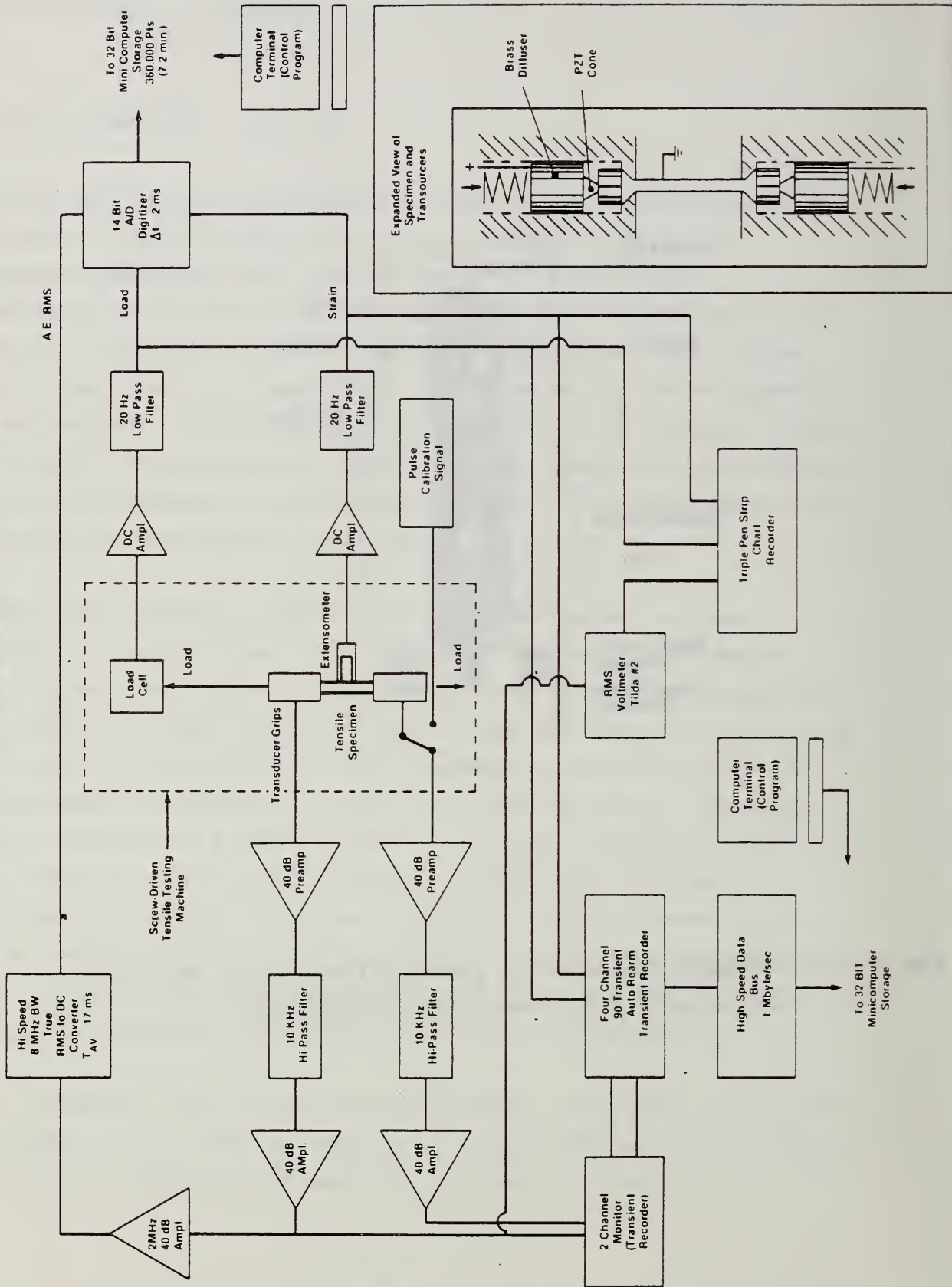


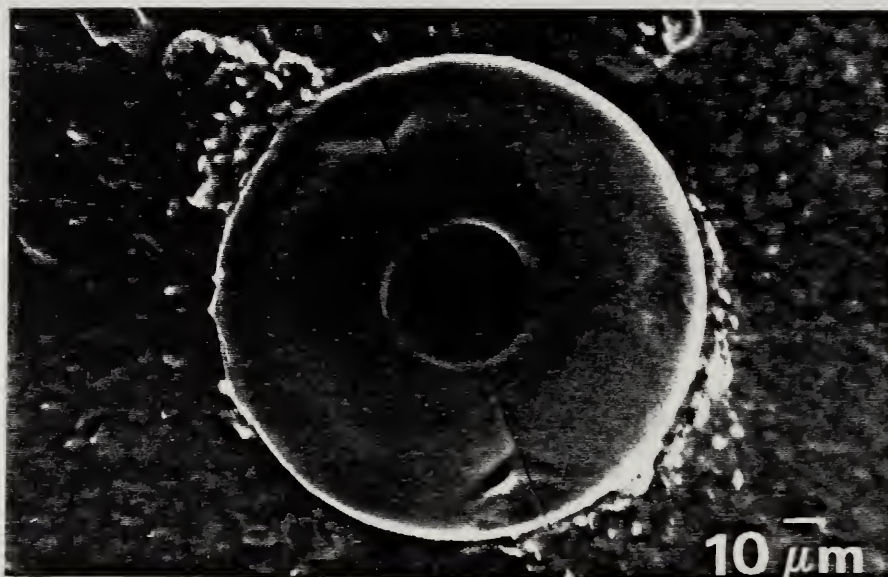
Fig. 5.4 Acoustic emission instrumentation for monitoring composite tensile tests.

unmodified surfaces using a Bridgman technique shown schematically in Figure 5.3. A high density graphite mold was internally machined to accommodate the growth of an aluminum single crystal with a 57 mm gauge length and 4 mm gauge diameter. The fiber was centrally located down the longitudinal axis of the mold, retained at the top by means of a screw and at the bottom by graphite glue attachment to a plug. The plug acted as a weight on the fiber, maintaining it centrally during subsequent crystal growth.

The mold was attached to a water-cooled pedestal, the system evacuated and backfilled with argon and then heated using a radio frequency induction furnace. The mold was heated to approximately 900°C and solidification achieved by lowering through a water-cooled copper chill at constant velocity. A combination of steep temperature gradient and slow growth speed was used to ensure a single crystal solidification [13]. Two growth velocities, with drastically different resulting reinforcement-matrix interfaces, were used. Samples with shallow reaction zones were grown at 0.41 mms⁻¹ (140 s solidification time) while samples with extensive reaction zones were grown at a velocity of 0.0083 mms⁻¹ (1.9 h solidification time). Samples with no fibers were also grown so that fiber effects could be separated from matrix behavior.

The oxide normally present on an aluminum single crystal is a potential extraneous acoustic emission source during tensile testing. It was removed by electropolishing the entire sample in a 6% perchloric acid/methanol solution at -30°C.

The specimens were mechanically loaded in tension using a screw-type machine driven at constant crosshead velocity (0.5 mm/min), (Fig. 5.4). The effective machine stiffness was measured to be 0.96 MNm⁻¹ using the maximum load rate method [14]. The load cell and strain gauge voltages were continuously digitized throughout the tests, the data stored on a minicomputer for later analysis.



(a)



(b)

Fig. 5.5 SEM micrographs of transverse sections of SiC filament in Al showing development of Al_4C_3 interface with increasing solidification times: (a) Rapidly solidified materials (140 s), (b) More slowly solidified (1.9 h).

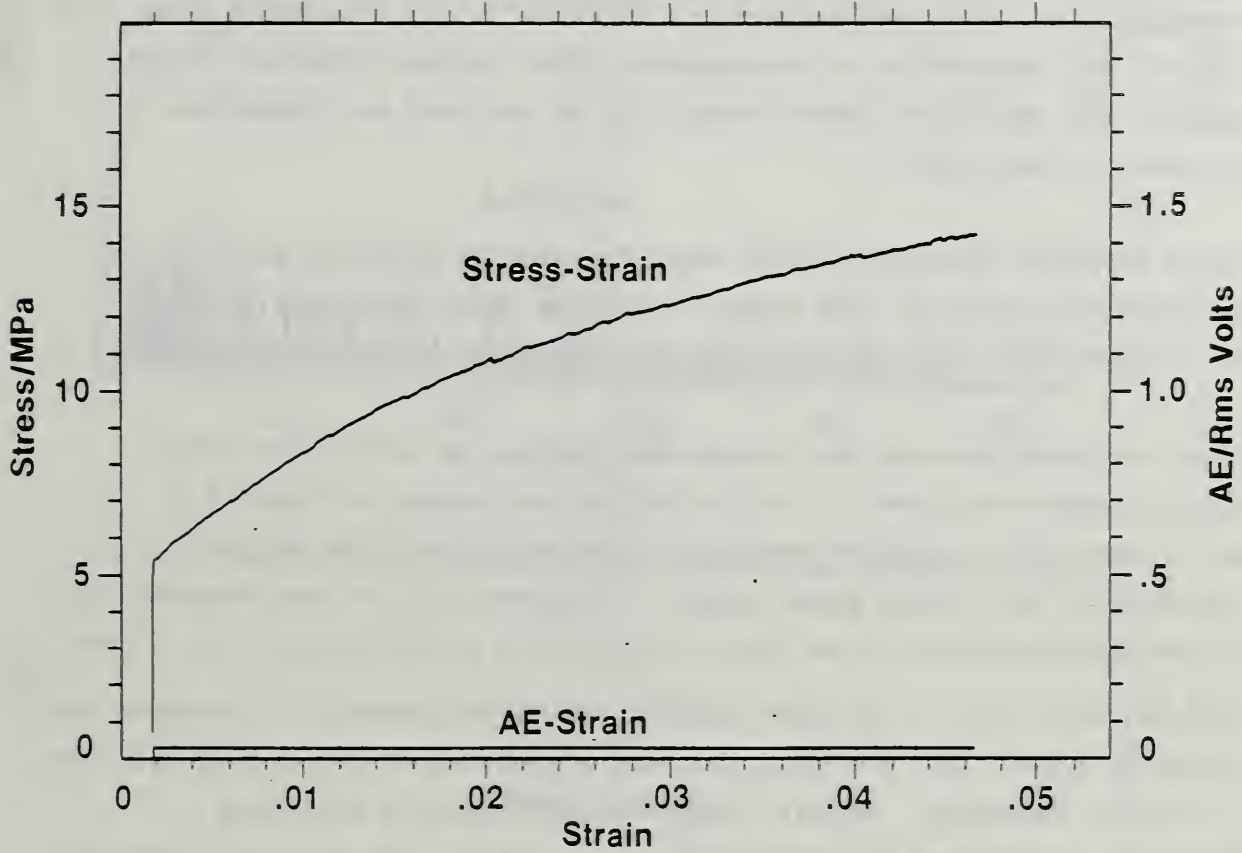


Fig. 5.6 Stress-strain and AE-strain curves for single crystal Al specimen with no SiC fiber.

Acoustic emission was continuously measured during testing using a specially designed system shown schematically in Figure 5.4. Conical PZT-5 piezoelectric elements were used as transducers attached to either sample end. The signals from these were amplified, bandpass filtered and passed through a high speed digital rms-to-dc converter with a 17 ms averaging time. The rms voltage was digitized at 14 bits per 1.5 ms interval and recorded on a minicomputer. The largest transient bursts exceeded the amplifier linear range (200 mV rms) and are therefore nonlinear in amplitude.

A dual waveform recording system was also used in parallel with the rms measurements system so that signals could be later evaluated in detail. This system featured 8-bit digitization with a 50 ns sampling interval.

SEM micrographs showing the transverse sections of undeformed single crystal composites grown at two velocities are shown in Figure 5.5. It can be seen that extensive reaction occurred at the fiber-matrix interface in the slowly grown sample. This resulted in the formation of a layer approximately 10 μm thick Al_4C_3 at the interface in 1.9 h. Less reaction was found in the more rapidly solidified material. Assuming the parabolic growth law, the reaction zone present after 139 s of growth was $\sim 1.4 \mu\text{m}$ in thickness. Radial cracks in the fiber are polishing artifacts, aggravated by fiber degradation, since they were not observed in the fibers extracted by dissolving the matrix.

Stress-strain and acoustic emission-strain behaviors for the two composites and an aluminum single crystal with no fiber show that:

- o The aluminum single crystal containing no fiber had a smooth stress-strain and acoustic emission-strain behavior (Fig. 5.6). The data was in agreement with that reported for similar material in the past [16].

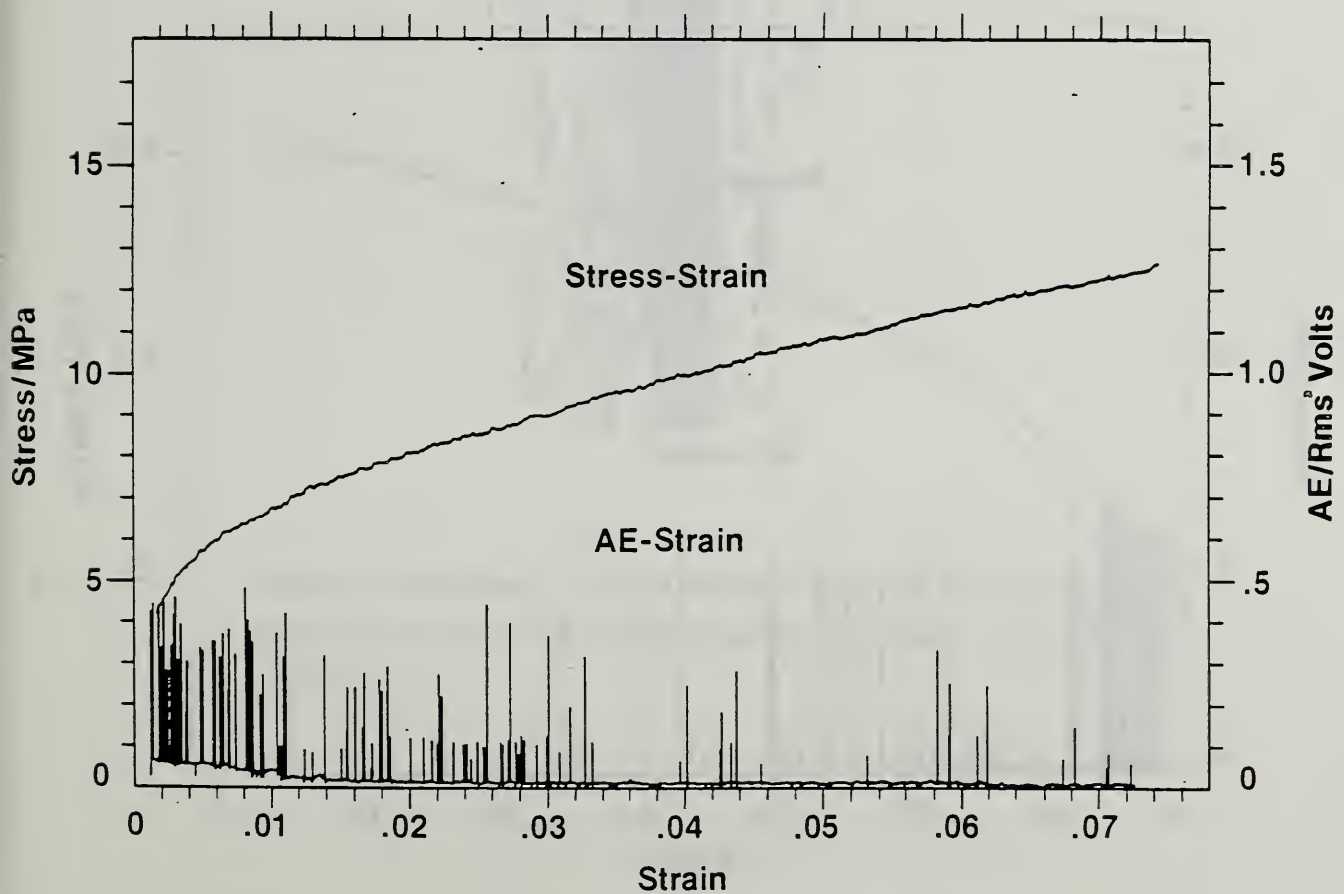
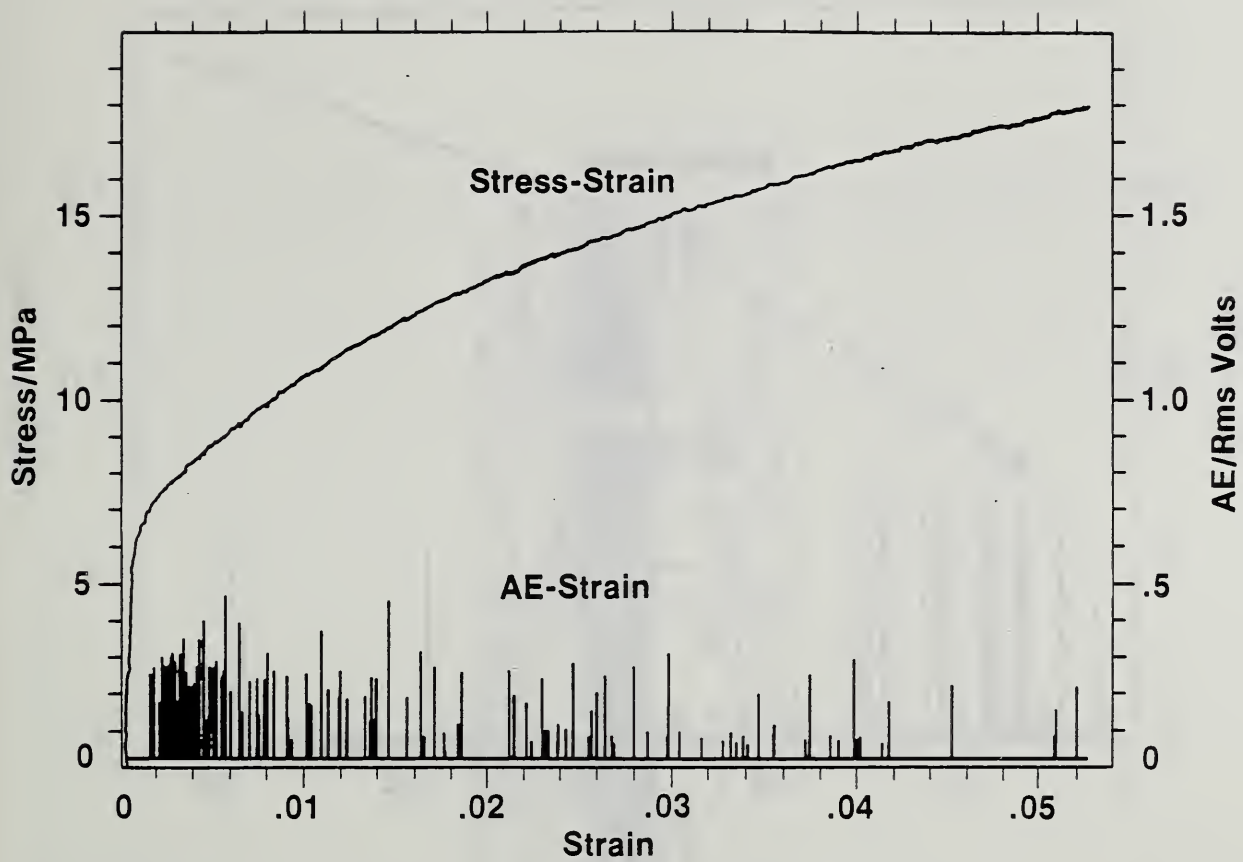


Fig. 5.7 Stress-strain and AE-strain curves for monofilament SiC/Al single crystal composites grown at slower rate (1.9 h solidification time).

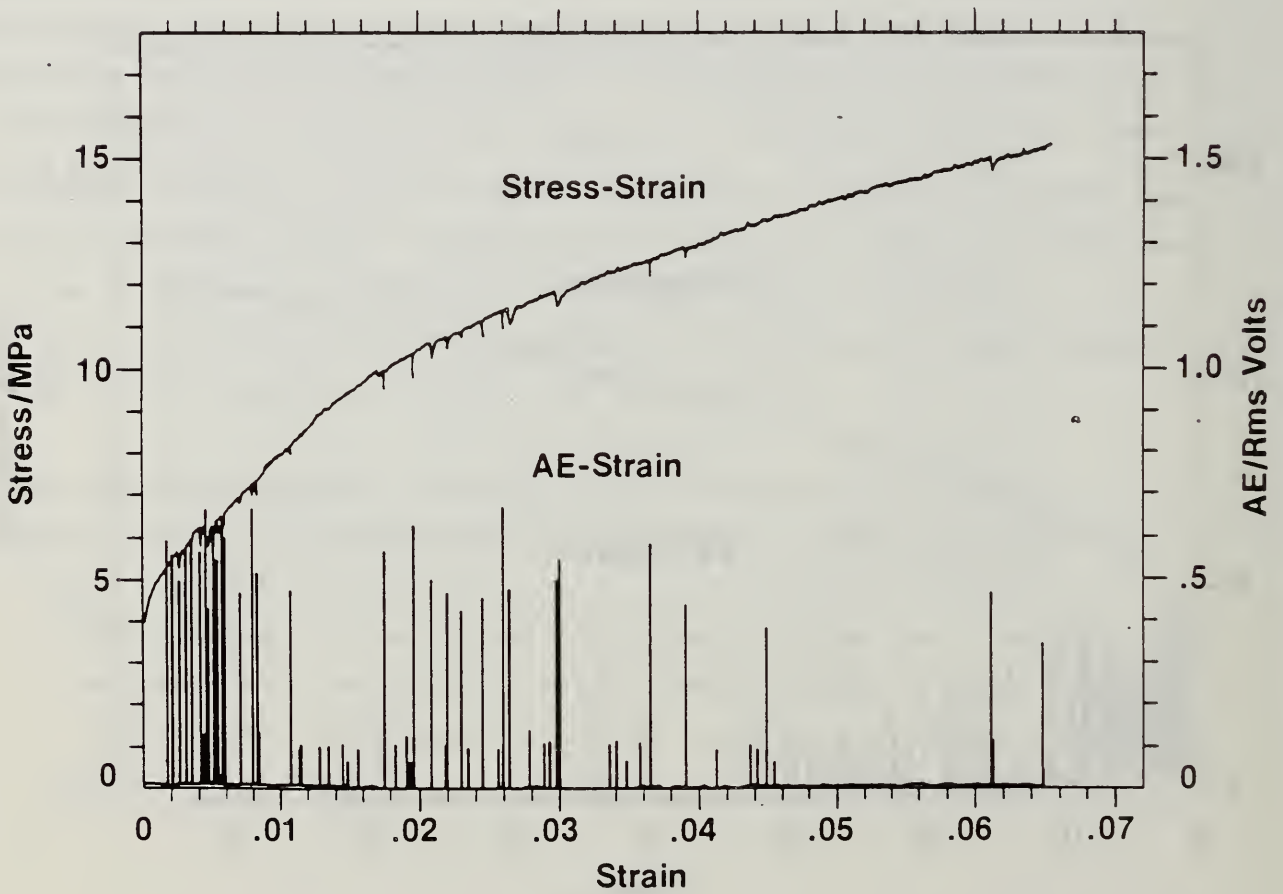
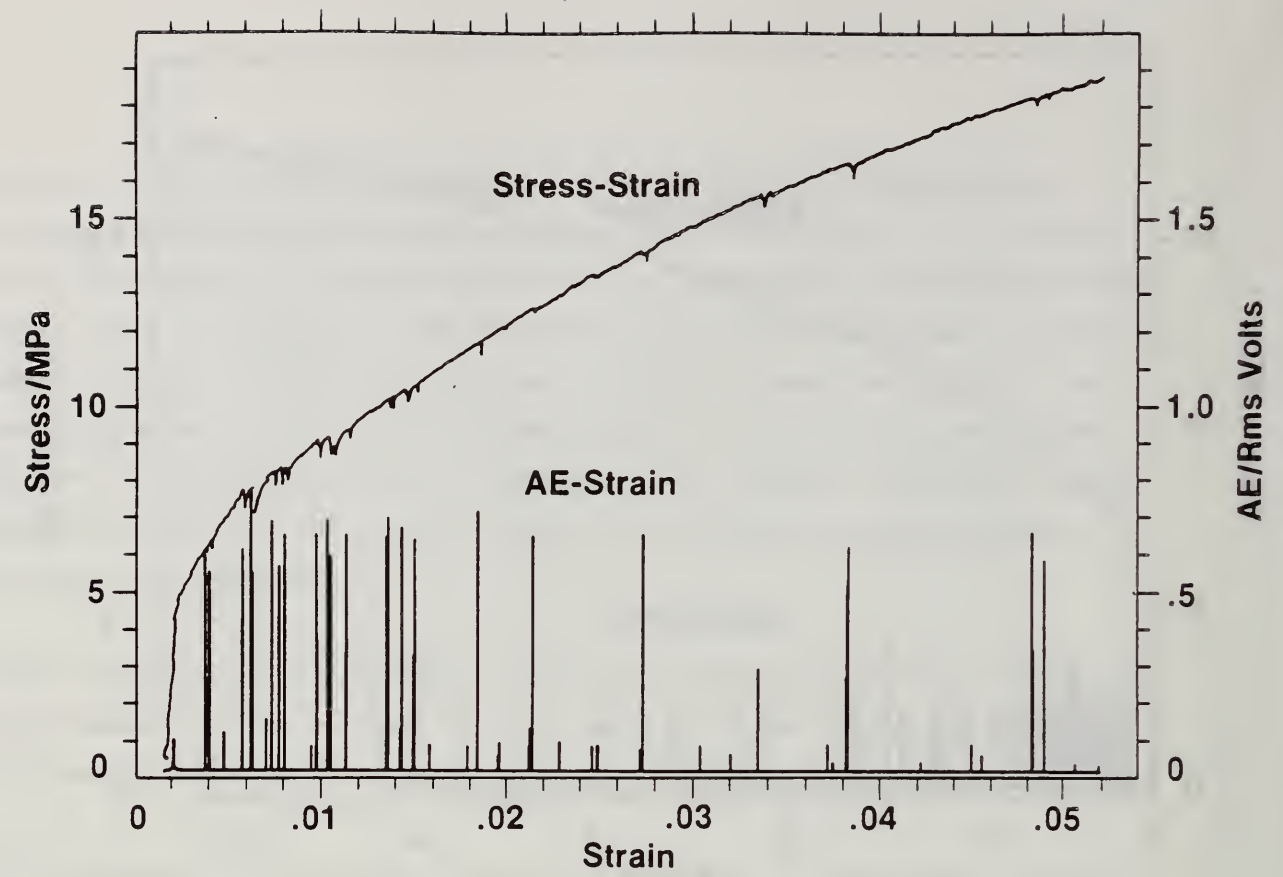


Fig. 5.8 Stress-strain and AE-strain curves for monofilament SiC/Al rapidly solidified single crystal composites (140 s solidification time).



Fig. 5.9 Optical micrograph. Longitudinal section of slowly grown composite pulled ~5% showing multiple transverse fiber fractures.

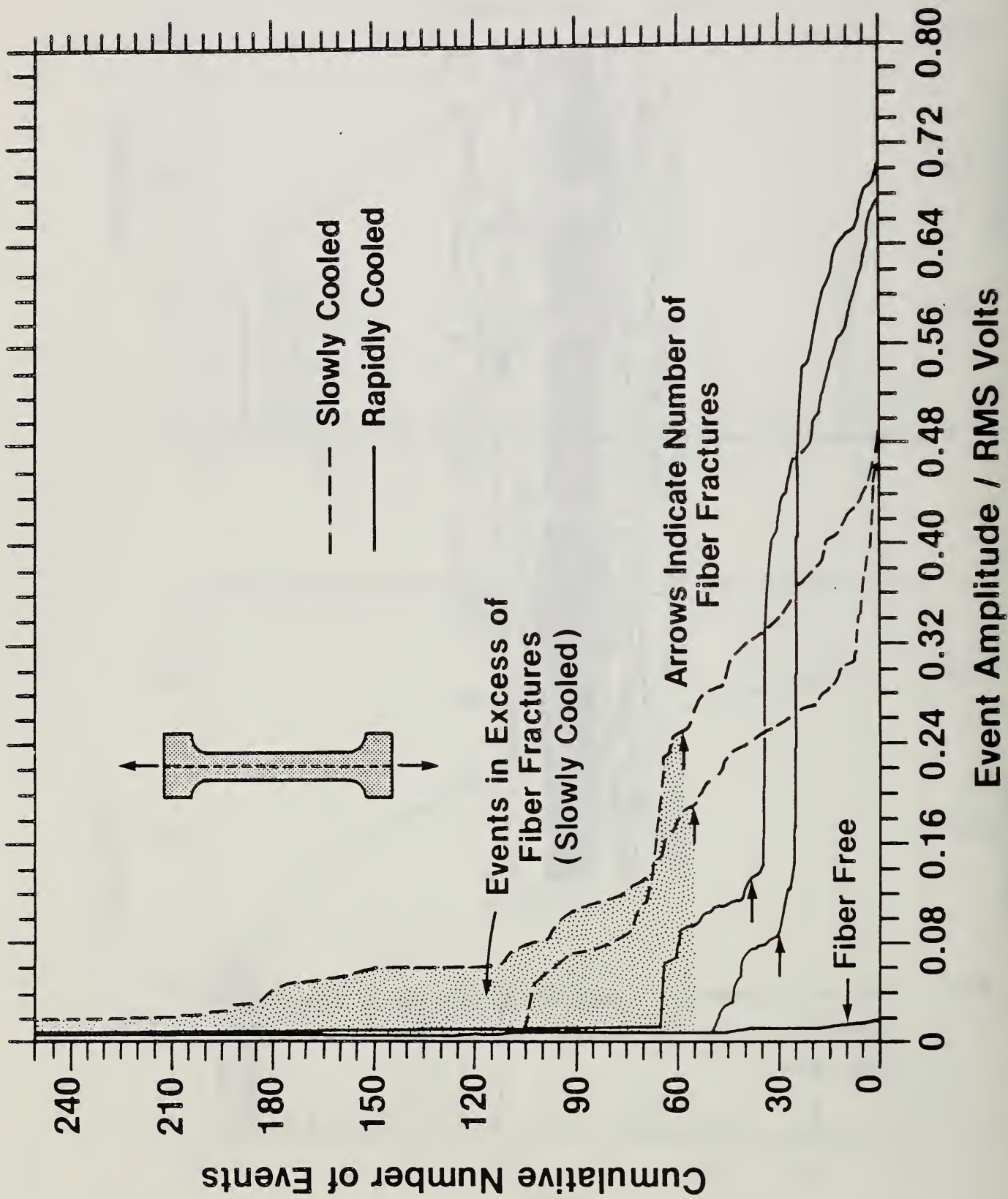


Fig. 5.10 Cumulative amplitude distribution of AE events in Figs. 5.6 through 5.8.

- o The more slowly grown composite exhibited a smooth stress-strain behavior but large "burst" acoustic emissions were observed superimposed on a smooth background behavior (Fig. 5.7).

- o The more rapidly grown composite exhibited a discontinuous stress-strain curve with 23 large load drops (Fig. 5.8). Strong acoustic emission signals accompanied each load drop.

The samples were pulled to a plastic strain of approximately 6%. Following testing, samples were longitudinally sectioned and polished to reveal the state of the SiC fibers. Figure 5.9 shows a typical result indicating multiple transverse fractures of the fiber. To determine the number of fractures, samples were immersed in a 10% NaOH solution at 50°C to dissolve the aluminum matrix, leaving behind the fragmented fiber.

The cumulative distributions of amplitudes of the AE events in Figures 5.6-5.8 is shown in Figure 5.10, which summarizes the results of five tests. For the more rapidly grown materials, there is a close correlation between the number of events and number of fiber fractures as indicated by the arrows. The number of events (30 and 38) are also close to the number of load drops (23 and 27), and this is improved if we consider that some of these drops resulted from multiple fractures. On the other hand, fiber fractures can only account for about half of the AE events observed during testing of the more slowly grown material. Since plasticity sources are probably unaffected by the solidification times used, we suggest that these extra signals are associated with interface cracking.

5.4 Discussion

It is possible to measure the fiber and interfacial strength in situ through the use of tensile tests, acoustic emission monitoring, and post-test examination of the specimen and fractured fibers. First, the tensile test is used to estimate the fiber strength σ_f . Then, post-test examination of the lengths of the broken fibers provides the critical aspect ratio ℓ_c/d . The interface strength can then be directly calculated from the shear lag formula.

The size of the load drops in the tensile tests can be used to estimate the fiber strength, since each load drop corresponds to a fiber fracture. This is a function of machine stiffness, so that it is important to examine the machine effects on load drop magnitude.

Consider a tensile specimen with a single fiber oriented along the tensile axis. If the fiber breaks, there will be a localized plastic strain, which causes a load drop whose magnitude depends on the machine stiffness. For example, if a dead weight ("soft") load mechanism is used, extensions occur instead of load drops. Our analysis assumes use of a "hard" or constant crosshead velocity machine and follows that of Clough [14]. The total extension of the crosshead moving at velocity V over time duration Δt is equal to the sum of the extensions u_p of the machine length (pull rods, grips, load cell) and u_s of the specimen:

$$V\Delta t = u_p + u_s = P/k + u_s \quad ,$$

where P is the load and k is the machine stiffness (N/m). If a fiber fractures, during time increment dt there will be a sudden drop in load with the corresponding extensions:

$$d(V\Delta t) = Vdt = du_s + dP/k$$

Crosshead motion is negligibly small during the load drop so that we can omit the term Vdt ³ and express the load drop as

$$\Delta P = k\Delta u_s$$

The fracture of a fiber of length $2\ell_c$ into lengths ℓ_c will cause a localized increase in cross-sectional stress $\Delta\sigma = A_f\sigma_f/A_s$ at the

³The duration of the load drop is $\Delta t = \Delta e_\rho / \dot{e}_\rho$, where Δe_ρ is the load drop plastic strain at the fracture and \dot{e}_ρ is the local strain rate at the fracture. We can estimate the strain increment from $\Delta e_\rho = \Delta\sigma / (d\sigma/de_\rho)$, where $\Delta\sigma$ is the stress increment $(A_f/A_s)\sigma_f$ and $(d\sigma/de_\rho)$ is the local rate of strain hardening. Taking typical values of these we obtain a strain of 0.001. Assuming the deformation to be entirely localized during the load drop, the local strain rate will be increased by the rate sensitivity of the stress. Rate sensitivity data on pure Al (Clough [15]) gives an increase in strain rate by a factor of 3.5 for a 2% stress change (calculated from the loss in fiber reinforcement). Since the local strain rate before fracture was $V/\ell_c = (8.3 \times 10^{-6}) / (0.001) = 0.0083s^{-1}$, the local strain rate during the load drop will be $\sim 3.5 \times 0.0083 = 0.029s^{-1}$. Thus the duration of the load drop will be $e_\rho / \dot{e}_\rho = 0.0001 / 0.029 = 33.2$ ms. During this time the cross-head will extend $Vdt = (8.3 \times 10^{-6})(0.0332) = 0.28 \mu m$. The sample itself will extend an amount dP/k , where dP is the load drop (typically 7 N) and k is the machine stiffness (10^6 N/m), or 7 μm . Thus the cross-head displacement is negligible in comparison to sample extension during a load drop and we can omit the term Vdt .

fracture, where A_f and A_s are the fiber and specimen cross-sectional areas and σ_f is the fiber strength. The plastic strain extends approximately $\ell_c/2$ along each fiber, over the length of ineffective fiber reinforcement, where the matrix tensile stress is higher. This will cause an increase in length of the specimen of approximately

$$\Delta u_s = \ell_c \Delta e_c = \ell_c \Delta \sigma / (\partial \sigma / \partial e) = \ell_c \sigma_f (A_f / A_s) / (\partial \sigma / \partial e) \quad ,$$

where Δe_c is the localized plastic strain and $(\partial \sigma / \partial e)$ is the localized rate of work-hardening $(\partial \sigma / \partial e_\rho)$. When $\ell = \ell_c$, this is equal to the macroscopic rate of work-hardening. The fiber strength (combining the above two equations) is then

$$\sigma_f = \Delta P (A_s / A_f) (\partial \sigma / \partial e) / k \ell_c \quad . \quad (5.6)$$

The last three load drops of the rapidly solidified composite averaged 4.5 N (0.31 MPa), $A_s / A_f = 943$, $\partial \sigma / \partial e = 0.18$ GPa, $k = 0.91 \text{ MNm}^{-1}$ and $\ell_c \sim 2.4$ mm. Thus, the fiber strength σ_f is ~ 0.3 GPa, only 10% of that of a virgin fiber prior to composite processing.

Fiber loading theory indicates that the shear strength for fiber fracture is given by the relation [3]

$$\tau_i = \sigma_f d / 2 \ell_c \quad (5.7)$$

where d is the fiber diameter. As a sample calculation, for a rapidly grown sample, substituting $\ell_c = 2.4$ mm, $\sigma_f = 300$ MPa and $d = 0.14$ mm gives a value for $2\tau_i \sim 17.5$ MPa. Equating $2\tau_i$ with the tensile stress indicates that the interfacial shear strength in the rapidly solidified

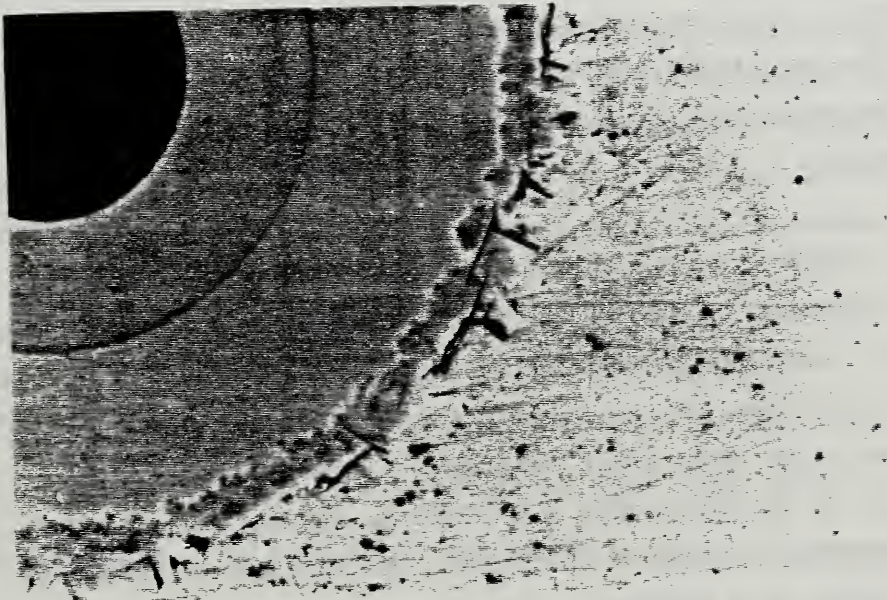


Fig. 5.11 SEM micrograph of interfacial region in slowly-grown composite (non-deformed) showing presence of several interface cracks prior to testing (courtesy C. Handwerker).

sample is approximately equal to the matrix shear strength at 5% strain. Thus fiber-matrix failure occurs here by matrix shear rather than interfacial fracture.

Turning now to the slowly grown material, we see that though many fiber fractures occurred, no detectable load drops were observed on the stress-strain curve. The noise-limited smallest detectable load drop is $\sim 0.4\text{N}$ (0.03 MPa). Thus $\sigma_f < 30$ MPa, an order of magnitude less than that of the rapidly grown sample. This degradation of strength is likely associated with notch cracking of the $10\ \mu\text{m}$ thick (brittle) Al_4C_3 layer at the interface. Results quoted below also indicate low fracture toughness of the near-interface matrix, so that the notches could initiate in the matrix and be much larger than $10\ \mu\text{m}$, greatly lowering the fiber strength.

Metallography provides additional information on failure mechanisms. The plastic strain appears to be, as assumed in the above model, largely localized to the sections between fiber fracture. Evidence that the deformation is localized to the fiber ends is obtained by examining the distance between fiber ends after testing. If the total elongation, after 5% strain, is $(0.057)(0.05) = 0.00285$ m, and this is divided between the separations between 51 pieces, the average displacement between fibers will be $0.00285/50 = 57\ \mu\text{m}$, or about 1 radius. This is comparable to the separations between fiber ends in Figure 5.9, so that the strain appears to be localized as assumed.

Interface cracking occurred in this material and this provides important information on the properties of the matrix just external to the interface. An SEM micrograph (courtesy C. Handwerker) of the interface region in a slowly solidified sample (Fig. 5.11) shows the presence of several small ($\sim 10\ \mu\text{m}$) interfacial cracks present prior to pulling the sample.

Radial cracks are also present in the Si-rich matrix, which, although possibly caused by polishing, nevertheless indicate severe embrittlement of the matrix near the interphase. If we conservatively assume the stress limited by the matrix flow stress (~ 20 MPa) and take the crack half length to be $c = 5 \mu\text{m}$, then $K_c \sim \sigma_{\text{net}} \sqrt{\pi c} = 0.08 \text{ MPam}^{1/2}$, indicating severe embrittlement. This is close to the value of $K_c < 0.1 \text{ MPam}^{1/2}$ obtained from load drop magnitudes (Table 5.2). Further, we estimate that $\gamma_i = G_c/2 \sim K_c^2/2E_f = 0.04 \text{ J/m}^2$, or about 4% of the surface energy of Al, indicating poor bonding. These observations indicate that the model of Ochiai and Murakami [4,12] ought to be modified if there is any embrittlement of the matrix material just outside of the interphase. The low fracture toughness of the matrix surrounding the fiber can effectively act as an additional brittle layer surrounding the fiber and interphase, roughly doubling the notch crack size.

We can calculate the interface strength from the shear lag equation (5.7). The critical length ℓ_c was reduced in the slowly solidified material. Typically $\ell_c \sim 1.4 \text{ mm}$ so that from the shear lag equation $2\tau_i < 3 \text{ MPa}$. This is much less than the matrix shear strength and is consistent with brittle shear failure in the locally embrittled matrix or at the matrix-interphase boundary. Tensile and shear fractures in or just outside the layer may be the source of the additional acoustic emission signals in this material (Fig. 5.7). Such a thick layer and Si-enriched matrix are absent in the more rapidly grown material, which also does not emit these extra signals.

As preliminary examples of the use of the measurement technique, the following table summarizes measured fiber and interface strengths as well as interface fracture toughness and interface adhesive energy for two rapidly cooled, and two slowly cooled SiC fiber/Al single crystal composites grown from the melt.

TABLE 5.2
MEASURED FIBER AND INTERFACE STRENGTHS

Property	Rapidly Solidified (139 s)	Comments	Slowly Solidified (1.9 h)	Comments
Fiber Tensile Strength (MPa) (Eqn. 5.6)	300 288	Fiber Fracture	<30 <40	Fiber Fracture
Matrix Shear Strength (MPa) (Figs. 5.7 and 5.8)	9.5 7.7		9.0 6.4	
Interface Shear Strength (MPa) (Eqn. 5.7)	8.7 9.8		<3.0 <2.8	
Interface Critical Stress Intensity K_c (MPam ^{1/2}) (Eqn. 5.7)	>1.2 >1.2	No Interfacial Fracture	<0.12 <0.16	Interfacial Fracture
Interface Adhesive Energy γ_i (J/m ²) (Eqn. 5.4)	>1.4 >1.4		<0.014 <0.026	

As can be seen, the time of exposure to the melt greatly affects the fiber and interface strengths. The interfacial fracture toughnesses and adhesive energies of the slowly cooled composites are extremely low, again consistent with the interpretation of brittle shear fracture of the interface as monitored by acoustic emission. The adhesive energy of the rapidly cooled composite is found to be greater than that of pure Al (~1.0 J/m² [1]), in agreement with acoustic emission results that there was little or no interfacial fracture in that material.

5.5 Future Directions

By using specially designed specimens, combined with analyses of tensile test and acoustic emission results, direct, in situ measurements have

been made of fiber and interface strengths, adhesive energy and fracture toughness. By changing the sample configuration and type of loading (e.g., compressive vs. tensile), determination can be made of other parameters, such as the relative effect of interface friction on cohesive strength. Compressive longitudinal tests appear attractive as opposed to transverse loading because the radial symmetry under compressive loading imposes a constant radial stress around the interface.

Since measurements are made of individual fracture events, rather than statistical ensembles, the data from the individual events can be combined to unambiguously evaluate the accuracy of statistical theories of strength. This is the inverse of the conventional practice of inferring individual microfracture properties from bulk properties. As a simplified example, the average length of fiber can be determined during testing from the number of large AE events (i.e., the number of fiber fractures). Since the individual fiber fracture strengths are known from the load drops, a Weibull-type statistical distribution of fiber strength versus length can be constructed. Such a result awaits further analysis of data already at hand.

While these experiments have been carried out on a model system, the technique can be extended to other, more complex advanced structural composites. We are at present in the process of making arrangements to test multiple fiber MMCs produced at the MIT facilities using techniques similar to those described here.

5.6 References

- [1] A. Argon, J. Im, and R. Safoglu, *Met. Trans.* 6A (1975), p. 825.
- [2] K. Gutfreund, L.J. Broutman and E.H. Jaffe, "International Investigations of Boron Fiber-Reinforced Plastics," Advanced Fibrous Reinforced Composites, 10, pp. E-25 to E-40, Society of Aerospace Material and Process Engineers (SAMPE), 1966.
- [3] A. Kelly, Strong Solids, Oxford, Clarendon Press (1977), p. 131.
- [4] S. Ochiai and Y. Murakami, *J. Materials Sci.*, 14 (1979), pp. 831-840.
- [5] R.B. Clough, "Energetics of AE Source Characterization," to be published (March-May 1987) in Materials Evaluation.
- [6] A.C. Evans, M.C. Lu, S. Schmauder, and M. Ruhle, *Acta. Met.* 34 (1986), 1643.
- [7] C.R. Crowe, R.A. Gray, and D.F. Hasson, "Microstructure Controlled Fracture Toughness," Fifth Int. Conf. on Composite Materials ICCM-V, W. Harrigan, ed., AIME (1985), p. 843.
- [8] R.J. Arsenault and C.S. Pande, *Scripta Met.* 18 (1984), p. 1131.
- [9] J. Gurland and J. Plateau, *Trans. ASM*, 36 (1963), p. 442.
- [10] J.D. Outwater and M.C. Murphy, Paper 11c, 24th Annual Technical Conf. on Composites, (The Society of the Plastics Industry, New York, NY, 1969).

- [11] J.K. Wells and P. Beaumont, *J. Materials Sci.*, 20 (1985), pp. 1275-1284.
- [12] S. Ochiai and Y. Murakami, *Z. Metallkunde*, 72 (1981), pp. 827-831.
- [13] M.C. Flemings, Solidification Processing, McGraw-Hill, NY (1974), p. 54.
- [14] R.B. Clough, "Rational Basis and New Methods for Proportional Limit, Machine Stiffness, Critical Stress Intensity, and Crack Velocity Measurements," in Recent Developments in Mechanical Testing, STP 608, Philadelphia: American Society for Testing and Materials (1976), pp. 20-44., see Equation (10).
- [15] R.B. Clough, "Effects of Composition and Strain Rate on the Tensile Behavior of Selected High-Purity Aluminum Alloys," M.S. Thesis, Univ. of Arizona, Tucson (1965), p. 62.
- [16] C. Scruby, H. Wadley, and J.E. Sinclair, *Phil. Mag.*, 44 (1981), pp. 249-274.

Appendix I

2. MICROSCOPIC ORIGINS

by

H. N. G. WADLEY and J. A. SIMMONS

CONTENTS

- 2.1 Introduction
- 2.2 Micromechanical Modeling
 - 2.2.1 Formulation
 - 2.2.2 Transducer spectral sensitivity
 - 2.2.3 Detectability criteria
 - 2.2.4 Source directivity
- 2.3 Microscopic Dislocation Sources
 - 2.3.1 Detectability
 - 2.3.2 Single crystal deformation
 - 2.3.3 Grain size effects
 - 2.3.4 Precipitation effects
- 2.4 Microscopic Fracture Sources
 - 2.4.1 Detectability
 - 2.4.2 Cleavage microfracture
 - 2.4.3 Intergranular microfracture
 - 2.4.4 Particle microfracture
 - 2.4.5 Microvoid coalescence
 - 2.4.6 Environmental factors
 - 2.4.7 Amplification factors
- 2.5 Microscopic Phase Changes
 - 2.5.1 Solid state phase transformations
 - 2.5.2 Detectability of martensitic transformations
 - 2.5.3 Liquid-solid transformations

2.1 Introduction

Acoustic emission can be thought of as the naturally generated ultrasound created by local mechanical instabilities within a body. Imagine, for example, a body which had been placed under load sometime in the past and is now in elastic equilibrium throughout. Suppose a small crack appears within the body at a point distant to that where the loads were applied. The surfaces of the crack are able to move in such a manner that they become stress free. In so doing, they release some of the stored elastic energy in the body.

This release of elastic energy is in the form of elastic waves that propagate freely throughout the body suffering reflections/mode conversions at its boundaries. In fact, the propagation of these elastic waves is the mechanism for communication of the changed elastic state in the immediate vicinity of the crack to the rest of the body. The waves enable the entire body to change its shape and accommodate the crack, and each propagating wavefront carries a component of this shape change. In the perfectly elastic body used for mathematical modeling, these waves would propagate indefinitely and mechanical equilibrium would never be established. However, in practical materials, absorption (conversion to heat) occurs, and the waves eventually dissipate allowing the body to assume a new (cracked) shape and establish a new equilibrium with the loads throughout.

A transducer attached to a body is capable of detecting the motion of the surface with which it is in contact. Its response, following a local crack extension, is the acoustic emission we

observe in experiments and tests. Since the transducers are usually constructed from piezoelectric slabs and have a resonant behavior, their sensitivity varies with frequency and is usually greatest in the range 0.1 - 2.0 MHz. It is only these frequency components of the emitted waves that are sensed. Neither the static surface strains (the difference in shapes of the two equilibrium states discussed above) or the very high frequency components are sensed.

Observed acoustic emission signals, at least close to the source are dominated by surface displacements associated with wavefront arrivals at the transducer location. If the wavefront contains appreciable frequency components in the transducer bandwidth, then a voltage will be created across the faces of the transducer, and provided this exceeds the background noise, the emission will have been detected.

The detectability of acoustic emission, then, depends upon the temporal nature of the source because this determines the amplitude of each spectral component in each wavefront. If the source operates so slowly that there is sufficient time for the body to return to quasi-equilibrium before the crack has appreciably extended, it is possible that no detected signal will be emitted (however a (static) strain gauge might register the change of shape if the crack grows sufficiently large). Conversely, if the crack extends rapidly and then stops so that its growth time was around $1 \div$ transducer bandwidth, then the emitted wavefronts would be dominated by frequency components in the detectable range.

Clearly, it is very important to gain a deeper understanding of

the microscopic origins of acoustic emissions, since this will allow us to determine the likelihood of detecting various events of potential interest and of distinguishing between them.

The purpose of this part is, therefore, to develop an understanding of the relationship between local mechanical instabilities and the ensuing acoustic emission. In particular, we will develop expressions for the surface motion produced by such microscopic acoustic emission sources as dislocations, micro-cracks and phase transformations, particularly those involving the formation/annihilation of martensite. Using simple results from tensor wave propagation theory, we shall then use these micromechanical models to develop detectability criteria for microscopic sources. These criteria are finally used to identify the origin of acoustic emission in materials undergoing deformation, fracture and phase changes.

In this part, we employ the usual assumption of linear isotropic elasticity. All metals only approximate these assumptions. In practice, metals exhibit weak nonlinear behavior due to internal friction mechanisms, are anisotropic to a greater or lesser degree, and if preferred grain orientation (texture) is present, will not exhibit spherical wave spreading. In addition, the polycrystalline nature of engineering materials results in grain scattering which can be particularly strong for spectral components whose wavelengths approach or exceed the grain size. In what follows, all these effects have been ignored, not because they cannot be treated, but rather because the relative contribution they make is

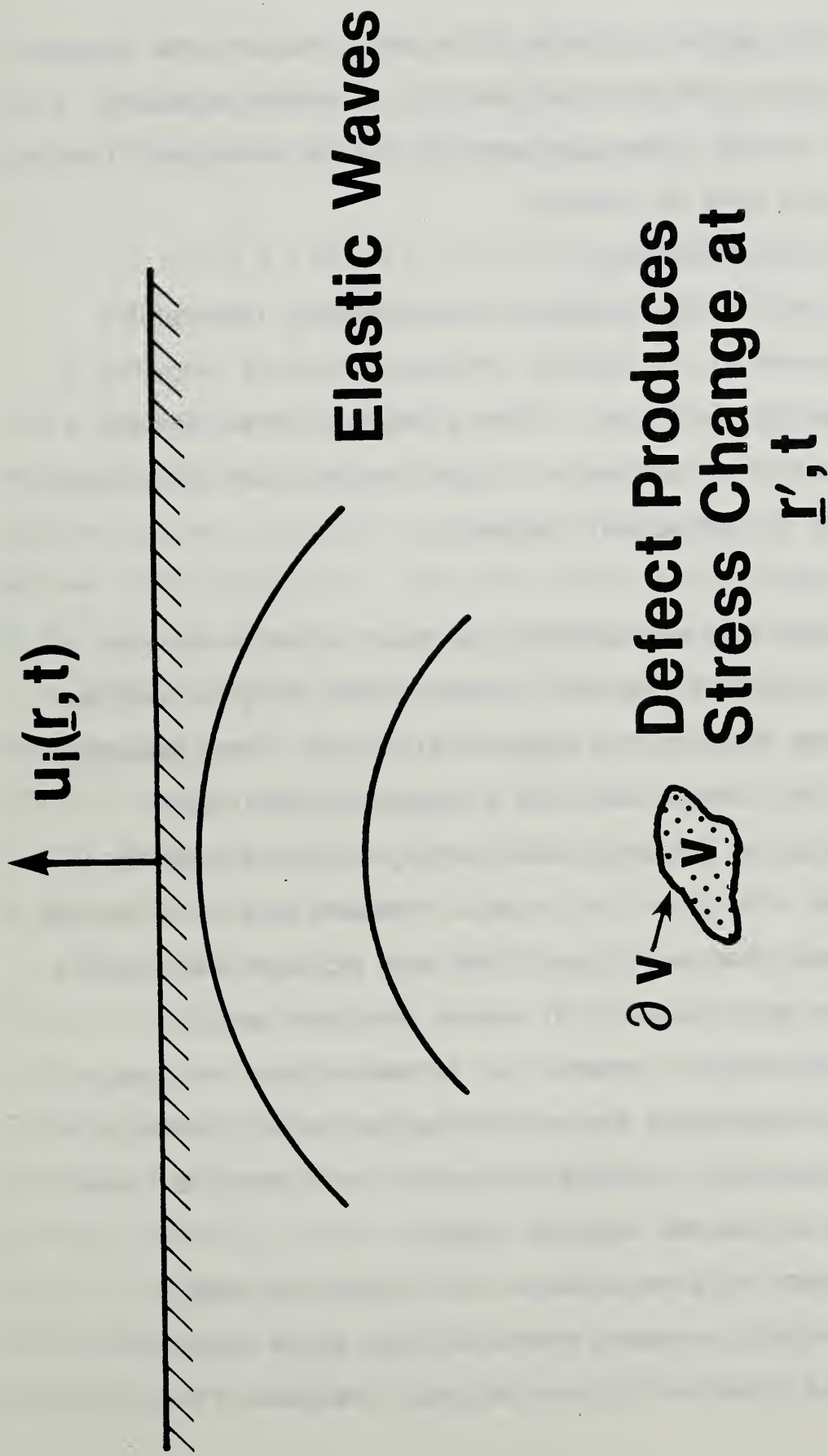


Fig. 1. Schematic diagram of the acoustic emission process.

very sensitive to detailed aspects of the microstructure and varies from case to case. The treatment does not extend to situations where sample normal modes dominate the acoustic emission. This is still an emerging area of research.

2.2 Micromechanical Modeling

In this section, the principles for developing detectability criteria are presented for acoustic emission occurring following a general mechanical instability. These principles will be applied to acoustic emission from dislocation motion, crack growth and phase transformations in subsequent sections.

2.2.1 Formulation

The sequence of events giving rise to an acoustic emission signal are summarized in Figure 1. Elastic waves are generated due to a local change of stress in a region of Volume V . These propagate (spherically in an isotropic body) as a mechanical disturbance through the structure causing a time varying surface displacement $\underline{u}(t)$. $\underline{u}(t)$ varies with source and receiver positions due to (i) inverse square law decay (because of wavefront area increase with distance between source and receiver), (ii) source directivity and (iii) wavefront reflection/mode conversion at a free surface. A sensor located on the body detects the surface disturbance and generates a voltage waveform which, provided it exceeds the background noise, is observed as an acoustic emission signal.

Viewed from the perspective of the surrounding elastic structure, the acoustic emission source appears as an apparent change of stress (stress drop) and changes in tractions at the

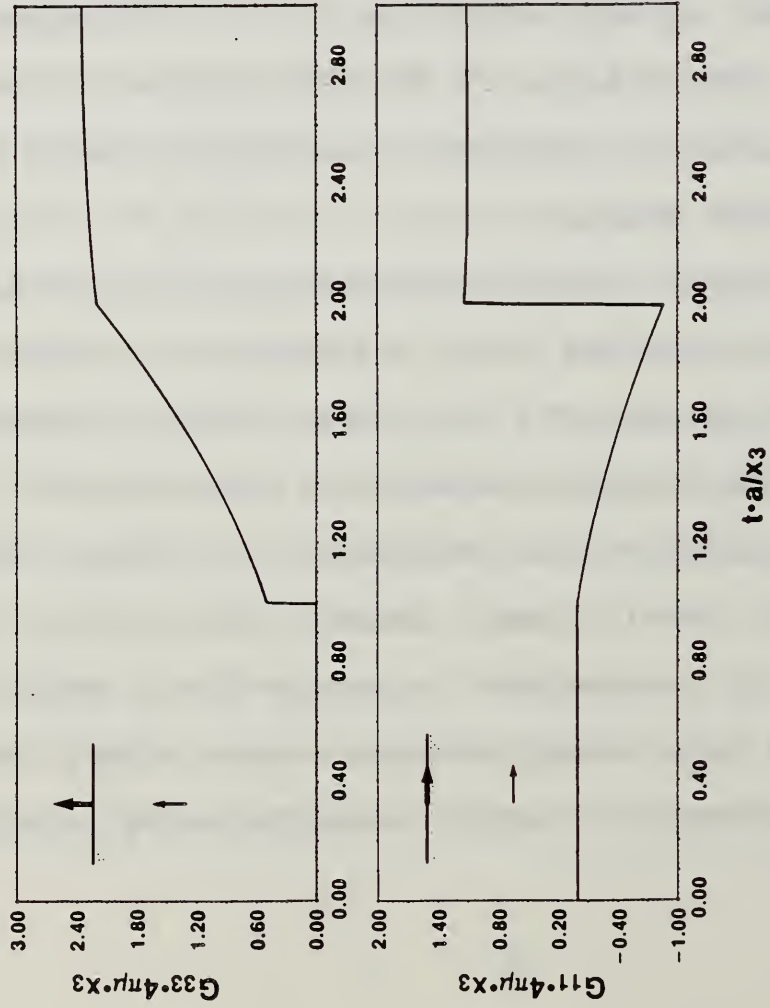
surface of the structure. Using a Green's function approach we can write¹ the displacement at position \underline{r} as arising from both internal (volume stress) and surface (traction) sources:

$$u_i(\underline{r},t) = \int d\underline{r}' \int G_{ij,k'}(\underline{r},\underline{r}',t-t') \Delta\sigma_{jk}(\underline{r}',t') dt' - \int dS'_{k'} \int G_{ij}(\underline{r},\underline{r}',t-t') \Delta\tau_{jk}(\underline{r}',t') dt' \quad (1)$$

where $G_{ij}(\underline{r},\underline{r}',t)$ are components of the dynamic elastic Green's tensor representing displacement in the x_i -direction at \underline{r} as a function of time, t , due to a unit strength force impulse applied at \underline{r}' and $t=0$ in the x_j -direction. Thus the Green's tensor is the solution to the wave equation for a unit force impulse source. The notation \prime is used to denote partial differentiation so that $G_{ij,k'}$ is the corresponding wave equation solution for a unit force derivative (dipole) impulse. $\Delta\sigma_{jk}$ and $\Delta\tau_{jk}$ are the volume stress and surface traction changes associated with the source and \underline{S}' a vector normal to the surface of the structure.

The time integral in equation (1) comprises a convolution. This convolution provides the basis, in principle, for predicting surface displacement waveforms from stress change sources if the Green's tensor is known (either calculated or measured). In subsequent sections these stress changes will be deduced for internal microscopic defect sources. Because the source and sensor are of finite size the representation requires a Green's tensor to be evaluated between every source and every receiver point. This is a numerically exhausting task beyond normal computing capabilities

(a) MONOPOLE WAVEFORMS



(b) DIPOLE WAVEFORMS

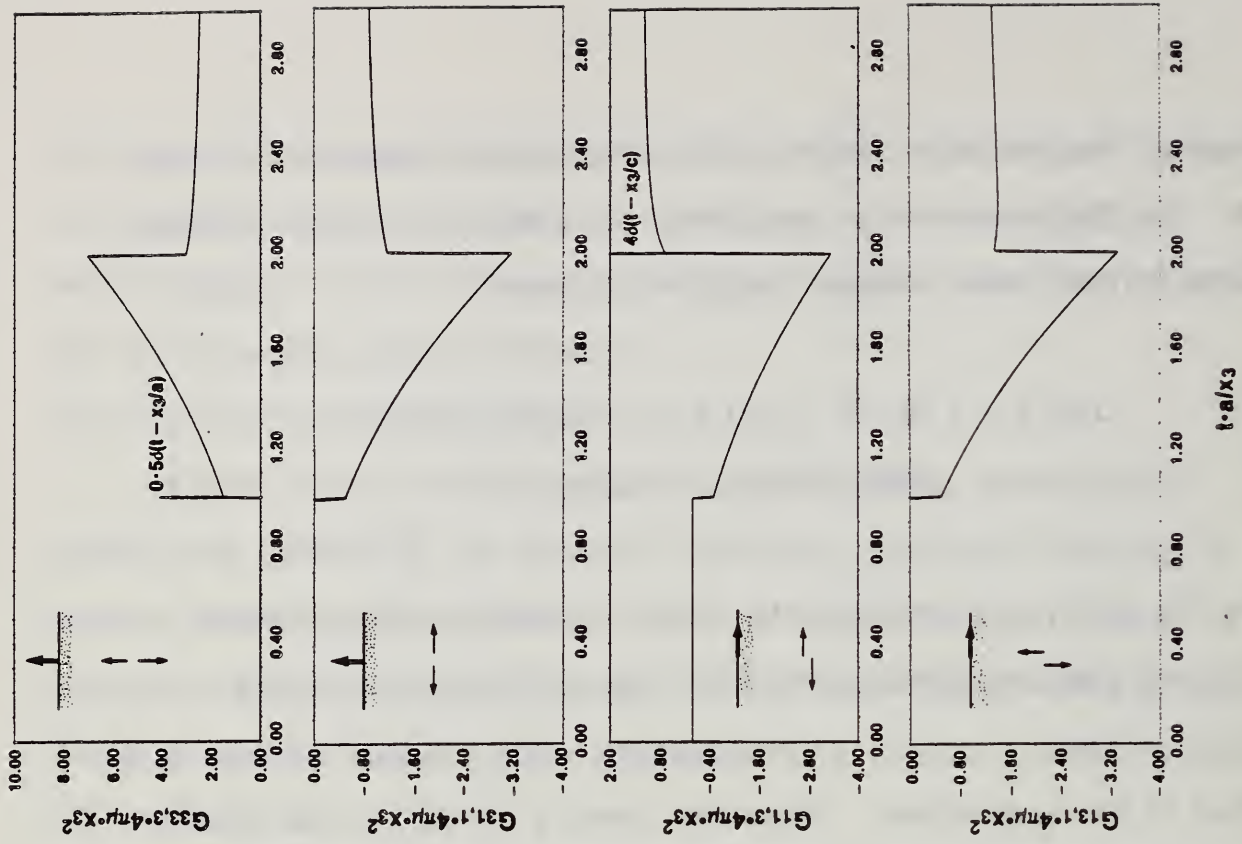


Fig. 2. Epicenter displacement waveforms for various infinitesimal multipole sources in an isotropic elastic half-space, a) Monopole sources, b) Dipole sources.

(c) QUADRUPOLE WAVEFORMS

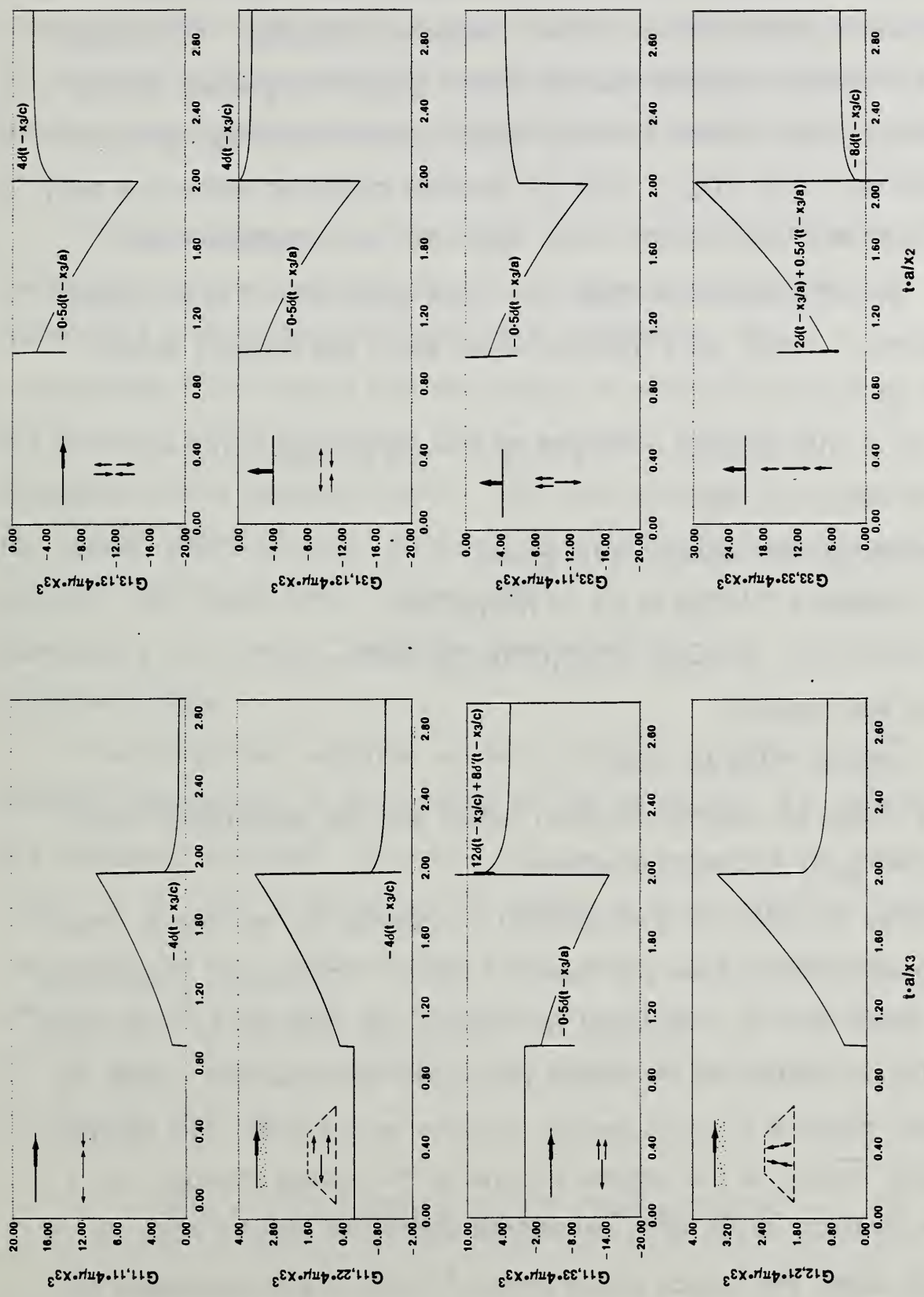


Fig. 2 (c). Epicenter displacement waveforms for various infinitesimal quadrupole sources in an isotropic elastic half-space.

and is further compounded by the possibility that each stress component might have a different temporal character. To simplify the formulation we note that the stress change is greatest at the centroid of the source, and that defect sources are often small in comparison with $|\underline{r}-\underline{r}'|$. Also for sources contained within the body, the surface traction source term, $\Delta\tau_{jk}$, can be considered zero.

For infinitesimal sources, the usual approach ^{2,3} is to expand the Green's tensor as a Taylor's series about the centroid source point \underline{r}_0 :

$$G_{ij,k'}(\underline{r},\underline{r}',t) = G_{ij,k'}(\underline{r},\underline{r}_0,t) + G_{ij,k'l'}(\underline{r},\underline{r}_0,t)\Delta r_{l'} + \dots$$

where $\Delta r_{l'} = r_{l'} - r_{0l}$.

Substituting into equation (1), gives:

$$u_i(\underline{r},t) = \int G_{ij,k'}(\underline{r},\underline{r}_0,t-t')\overline{\Delta\sigma_{jk}}(t')dt' + \int G_{ij,k'l'}(\underline{r},\underline{r}_0,t-t')\Delta\Gamma_{jkl}(t')dt' + \dots$$

where the quantity:

$$\overline{\Delta\sigma_{jk}}(t) = \int \Delta\sigma_{jk}(r',t)dr'$$

is the dipole (or seismic moment) tensor and the quadrupole tensor

$$\Delta\Gamma_{jkl}(t) = \int \Delta\sigma_{jk}(r',t)\Delta r_{l'}dr' .$$

Examples of epicenter displacement waveforms for monopole, dipole and quadrupole sources are shown in Fig. 2. At practical frequencies only small error is introduced for microscopic sources by truncating the Taylor's series at the dipole (first) term provided the source to receiver distance is much greater than the source size. The source quantity $\overline{\Delta\sigma_{jk}}(t)$ is the volume integral of the stress change, i.e., it is the average stress drop considered distributed on the point \underline{r}_0 . It is also called the source dipole tensor ^{4,5} and is also equivalent to

the quantity referred to as the seismic moment in seismology⁶. Since the stress drop can be thought of as a dipole density, equation (1) amounts to a summation of convolutions between the dipole density at each source point \underline{r}' and the Green's tensor between \underline{r}' and \underline{r} .

The final step of the formulation is to include the effect of the transduction process upon the signal. To date, only "nondisturbing" transducers of finite area S_T have been considered¹. By "nondisturbing" one means that the change in waveform caused by the presence of the transducer can be neglected because it is small compared to the waveform itself. This approximation is excellent for optical interferometric detection schemes⁷, electromagnetic acoustic and capacitance transducers⁸. Its validity for piezoelectric transducers is, however, yet to be determined, for they undoubtedly load the surface.

The transducer response will be considered in terms of the surface displacement at the location of the transducer, S_T , without the transducer attached. The point impulse response will be denoted $T_i(\underline{r}, t)$, $\underline{r} \in S_T$, and is defined as the voltage at time t produced from the transducer by a displacement which, without the transducer present, would have been a δ -function at point \underline{r} in the i -direction at time zero. Under this definition, the voltage at time t due to an infinitesimal source is:

$$V(t) = \iint_{S_T} T_i(\underline{r}, t-t') G_{ij,k'}(\underline{r}, \underline{r}', t'-t'') \overline{\Delta \sigma_{jk}}(t'') d\underline{r} dt'' \quad (2)$$

This equation for a point transducer simply has the form of a convolution between the source function, the impulse response of the body, and that of the transducer. In the frequency domain the convolutions become products and so we can write that the complex (but scalar) voltage as a function of frequency ω :

$$V(\omega) = T_i(\omega)G_{ij,k'}(\omega)\overline{\Delta\sigma}_{jk}(\omega). \quad (3)$$

It is important to note that under this definition of transducer sensitivity, the impulse response $T_i(t)$ is a vector quantity. The output depends both on the magnitude and direction of the surface displacement. Normally it is assumed that sensitivity exists only for one displacement direction reducing the formulation to a scalar one. Schemes for vector transducer calibration are emerging which can determine the full vector impulse response⁹.

2.2.2 Transducer Spectral Sensitivity.

Examination of equation (3) indicates that information is transmitted independently, frequency by frequency, from the source to the observed voltage signal. Thus, the detectability of an acoustic emission signal is a frequency dependent concept and is determined by the signal:noise ratio at each frequency, or band of frequencies. It is obviously very dependent upon the frequency dependence of the transducer. In Table 1 we list the estimated smallest detectable signals (sensitivities) in a typical laboratory background noise environment.

TABLE 1

BANDWIDTHS AND MINIMUM DETECTABLE SIGNALS FOR A.E. TRANSDUCERS

Transducer type	Passband (MHz)	Sensitivity
Air gap capacitor	DC - 50	10^{-12} m
Electromagnetic Acoustic	0.5 - 15	$1-2 \times 10^{-4}$ ms ⁻¹
Damped PZT	0.1 - 2	10^{-13} m
Resonant PZT	0.1 - 0.3	10^{-14} m

Common types of transducers used for quantitative acoustic emission measurements are damped PZT or air gap capacitors. Both are principally displacement sensitive with sensitivities of 10^{-13} and 10^{-12} m respectively. Other, more sensitive, but narrower bandwidth transducers are frequently used for source detection and location work in the field. Some piezoelectric transducers and all electromagnetic acoustic transducers (EMAT's) respond to surface velocity. For an EMAT, the smallest detectable velocity is $\sim 0.1-0.2$ mm.s⁻¹, and a piezoelectric device might be 1-2 orders of magnitude more sensitive.

2.2.3 Detectability Criteria.

With these sensitivities in hand, we can now attempt to delimit the concept of detectable acoustic emission sources. For the purpose of the present discussion, we shall assume point-like transducers located in the far-field of the source on the surface of a half-space. Examination of the Green's tensor components, $G_{jk,l}$, for a linear elastic isotropic half-space show that for a source at a distance x_3 perpendicular to the surface at which the transducer is attached, the waveform is dominated by longitudinal and transverse

wavefront arrivals with $\dot{\delta}(t)$ form (. here implies time derivative).
It can be shown that:

$$G_{jk,l}(t) \sim \frac{\delta_{l3}}{2\pi\rho x_3} \left(\frac{\delta_{j3} \delta_{k3} \delta(t-x_3/a)}{a^3} + \frac{(\delta_{jk}-\delta_{j3}\delta_{k3}) \delta(t-x_3/c)}{c^3} \right) \quad (4)$$

where a and c are the longitudinal and transverse wave speeds respectively and δ_{jk} is Kronecker's delta (1 for $j = k$ and 0 otherwise).

Substituting equation (4) into equation (2) and assuming the source is of infinitesimal size with $\delta(t)$ time dependence allows us to simply deduce the epicenter displacement waveform. In order to achieve detectability the maximum value of this signal must exceed the minimum displacement sensitivity, i.e.,

$$d_j \leq \frac{\kappa(\tau)}{2\pi\rho x_3} \max_{t > 0} \left[\frac{\delta_{j1}}{c^3} \dot{\Delta\sigma}_{13}(t-x_3/c) + \frac{\delta_{j2}}{c^3} \dot{\Delta\sigma}_{23}(t-x_3/c) + \frac{\delta_{j3}}{a^3} \dot{\Delta\sigma}_{33}(t-x_3/a) \right] \quad (5a)$$

or

$$v_j \leq \frac{\kappa'(\tau)}{2\pi\rho x_3} \max_{t > 0} \left[\frac{\delta_{j1}}{c^3} \ddot{\Delta\sigma}_{13}(t-x_3/c) + \frac{\delta_{j2}}{c^3} \ddot{\Delta\sigma}_{23}(t-x_3/c) + \frac{\delta_{j3}}{a^3} \ddot{\Delta\sigma}_{33}(t-x_3/a) \right] \quad (5b)$$

where d_j represents the smallest detectable displacement and v_j the smallest detectable velocity, both in direction x_j .

Since no transducer is of broader band than all microscopic acoustic emission sources, we have introduced factors $\kappa(t)$ and $\kappa'(t)$

which account for transducer filtering. Here, τ is the source duration, and if the transducer is of constant sensitivity from DC- $1/\tau$, κ and κ' are unity. They will be less than unity for transducers with bandwidths smaller than that of the source.

To estimate the value of $\kappa(t)$ for a real transducer let us assume the displacement pulse to be detected is of Gaussian form to which we assign a width τ and magnitude M , i.e.,

$$u(t) = M \exp[-t^2/\tau^2] \quad (6a)$$

with Fourier Transform

$$u(\omega) = M\tau\sqrt{\pi} \exp[-\omega^2\tau^2/4] \quad (6b)$$

Let us assume that the response spectrum of the displacement transducer is Gaussian with bandwidth B by which we mean:

$$R(\omega) = k \exp[-\omega^2/4B^2] \quad (7)$$

where k is a normalization constant and $R(\omega)$ is the voltage produced from a c-w excitation of frequency ω . To determine k we assume that the transducer will produce a signal of magnitude 1, independent of B , if the input is a constant in time of magnitude 1. Thus, if $u(t)=1$, so that $u(\omega)=2\pi\delta(\omega)$, then the response is $2\pi k\delta(\omega)$, whence $k=1$. This is equivalent to $R=1$ at $\omega = 0$ or $\int R(t)dt=1$.

The output from such a transducer has the frequency spectrum $M\tau\sqrt{\pi} \exp[-\omega^2/4B^2] \exp[-\omega^2\tau^2/4]$ whose time response is

$$\frac{M\tau B}{\sqrt{1 + B^2\tau^2}} \exp[-t^2B^2/(1 + B^2\tau^2)]$$

a Gaussian whose peak at $t = 0$ has been reduced by the factor of $\tau B / \sqrt{1 + B^2 \tau^2}$. Therefore, we define

$$\kappa(\tau) = \tau B / \sqrt{1 + B^2 \tau^2} \quad (8)$$

To find $\kappa'(\tau)$ for a velocity sensitive transducer, we shall use a differentiating filter of the form $k\omega \exp[\omega^2/4B^2]$ where, as above, it can be shown that normalizing using a time function of constant slope 1 gives $k=-i$. Again we use the time function given in (6) whose maximum derivative, $\sqrt{(2/e)} M/\tau$ occurs at $t = \pm \tau/\sqrt{2}$. After filtering, with the differentiation filter, we have a frequency spectrum $-iM\tau\omega\sqrt{\pi} \exp[-\omega^2(1 + B^2 \tau^2)/4B^2]$ whose inverse transform is $M\tau B / \sqrt{1 + B^2 \tau^2} d/dt (\exp[-t^2 B^2 / (1 + B^2 \tau^2)])$. The maximum derivative for this time response is $\sqrt{(2/e)} M\tau^2 B^2 (1 + B^2 \tau^2)$ occurring at $t = \pm \sqrt{B/2(1 + B^2 \tau^2)}$.

Thus,

$$\kappa'(\tau) = \frac{\tau B^2}{1 + B^2 \tau^2} \quad (9)$$

2.2.4 Source Directivity

The final factor affecting detectability is the directionality (or directivity) of the source. In linear isotropic elastic materials the stress change tensor is symmetric i.e., $\Delta\sigma_{ij} = \Delta\sigma_{ji}$. We can therefore, use a representation quadric to describe the directivity of the source.

Let the stress drop tensor be represented by its principal values $\lambda_1, \lambda_2,$ and λ_3 ($|\lambda_1| < |\lambda_2| < |\lambda_3|$) along principal directions $\underline{e}_1, \underline{e}_2$ and \underline{e}_3 . Then the equation of the directivity surface is:

$$\lambda_1 e_1^2 + \lambda_2 e_2^2 + \lambda_3 e_3^2 = 1. \quad (10)$$

In terms of the regular axes, $x_i, \underline{e}_i = E_{ij} \underline{x}_j$ where E is an orthogonal

matrix with $E^t = E^{-1}$ whose components E_{ij} are the cosine of the angle between e_j and x_j . Thus, the three stress change components, $\dot{\Delta\sigma}_{i3}$ (or $\dot{\Delta\sigma}_{i3}$) are given by:

$$\dot{\Delta\sigma}_{i3} = E_{ji} \lambda_j E_{j3} . \quad (11)$$

First let us consider the stress change component, $\dot{\Delta\sigma}_{33}$, that causes out of plane motion at epicenter.

$$\begin{aligned} \dot{\Delta\sigma}_{33} &= \lambda_1 E_{13}^2 + \lambda_2 E_{23}^2 + \lambda_3 E_{33}^2 \\ &= \Lambda + (\lambda_1 - \Lambda) E_{13}^2 + (\lambda_2 - \Lambda) E_{23}^2 + (\lambda_3 - \Lambda) E_{33}^2, \end{aligned} \quad (12)$$

where $\Lambda = (\lambda_1 + \lambda_2 + \lambda_3)/3$ gives the dilatational component of the stress drop tensor. Thus, the directivity pattern for $\dot{\Delta\sigma}_{33}$ contains an omnidirectional term (Λ) and terms which are proportional to the square of the cosine of the angle between the e_j and x_3 axes. The maximum value in this pattern is λ_3 and occurs when the e_3 axis points in the x_3 direction. Should two of the principal stresses be of opposite sign, there will exist orientations for which there is no vertical motion at the epicenter surface due to $\dot{\Delta\sigma}_{33}$. Provided all three principal stresses are of the same sign, there will then always be a non-zero minimum vertical motion whose magnitude will be determined by the smallest principal stress, λ_1 .

The analysis of directivity for either of the stress change components $\Delta\sigma_{13}$ or $\Delta\sigma_{23}$, that produce in-plane epicenter motion is

similar. Thus, we only consider $\dot{\Delta\sigma}_{13}$:

$$\begin{aligned}
 \Delta\sigma_{13} &= \lambda_1 E_{13} E_{11} + \lambda_2 E_{23} E_{21} + \lambda_3 E_{33} E_{31} \\
 &= (\lambda_1 - \lambda_3) E_{13} E_{11} + (\lambda_2 - \lambda_3) E_{23} E_{21} \\
 &= (\lambda_1 - \lambda_2) E_{13} E_{11} + (\lambda_3 - \lambda_2) E_{33} E_{31} \\
 &= (\lambda_2 - \lambda_1) E_{23} E_{21} + (\lambda_3 - \lambda_1) E_{33} E_{31}
 \end{aligned} \tag{13}$$

The latter three equalities following from the orthogonality of \underline{x}_1 and \underline{x}_3 . The maximum in-plane motion at epicenter is determined by the maximum of the three quantities $|\lambda_1 - \lambda_2|$, $|\lambda_1 - \lambda_3|$ and $|\lambda_2 - \lambda_3|$. Suppose $|\lambda_i - \lambda_j|$ is largest, and the direction orthogonal to both \underline{e}_i and \underline{e}_j is \underline{e}_k . Then, the maximum epicenter motion will be obtained when $\underline{x}_2 = \underline{e}_k$, and \underline{e}_i and \underline{e}_j are in the $\underline{x}_2 = 0$ plane at $\pm 45^\circ$ to the \underline{x}_1 axis. The magnitude of the maximum radiation for equation (13) is $\pm |\lambda_i - \lambda_j|/2$ and is polarized in the \underline{x}_1 direction. Should two of the principal stresses be identical, then there will exist an orientation in which there is no horizontally polarized motion anywhere in the x_1, x_2 plane. If all three principal stress values differ, then there is always a horizontally polarized component in the x_1, x_2 plane, and this component is greater than $\min |\lambda_i - \lambda_j|/2$.

2.3 Microscopic Dislocation Sources

2.3.1 Detectability.

The stress change ($\Delta\sigma_{kl}$) or dipole tensor (D_{kl}) created by the formation of a dislocation loop in a linear elastic body has been evaluated by Eshelby¹⁰, Kroner¹¹, Kroupa¹² and Burridge and Knopoff¹³. The latter developed a simple relation between the dipole tensor and the dislocation Burgers vector together with the dislocation loop normal:

$$D_{kl}(t) = C_{ijkl} b_i A_j(t) \quad (14)$$

Here C_{ijkl} are the elastic stiffness constants, b_i are the components of the dislocation Burgers vector and $A_j(t)$ the projected swept out area on the plane whose normal is in the x_j direction.

For the case of isotropic elasticity:

$$C_{ijkl} = \lambda \delta_{ij} \delta_{kl} + \mu (\delta_{ik} \delta_{jl} + \delta_{il} \delta_{jk}) \quad (15)$$

where λ and μ are Lamé constants, which are related to the longitudinal and transverse wavespeeds:

$$\rho a^2 = \lambda + 2\mu \quad (16a)$$

$$\rho c^2 = \mu \quad (16b)$$

where ρ is the density.

To determine detectability criteria for a dislocation source, consider the case of the formation of a planar dislocation loop on a plane with normal \underline{n} at a depth r in a half space, Fig. 3a. Using expression 5a for the displacement detectability at epicenter we obtain:

$$2\pi x_3 d_j < \kappa(\tau) \left[\frac{2c^2 b_3 n_3}{a^3} \delta_{j3} + \frac{(b_1 n_3 + b_3 n_1) \delta_{j1} + (b_2 n_3 + b_3 n_2) \delta_{j2}}{c} \right] \max_t \dot{A}(t) \quad (17)$$

Similarly, the velocity detectability at epicenter is given by:

$$2\pi x_3 d_j < \kappa'(\tau) \left[\frac{2c^2 b_3 n_3}{a^3} \delta_{j3} + \frac{(b_1 n_3 + b_3 n_1) \delta_{j1} + (b_2 n_3 + b_3 n_2) \delta_{j2}}{c} \right] \max_t \ddot{A}(t) \quad (18)$$

where $\kappa(t)$ and $\kappa'(t)$, as given by equations (8) and (9), account for filtering by the transducer. If \underline{b} , \underline{n} , and \underline{x}_3 are coplanar, these expressions can be more simply expressed in terms of twice the angle between \underline{n} and the x_1, x_2 plane.

The first term on the right hand side in (17) and (18) corresponds to the out-of-plane (normal) motion at epicenter associated with the arrival of a longitudinal wave, while the second term corresponds to in-plane (tangential) motion (parallel to the projection of the Burgers vector) at epicenter associated to the arrival of a shear wave. It is of interest to note that while acoustic emission due to the latter, in-plane, motion is sensitive to the Burgers vector and slip plane orientation, it is not, to first order, sensitive to the direction of dislocation motion; that is, it cannot distinguish between edge dislocations slipping in one direction and screw dislocations slipping in the perpendicular direction.

The greatest sensitivity to dislocation motion is obtained from an in-plane sensitive transducer with its poling axis aligned with the Burgers vector direction from dislocations slipping in the horizontal plane, or from dislocations slipping in a vertical plane with vertical Burgers vector and with the poling axis of the

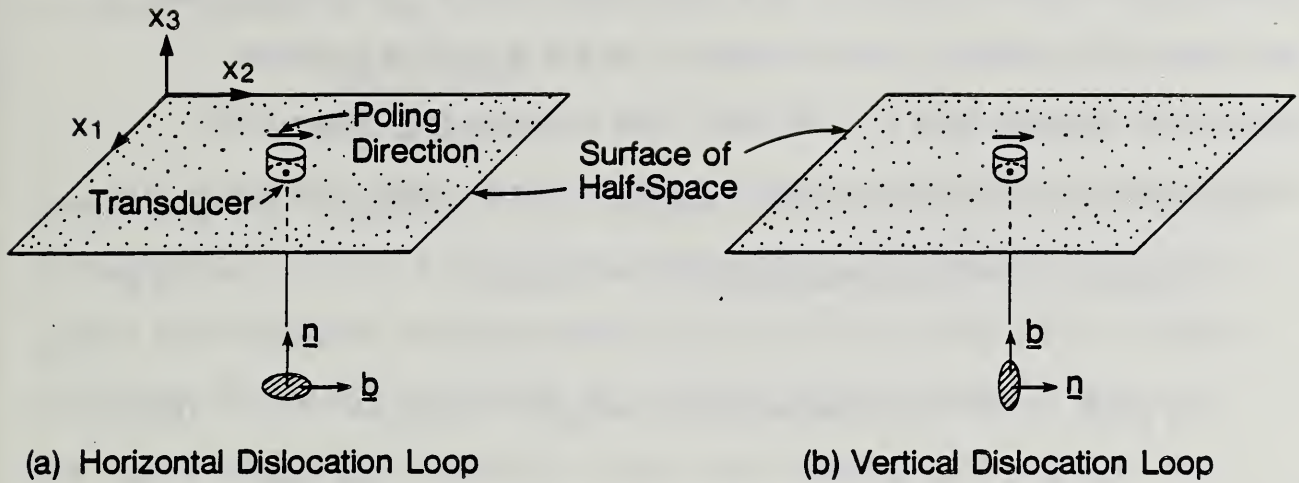


Fig. 3. The strongest horizontal displacement from an infinitesimal dislocation occurs either when (a) \underline{b} is coplanar and \underline{n} perpendicular to the surface or (b) vice versa.

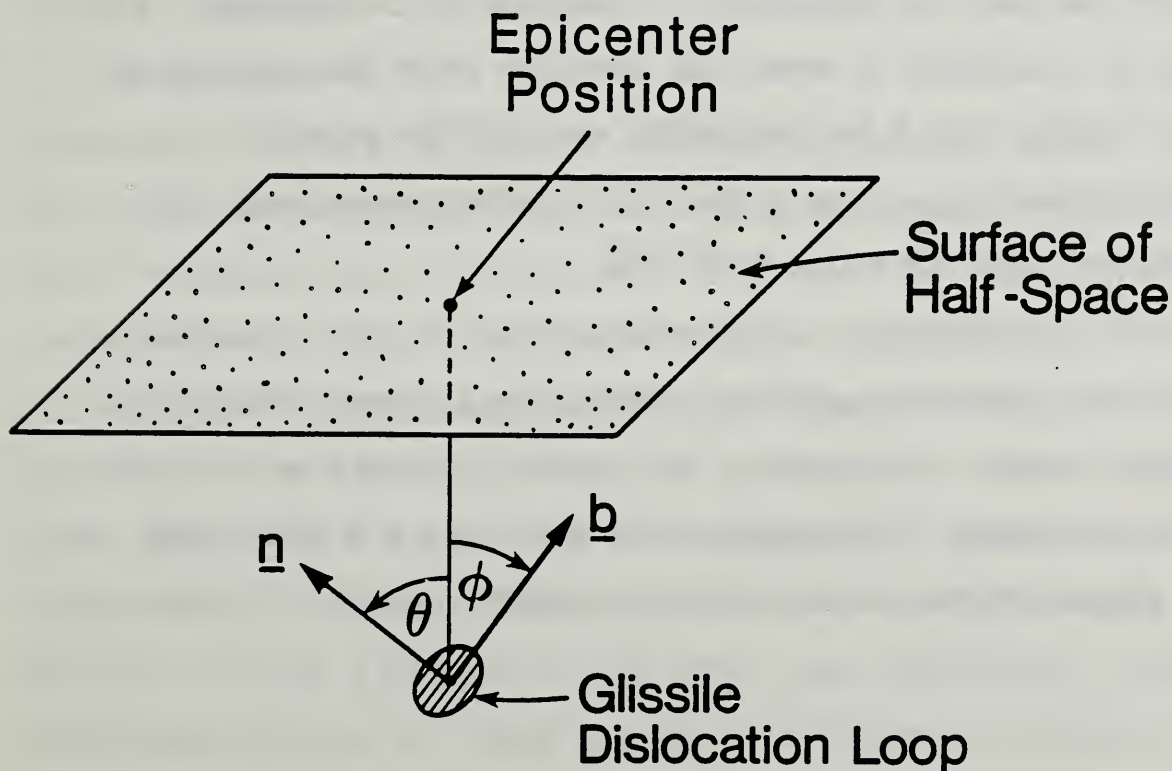


Fig. 4. An inclined dislocation loop buried in an isotropic elastic half-space.

transducer aligned normal to the slip plane, Fig 3. In either case, if we set $a=6.4 \text{ mm}\mu\text{s}^{-1}$, $c=3.2 \text{ mm}\mu\text{s}^{-1}$, $b=2.9 \times 10^{-10} \text{ m}$ (typical aluminum values) and $r = 40 \text{ mm}$, the detectability criteria for horizontally sensitive transducers become (from eqs (17) and (18)):

$$d_j \leq 3.6 \times 10^{-10} \kappa(\tau) \max_t [\dot{A}(t)] \text{ mm} \quad j = 1,2 \quad (19)$$

$$v_j \leq 3.6 \times 10^{-10} \kappa'(\tau) \max_t [\ddot{A}(t)] \text{ mm}\mu\text{s}^{-1} \quad j = 1,2 \quad (20)$$

If, for instance, the horizontal (d_1, d_2) displacement detection threshold is 10^{-14} m and B is 5 MHz , then $\kappa(\tau) \sim 0.035$ for a dislocation that propagated for a time $\tau = 15 \text{ ns}$. Then the dislocation loop would have to have a radial velocity of $3 \text{ mm}\mu\text{s}^{-1}$ expanding to a $45 \mu\text{m}$ radius in order to be detectable. Such a calculation highlights the often neglected importance of transducer bandwidth (as well as sensitivity) in determining detectability. For instance, it is possible to show that detection could be achieved for a $1.5 \mu\text{m}$ radius loop if the bandwidth were infinite provided dislocation speeds are close to the limiting shear wavespeed. In fact, if $\tau B \ll 1$, $\kappa(\tau) \sim \tau B$ and $\tau \sim 1/r\sqrt{18\pi B}$.

While the dislocation configurations shown in Fig. 3 produce the maximum horizontal epicenter displacements, they produce no out-of-plane motion. If, however, the source is rotated so that the first term in equation (17) becomes non zero for $j = 3$, then finite vertical displacements are produced at epicenter (Fig. 4). For the

situation shown in Fig. 4;

$$b_3 = b \cos \phi$$

$$n_3 = \cos \theta$$

where b is the magnitude of the Burgers vector and \underline{n} the unit normal to the plane of slip. For a glissile dislocation, \underline{b} is perpendicular to \underline{n} and the maximum displacement occurs at $\theta = \phi = 45^\circ$. It is 1/8 the maximum horizontal amplitude for a horizontal or vertical loop of the same radius and velocity. Thus, the detectability criterion is:

$$d_3 \leq 0.45 \times 10^{-10} \kappa(\tau) \max_t [\dot{A}(t)] \text{ mm} \quad (21)$$

$$v_3 \leq 0.45 \times 10^{-10} \kappa'(\tau) \max_t [\ddot{A}(t)] \text{ mm}\mu\text{s}^{-1} \quad (22)$$

If a transducer is used with 10^{-14} m displacement sensitivity and bandwidth such that $\kappa(t)$ is always unity, then the detectability criteria becomes:

$$r\dot{r} \geq 0.03 \text{ m}^2\text{s}^{-1} \quad (23)$$

Detectability criteria for velocity sensitive transducers depend upon the transducers sensitivity i.e., its smallest detectable velocity, and upon the acceleration of the source. At present, only very crude estimates exist for the former (even though it appears some conventional AE transducers are at least partially velocity sensitive). The acceleration history of a dislocation is even less clear, and will be extremely mechanism dependent. Small changes of temperature, composition, heat treatment, cold work, grain size, etc. can all have a potentially large effect upon acceleration. While this shows promise for those interested in fundamental studies of the dynamics of dislocations (as well as cracks and phase

transformations), it raises serious questions about reliability of such transducers for source detection and characterization in NDE applications.

Restricting further discussion to displacement detectability criteria only, we see that, from equation (23), $r\dot{r} \geq 0.03 \text{ m}^2\text{s}^{-1}$ for $x_3=40 \text{ mm}$ and aluminum physical property values. Unstable dislocation motion in polycrystalline metals is likely to proceed at velocities \dot{r} of 0.1 to 1 times the shear wavespeed (i.e. $\sim 300\text{-}3,000 \text{ ms}^{-1}$). Thus a single dislocation propagating $10\text{-}100 \text{ }\mu\text{m}$ is potentially detectable. This is indicative of the extraordinary sensitivity of acoustic emission instrumentation. The distance of dislocation propagation is, however, strongly influenced by microstructure, as will be discussed below, and not all dislocation motion is detectable.

One further factor can have a very important effect upon detectability, and this is the possibility for cooperative slip involving simultaneous motion of large numbers of dislocations. These "microyield" phenomena typically involve thousands of dislocations simultaneously moving on the same slip system. If the dislocations are closely spaced (c.f. the shortest wavelength of observation), and if they move synchronously, then their emitted wavefields add. The detectability criterion then becomes

$$nr\dot{r} \geq 0.03 \text{ m}^2\text{s}^{-1} \quad (24)$$

where n is the number of moving dislocations. This criterion is very easy to satisfy for many metals, especially near the onset of general yield.

2.3.2 Single Crystal Deformation

The most well understood case of plastic deformation is that of a single crystal oriented for initially single slip. This has been the starting point for studies of acoustic emission by a number of groups¹⁴⁻¹⁶. A typical experimental result is shown in Fig. 5 for high purity aluminum¹⁴. In the experiment, the sample was deformed at a relatively slow constant strain rate of $\sim 10^{-4} \text{ s}^{-1}$ and acoustic emission in the 0.1-1.0 MHz frequency range recorded with a principally vertical displacement sensitive transducer ($\sim 10^{-14} \text{ m}$ sensitivity) located on the tensile axis. The acoustic emission in this experiment was first detected during nominal elastic loading and reached a maximum intensity after straining about 2% beyond general yield. Beyond this point, acoustic emission decreased, even though the slip per unit time (strain rate) remained essentially constant. Other studies by Fleischman et al,¹⁶ indicate that the strain at which the maximum occurs is bandwidth sensitive, and occurs at higher strains when larger bandwidths are used.

For an explanation of this behavior, it is necessary to consider the microscopic nature of slip. In an *fcc* single crystal slip tends to occur in $\langle 110 \rangle$ directions on the closed packed $\{111\}$ planes. There are many possible slip systems that could be activated by the application of stress -- typically, the system with highest resolved shear stress in the slip direction will be activated. If in Fig. 4 the stress is normal to the surface (σ_{33}), then the system with $\cos\theta \cos\phi$ closest to 0.5 will be the first activated; that is the system for which $\theta \sim \phi \sim 45^\circ$. Thus, we expect these dislocations to generate

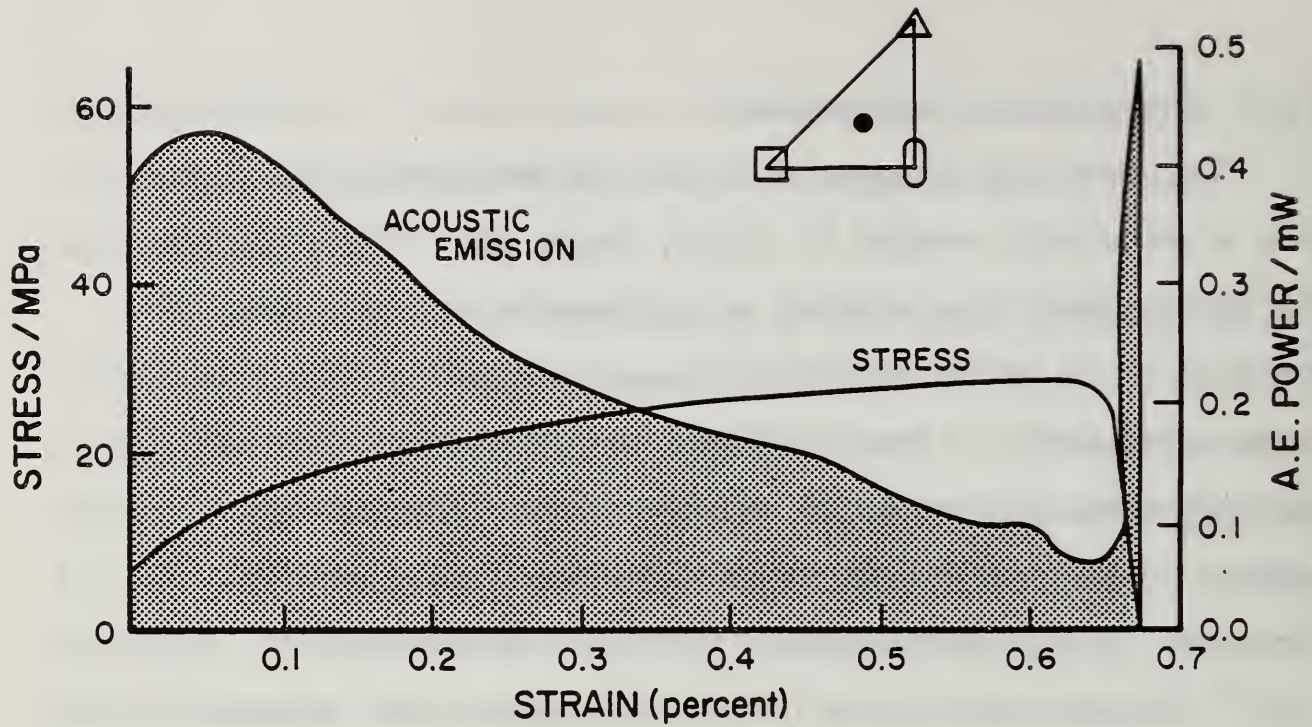


Fig. 5. The variation of acoustic emission with stress and strain for a high purity aluminum single crystal undergoing constant strain rate uniaxial tensile deformation. The measurements were made over a frequency band of 0.1 - 1.0 MHz with an amplification of 98 dB.

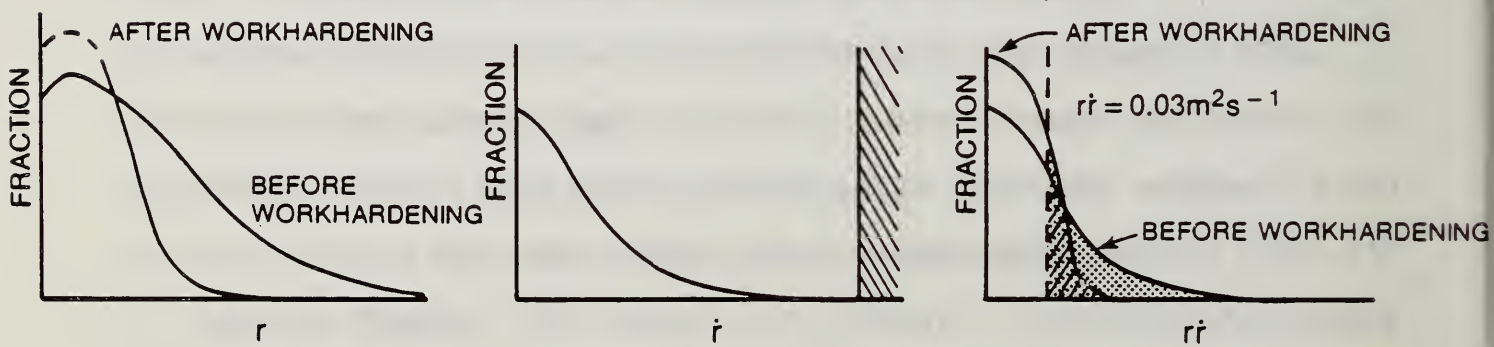


Fig. 6. Schematic diagrams of (a) the hypothetical slip distance distribution, (b) the velocity distribution and (c) the distribution of the \dot{r} product. Only events for which $\dot{r} \geq 0.03 \text{ m}^2 \text{ s}^{-1}$ generate detectable acoustic emission. In pure metals this occurs more frequently before workhardening begins.

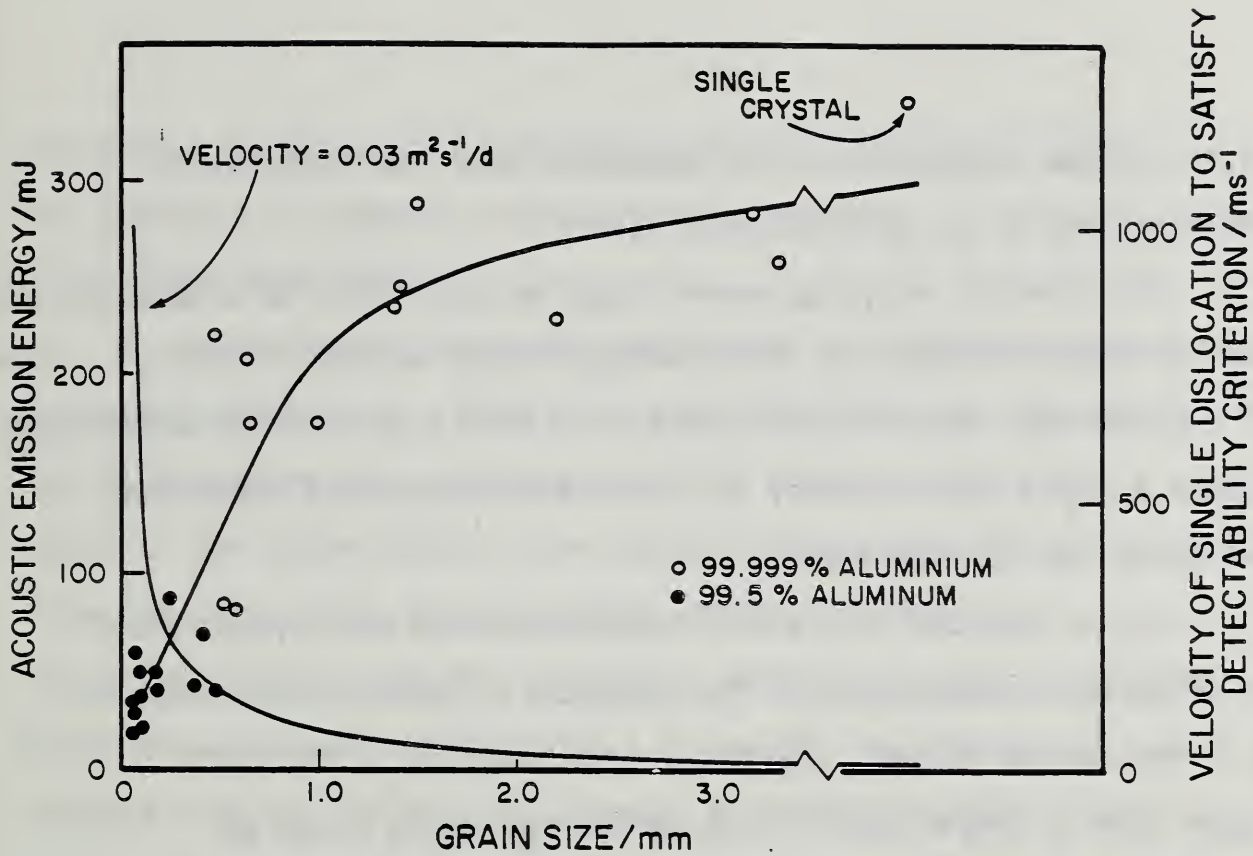


Fig. 7. The integrated acoustic emission power (energy) for polycrystalline aluminum decreases with decreasing grain size. Also shown is the necessary dislocation velocity for a single dislocation to generate a detectable acoustic emission signal.

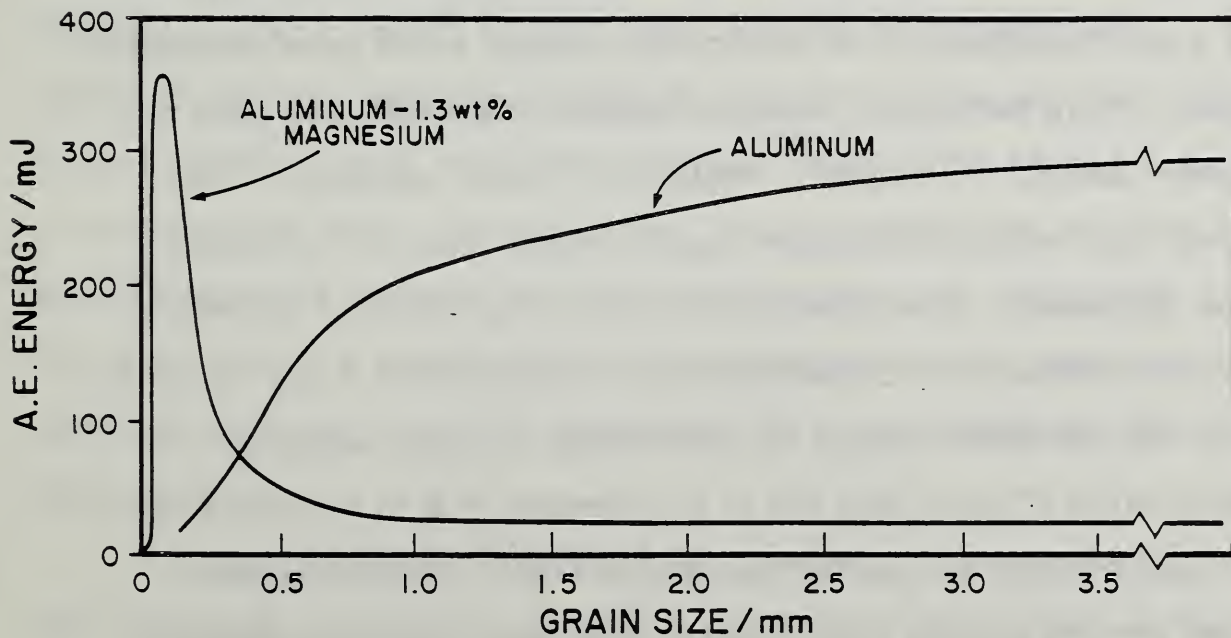


Fig. 8. A comparison of the grain size dependence of acoustic emission for high purity aluminum and an Al-Mg alloy solid solution. The effects of Mg are to enhance the emission at small grain size and suppress it at large grain size.

finite vertical displacements at epicenter and the detectability criterion (24) to be valid provided $\kappa(t)=1$.

For example, a typical event might be the motion of a dislocation to form a $150\mu\text{m}$ radius loop at an average radial velocity of 300ms^{-1} . Then $\dot{r} = 0.045 \text{ m}^2\text{s}^{-1}$ and $\tau B \sim 0.5 \times 10^{-6}\text{s} \times 10^6 \text{ Hz} \sim 1.0$ so that the event should create a signal approximately 1.5 times the background noise and, therefore, be just detectable.

Let us suppose that a is a large fraction of the crystal radius (a reasonable supposition at the initiation of plastic deformation of a perfect single crystal), say about 1mm , then for a detectable signal from a single loop, \dot{r} must be $\sim 35 \text{ ms}^{-1}$ which is not an unreasonable value to expect. In practice, both r and \dot{r} for slip events are statistically distributed, Fig. 6, and only those events whose $n\dot{r}$ products are at the extreme right of the distribution generate detectable events. At the initiation of deformation a substantial fraction of slip events may propagate sufficiently far that even moderately slow dislocation groups would give detectable signals. Work hardening, however, reduces the mean free path between sessile dislocations, restricting r and resulting in few events that radiate detectable elastic waves; thus the emission power decreases. At a strain of $\sim 2\%$ and a bandwidth of $\sim 2 \text{ MHz}$, a maximum emission is observed which indicates this is the strain at which the greatest fraction of deformation events satisfy the criteria $n\dot{r} > 0.03 \text{ ms}^{-1}$ and $\kappa(t) = 1$. However, if B is increased, $\kappa(t)$ can tend to unity for shorter duration events. Shorter duration events tend to become more numerous as work hardening develops

(because r decreases and $\dot{\epsilon}$ remains constant or increases), and so the maximum in emission shifts to higher strain¹⁶.

2.3.3 Grain Size Effects

It is well known that grain boundaries are effective barriers to moving dislocations. Thus in a polycrystalline metal the distance that a dislocation loop can expand will, at most, be that of the radius of the largest grain in the sample. The distribution of slip distances over some range of plastic strains will now be a complicated function of the grain size distribution and grain interior dislocation-dislocation interactions. It seems reasonable to suppose that, at the initiation of slip, a substantial fraction of moving dislocations will propagate over a distance equal to about the mean grain diameter.

As the grain size is reduced, the critical velocity of a single dislocation required to give a detectable signal increases. For example, for a mean grain diameter of 1mm, $\dot{\epsilon} \approx 35 \text{ ms}^{-1}$ while, for a diameter of about $35 \mu\text{m}$, $\dot{\epsilon} \approx 1000 \text{ ms}^{-1}$. In *fcc* pure metals we expect dislocation velocities of several hundred meters per second so that emission from small-grain material must come from groups of cooperatively moving dislocations. The probability that enough dislocations move together to give a detectable signal decreases with grain size. A disappearance of detectable acoustic emission has been observed, Fig. 7, by several groups in agreement with the above model.

A note of caution should be given, however. Some workers¹⁷ have observed an apparent increase, at very small grain sizes, in the acoustic emission. Up to the present time this controversial

observation has not been fully resolved. If the observations are ultimately confirmed, they may be linked to an increase in the yield stress with decreasing grain size which increases the average dislocation velocity.

In alloys of aluminum, substitutional impurity segregation to dislocations can occur, even when the alloy element concentration is below the solid solubility limit. This drastically alters the dynamics of dislocations and leads to effects such as yield points, Luders' band propagation and dynamic strain aging during mechanical deformation. The occurrence of these phenomena is almost invariably accompanied by intense acoustic emission signals. Both the incidence of the effects themselves and their associated acoustic emission signals vary greatly with grain size; see for example Fig. 8 where the acoustic emission energy is plotted as a function of grain size for an Al-1.3wt.%Mg alloy solid solution and compared with the result for aluminum.

The peak in the acoustic emission of the solid solution at a grain size of around 80 μm arises from a competition between two effects; as the grain size increases, the duration, τ , increases but $\dot{\epsilon}$ decreases. The velocity decrease occurs because of the fall in flow stress with increasing grain size and, for grain sizes greater than about 500 μm , the yield stress is insufficient to separate mobile dislocations from the cloud of impurity atoms (Cottrell atmosphere) segregated to their core¹⁴. This results in the drift-controlled motion of dislocations at velocities too low to give acoustic emission, even though propagation distances may be greater than

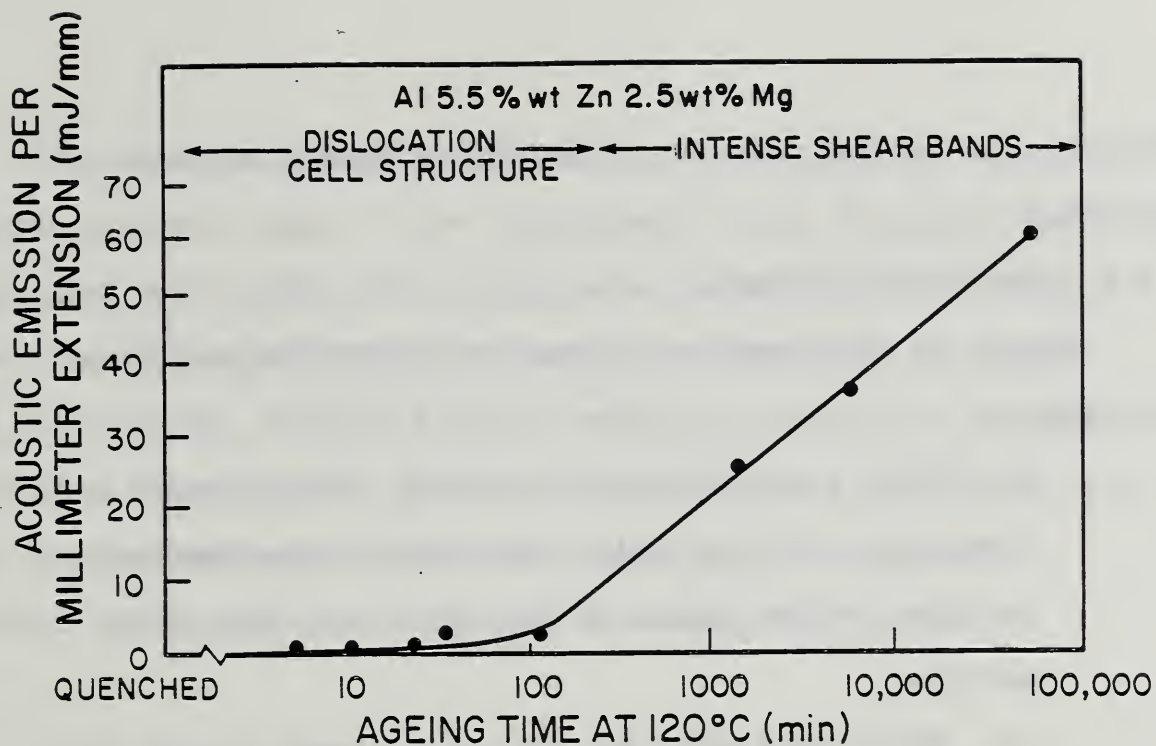


Fig. 9. Ageing supersaturated solid solutions (in this case Al-5.5wt%Zn-2.5wt%Mg) may produce "shearable" precipitates which cause an "intense shear band" mechanism of slip with enhanced acoustic emission.

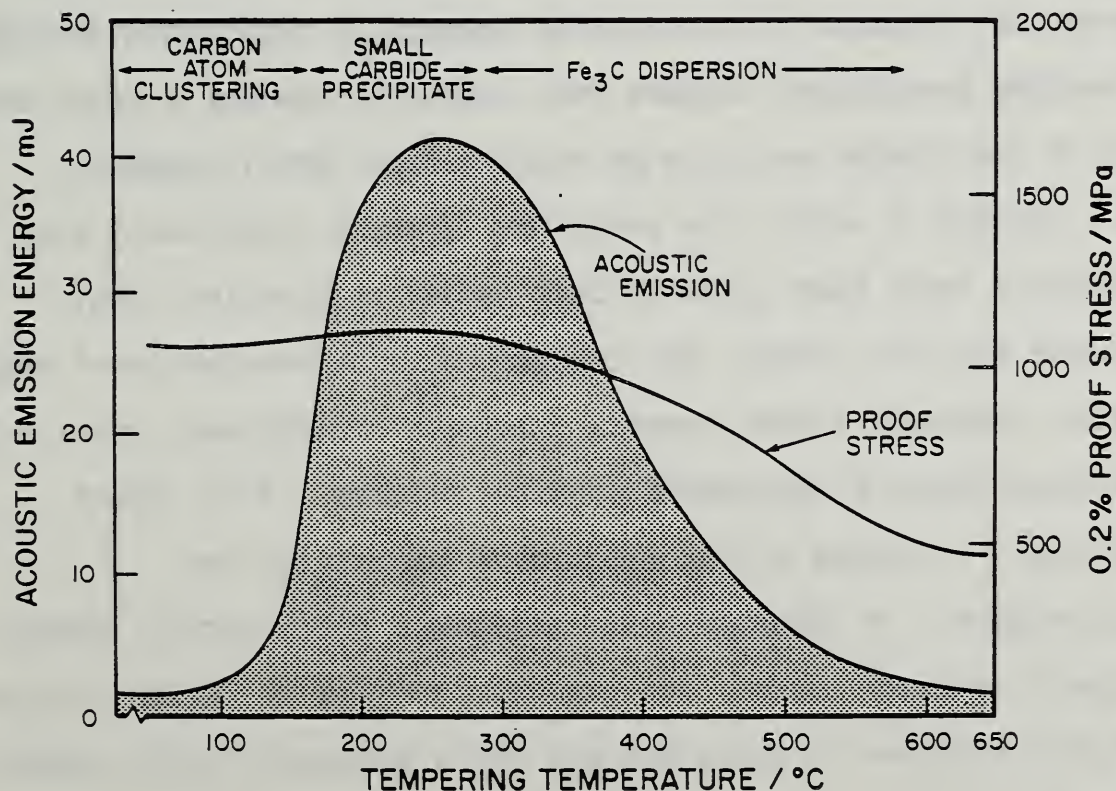


Fig 10. The acoustic emission due to plastic deformation in Fe-base (in this case Fe-3.25wt%Ni-0.21wt%C) alloys is strongly influenced by tempering.

that required for the radiation of detectable signals in pure aluminum.

2.3.4 Precipitation Effects

There are two extreme classes of dislocation-precipitate interaction.

(1) When the precipitates are strong, widely spaced and incoherent with the matrix, dislocations bow between particles, leaving behind a dislocation loop around the particle.

(2) When the precipitates are weak, closely spaced and coherent with the matrix, dislocations may penetrate the precipitates and shear them.

Process (1) encourages uniformly distributed slip while process (2) leads to the formation of intense slip bands. These bands form because the successive passage of dislocations through shearable precipitates reduces their strength, creating a local weak spot in the crystal and thus an ensuing local strain instability.

Studies in which the precipitate strength, distribution and coherency have been systematically varied in aluminum alloys indicate that the uniform slip process of dispersion-hardened alloys (strong relatively widely spaced incoherent precipitates) gives only moderate levels of detectable acoustic emission. This occurs because r is limited to the interparticle spacing (a few micrometers). In contrast, when precipitate shear occurs, intense acoustic emission signals are observed¹⁸⁻²⁰ Fig. 9. Similar results are also obtained in quenched and lightly tempered ferritic steels²¹ Fig. 10.

These studies serve to illustrate the complementary role that acoustic emission plays in the experimental study of plastic flow. In contrast with stress-strain measurements and hardness testing where the integrated static response of the material to an applied load is measured, acoustic emission measures that part of the slip distribution for which the criterion $n\dot{\epsilon} > 0.03 \text{ m}^2\text{s}^{-1}$ is satisfied (the high speed events), and this is very sensitive to metallurgical variables, often much more so than the stress-strain curve.

2.4 Microscopic Fracture Sources

2.4.1 Detectability

We are here concerned with the acoustic emission generated by the formation of isolated microcracks and the extension of macrocracks by the coalescence of microcracks at a cracktip. A crack can be viewed as a material inhomogeneity; thus the combination of dipole components that are equivalent to the crack depend upon the ambient stress in addition to the radius of the crack.

For infinitesimal cracks circular in shape (penny-shaped) the dipole tensor is given by:

$$D_{kl}(t) = \frac{8(1-\nu)}{3\mu(2-\nu)} C_{klmn} n_n n_q \sigma_{pq} W_{mp} r^3(t), \quad (25a)$$

where ν is Poisson's ratio, μ the shear modulus, C_{klmn} is the elastic stiffness tensor, \underline{n} is a unit vector normal to the crack face, σ_{pq} the ambient stress, r the crack radius and W_{mp} are the components of the matrix:

$$W = \begin{vmatrix} 2-n_1^2\nu & -\nu n_1 n_2 & -\nu n_1 n_3 \\ -\nu n_1 n_2 & 2-n_2^2\nu & -\nu n_2 n_3 \\ -\nu n_1 n_3 & -\nu n_2 n_3 & 2-n_3^2\nu \end{vmatrix} \quad (25b)$$

Substituting equation (25) into equation (5) gives the expression for detectability of a microcrack at a depth x_3 beneath the epicenter of a half space:

$$d_j \leq \frac{4(1-\nu)\kappa(\tau)}{\pi\rho(2-\nu)x_3} \max_{t>0} \left[(\delta_{j1} (w_1 n_3 + w_3 n_1) + \delta_{j2} (w_2 n_3 + w_3 n_2)) \frac{r^2(t-x_3/c) \dot{r}(t-x_3/c)}{c^3} + 2\delta_{j3} \left(\frac{\nu(\underline{n} \cdot \underline{w})}{1-2\nu} + w_3 n_3 \right) \frac{r^2(t-x_3/a) \dot{r}(t-x_3/a)}{a^3} \right] \quad (26a)$$

$$v_j \leq \frac{4(1-\nu)\kappa'(\tau)}{\pi\rho(2-\nu)x_3} \max_{t>0} \left[(\delta_{j1} (w_1 n_3 + w_3 n_1) + \delta_{j2} (w_2 n_3 + w_3 n_2)) \frac{2r(t-x_3/c) \dot{r}^2(t-x_3/c) + r^2(t-x_3/c) \ddot{r}(t-x_3/c)}{c^3} + 2\delta_{j3} \left(\frac{\nu(\underline{n} \cdot \underline{w})}{1-2\nu} + w_3 n_3 \right) \frac{2r(t-x_3/a) \dot{r}^2(t-x_3/a) + r^2(t-x_3/a) \ddot{r}(t-x_3/a)}{a^3} \right] \quad (26b)$$

where \underline{w} is a vector in the direction of maximum crack face displacement; i.e.,

$$w_m = 2(2-\nu)W_{mp} \sigma_{pq} n_q \quad (27)$$

If the force $\sigma_{pq} n_q$ is parallel to \underline{n} , the crack is termed mode I while if the force is in the crack plane it is mode II /III type. For these particular cases, \underline{w} is parallel to $\sigma_{pq} n_q$ (although this would not be so for mixed mode cracks since \underline{w} has differing eigenvalues of 2 and $2-\nu$ in the crack plane and perpendicular to the crack plane respectively).

The directivity pattern of the acoustic emission from a mode II/III crack is the same as that for slip (glissile) dislocations with \underline{w} assuming the role of \underline{b} . Indeed, it can be shown that the coefficients of the two horizontal ($j = 1,2$) terms in equation (26) correspond to

the projection of the vector $w_3 \underline{n} + n_3 \underline{w}$ into the x_1, x_2 plane using one projection factor, while the vertical ($j = 3$) term involves the projection of the same vector onto the x_3 axis using a different projection factor plus a vector which is independent of the position of x_3 .

The relative epicenter displacement magnitude as a function of angle for both cracks and slip dislocations is summarized in Table 2 for the case that the x_3 axis, \underline{w} (or \underline{b}) and \underline{n} are coplanar.

TABLE 2

DIRECTIONALITY FACTORS FOR δ -FUNCTION WAVEFRONT COMPONENTS FOR MODE I AND MODE II /III MICROCRACKS

SOURCETYPE	LONGITUDINAL WAVEFRONT (out of plane displacement)	SHEAR WAVEFRONT (in plane displacement)
MODE I MICROCRACK (or prismatic dislocation)	$\alpha(1-\alpha^2) + \alpha^3 \cos 2\theta$	$\sin 2\theta$
MODE II/III MICROCRACK (or slip dislocation)	$\alpha^3 \sin \phi$	$\cos 2\phi$
where	$\alpha = c/a =$ ratio of shear to longitudinal wavespeeds $\theta =$ angle between crack face (dislocation plane) normal and the x_3 axis $\phi =$ angle between the x_3 axis and \underline{w} (or \underline{b}).	

Using similar methods to those shown for dislocation sources, it is possible to determine detectability criteria for microcrack sources. As an example, suppose a vertical displacement sensitive transducer is used to detect signals from a mode I horizontal microcrack a depth x_3 below the surface. Then, $\underline{w} = (0,0,w_3)$, $\underline{n} = (0,$

0, n_3), and from equation (26a)

$$d_3 < \left[\frac{2(2-\nu) \cdot 8 \cdot (1-\nu)^2}{\pi \rho (1-2\nu) a^3} \right] \frac{\kappa(\tau) \sigma_{33} r^2 \dot{r}}{x_3} \quad (28)$$

Using physical properties of steel ($\nu = 0.29$, $\rho = 7.8 \times 10^3 \text{ Kgm}^{-3}$ and $a = 5.9 \times 10^3 \text{ ms}^{-1}$), the detectability criteria is:

$$\sigma_{33} r^2 \dot{r} > 1.6 \times 10^{14} \kappa(\tau) x_3 d_3 \text{ (mks units).}$$

Source factors favoring detectability are high ambient stress, large crack radius and fast crack speed. The criterion is affected by elastic properties so that for aluminum ($\nu = 0.34$, $\rho = 2.7 \times 10^3 \text{ Kgm}^{-3}$, $a = 6.4 \times 10^3 \text{ ms}^{-1}$): $\sigma_{33} r^2 \dot{r} \geq 0.6 \times 10^{14} \kappa(\tau) x_3 d_3$ (mks units)

It can be seen that in aluminum, cracks of only a third the area of those in steel are detectable, other conditions being equal.

In metals, the dimensions of microcracks induced by deformation are closely coupled to the dimensions of microstructure constituents such as grain size, inclusion or precipitate diameter, inter-particle spacing etc. For example, in a ferritic steel at or below its ductile to brittle transition, cleavage cracks that are typically a grain diameter in size form during deformation. Thus, within the statistical variations of the microstructure, it is possible to obtain estimates of r in equation (28). It is well known that brittle microcracks such as those associated with the cleavage described above propagate at velocities close to the limiting value of the shear wave speed while at the other extreme, ductile microvoid coalescence occurs under essentially quasi-static conditions. Thus, it is possible to estimate crude values for r in equation (28) for various fracture micromechanisms. If we assume

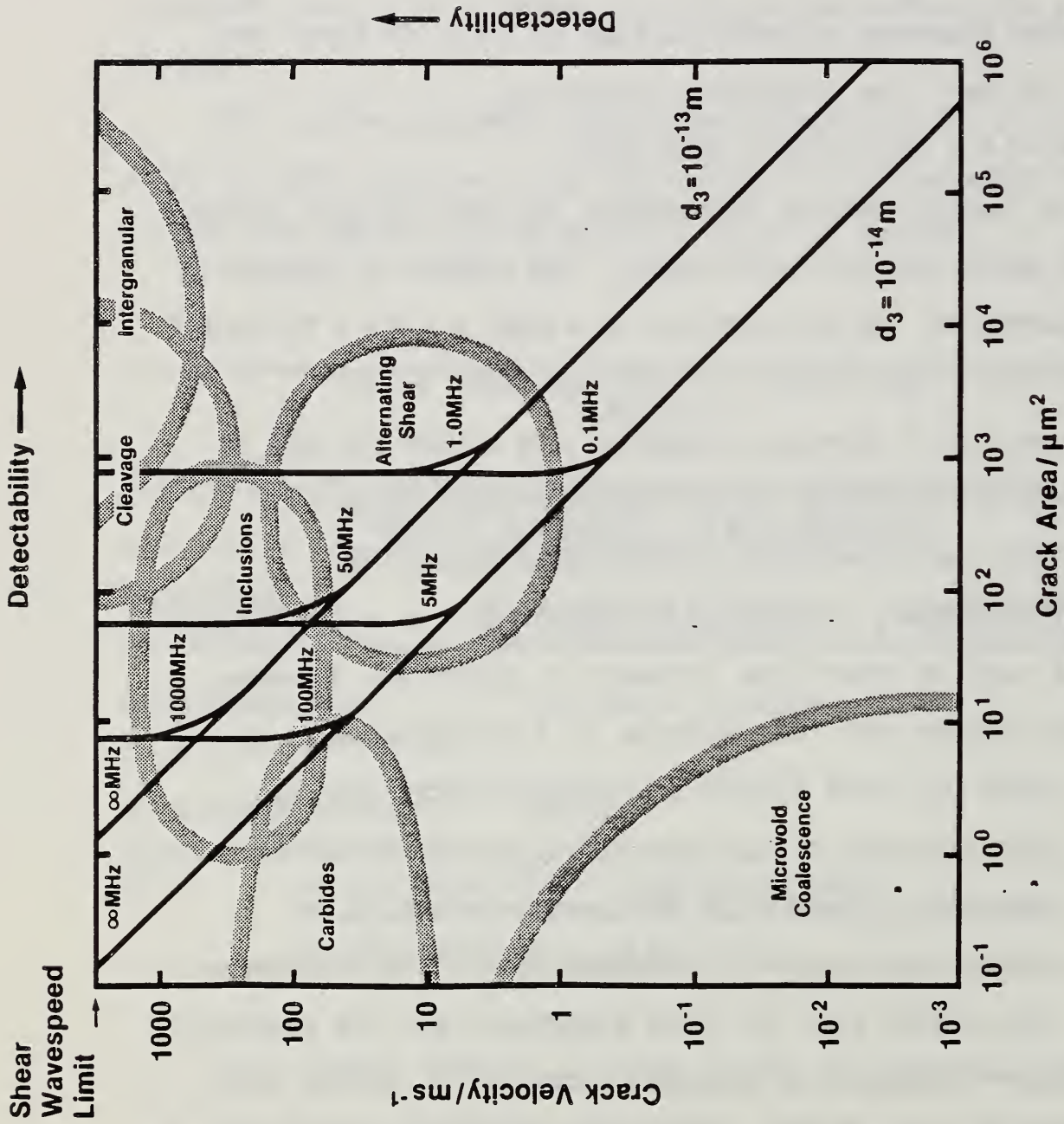


Fig. 11. An acoustic emission detectability map for the fracture micromechanisms of steel. The solid lines correspond to detectability criteria for transducers of varying sensitivity (d_3) and bandwidth (in MHz). The dotted fields are the approximate domains in r and πr^2 space for various fracture micromechanisms. Mechanisms above and to the right of a detectability line are detectable. The imposed uniaxial tensile stress is 500 MPa and the distance to the transducer is 40 mm.

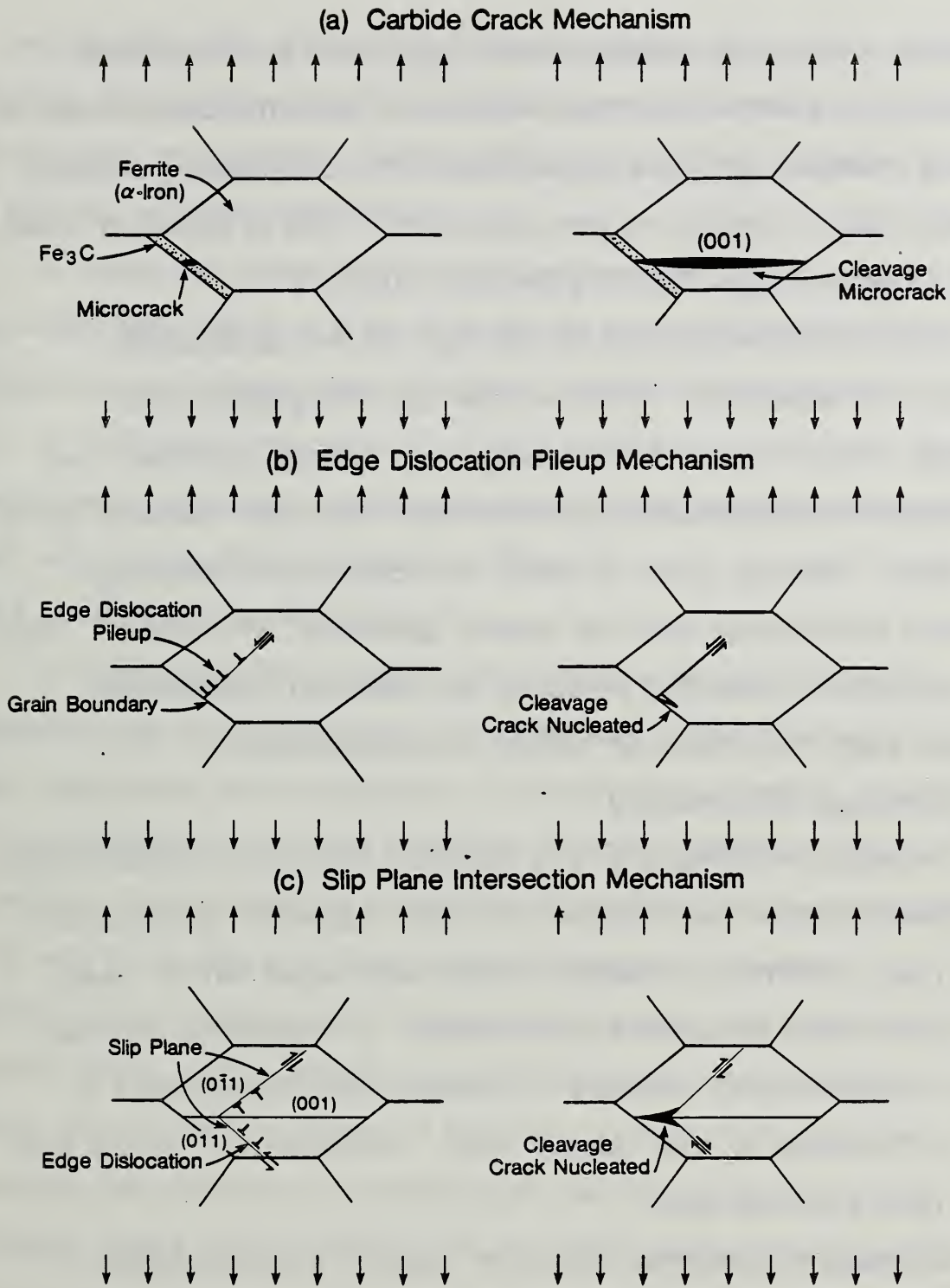


Fig. 12. Schematic diagram of three micromechanisms of cleavage crack nucleation in iron-carbon alloys. (a) nucleation by a grain boundary Fe_3C film, (b) grain boundary edge dislocation pile-up nucleation and (c) nucleation by intersection of edge dislocations on $\{011\}$ slip planes.

all events to occur at constant stress (σ_{33}) and source-receiver distance (x_3), then we can map the fields of each micromechanism on a plot of \dot{r} verses πr^2 , and superimpose the detectability criterion (equation 28) for various d_3 and $\kappa(t)$ values. This is shown for steel in Fig. 11 where $\sigma_{33} = 500$ MPa and $x_3 = 0.04$ m.

Only micromechanisms to the right of the detectability criterion are detectable. Thus we see that intergranular and cleavage brittle fracture are probably very reliably detected even with insensitive transducers provided their bandwidth extends up to ~ 1.0 MHz. However there is clearly no possibility of detecting microvoid coalescence with the current generation of sensors. Thus, the reliability of acoustic emission for detecting crackgrowth depends upon the operative fracture micromechanisms.

2.4.2 Cleavage Microfracture

Cleavage microfracture is a common fracture micromechanism in materials below their ductile to brittle transition temperature. Thus, many ceramics, refractory metals and some ferritic steels fail by this mode at ambient temperature. In composite materials where ceramic fibers, whiskers or particles are incorporated in order to reinforce a soft, ductile matrix, reinforcement failure also often occurs by cleavage.

Cleavage microcracks occur on specific crystallographic planes, $\{001\}$ for instance in Fe. They are believed to be nucleated either by pre-existing flaws (e.g. iron carbide cracks in steels), dislocation pile-ups at internal boundaries or at the intersection of slip planes, Fig 12. Very limited plasticity may accompany microcrack propagation which may thus proceed at velocities close

to that of the shear wavespeed (the theoretical upper limit). At low stresses, the cracks are often arrested at grain boundaries due to the absence of optimally oriented {100} planes in the adjacent grain at the site of crack impingement.

A horizontal microcrack in steel with $r = 10 \mu\text{m}$, $\dot{r} = 1000 \text{ ms}^{-1}$, $\sigma_{33} = 500 \text{ MPa}$ and $x_3 = 0.04 \text{ m}$ gives rise to a vertical displacement epicenter signal whose peak amplitude (equation 28) is $u_3 \sim 2.5 \times 10^{-11} \text{ m}$ and has a time scale of $\sim 10^{-5} \text{ m} + 10^3 \text{ ms}^{-1}$, i.e. 10 ns. Such a displacement signal is readily detectable under laboratory conditions even with narrow band transducers, Fig. 11.

2.4.3 Intergranular Microfracture

In many engineering alloys, grain boundaries are a site of weakness and may prematurely fail under load. This weakness is often associated with segregation of embrittling chemical species to the interface or with the formation of brittle phases at the boundary. For example, in some low alloy steels the co-segregation of Ni with P, As, Sb and Sn to grain boundaries will cause a transition from cleavage to intergranular fracture and appreciable upward shifts in the ductile to brittle transition temperature. Glassy grain boundary phases in ceramics such as Al_2O_3 are also linked to the formation of intergranular fracture in ceramics. In aluminum alloys, liquid metals such as indium and gallium promote intergranular fracture.

In these systems an intergranular crack, once nucleated, is capable of rapid propagation over considerable distances due to the absence of crack arresting features in the microstructure. Only when the crack reaches a grain boundary triple point and must

branch radically from the maximum tensile stress plane is arrest possible in materials with uniformly weak grain boundaries. If the distribution of embrittling agent is not uniform, as for example occurs in some ceramic systems, then the dimensions of the embrittled region act to control the crack advance distance.

Systems exhibiting brittle intergranular fracture are often copious emitters of detectable acoustic emission. Crack radii are often 5 - 10 times those of cleavage microcracks and crack velocities are at least as high (and sometimes greater) than those during cleavage. Thus, acoustic emission strengths of 20 - 100 times those of cleavage are possible.

In composites, fiber delamination can be likened to intergranular fracture since an interface debond is the basic crack advance mechanism, and the crack advance distance can be many fiber diameters. Since fiber cleavage and debonding are two of the main damage accumulation processes in composite materials, it is clear that their damage evolution has a high acoustic emission detection probability and is the reason for the success of many acoustic emission monitoring activities in these materials.

2.4.4 Particle Microfracture

Some inclusions and precipitates in engineering alloys are brittle at ambient temperature and will undergo brittle (cleavage) fracture under tensile loading. The interface at these inhomogeneities is also often weak and frequently fails at low stress. The generation of acoustic emission from these microstructure constituents, then, depends upon the intrinsic properties of the particles: the strength of their interfaces and the

particle dimensions.

In steels, the fracture of manganese sulphide particles appears to be an important emission source, particularly in the absence of cleavage or intergranular failure modes. Ono et al²² have examined this source of emission in detail. They observed a strong orientation dependence of the emission from MnS inclusions. During hot rolling of steel, the inclusions are elongated in the rolling direction and flattened in the rolling plane forming an ellipsoidal shape. When stress was applied in the rolling plane along the prior rolling direction (L orientation), or perpendicular to the rolling direction (T orientation), very weak signals were observed. These signals apparently originated from cracks/disbonds over the minor axis of the ellipsoid. However, when the steel was tested so that stress was applied normal to the rolling plane (ST orientation), copious acoustic emission was observed, presumably associated with fractures extending over the major axis.

The sulfur content (i.e. number of inclusions), size and aspect ratio of the inclusions, together with the stress state, control the acoustic emission from inclusions. The inclusion size and shape is determined by the solidification pathway and by post solidification thermomechanical processing. In heavily rolled steels, with sulphur contents greater than about 0.06 wt%, manganese sulfide fractures associated with short transverse loading can be a significant emission source.

In many steels, crack growth occurs predominantly near welds where MnS has been melted and then reformed at interdendritic interstices during resolidification. If the sulphur content is high,

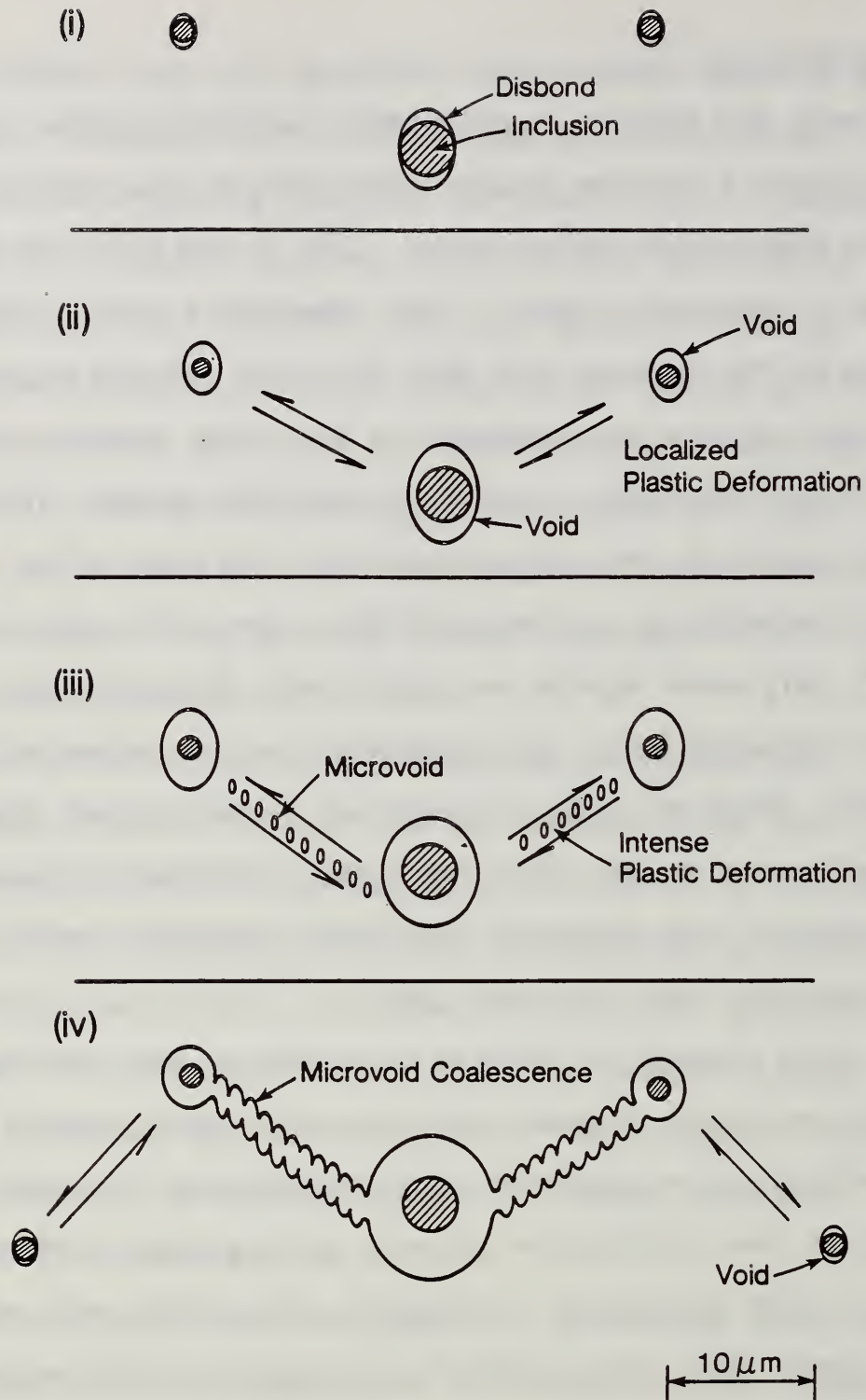


Fig. 13. The sequence of micromechanisms involved in the growth of a ductile crack. The process begins (i) with debonding at inclusion-matrix interfaces. (ii) Voids grow at the interface and plastic deformation localizes between adjacent voids. (iii) The intense deformation nucleates further microvoids at precipitate interfaces. (iv) Coalescence of the microvoids results in a ductile crack.

large elongated inclusions are deposited. These can subsequently become the site of defects such as lamellar tears. Since defect formation involves crack growth distances of $>10 \mu\text{m}$, they are substantial acoustic emitters.

Numerous types of inclusions of varying ductility are found in aluminum alloys. McK. Cousland and Scala²³ and others have found that only those that are rich in iron ore fracture at ambient temperature. These are found to give detectable signals and like the signals from MnS in steels, the amplitude distribution of the acoustic emission scales with size distribution of fracturing particles.

Precipitates, due to their smaller size, and (usually) reduced aspect ratio are less prone to fracture until very high stresses have been attained. Because of the small size (often $\sim <1 \mu\text{m}$) they are undetectable emitters. The exception has been in some specially heat treated steels containing large ($>5 \mu\text{m}$) spheroidal carbides, but these are not usually present in engineering alloys.

2.4.5 Microvoid Coalescence

Ductile fracture occurs by a sequence of processes, depicted schematically in Fig. 13.

- (i) Early during loading cracks/disbonds occur at inclusions, causing a stress concentration in the matrix between inclusions.
- (ii) Plastic deformation of inter-inclusion ligaments occurs resulting in the growth of the inclusion nucleated voids and an intensification of the local stress.

- (iii) Secondary voids are nucleated at finely distributed precipitates within the deforming ligaments.
- (iv) The secondary voids grow and link up resulting in a crack whose dimension is the inter-inclusion spacing.

The link-up of voids may occur by one of two modes. In materials with low yield strength and high work hardening capacity, the decrease in net load supporting area (due to void growth) is balanced by the increased flow stress (due to work hardening) of the deforming intervoid ligament. Under this stable condition, hole growth continues almost until the voids overlap. This quasi-static mode of coalescence is likely to be undetectable due to the very low crack growth velocity and small intercarbide ligament thickness. However, in materials with high yield strength and limited work hardening capacity, hole growth causes a loss of load supporting area that cannot be compensated by work hardening, and unstable strain ensues resulting in a premature shear coalescence. This latter process may occur at intermediate velocity over distances determined by the inter-inclusion separation (10-100 μm). This alternating shear is thus a potentially detectable source of acoustic emission.

The design of structures is usually based upon the premise that crack growth occurs by stable microvoid coalescence, and, therefore, efforts are made during materials selection and design to ensure that insufficient stress develop during service for this mode of fracture to exist. Should undetected defects exist in construction materials, or if a manufactured component is subjected to greater than

anticipated stress, ductile crack advance may occur. In tough low strength steels, only intermittent inclusion fractures will indicate this, and, if these inclusions are absent or the region ahead of the crack was appreciable prestressed in the past (e.g. during proof testing) so that inclusions are already fractured, the possibility exists for silent crack growth - a disconcerting phenomena to those interested in the use of acoustic emission for NDE purposes.

Today, given the improved quality of materials and fracture mechanics analyses, the likelihood of a ductile fracture failure is becoming rare. Rather, the emerging concern is that some kind of embrittling phenomenon occurs due to environmental effects. This reduces the materials resistance to crack growth and changes the mechanism of fracture from a ductile to brittle one; one that is often detectable. Thus, acoustic emission monitoring for these situations may well be worthy of further study.

2.4.6 Environmental Factors

The generation of detectable acoustic emission signals during environmentally assisted fracture such as hydrogen embrittlement, stress corrosion cracking and corrosion fatigue will depend upon the mechanism of crack extension favored. As an example of this, McIntyre and Green²⁴ have measured the acoustic emission per unit area of crack extension (dE/dA) in three ferritic steels under various environmental conditions. Under vacuum the ambient temperature fracture mode involves microvoid coalescence and, therefore, is not a major emission source. However, as shown in Table 3, considerable differences in emission/unit area were obtained through variation of grain size and environment.

TABLE 3

**EFFECT OF METALLURGICAL AND ENVIRONMENTAL VARIABLES ON dE/dA
FOR THREE FERRITIC STEELS**

Steel	Grain Size (Microns)	Fracture Mode	Environment	$dE/dA(10^{-2}V^2s/mm^2)$
817 M40	17	Intergranular	3.5% NaCl	9
"	100	"	"	108
"	17	"	H ₂ at 26600 Pa	31
897 M39	10	Transgranular	3.5% NaCl	5
"	10	"	H ₂ at 39000 Pa	2
"	10	"	H ₂ at 101000 Pa	1.5
AISI 4340	11	Intergranular	3.5% NaCl	31
"	200	"	"	210
"	11	"	H ₂ at 26600 Pa	37

During intergranular fracture the acoustic emission activity unit area was approximately proportional to grain size. For a fixed grain size, transgranular cleavage generated an order of magnitude less acoustic emission than the intergranular mode.

A great deal remains to be done to fully understand the role of environmental factors upon fracture micromechanisms and the ensuing acoustic emission. Nevertheless, it is evident that there exists considerable potential for acoustic emission, particularly when the favored crack advance mechanism involves intergranular failure, and the microstructure contains coarse grains.

2.4.7 Amplification Factors

In Section 2.4.1 it is shown that the acoustic emission amplitude is proportional to the crack face displacement w . In determining a detectability criterion it was assumed that w occurred only by elastic strain and that no plastic deformation

occurred. In practice, even brittle fractures have some associated dislocation emission at the crack tip. This plastic deformation is capable of allowing \underline{w} to increase beyond the value attained purely elastically. Indeed, it is quite common for \underline{w} to increase 1-3 orders of magnitude in low yield strength materials by crack tip flow processes. If this plastic deformation occurs entirely during the period of crack growth, then the acoustic signal emitted potentially could be amplified by the ratio of elastic to plastic crackface displacements.

A second source of signal enhancement stems from the relaxation of the faces of a precrack when microcrack extension occurs at its tip^{25,26}. Once again, we note that to first order the acoustic emission amplitude is proportional to the change in crack volume. If a microcrack occurs at the tip of a pre-existing crack, the volume in question is now the sum of the microcrack volume and the change in macrocrack volume facilitated by its crack tip extension. This factor may amplify the microcrack signals by 1-3 orders of magnitude, and also seriously affects the spectrum of the emitted wavefield.

2.5 Microscopic Phase Changes

2.5.1 Solid State Phase Transformations

Solid state phase transformations almost invariably cause the development of an internal stress due to density, modulus and thermal contraction differences between the different phases of an alloy. Consequently, we expect that the development of the stress field itself together with microfracture, microplasticity or other mechanisms by which the stress field is relaxed (e.g., loss of coherency) are potential sources of acoustic emission.

Speich and Schwoeble²⁷ have systematically investigated the effect of cooling rate on the acoustic emission accompanying the austenite-ferrite transformation in plain carbon steels. As the cooling rate increased, the reaction products changed from pearlite through bainite to martensite. Their observations are summarized in Table 4.

TABLE 4

ACOUSTIC EMISSION DURING CONTINUOUS COOLING OF PLAIN CARBON STEEL		
Transformation product	Phase transformations	Acoustic emission activity
Pearlite	Diffusion-controlled simultaneous growth of lamellar ferrite and cementite	None detectable
Bainite	Diffusion-controlled growth of small carbides (<1 μm) and lath ferrite	None detectable
Martensite	Diffusionless transformation in which laths or plates typically 20 μm in diameter and several micrometers thick transform from f.c.c. to body-centered tetragonal structure at 10-80% of the shear wave speed.	Very energetic signals detected

From their work it is clear that the diffusion-controlled nucleation and growth of ferrite and carbides, while probably

causing the development of appreciable stresses, fail to generate detectable elastic waves in the acoustic emission range of frequencies. However, the diffusionless transformation of austenite to martensite, is easily detectable and provides the basis for a simple non-destructive method of deducing, M_S , the temperature at which martensite starts to form on cooling and, M_f , (the temperature at which martensite formation on cooling is essentially completed).

2.5.2 Detectability of Martensitic Transformations

Martensitic transformations are diffusionless changes of phase involving local shear and dilatations that cause changes of shape. In some respects they are similar to the formation of deformation twins in that both involve invariant planes of strain, i.e., the region that transforms has a characteristic habit plane, \underline{h} , with components h_j defined by:

$$h_j x_j = 0 \quad \text{and} \quad h_1^2 + h_2^2 + h_3^2 = 1 \quad (29)$$

The plane of a twin is usually a low index rational plane; that of martensite, however, is usually not. In addition to the habit plane, there is also a characteristic deformation direction \underline{d} , defined with $|\underline{d}| = 1$ and a deformation magnitude m proportional to the distance from the habit plane. The invariant plane strain then takes the matrix form: $I + m\underline{d}\underline{h}^t$ where \underline{d} and \underline{h} are each column vectors, and t stands for transpose.

For the deformation twinning case the habit plane is a twinning plane (e.g. $\{112\}$) and the deformation direction a twinning direction (e.g. $\langle 111 \rangle$). The subsequent transformed region, thus, has

the same lattice as the parent phase, and is only transformed by one of the point group symmetry properties of the parent phase (e.g. it may be a mirror image of the surrounding phase).

In a martensitic transformation, the lattice structure of the transformation product is different to that of the parent phase. The habit plane is usually irrational and the deformation direction may not be coplanar with the habit plane which results in a nonzero volume change (dilatation). Thus, the region that transforms undergoes a change of shape. This change of shape is a mechanism for the generation of acoustic emission, and given \underline{m} , \underline{h} and the initial shape, we could evaluate the source function as discussed above.

However, this would fail to incorporate important other effects. First the change of shape occurs in a constraining medium so that (residual) stresses form which interact with the change in elastic constants of transformed region to generate further emission. If the value of \underline{m} is small, the residual stress can be accommodated elastically leading to a thermoelastic transformation. However, often the stress is such that considerable plastic deformation and twinning occur. These can be additional emission sources. Also, the change of shape is different to that of the unconstrained case. Thus, in attempting to predict acoustic emission from martensite, care must be taken in choosing the appropriate shape change.

The expression for the stress change associated with the martensitic transformation of an ellipsoidal region of volume v has been derived by Simmons and Wadley²⁸:

$$\overline{\Delta\sigma}(t) = [I + \Delta CD]^{-1} [(C + \Delta C)\beta^* - \Delta C\beta^0] v(t) \quad (30)$$

where C is the stiffness matrix (using Voigt notation) of the parent phase, $C + \Delta C$ that of martensite, β^* the unconstrained shape change, β^0 any pre-existing elastic strain (from an imposed stress or nearby source of residual strain) and D is a shape matrix.

Examination of equation (30) reveals that six factors associated to the transformation affect the acoustic emission:

- Volume of region transformed.
- Dilation strain.
- Shear/rotational strain.
- Habit plane.
- Residual stresses (through interaction with ΔC).
- Time dependence of the transformation.

Equation (30) can be considerably simplified if we suppose ΔC is very small (it is actually unknown for most transformations):

$$\overline{\Delta\sigma}(t) \sim C\beta^*v(t) \quad (31)$$

This is an expression very similar to that deduced for a plastic deformation.

To get some idea of the type and magnitude of acoustic emission signals from actual martensitic transformations we need data concerning the change of shape. Dunne and Bowles²⁹ have made careful measurements of this at the surface of an Fe-21.89°Ni-0.82°C alloy. (Caution: it may however be different internally.)

They find for one case studied that

$$\underline{h} = \begin{pmatrix} 0.1752 \\ 0.5550 \\ 0.8131 \end{pmatrix} \quad \underline{d} = \begin{pmatrix} -0.2006 \\ -0.6550 \\ 0.7284 \end{pmatrix} \quad (32)$$

and the magnitude of the plane strain vector, $m = 0.19$.

We shall assume isotropic elasticity and estimate values for λ and μ from Ledbetter and Reed³⁰: $\lambda = 10.5 \times 10^{-2} \text{ MNmm}^{-2}$, and $\mu = 7.3 \times 10^{-2} \text{ MNmm}^{-2}$. If $\rho = 8.09 \times 10^3 \text{ Kgm}^{-3}$, then $a = 5.57 \text{ mm}\mu\text{s}^{-1}$ and $c = 3 \text{ mm}\mu\text{s}^{-1}$.

To fully predict the source function we need to know the velocity surface of the transformation. The mechanism of growth of a region of martensite is very poorly understood, but it is generally thought that the velocity in the habit plane is much greater than that in the perpendicular direction. Here, we shall consider an ellipsoidal shaped region with a circular habit plane in which the radial velocity is independent of direction and has a value of $2 \text{ mm}\mu\text{s}^{-1}$ while the rate of semi-axis growth perpendicular to the habit plane is assumed 10% of this.

Thus:

$$\begin{aligned} v(t) &= (3.2)\pi t^3 \quad \text{mm}^3 \\ v(t) &= 10t^2 \quad \text{mm}^3\mu\text{s}^{-1} \end{aligned}$$

From equation (31) we can write that the stress change rate is:

$$\dot{\Delta\sigma}(t) = t^2 \begin{bmatrix} -0.0287 & -0.0157 & -0.0244 \\ -0.0159 & -0.0623 & -0.0089 \\ -0.0244 & -0.0890 & 0.2032 \end{bmatrix} \text{ MNmm}\mu\text{s}^{-1} \quad (33)$$

Using the method described in 2.2, we can identify the principal values of the stress change:

$$\Delta\sigma(t) = t^2 \begin{bmatrix} 0.176 & 0 & 0 \\ 0 & 0.085 & 0 \\ 0 & 0 & 0.550 \end{bmatrix} \text{ MNmm}\mu\text{s}^{-1} \quad (34)$$

where the associated directions are such that the third principle direction is parallel to the x_3 axis (the [001] crystallographic axis), while the others lie in the x_1, x_2 plane, but rotated 80.46° in the clockwise sense.

Rotation about the [001] axis enables achievement of maximum vertical and horizontal displacements at epicenter. Both displacement components have a parabolic time dependence, like that of the microcrack case considered earlier.

Assuming the source to be 40 mm beneath epicenter, we can estimate, as before, that for a vertical displacement transducer with 5 MHz bandwidth, 10^{-11} mm sensitivity and $\tau = 0.3t$, the smallest detectable -- if optimally oriented -- lath has a $3.25 \mu\text{m}$ diameter and a growth time of 1.62 ns. Of course, since in this case one principle stress change value is negative, a direction will exist in which no vertical (out of plane) signal is generated.

The maximum horizontal motion occurs in a plane containing the [001] direction at 80.46° from [100] in a clockwise sense. Using identical bandwidth and sensitivity, the smallest detectable lath of optimal orientation would have a $1.6 \mu\text{m}$ diameter and a 0.8 ns growth period. Since all the principle stress change values differ, a horizontal displacement occurs for all orientations. It can be shown that a $2.25 \mu\text{m}$ diameter lath can produce a detectable horizontal displacement even when oriented such that the weakest signal propagates to the receiver.

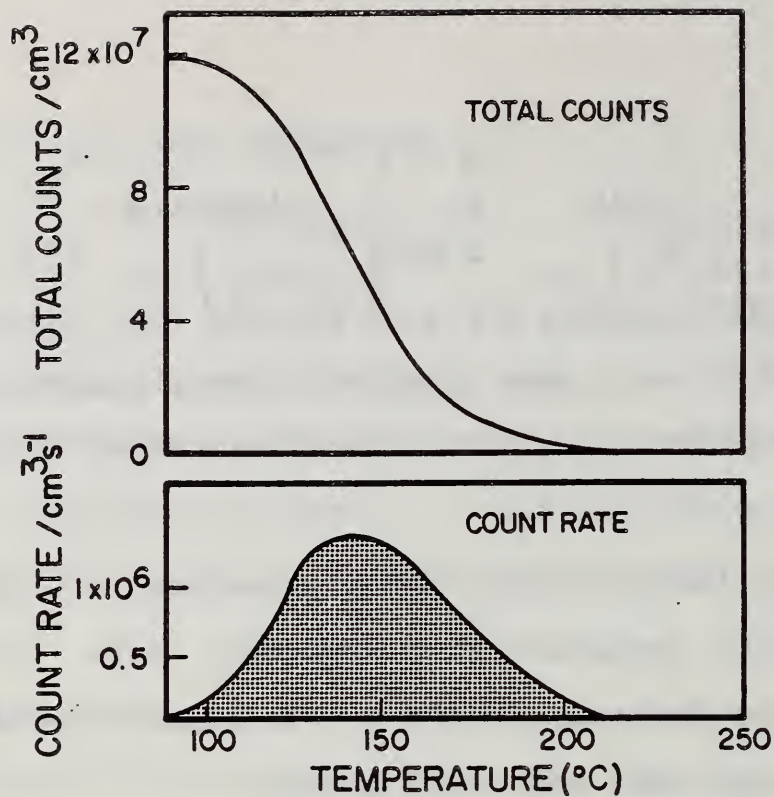


Fig. 14. On cooling a high carbon steel ($M_S \sim 200^\circ\text{C}$) acoustic emission signal (counts) are detected.

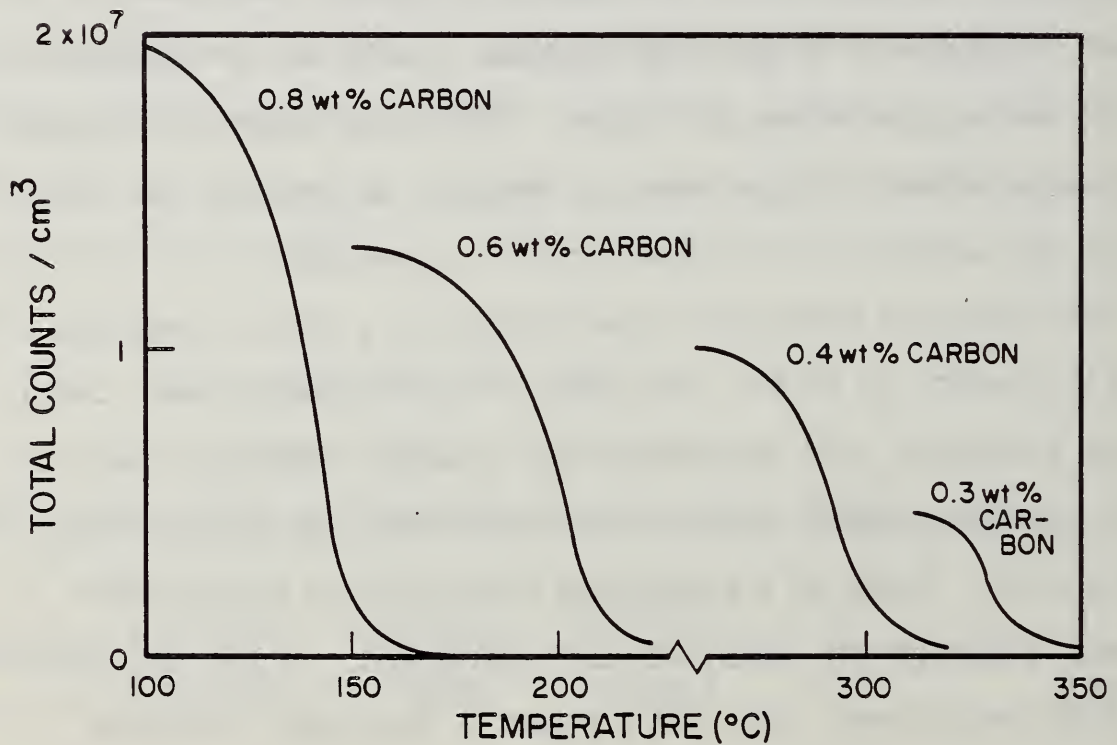


Fig. 15. The total number of martensite generated by acoustic emission signals per unit volume is dependent upon carbon content in Fe-base (here 4300 series) alloys. The M_S temperature also decreases with increasing carbon concentration.

Acoustic emission techniques are very useful for following the kinetics and measurement of the dynamics of martensitic transformations. For example, in Fig. 14 the acoustic emission emitted during the continuous cooling of a high carbon steel is shown. M_S for this steel was about 200°C; only a few acoustic emissions were generated above this temperature, possibly associated with a local stress-assisted transformation. As the temperature continued to decrease below M_S , increasing rates of emission were observed, each emission presumably associated with the rapid growth of a martensitic plate across an austenite grain. The maximum transformation rate appeared to be about 60°C below M_S and emission ceased entirely at about 100°C below M_S .

The observation that intense acoustic emission signals are emitted at the beginning of martensite transformations has been used by Ono et al³¹ to measure M_S values as part of an alloy development program. They reported M_S values for numerous steel alloys with different compositions and microstructures and report the technique to be a simple accurate method for deducing martensite transformation temperatures. They also reported that the acoustic emission accompanying the transformation was extremely sensitive to the microscopic processes involved in the transformation.

The carbon concentration of low alloy steels²⁷ has a very strong effect on both the temperature dependence of the emission during continuous cooling and the number of detectable signals per unit volume, Fig. 15. The temperature dependence of the emission is consistent with the decrease in M_S with increasing carbon

concentration. The effect of carbon concentration on the number of detectable signals, however, is more likely to be a manifestation of changes in the dynamics and morphology of the martensite transformation.

Cold work also influences the acoustic emission during the martensitic transformation of steel. The nature of the cold work effect is very sensitive to the carbon and nickel concentrations which control martensite morphology and the transformation kinetics. The cold work effect, like the carbon concentration effect resides in changes to the morphology and dynamics of individual martensitic transformations. Further measurements of the individual signals may provide a much improved understanding of this aspect of the martensite transformation. Measurements of the rate at which emission is detected, which measures the rate at which laths form, may throw light on the kinetics of the transformation, and particularly on auto-catalytic phenomena where they occur.

While almost all solid state phase transformations result in the development of internal stresses, only those associated with rapid martensitic transformations apparently generate detectable elastic waves directly. However, plastic deformation and even fracture are sometimes induced by internal stresses, providing indirect detection of their development.

For example, rapidly cooled high carbon steels have a very high internal stress which is normally relieved by a tempering treatment that allows dislocation and impurity atom migration. Shea and Harvey³² have observed, using acoustic emission methods, that

isothermal tempering at too low a temperature will result in micro-cracking, believed to be due to impurity atoms locking of dislocations.

Similarly, while the development of stress in and around a second-phase precipitate has so far not proven directly detectable by acoustic emission methods Cannelli and Cantelli³³ have observed signals from hydride precipitates of niobium, tantalum and vanadium as they relax this localized stress by fracture and adjacent lattice plastic deformation, Fig. 16. These results suggest that there may well be some merit in researching the use of acoustic emission techniques to detect the point during aging when the coherency stresses of small precipitates are relaxed by the formation of interfacial dislocation structures around semicoherent precipitates (e.g. when $\theta'' \rightarrow \theta'$ in the Al-Cu system). The prismatic punching of dislocation loops during precipitation and cooling in other alloy systems (e.g. Mo-C) might also be worthy of investigation.

Magnetic domain walls in ferromagnetic materials can be induced to move by the application of magnetic fields. This is accompanied by electromagnetic emission (the Barkhausen effect). The motion of these walls under the action of monotonic or alternating magnetic fields has also been found to generate elastic radiation (acoustic emission), the details of which have been found to be dependent on microstructure variables such as dislocation density and carbide distribution. It has been suggested that measurement of this emission would provide a non-destructive method of microstructure characterization. Ono and Shibata³⁴ have also been able to estimate the residual stress for a given

microstructure state since the emission from domain wall motion is sensitive to the stress state. The potential also exists to determine other microstructure information if residual stresses are absent.

2.5.3 Liquid-Solid Transformations

There have been few studies of acoustic emission during solidification. Work on Pb-Sn and Sn-Bi³⁵ indicate the generation of acoustic emission signals when solidification conditions are such that interdendritic porosity (solidification shrinkage of the final interdendrite liquid) occurs. The emission associated with this process is very intense, although the precise physical mechanism is unclear. This work indicates that the plastic deformation of primary dendrites could also generate low intensity acoustic emissions.

TABLE 5

**SUMMARY OF RESULTS FOR SOLIDIFICATION EMISSION OF
AL-4.5wt. %Cu-0.2wt.%Ti ALLOY**

H ₂ contents per 100 g at STP (cm ⁻³)	Total acoustic emission count	Pore fraction %
0.05	1.05 x 10 ⁴	0.19
0.17	2.75 x 10 ⁴	0.46
0.23	6.35 x 10 ⁴	0.63

Feurer and Wunderlin³⁶ measured the acoustic emission during solidification of an Al-4.5wt.%Cu-0.2wt.%Ti alloy and observed acoustic emission generated, they believed, by the formation of porosity. They varied the volume fraction of porosity by adjusting the hydrogen content of the melt and found that the solidification

acoustic emission was proportional to the volume fraction of porosity (Table 5).

They considered the emission to be generated by the unstable formation of hydrogen "bubbles" in the melt close to the liquid-solid interface. The lower hydrogen solubility of solid aluminum results in a hydrogen supersaturation in the melt close to the liquid-solid interface. The relief of this supersaturation acts as the driving force for hydrogen bubble formation in an analogous role to that of strain energy reduction in the formation of cracks. This dilation source then radiates longitudinal elastic waves that are transmitted through the liquid-solid interface and are ultimately detected by a transducer as acoustic emission.

Rapid solidification, where solidification occurs at speeds up to 1 or 2 ms^{-1} , has become a vigorous area of research because of the advantageous properties that may be achieved through refined microstructure and homogeneous distributions of alloy elements. There is a pressing need for process control sensors that could characterize microstructure and measure process variables during solidification.

Clough et al³⁷ have made acoustic emission measurements on aluminum alloys during pulsed electron beam melting-solidification. It has been found that acoustic emission signals are emitted during solid state electron beam heating (because of thermoelastic effects similar to those well known to be responsible for laser generation of elastic waves), melting and resolidification. The acoustic emission emitted during resolidification, following beam cut-off after attainment of a steady state temperature field, increases in

this situation with the electron flux, probably as a result of the increased volume of resolidifying metal. For a given melt depth the acoustic emission from an aluminum alloy (2219) is up to 100 times more energetic than that from nominally pure aluminum (alloy 1100) Fig. 17.

Metallographic studies on the copper containing 2219 alloy indicated the occurrence of solidification cracking and coarse slip bands. Both phenomena were absent in the commercial purity aluminum (alloy 1100). These results indicate that the large solidification and thermal contraction stresses set up during rapid solidification are responsible for plastic deformation in both materials. The acoustic emission from dislocations is very weak in the fine-grained aluminum alloy 1100 whereas in alloy 2219 it is much stronger. Work by Hsu and Ono³⁸ indicates that dislocation motion in aluminum alloys at high temperatures generates more energetic emission than dislocation motion at room temperature. This, together with the additional emission of hot tearing, is considered to result in much greater levels of detectable emission.

References

1. J.A. Simmons and R.B. Clough "Theory of Acoustic Emission" in Proc. Int. Conf. Dislocation Modelling of Physical Systems, J. Hirth and M. Ashby Eds, Pergamon Press 1981.
2. J.E. Sinclair, J. Phy. D., 12, p. 1309, 1979.
3. J. A. Simmons and H.N. G. Wadley, Unpublished Work.
4. C.B. Scruby, H.N.G. Wadley, J.E. Sinclair, Phil. Mag. A44, p. 240, 1981.
5. C.B. Scruby, C. Jones, J.M. Titchmarsh and H.N.G. Wadley, Met. Sci. 15, p. 241, 1981.
6. K. Aki and P.G. Richards, Quantitative Seismology, W.H. Freeman, San Francisco, 1980.
7. L.E. Drain, J.H. Speake and B.C. Moss, SPIE, 136, p. 52, 1977.
8. C.B. Scruby and H.N.G. Wadley, J. Phys. D, 11, p. 1487, 1976.
9. J.A. Simmons ,Christian D. Turner and H.N.G. Wadley, J. Acoust. Soc. Am. 82 (4), 1987.
10. J.D. Eshelby, "The Continuum Theory of Lattice Defects", in Solid State Physics, F. Seitz and D. Turnbull, Eds, 3, p. 79, 1956, Academic Press.
11. E. Kroner, Erg. Angew. Math, 5, p. 1, 1958.
12. N. Haskell, Bull. Seism. Soc. Am. 54, p. 1811, 1964.
13. R. Burridge and L. Knopoff, Bull. Seism. Soc. Am., 54, p. 1875, 1964.
14. H.N.G. Wadley, C.B. Scruby and J. H. Speake, Int. Met. Rev., 25, (2), p. 41, 1980.
15. N. Kiewewetter and P. Schiller, Phys. Status Solidi A, 48, p. 439, 1978.

16. P. Fleischman, F. Lakestani, J.C. Baboux and D. Rouby, *Mat. Sci. Eng.* 29, 205, 1977.
17. R.C. Bill, J.R. Frederick and O. K. Felbeck, *J. Mat. Sci.*, 14, p. 25, 1977.
18. K. L. Rusbridge, C.B. Scruby and H.N.G. Wadley, *Mat. Sci. Eng.*, 59, 151, 1983.
19. C.B. Scruby, H.N.G. Wadley and K.L. Rusbridge, *Mat. Sci. Eng.*, 59, 169, 1983.
20. S. Hsu and K. Ono, "Acoustic Emission of Plastic Flow - II Alloys", in *Proc. 5th Int. Acoustic Emission Symp.*, Tokyo, p. 294, 1980.
21. H.N.G. Wadley, C.B. Scruby, P. Lane and J.A. Hudson, *Met. Sci.*, 15, p. 514, 1981.
22. K. Ono, M. Shibata and M. A. Hamstad, *Met. Trans.*, 10A, p. 761, 1979.
23. S. McK. Cousland and C.M. Scala, *Met. Sci.*, 15, p. 609, 1981.
24. P. McIntyre and G. Green, *Brit. J. NDT*, p. 135, 1978.
25. Achenbach, J. D. and J. G. Harris, *Jour. App. Mech.* (46), p. 107, 1979.
26. H.N.G. Wadley and C. B. Scruby, *Int. J. Fract.*, p. 117, 1983.
27. G.R. Speich and A. J. Schwoeble, *ASTM Spec. Tech. Publ.* 571, p. 40, 1975.
28. J.A. Simmons and H.N.G. Wadley, *Theory of Acoustic Emission from Inhomogeneous Inclusions in Wavepropagation in Homogeneous Media and Nondestructive Evaluation*, G.C. Johnson, Ed., *AMD-62*, p. 51, ASME, New York, 1984.
29. D. P. Dunne and J.S. Bowles, *Acta. Met.* 17, p. 201, 1969.
30. H.M. Ledbetter and R. P. Reed, *Mat. Sci. and Eng.* 5 (6), p. 341, 1970.

31. K. Takashima, Y. Higo and S. Nunomura, Acoustic Emission during the Martensitic Transformation of 304 Stainless Steel in Proc. 5th Int. Acoustic Emission Symposium, Tokyo, p. 261, 1980.
32. M.M. Shea and D. J. Harvey, Scr. Met. 16, p. 135, 1982.
33. G. Cannelli and R. Cantelli, Acoustic Emission Stimulated by Hydride Formation in Niobium, Tantalum and Vanadium, in Advances in Acoustic Emission, H.L. Dunegan and W.F. Hartman (Eds), p. 330, 1981, Dunhart, Knoxville.
34. K. Ono and M. Shibata, NDT International, p. 227, Oct. 1981.
35. H.M. Tensi and W. Radtke, Metall. 32 (7), p. 681, 1978.
36. J. Feurer and R. Wunderlin, Proc. Int. Conf. on Solidification and Casting, 2, Metals Society, p. 18, 1977, London.
37. R.B. Clough, H.N.G. Wadley and R. Mehrabian, Heat Flow-Acoustic Emission-Microstructure Correlations in Rapid Surface Solidification, in Proc. 2nd Int. Conf. on Use of Electron and Laser Beams for Metals Proc., E.A. Metzbower (Ed), p. 37, 1983, ASM, Metals Park.
38. S.Y.S. Hsu and K. Ono, Acoustic Emission of Plastic Flow - I. Metals. Proc. 5th Int. Acoustic Emission Symposium, Tokyo, p. 283, 1980.

U.S. DEPT. OF COMM. BIBLIOGRAPHIC DATA SHEET <i>(See instructions)</i>	1. PUBLICATION OR REPORT NO. NBSIR 87-3630	2. Performing Organ. Report No.	3. Publication Date March 1988
4. TITLE AND SUBTITLE Composite Materials Interface Characterization			
5. AUTHOR(S) Wadley, Simmons, Clough, Krasicka, Biancaniella, Rosen, Hsieh			
6. PERFORMING ORGANIZATION <i>(If joint or other than NBS, see instructions)</i> NATIONAL BUREAU OF STANDARDS U.S. DEPARTMENT OF COMMERCE GAITHERSBURG, MD 20899		7. Contract/Grant No.	8. Type of Report & Period Covered
9. SPONSORING ORGANIZATION NAME AND COMPLETE ADDRESS <i>(Street, City, State, ZIP)</i>			
10. SUPPLEMENTARY NOTES <input type="checkbox"/> Document describes a computer program; SF-185, FIPS Software Summary, is attached.			
11. ABSTRACT <i>(A 200-word or less factual summary of most significant information. If document includes a significant bibliography or literature survey, mention it here)</i> Interfaces and interface zones in composites are studied using ultrasonic and acoustic emission techniques on models of single reinforcing elements in a matrix. The theory of ultrasonic scattering and guided interface waves is developed for a model composite with a planar, cylindrical or spherical interface zone with viscoelastic properties varying in a direction perpendicular to the interface zone. Experimental confirmation was carried out for both the planar and cylindrical geometrics with a perfect interface. Both Stoneley and leaky waves were detected on the planar geometry for a Steel-Ti system. Leaky waves were quantitatively measured in the cylindrical geometry for steel fibers in aluminum and were detected for SiC fibers in aluminum. By using specially designed specimens of SiC fibers in aluminum, acoustic emission and tensile testing permitted determination of fiber and interface strengths as well as adhesive energy and fracture toughness. The results show that interface mechanical properties are sensitive to processing variables. Acoustic emission provides an effective technique for discriminating between failure mode types such as fiber fracture or delamination.			
12. KEY WORDS <i>(Six to twelve entries; alphabetical order; capitalize only proper names; and separate key words by semicolons)</i> acoustic emission; Al-SiC; Al-Steel; composites; fiber reinforced composites; guided interface waves; interface; interphase; leaky waves; shear lag model; Stoneley waves; ultrasonics			
13. AVAILABILITY <input checked="" type="checkbox"/> Unlimited <input type="checkbox"/> For Official Distribution. Do Not Release to NTIS <input type="checkbox"/> Order From Superintendent of Documents, U.S. Government Printing Office, Washington, D.C. 20402. <input checked="" type="checkbox"/> Order From National Technical Information Service (NTIS), Springfield, VA. 22161		14. NO. OF PRINTED PAGES 205	15. Price \$24.95

